

NORTHWESTERN UNIVERSITY

Homogeneous Metallocene-Mediated Propylene Polymerization:
Catalyst Symmetry, Ion-Pairing, and Counteranion Effects on
Polymerization Kinetics, Selectivity, and Specificity.

A DISSERTATION

SUBMITTED TO THE GRADUATE SCHOOL IN PARTIAL
FULFILLMENT OF THE REQUIREMENTS

for the degree

DOCTOR OF PHILOSOPHY

Field of Chemistry

By

JOHN ANDREW STEVENS ROBERTS

EVANSTON, ILLINOIS

December 2006

ABSTRACT

Homogeneous Metallocene-Mediated Propylene Polymerization:
Catalyst Symmetry, Ion-Pairing, and Counteranion Effects on
Polymerization Kinetics, Selectivity, and Specificity.

JOHN ANDREW STEVENS ROBERTS

Counteranion effects on the rate and stereochemistry of propylene polymerization mediated by ion-pair complexes derived from dimethylzirconocene precatalysts activated with strongly Lewis-acidic perfluoroarylmatalloid cocatalyst/activators are shown to arise from the strength of the cation-anion interaction. This is quantified using C_S -symmetric $\text{Me}_2\text{C}(\text{Cp})(\text{Flu})\text{ZrMe}_2$ ($\text{Cp} = \text{C}_5\text{H}_4$, η^5 -cyclopentadienyl; $\text{Flu} = \text{C}_{13}\text{H}_8$, η^5 -fluorenyl) and C_1 -symmetric $\text{Me}_2\text{Si}(\text{OHF})(\text{CpR}^*)\text{ZrMe}_2$ ($\text{OHF} = \text{C}_{13}\text{H}_{16}$, η^5 -octahydrofluorenyl; $\text{CpR}^* = \eta^5$ -3-(-)-menthylcyclopentadienyl, $\text{R}^* = (1R,2S,5R)$ -*trans*-5-methyl-*cis*-2-(2-propyl)cyclohexyl; ((-)-menthyl) precatalysts activated using a broad family of mononuclear and polynuclear perfluoroarylborate, -aluminate, and -gallate cocatalysts/activators, including $\text{B}(\text{C}_6\text{F}_5)_3$, $\text{B}(o\text{-C}_6\text{F}_5\text{C}_6\text{F}_4)_3$, and $\text{Al}(\text{C}_6\text{F}_5)_3$, trityl salts $\text{Ph}_3\text{C}^+ \text{B}(\text{C}_6\text{F}_5)_4^-$ and $\text{Ph}_3\text{C}^+ \text{FAl}(o\text{-C}_6\text{F}_5\text{C}_6\text{F}_4)_3^-$, *in situ* generated $\text{Ga}(\text{C}_6\text{F}_5)_3$, and new mono- and polymetallic trityl perfluoroarylhalometallate salts $\text{Ph}_3\text{C}^+ \text{FB}(\text{C}_6\text{F}_5)_3^-$, $\text{Ph}_3\text{C}^+ \text{FB}(o\text{-C}_6\text{F}_5\text{C}_6\text{F}_4)_3^-$, $(\text{Ph}_3\text{C}^+)_x \text{F}_x[\text{Al}(\text{C}_6\text{F}_5)_3]_y^{x-}$ ($x = y = 1$; $x = 1, y = 2$; $x = 2, y = 3$), $\text{Ph}_3\text{C}^+ (\text{C}_6\text{F}_5)_3\text{AlFAl}(o\text{-C}_6\text{F}_5\text{C}_6\text{F}_4)_3^-$, $\text{Ph}_3\text{C}^+ \text{XAl}(\text{C}_6\text{F}_5)_3^-$ ($\text{X} = \text{Cl}$; $\text{X} = \text{Br}$), and $\text{Ph}_3\text{C}^+ \text{F}[\text{Ga}(\text{C}_6\text{F}_5)_3]_2^-$. Catalyst system cation-anion interaction strength is of central importance in determining monomer insertion rates as well as competing misinsertion, reorganization, and

chain release reactions, thus determining polymer physical characteristics such as overall tacticity and molar mass. This is demonstrated by fixing the metallocene precatalyst and modulating the perfluoroarylmetalloid cocatalyst, giving a series of ion-pair species showing a wide range of cation-anion binding characteristics. Systematic cocatalyst/counteranion dependences of the *individual rates* of different monomer insertion, misinsertion, catalyst ion-pair reorganization, and chain release processes are first quantified in syndiospecific propylene polymerizations catalyzed by systems using C_S -symmetric precatalyst $\text{Me}_2\text{C}(\text{Cp})(\text{Flu})\text{ZrMe}_2$. Generality is then shown to extend to isospecific polymerizations catalyzed by systems based on C_1 -symmetric analog $\text{Me}_2\text{Si}(\text{OHF})(\text{CpR}^*)\text{ZrMe}_2$. Structural and dynamic features of the present catalyst complexes are determined by single-crystal X-ray diffractometry and one- and multidimensional Nuclear Magnetic Resonance spectroscopy. Polymerization behavior is gauged by examination of the product polymer materials, including polymer end-group morphologies, polymer molar mass distributions, melt behavior, and, most importantly, polymer production rates and the distribution of stereosequences in the polymer backbone. Modeling of these stereosequence distributions constitutes the primary tool for determination of absolute rates for a collection of reaction pathways proposed to be available during polymerization, and establishes the relationships between these rates and strength of ion-pairing in the catalyst systems.

ACKNOWLEDGEMENTS

This thesis follows a line of research that was begun in 2001 by Prof. Ming-Chou (Mike) Chen, National Central University, Jhong-Li, Taiwan, then a postdoctoral associate with Prof. Tobin J. Marks, Northwestern University, Evanston, IL USA, the corresponding author of each publication presented herein. Your author joined this effort in 2003, and completed the last of the series' three articles in 2006. The preparation, isolation, and characterization of precatalysts, cocatalysts, and ion-pair complexes, including development of methodologies and determination of attractive targets was accomplished by Prof. Chen with later assistance on ones own part. This formidable collection of novel chemicals represents a mastery of synthetic organometallic chemistry typical of endeavors within Prof. Marks' research group. In several instances, detailed examination beyond basic one-dimensional Nuclear Magnetic Resonance spectroscopy of the present catalyst systems was warranted; this was accomplished with generous assistance from Dr. Yuyang Wu, Northwestern Univ. Dept. of Chemistry Analytical Laboratories. Related work on solution-phase ion pairing phenomena was carried out contemporaneously by Dr. Crisitano Zuccacia, Univ. of Perugia, Italy, and Dr. Nicholas Stahl, Intel Inc., respectively a former postdoctoral associate and a former graduate student of Prof. Marks'. This work, along with Prof. Chen's and my many in-depth discussions with Drs. Stahl and Zuccacia, contributed immeasurably to our general understanding of ion pairing. Some 14 crystal structures of both cocatalysts and ion-pair complexes appear throughout the manuscripts, and constitute a significant portion of the present work. Isolation of the crystal samples, determination of structural solutions, and structure analyses are the result of the combined work of Prof. Chen, Dr. Charlotte Stern, Northwestern Univ. Analytical Laboratories, and oneself.

PREFACE

The first and second chapters, published as of this writing, and the last, submitted for peer review, are presented here in the order of their submission for publication and constitute a series, with each building on the one before it. The chapters focus both on the catalyst species themselves and on their available reaction pathways, and detail how these catalyst systems mediate the propylene polymerization reactions described herein. These catalyst systems are ion-pair complexes generated via reaction of group 4 dimethylmetallocene derivatives with very strongly Lewis-acidic molecular activators, the latter generally effecting partial or complete abstraction of one methide ligand from the former to yield a highly reactive “contact ion-pair,” i.e. an ion-pair system in which the cation and anion substantially interact with one another in ways that significantly influence catalyst reactivity when dissolved in low-polarity media. The notion of a contact ion-pair encapsulates a broad array of possible modes of cation-anion interaction, and the nature of the cation-anion interaction appears to be one of the key elements in the structure-function relationship that dictates the shape of the “polymerization reaction” coordinate surface. The term “polymerization reaction” is our descriptor for the conversion of propylene into polypropylene, which in the present cases consists of a variety of different bond-breaking and bond-forming pathways, each contributing to the product polymer’s microstructural features and molar mass distribution, and each having its unique dependency upon the structure of the catalyst, and particularly on the nature of the all-important cation-anion interaction. That this interaction is important follows naturally from the following observations: a) that the chemical bond rearrangements that convert propylene into polypropylene are all mediated at a transient coordination vacancy at the cation’s metal center, and b) that this transient coordination vacancy is at times also occupied by the anion.

The central hypothesis of the present work is that cation-anion interactions in these catalyst systems affect polymerization reaction kinetics in a systematic way, attenuating reactivity inasmuch as the cation-anion interaction is strong. This hypothesis is appraised first in a limited series of related cases, by fixing the proto-cation (the “precatalyst”) and modulating the proto-anion (the “cocatalyst”), which gives a class of related ion-pair species whose physical and chemical properties are examined with regard to ion pairing, both in isolation and in conditions in which polymerization catalysis is possible. This hypothesis is tested in the first chapter using a small collection of related systems having properties that make them ideal for a combined analytical (of the catalysts themselves) and kinetic (of their catalytic behavior) approach. The second chapter introduces a totally novel collection of cocatalysts whose defining characteristic is the presence of reactive metal-halogen bonds and the involvement of these bonding interactions in activation *and* catalytic chemistry. This, together with the introduction of a second, substantially different proto-cation, broadens considerably the collection of available ion-pair complexes, and allows for the broadening and generalizing the central hypothesis, which task is accomplished in the third chapter.

The present work relies on combined observations of the catalysts in isolation and of their catalytic behavior. It is self-evident that the catalytically active species are *not* chemically identical to the species that arise immediately on reaction of the precatalyst with the cocatalyst. So, any correlation between *ex-situ* and *in-situ* catalyst features requires the invocation of a collection of assumptions concerning the details of catalyst chemistry. Invoking these assumptions requires their identification and in each instance an assessment of their strength; these tasks are undertaken on a thoroughgoing basis. Moreover, in contrast to systems in which the concentrations of specific participants can be followed as catalysis is happening, the present

systems are gauged by examination of the distribution of detectable features in the product polymer materials *after* catalysis has been terminated. This approach relies on the reasonable assumption that product polymer macroscopic properties such as molar mass averages and melting behavior, and also the relative abundances of atomic-level structural features (“microstructure”) within the polymer backbone, are substantially invariant with respect to termination of catalysis and product workup. The aforementioned microstructural features arise only when a prochiral monomer such as propylene is employed, and in the present work this particular substrate is employed in exclusivity.

What ensues is as much a journey as a report, one which your author sincerely hopes will be as interesting and enlightening to you the reader as to the scientists who have participated in its undertaking.

TABLE OF CONTENTS

List of Figures	11
List of Tables	15
List of Schemes	20
List of Appendices	21
Chapter 1.	22
Marked Counteranion Effects on Single-Site Olefin Polymerization Processes. Correlations of Ion Pair Structure and Dynamics with Polymerization Activity, Chain Transfer, and Syndioselectivity.	
Introduction	24
Experimental Section	29
Results and Discussion	42
I. Zirconocenium Cations Generated via Reaction of $[\text{Me}_2\text{C}(\text{Cp})(\text{Flu})]\text{ZrMe}_2$ with Cocatalysts 3–6 .	43
II. Catalytic Propylene Polymerization Mediated by Complexes 7–10 .	55
Conclusions	71
Chapter 2.	101
Diversity in Weakly Coordinating Anions. Mono and Polynuclear Halo Perfluoroarylmethylates as Cocatalysts for Stereospecific Olefin Polymerization: Synthesis, Structure, and Reactivity.	
Introduction	103
Experimental Section	109

Results and Discussion	113
I. Synthesis and Characterization of Cocatalysts 6 – 14 . General Considerations.	114
II. Activation of Metallocene $\text{Me}_2\text{C}(\text{Cp})(\text{Flu})\text{ZrMe}_2$ (15) with Cocatalysts 6 – 14. General Considerations.	116
III. Trityl Perfluoroaryl Fluoroborates $\text{Ph}_3\text{C}^+ \text{FB}(\text{C}_6\text{F}_5)_3^-$ (6) and $\text{Ph}_3\text{C}^+ \text{FB}(o\text{-C}_6\text{F}_5\text{C}_6\text{F}_4)_3^-$ (7)	119
IV. A. Trityl Perfluoroaryl Fluoroaluminates $(\text{Ph}_3\text{C}^+)_x \text{F}_x[\text{Al}(\text{C}_6\text{F}_5)_3]_y^{x-}$ ($x = 1, y = 1$, 8 ; $x = 1, y = 2$, 9 ; $x =$ $2, y = 3$, 10) and $\text{Ph}_3\text{C}^+ (\text{C}_6\text{F}_5)_3\text{AlFAl}(o\text{-C}_6\text{F}_5\text{C}_6\text{F}_4)_3^-$ (11)	124
IV. B. Trityl Perfluoroaryl Haloaluminates $\text{Ph}_3\text{C}^+ \text{XAl}(\text{C}_6\text{F}_5)_3^-$ ($\text{X} = \text{Cl}$, 12 ; $\text{X} = \text{Br}$, 13).	132
V. Trityl Perfluoroaryl Fluorogallate $\text{Ph}_3\text{C}^+ \text{F}[\text{Ga}(\text{C}_6\text{F}_5)_3]_2^-$ (14).	133
Conclusions	135

Chapter 3. 166

Diverse Stereocontrol Effects Induced by Weakly Coordinating Anions. Stereospecific Olefin Polymerization Pathways at Archetypal C_S - and C_1 -Symmetric Metallocenium Catalysts Using Mono and Polynuclear Halo Perfluoroarylmatalates as Cocatalysts.

Introduction	167
Experimental Section	174
Results	180
I. Propylene Polymerization Mediated by $\text{Me}_2\text{C}(\text{Cp})(\text{Flu})\text{ZrMe}_2$ (1) Activated with Cocatalysts 5, 8 - 17 , “ $\text{Ph}_3\text{C}^+ \text{Cl}[\text{Al}(\text{C}_6\text{F}_5)_3]_2^-$,” and “ $\text{Ph}_3\text{C}^+ \text{Br}[\text{Al}(\text{C}_6\text{F}_5)_3]_2^-$.”	180
II. Propylene Polymerization Mediated by C_1 -Symmetric $\text{Me}_2\text{Si}(\text{CpR}^*)(\text{Octahydrofluorenyl})\text{ZrMe}_2$ (2 , $\text{R}^* =$	

	10
(1 <i>R</i> ,2 <i>S</i> ,5 <i>R</i>)- <i>trans</i> -5-methyl- <i>cis</i> -2-(2-propyl)cyclohexyl; (-)-menthyl) Activated with Cocatalysts 3 , 6 , 7 , 12 and 14 .	182
Discussion	184
I. Catalyst Systems Derived From Me ₂ C(Cp)(Flu)ZrMe ₂ (1) Activated with Trityl Perfluoroaryl Fluoroborates Ph ₃ C ⁺ FB(C ₆ F ₅) ₃ ⁻ (9) and Ph ₃ C ⁺ FB(<i>o</i> -C ₆ F ₅ C ₆ F ₄) ₃ ⁻ (10).	191
II. Catalyst Systems Derived From C _S -Symmetric Me ₂ C(Cp)(Flu)ZrMe ₂ (1) Activated with Trityl Perfluoroaryl Fluoroaluminates (Ph ₃ C ⁺) _x F _x [Al(C ₆ F ₅) ₃] _y ^{x-} (x = 1, y = 1, 11 ; x = 1, y = 2, 12 ; x = 2, y = 3, 13), Ph ₃ C ⁺ (C ₆ F ₅) ₃ AlFAl(<i>o</i> -C ₆ F ₅ C ₆ F ₄) ₃ ⁻ (14), Ph ₃ C ⁺ XAl(C ₆ F ₅) ₃ ⁻ (X = Cl, 15 ; X = Br, 16), and “Ph ₃ C ⁺ X[Al(C ₆ F ₅) ₃] ₂ ⁻ ” (X = Cl; X = Br).	193
III. Catalyst System Derived From C _S -Symmetric Me ₂ C(Cp)(Flu)ZrMe ₂ (1) Activated with Trityl Perfluoroaryl Fluorogallate Ph ₃ C ⁺ F[Ga(C ₆ F ₅) ₃] ₂ ⁻ (17).	202
IV. Propylene Polymerization Mediated by C ₁ -Symmetric Me ₂ Si(CpR*)(Octahydrofluorenyl)ZrMe ₂ (2 , R* = (1 <i>R</i> ,2 <i>S</i> ,5 <i>R</i>)- <i>trans</i> -5-methyl- <i>cis</i> -2-(2-propyl)cyclohexyl; (-)- menthyl) Activated with Cocatalysts 3 , 6 , 7 , 12 and 14 .	203
V. Polymer ¹³ C NMR Microstructural/Mechanistic Analysis of Polypropylenes Produced Using C ₁ -Symmetric Me ₂ Si(CpR*)(Octahydrofluorenyl)ZrMe ₂ (2 , R* = (1 <i>R</i> ,2 <i>S</i> ,5 <i>R</i>)- <i>trans</i> -5-methyl- <i>cis</i> -2-(2-propyl)cyclohexyl; (-)- menthyl) Activated with Cocatalysts 3 , 6 , 7 , 12 and 14 .	210
Conclusions	221
<i>Curriculum Vita</i>	275

LIST OF FIGURES

Chapter 1

- Figure 1. 75
High-pressure polymerization reaction system.
- Figure 2. 76
Perspective ORTEP drawing of the molecular structure of the complex $[\text{Me}_2\text{C}(\text{Cp})(\text{Flu})]\text{ZrMe}^+ \text{MeB}(\text{C}_6\text{F}_5)_3^-$ (**7**). Thermal ellipsoids are drawn at the 30% probability level.
- Figure 3. 77
Perspective ORTEP drawing of the molecular structure of the complex $[\text{Me}_2\text{C}(\text{Cp})(\text{Flu})]\text{ZrMe}^+ \text{FAl}(\text{C}_6\text{F}_5\text{C}_6\text{F}_4)_3^-$ (**10**). Thermal ellipsoids are drawn at the 30% probability level. The terminal C_6F_5 groups not only twist out of coplanarity with connected C_6F_4 fragments but also exhibit π - π interactions with the C_6F_4 groups on adjacent C_{12}F_9 ligands.
- Figure 4. 78
EXSY spectrum (in toluene- d_8) of complex **10**, 127.5°C, $\tau_m = 800\text{ms}$. Diagonal peaks, lower-left to upper-right, correspond to resonances $\text{H}_{\text{A}'}$, H_{A} , $\text{H}_{\text{a}'}$, and H_{a} , respectively. Spectra *a.* and *b.* are F2 slices passing through the points of greatest intensity in resonances H_{a} and $\text{H}_{\text{A}'}$, respectively.
- Figure 5. 79
Product molecular weight (M_w) data for polypropylenes produced by **1** + the indicated cocatalysts over the temperature range of -10° – +60°C under 1.0 atm of propylene.
- Figure 6. 80
Syndiotacticity (%*rrrr*) data and calculated *m* and *mm* stereodeflect production probabilities (relative to insertion, P_m and P_{mm} respectively, discussed below) for polypropylenes produced by **1** +

indicated cocatalysts under 1.0 atm of propylene over the temperature range of -10° – $+60^{\circ}\text{C}$ (A) and using propylene concentrations varying over the range 0.36M – 2.05M at 60°C (B).

Figure 7. 81

Product $1/P_n$ at 60°C plotted vs. $1/[\text{propylene}]$ for 1 + indicated cocatalysts (Table 8).

Figure 8. 81

Product P_m at 60°C plotted vs. $1/[\text{propylene}]$ for 1 + indicated cocatalysts (Table 8).

Figure 9. 82

Product P_{mm} at 60°C plotted vs. $1/[\text{propylene}]$ for 1 + indicated Cocatalysts (Table 8).

Figure 10. 82

Plots of $-\ln(k_p)$ vs. $1/(\text{polymerization temperature})$ for 1 + indicated cocatalysts under 1.0 atm propylene over the temperature range of -10° – $+60^{\circ}\text{C}$ in toluene (Table 7; k_p values corrected for $[\text{propylene}]$ temperature dependence).

Figure 11. 83

A. $\log(\text{polymerization activity})$, B. Polypropylene M_w , C. *rrrr* pentad intensity (%), and D. *xmrx* pentad intensity (%) data for polypropylenes produced by 1 + indicated cocatalysts under 1.0 atm of propylene at 25°C in octane, toluene, and 1,3-dichlorobenzene solutions.

Chapter 2

Figure 1. 137

Perspective ORTEP drawing of the molecular structure of cocatalyst reagent $\text{Ph}_3\text{C}^+ \text{FB}(\text{o-C}_6\text{F}_5\text{C}_6\text{F}_4)_3^-$ (7). Thermal ellipsoids are drawn at the 30% probability level.

Figure 2. 138

Perspective ORTEP drawings of the molecular structure of dinuclear Zr-(μ -F)-Zr complex $[\text{Me}_2\text{C}(\text{Cp})(\text{Flu})\text{ZrMe}]_2(\mu\text{-F})^+ \text{FB}(o\text{-C}_6\text{F}_5\text{C}_6\text{F}_4)_3^-$ (**17**). Thermal ellipsoids are drawn at the 30% probability level.

Figure 3. 139

Perspective ORTEP drawings of the molecular structure of cocatalyst reagent $(\text{Ph}_3\text{C}^+)_2 \text{F}_2[\text{Al}(\text{C}_6\text{F}_5)_3]_3^{2-}$ (**10**) viewed perpendicular the (noncrystallographic) Al-F-Al-F-Al axis (A), and viewed along this axis (B). Thermal ellipsoids are drawn at the 30% probability level.

Figure 4. 140

Perspective ORTEP drawings of the molecular structure of cocatalyst reagent $\text{Ph}_3\text{C}^+ (\text{C}_6\text{F}_5)_3\text{AlFAl}(o\text{-C}_6\text{F}_5\text{C}_6\text{F}_4)_3^-$ (**11**) viewed abroad the Al-F-Al axis (A), and showing mutual π - π or steric stacking among the $o\text{-C}_6\text{F}_5\text{C}_6\text{F}_4$ groups (B). Thermal ellipsoids are drawn at the 30% probability level.

Figure 5. 141

Perspective ORTEP drawings of the molecular structure of dinuclear Zr-(μ -Me)-Zr complex $[\text{Me}_2\text{C}(\text{Cp})(\text{Flu})\text{ZrMe}]_2(\mu\text{-Me})^+ (\text{C}_6\text{F}_5)_3\text{AlFAl}(\text{C}_6\text{F}_5)_3^-$ (**19**). Thermal ellipsoids are drawn at the 30% probability level.

Figure 6. 142

Perspective ORTEP drawings of the molecular structure of dinuclear Zr-(μ -Me)-Zr complex $[\text{Me}_2\text{C}(\text{Cp})(\text{Flu})\text{ZrMe}]_2(\mu\text{-Me})^+ (\text{C}_6\text{F}_5)_3\text{AlFAl}(o\text{-C}_6\text{F}_5\text{C}_6\text{F}_4)_3^-$ (**20**; A), and of the anion in **20** (B). Thermal ellipsoids are drawn at the 30% probability level.

- Figure 7. 143
 Perspective drawings of free (G) and associated (H) (tris)perfluorobiphenyl fluorometallate ligands.
- Figure 8. 144
 Perspective ORTEP drawings of the molecular structures of cocatalyst reagents $\text{Ph}_3\text{C}^+ \text{ClAl}(\text{C}_6\text{F}_5)_3^-$ (**12**; A) and $\text{Ph}_3\text{C}^+ \text{BrAl}(\text{C}_6\text{F}_5)_3^-$ (**13**; B). Thermal ellipsoids are drawn at the 30% probability level.
- Figure 9. 145
 Perspective ORTEP drawings of the molecular structure of $\text{Me}_2\text{C}(\text{Cp})(\text{Flu})\text{ZrCl}(\text{C}_6\text{F}_5)$ (**21**). Thermal ellipsoids are drawn at the 50% probability level.
- Figure 10. 146
 Perspective ORTEP drawings of the molecular structure of the $[\text{Me}_2\text{C}(\text{Cp})(\text{Flu})\text{Zr}(\mu_2\text{-Br})_2]^{2+}$ dication in complex $[\text{Me}_2\text{C}(\text{Cp})(\text{Flu})\text{Zr}(\mu_2\text{-Br})_2]^{2+} [\text{Al}(\text{C}_6\text{F}_5)_4]_2^-$ (**22**; A), and the $\text{Al}(\text{C}_6\text{F}_5)_4^-$ monoanion (B). Thermal ellipsoids are drawn at the 30% probability level.
- Figure 11. 147
 Perspective ORTEP drawing of the molecular structure of the cocatalyst reagent $\text{Ph}_3\text{C}^+ \text{F}[\text{Ga}(\text{C}_6\text{F}_5)_3]_2^-$ (**14**). Thermal ellipsoids are drawn at the 30% probability level.

Chapter 3

- Figure 1. 225
 ^{13}C NMR of the isotactic polypropylene generated from $\text{Me}_2\text{Si}(\text{OHf})(\text{CpR}^*)\text{ZrMe}_2$ (**2**) + $\text{Ph}_3\text{C}^+ \text{B}(\text{C}_6\text{F}_5)_4^-$ (**6**) under 1.0 atm of propylene at 60°C in toluene (Table 3, entry 8).

Figure 2 226

Plots of $-\ln(k_p)$ vs. $1/(\text{polymerization temperature})$ for $\text{Me}_2\text{C}(\text{Cp})(\text{Flu})\text{ZrMe}_2$ (**1**) + cocatalysts $\text{Ph}_3\text{C}^+ \text{FAl}(o\text{-C}_6\text{F}_5\text{C}_6\text{F}_4)_3^-$ (**7**) and $\text{Ph}_3\text{C}^+ (\text{C}_6\text{F}_5)_3\text{AlFAl}(o\text{-C}_6\text{F}_5\text{C}_6\text{F}_4)_3^-$ (**14**) under 1.0 atm propylene over the temperature range of -10° to 25°C in toluene (Table 2; k_p values corrected for [propylene] temperature dependence). Lines accompanying the data points are presented as a guide to the eye.

Figure 3 227

A. Polymerization activity as a function of solvent, temperature, and propylene pressure, **B.** *mmmm* (%) data for polypropylenes produced by C_1 -symmetric metallocene $\text{Me}_2\text{Si}(\text{OHf})(\text{CpR}^*)\text{ZrMe}_2$ (**2**) + the indicated cocatalysts (labeling defined in Scheme 1) under the specified polymerization conditions.

LIST OF TABLES

Chapter 1

Table 1.	84
Summary of the Crystal Structure Data for Complexes $[\text{Me}_2\text{C}(\text{Cp})(\text{Flu})]\text{ZrMe}^+ \text{MeB}(\text{C}_6\text{F}_5)_3^-$ (7) and $[\text{Me}_2\text{C}(\text{Cp})(\text{Flu})]\text{ZrMe}^+ \text{FAl}(2\text{-C}_6\text{F}_5\text{C}_6\text{F}_4)_3^-$ (10).	
Table 2.	85
Selected Bond Distances (\AA) and Angles (deg) for Complex $[\text{Me}_2\text{C}(\text{Cp})(\text{Flu})]\text{ZrMe}^+ \text{MeB}(\text{C}_6\text{F}_5)_3^-$ (7).	
Table 3.	86
Comparison of Selected Bond Distances (\AA) and Angles (deg) in Complex $[\text{Me}_2\text{C}(\text{Cp})(\text{Flu})]\text{ZrMe}^+ \text{MeB}(\text{C}_6\text{F}_5)_3^-$ (7) to those of Analogous Zirconocenium- $\text{MeB}(\text{C}_6\text{F}_5)_3^-$ Ion Pairs.	

Table 4.	87
Selected Bond Distances (Å) and Angles (deg) for Complex [Me ₂ C(Cp)(Flu)]ZrMe ⁺ FAl(2-C ₆ F ₅ C ₆ F ₄) ₃ ⁻ (10).	
Table 5.	88
Comparative Bond Distances (Å) and Angles (deg) for Complexes [Me ₂ C(Cp)(Flu)]ZrMe ⁺ MeB(C ₆ F ₅) ₃ ⁻ (7). and [Me ₂ C(Cp)(Flu)]ZrMe ⁺ FAl(2-C ₆ F ₅ C ₆ F ₄) ₃ ⁻ (10).	
Table 6.	89
NMR-Derived Rate Constants and Free Energies of Activation for Solution Dynamic Processes of Complexes [Me ₂ C(Cp)(Flu)]ZrMe ⁺ MeB(C ₆ F ₅) ₃ ⁻ (7). and [Me ₂ C(Cp)(Flu)]ZrMe ⁺ FAl(2-C ₆ F ₅ C ₆ F ₄) ₃ ⁻ (10) in toluene- <i>d</i> ₈ . Confidence Intervals Presented at the 90% Confidence Level.	
Table 7.	90
Propylene Polymerization Results for the Reactions Mediated by [Me ₂ C(Cp)(Flu)]ZrMe ₂ (1) + Indicated Cocatalysts under 1.0 atm of Propylene over the Temperature Range of -10° – +60°C. ^a	
Table 8.	91
Propylene Polymerization Results for the Reactions Mediated by [Me ₂ C(Cp)(Flu)]ZrMe ₂ (1) + Indicated Cocatalysts at 60°C over the Pressure Range of 1 – 5 atm of Propylene.	
Table 9.	92
Slopes, Intercepts, and Rate Ratios (%) of <i>m</i> Stereodefects Originating from Site Epimerization vs. "Back-Side" Misinsertion Obtained from P _{<i>m</i>} vs. 1/[Propylene] Plots for Polymerizations Mediated by [Me ₂ C(Cp)(Flu)]ZrMe ₂ (1) + Indicated Cocatalysts under 1.0 – 5.0 atm Propylene at 60°C. Confidence Intervals Presented at the 90% Confidence Level.	
Table 10.	93
Slopes, Intercepts, and Rate Ratios (%) of <i>mm</i> Stereodefects Originating from Chain Epimerization vs. Enantiofacial Misinsertion	

Obtained from P_{mm} vs. $1/[\text{Propylene}]$ Plots for Polymerizations Mediated by $[\text{Me}_2\text{C}(\text{Cp})(\text{Flu})]\text{ZrMe}_2$ (**1**) + Indicated Cocatalysts under 1.0 – 5.0 atm Propylene at 60°C. Confidence Intervals Presented at the 90% Confidence Level.

Table 11. 94

Estimated Absolute Rate Constants For Propagation, Site Epimerization, "Back-Side" Misinsertion, Chain Epimerization, and Enantiofacial Misinsertion Obtained from Activities, P_m vs. $1/[\text{Propylene}]$ Plots, and P_{mm} vs. $1/[\text{Propylene}]$ Plots for Polymerizations Mediated by $[\text{Me}_2\text{C}(\text{Cp})(\text{Flu})]\text{ZrMe}_2$ (**1**) + Indicated Cocatalysts under 1.0 – 5.0 atm Propylene at 60°C. Confidence Intervals Presented at the 90% Confidence Level; k_p , k_{se} , k_{bsa} , k_{ce} , and k_{em} as Defined in Eqs. 10 and 11.

Table 12. 95

Propylene Polymerization Results for the Reactions Mediated by $[\text{Me}_2\text{C}(\text{Cp})(\text{Flu})]\text{ZrMe}_2$ (**1**) + Indicated Cocatalysts in 1,3-dichlorobenzene^a or Octane^a under 1.0 atm of Propylene at 25°C.

Table 13. 96

Concentration Effects on Propylene Polymerization Results for the Reactions Mediated by $[\text{Me}_2\text{C}(\text{Cp})(\text{Flu})]\text{ZrMe}_2$ (**1**) + $\text{B}(\text{C}_6\text{F}_5)_3$ (**3**) in Toluene under 1.0 atm of Propylene at 25°C.

Table 14. 97

Propylene Polymerization Results for the Reactions Mediated by **1** + **3** with Addition of $\text{Li}^+ \text{MeB}(\text{C}_6\text{F}_5)_3^-$ (**11**) in Toluene under 1.0 atm of Propylene at 25°C.

Chapter 2

Table 1. 148

Summary of Crystal Structure Data for Cocatalysts **7** and **10 – 14** and Complexes **17, 19, and 20 – 22**.

Table 2.	150
Comparison of Selected Bond Distances (Å) for Cocatalysts Ph_3C^+ $\text{FAl}(o\text{-C}_6\text{F}_5\text{C}_6\text{F}_4)_3^-$ (4), Ph_3C^+ $\text{FB}(o\text{-C}_6\text{F}_5\text{C}_6\text{F}_4)_3^-$ (7), Ph_3C^+ $(\text{C}_6\text{F}_5)_3\text{AlFAl}(o\text{-C}_6\text{F}_5\text{C}_6\text{F}_4)_3^-$ (11), Ph_3C^+ $\text{ClAl}(\text{C}_6\text{F}_5)_3^-$ (12) Ph_3C^+ $\text{BrAl}(\text{C}_6\text{F}_5)_3^-$ (13), and Ph_3C^+ $\text{F}[\text{Ga}(\text{C}_6\text{F}_5)_3]_2^-$ (14).	
Table 3.	151
Selected Bond Distances (Å) and Angles (deg) for Cocatalyst Ph_3C^+ $\text{FB}(o\text{-C}_6\text{F}_5\text{C}_6\text{F}_4)_3^-$ (7).	
Table 4.	152
Selected Bond Distances (Å) and Angles (deg) for Dinuclear Metallocene Complex $[\text{Me}_2\text{C}(\text{Cp})(\text{Flu})\text{ZrMe}]_2(\mu\text{-F})^+ \text{FB}(o\text{-C}_6\text{F}_5\text{C}_6\text{F}_4)_3^-$ (17).	
Table 5.	153
Comparison of Selected Bond Distances (Å) and Angles (deg) for Dinuclear Metallocene Cations Containing Zr–F–Zr Linkages.	
Table 6.	154
Selected Bond Distances (Å) and Angles (deg) for Cocatalyst $(\text{Ph}_3\text{C}^+)_2\text{F}_3[\text{Al}(\text{C}_6\text{F}_5)_3]_3^{2-}$ (10).	
Table 7.	155
Selected Bond Distances (Å) and Angles (deg) for Cocatalyst Ph_3C^+ $(\text{C}_6\text{F}_5)_3\text{AlFAl}(o\text{-C}_6\text{F}_5\text{C}_6\text{F}_4)_3^-$ (11).	
Table 8.	156
Comparison of the Torsion Angles (deg) in $\text{FAl}(o\text{-C}_6\text{F}_4\text{C}_6\text{F}_5)_3^-$ and $\text{FB}(o\text{-C}_6\text{F}_4\text{C}_6\text{F}_5)_3^-$ Anions.	
Table 9.	157
Selected Bond Distances (Å) and Angles (deg) for Dinuclear Metallocene Complex $[\text{Me}_2\text{C}(\text{Cp})(\text{Flu})\text{ZrMe}]_2(\mu\text{-Me})^+ \text{F}[\text{Al}(\text{C}_6\text{F}_5)_3]_3^-$ (19).	

Table 10.	158
Selected Bond Distances (Å) and Angles (deg) for Dinuclear Metallocene Complex $[\text{Me}_2\text{C}(\text{Cp})(\text{Flu})\text{ZrMe}]_2(\mu\text{-Me})^+$ $(\text{C}_6\text{F}_5)_3\text{AlFAl}(o\text{-C}_6\text{F}_5\text{C}_6\text{F}_4)_3^-$ (20).	
Table 11.	159
Comparison of Selected Bond Distances (Å) and Angles (deg) for Dinuclear Metallocene Cations Containing Zr–Me–Zr Linkages.	
Table 12.	160
Selected Bond Distances (Å) and Angles (deg) for Cocatalysts Ph_3C^+ $\text{ClAl}(\text{C}_6\text{F}_5)_3^-$ (12) and Ph_3C^+ $\text{BrAl}(\text{C}_6\text{F}_5)_3^-$ (13).	
Table 13.	161
Selected Bond Distances (Å) and Angles (deg) for $\text{Me}_2\text{C}(\text{Cp})(\text{Flu})\text{ZrCl}(\text{C}_6\text{F}_5)$ (21).	
Table 14.	162
Selected Bond Distances (Å) and Angles (deg) for $[\text{Me}_2\text{C}(\text{Cp})(\text{Flu})\text{Zr}(\mu_2\text{-Br})]_2^{2+}$ $[\text{Al}(\text{C}_6\text{F}_5)_4]_2^-$ (22).	
Table 15.	163
Selected Bond Distances (Å) and Angles (deg) for Cocatalyst Ph_3C^+ $\text{F}[\text{Ga}(\text{C}_6\text{F}_5)_3]_2^-$ (14).	

Chapter 3

Table 1.	228
Comparison of propylene polymerization results with $\text{Me}_2\text{C}(\text{Cp})(\text{Flu})\text{ZrMe}_2$ (1) + the indicated cocatalysts at 25°C under 1.0 atm of propylene.	
Table 2	229
Propylene polymerization results with $\text{Me}_2\text{C}(\text{Cp})(\text{Flu})\text{ZrMe}_2$ (1) + the indicated cocatalysts.	

	20
Table 3	230
Propylene polymerization results with $\text{Me}_2\text{Si}(\text{OHf})(\text{CpR}^*)\text{ZrMe}_2$ (2) + the indicated cocatalysts.	
Table 4	231
Propylene polymerization results with $\text{Me}_2\text{Si}(\text{OHf})(\text{CpR}^*)\text{ZrMe}_2$ (2) + the indicated cocatalysts at 25°C under 1.0 atm of propylene, with 1,3-dichlorobenzene as solvent.	
Table 5	232
Submodel Descriptions, Assumptions, and Parameterizations for C_1 -Symmetric Metallocene-Mediated Propylene Polymerization.	
Table 6	232
Correlation Matrices for Models 1 - 3: Means and Standard Deviations Across All Data Sets for C_1 -Symmetric Metallocene-Mediated Propylene Polymerization.	

LIST OF SCHEMES

Chapter 1

Scheme 1.	98
Syndiospecific Propylene Polymerization and Stereodeflect Mechanisms – C_S -Symmetric Precatalyst.	
Scheme 2.	100
Solution-Phase Reorganization Pathways in $[\text{Me}_2\text{C}(\text{Cp})(\text{Flu})]\text{ZrMe}^+$ $\text{FAl}(2\text{-C}_6\text{F}_5\text{C}_6\text{F}_4)_3^-$ (10).	

Chapter 2

Scheme 1.	164
New trityl salt species arising from reaction of trityl fluoride with various known neutral cocatalyst species.	

Scheme 2.	165
Reactions of Me ₂ C(Cp)(Flu)ZrMe ₂ (15) with cocatalyst reagents 6 – 13 .	

Chapter 3

Scheme 1.	233
Chemical Structures, Compounds 1 - 17 .	
Scheme 2.	234
Syndiospecific Propylene Polymerization and Stereodeflect Mechanisms – C _S -Symmetric Precatalyst	
Scheme 3.	235
Isospecific Propylene Polymerization and Stereodeflect Mechanisms – C ₁ -Symmetric Precatalyst.	

LIST OF APPENDICES

Appendix I. Chapter 1 Supporting Information. 238

Additional polymerization results as an extension to results in Table 11, and a full-page, low peak-threshold EXSY spectrum for **10** at 127.5°C, τ_m = 800ms.

Appendix II. Chapter 3 Supporting Information. 251

Experimental and calculated pentad distributions, along with correlation matrices for each stochastic model employed.

Note Complete X-ray experimental details and tables of bond lengths, angles, and positional parameters for the two crystal structures appearing in Chapter 1 and the eleven structures appearing in chapter 2, omitted here for brevity, are available via the ACS website, <http://pubs.acs.org>. General experimental descriptions appear in the Experimental Sections of these chapters.

Marked Counteranion Effects on Single-Site Olefin Polymerization Processes. Correlations of Ion Pair Structure and Dynamics with Polymerization Activity, Chain Transfer, and Syndioselectivity.

Ming-Chou Chen, John A. S. Roberts, and Tobin J. Marks*

Department of Chemistry, Northwestern University

Evanston, Illinois 60208-3113

ABSTRACT

Counteranion effects on the rate and stereochemistry of syndiotactic propylene enchainment by the archetypal C_3 -symmetric precatalyst $[\text{Me}_2\text{C}(\text{Cp})(\text{Flu})]\text{ZrMe}_2$ (**1**; Cp = C_5H_4 ; Flu = C_{13}H_8 , fluorenyl) are probed using the cocatalysts MAO (**2**), $\text{B}(\text{C}_6\text{F}_5)_3$ (**3**), $\text{B}(o\text{-C}_6\text{F}_5\text{C}_6\text{F}_4)_3$ (**4**), $\text{Ph}_3\text{C}^+\text{B}(\text{C}_6\text{F}_5)_4^-$ (**5**), and $\text{Ph}_3\text{C}^+\text{FAl}(o\text{-C}_6\text{F}_5\text{C}_6\text{F}_4)_3^-$ (**6**), offering greatly different structural and ion pairing characteristics. Reaction of **1** with **3** affords $[\text{Me}_2\text{C}(\text{Cp})(\text{Flu})]\text{ZrMe}^+\text{MeB}(\text{C}_6\text{F}_5)_3^-$ (**7**). In the case of **4**, this reaction leads to formation the μ -methyl dinuclear diastereomers $\{([\text{Me}_2\text{C}(\text{Cp})(\text{Flu})]\text{ZrMe}\}_2(\mu\text{-Me})^+\text{MeB}(o\text{-C}_6\text{F}_5\text{C}_6\text{F}_4)_3^-$ (**8**). A similar reaction with **6** results in diastereomeric $[\text{Me}_2\text{C}(\text{Cp})(\text{Flu})]\text{ZrMe}^+\text{FAl}(o\text{-C}_6\text{F}_5\text{C}_6\text{F}_4)_3^-$ (**10**) ion pairs. The molecular structures of **7** and **10** have been determined by single-crystal X-ray diffraction. Reorganization pathways available to these species have been examined using EXSY and dynamic NMR, revealing that the cation- $\text{MeB}(\text{C}_6\text{F}_5)_3^-$ interaction is considerably weaker/more mobile than in the $\text{FAl}(o\text{-C}_6\text{F}_5\text{C}_6\text{F}_4)_3^-$ -derived analogue. Polymerizations mediated by **1** in toluene over the temperature range of -10° to $+60^\circ\text{C}$ and at 1.0 – 5.0 atm propylene pressure (at 60°C) reveal that activity, product syndiotacticity, m and mm stereodeflect generation, and chain transfer processes are highly sensitive to the nature of the ion pairing. Thus, the complexes activated with **4** and **5**,

having the weakest ion pairing, yield the highest estimated propagation rates, while with **6**, having the strongest pairing, yields the lowest. The strongly coordinating, immobile $\text{FAl}(o\text{-C}_6\text{F}_5\text{C}_6\text{F}_4)_3^-$ anion produces the highest/least temperature-dependent product syndiotacticity, lowest/least temperature-dependent *m* stereodeflect abundance, and highest product molecular weight. These polypropylene microstructural parameters, and also M_w , are least sensitive to increased propylene pressure for $\text{FAl}(o\text{-C}_6\text{F}_5\text{C}_6\text{F}_4)_3^-$, but highest with $\text{MeB}(\text{C}_6\text{F}_5)_3^-$. In general, *mm* stereodeflect production is only modestly anion-sensitive; [propylene] dependence studies reveal enantiofacial propylene misinsertion to be the prevailing *mm*-generating process in all systems at 60°C, being most dominant with **6**, where *mm* stereodeflect abundance is lowest. For 1,3-dichlorobenzene as the polymerization solvent, product syndiotacticity, as well as *m* and *mm* stereodeflects, become indistinguishable for all cocatalysts. These observations are consistent with a scenario in which ion pairing modulates the rates of stereodeflect generating processes relative to monomer enchainment, hence net enchainment syndioselectivity, and also dictates the rate of termination relative to propagation and the preferred termination pathway. In comparison to **3–6**, propylene polymerization mediated by MAO (**2**) + **1** in toluene reveals an estimated ordering in site epimerization rates as **5** > **4** > **2** > **3** > **6**, while product syndiotacticities rank as **6** > **2** > **5** ~ **4** > **3**.

INTRODUCTION

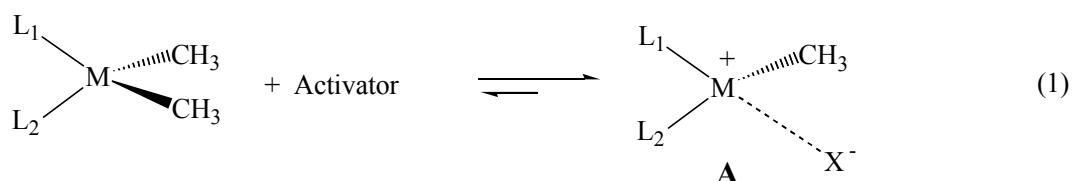
Cocatalysts are of great current interest as vital components of single-site olefin polymerization catalysts.^{1,2} Well-known cocatalysts include methylaluminoxane (MAO; **2**),³

1. For recent reviews, see: (a) Pédeutour, J.-N.; Radhakrishnan, K.; Cramail, H.; Deffieux, A. *Macromol. Rapid Commun.* **2001**, *22*, 1095-1123. (b) Chen, Y.-X.; Marks, T. J. *Chem. Rev.*, **2000**, *100* (4), 1391-1434. (c) Gladysz, J.A., Ed. *Chem. Rev.* **2000**, *100*, 1167-1682. (d) Marks, T.J.; Stevens, J.C., Eds. *Topics in Catalysis*, **1999**, *7*, 1-208. (e) Britovsek, G.J.P.; Gibson, V.C.; Wass, D.F. *Angew. Chem., Int. Ed. Engl.* **1999**, *38*, 428-447. (f) Jordan, R.F.; Ed. *J. Mol. Catal.* **1998**, *128*, 1-337.

2. For recent cocatalyst studies, see: (a) Busico, V.; Cipullo, R.; Cutillo, F.; Vacatello, M.; Van Axel Castelli, V. *Macromolecules* **2003**, *36*, 4258-4261. (b) Mohammed, M.; Nele, M.; Al-Humydi, A.; Xin, S.; Stapleton, R.; Collins, C. *J. Am. Chem. Soc.* **2003**, *125*, 7930-7941. (c) Li, L.; Metz, M. V.; Li, H.; Chen, M.-C.; Marks, T. J. *J. Am. Chem. Soc.* **2002**, *124*, 12725-12741. (d) Metz, M.V.; Schwartz, D.J.; Stern, C.L.; Marks, T.J.; Nickias, P.N. *Organometallics*, **2002**, *21*, 4159-4168. (e) Metz, M.V.; Sun, Y.M.; Stern, C.L.; Marks, T.J. *Organometallics*, **2002**, *21*, 3691-3702. (f) Wilmes, G.M.; Polse, J.L.; Waymouth, R.M. *Macromolecules* **2002**, *35*, 6766-6772. (g) Lancaster, S.J.; Rodriguez, A.; Lara-Sanchez, A.; Hannant, M.D.; Walker, D.A.; Hughes, D.H.; Bochmann, M. *Organometallics*, **2002**, *21*, 451-453. (h) Rodriguez, G.; Brant, P. *Organometallics*, **2001**, *20*, 2417-2420. (i) Kaul, F.A.R.; Puchta, G.T.; Schneider, H.; Grosche, M.; Mihailios, D.; Herrmann, W. A. *J. Organometallic Chem.* **2001**, *621*, 177-183. (j) Chen, Y.-X.; Kruper, W.J.; Roof G.; Wilson, D.R. *J. Am. Chem. Soc.* **2001**, *123*, 745-746. (k) Zhou, J.; Lancaster, S.J.; Walker, D.A.; Beck, S.; Thornton-Pett, M.; Bochmann, M. *J. Am. Chem. Soc.* **2001**, *123*, 223-237. (l) Kehr, G.; Roesmann, R.; Frohlich, R.; Holst, C.; Erker, G. *Eur. J. Inorg. Chem.* **2001**, 535-538. (m) Mager, M.; Becke, S.; Windisch, H.; Denninger, U. *Angew. Chem., Int. Ed. Engl.* **2001**, *40*, 1898-1902. (n) Chase, P.A.; Piers, W.E.; Patrick, B. O.; *J. Am. Chem. Soc.* **2000**, *122*, 12911-12912. (o) LaPointe, R.E.; Roof, G.R.; Abboud, K.A.; Klosin, J. *J. Am. Chem. Soc.* **2000**, *122*, 9560-9561. (p) Sun, Y.M.; Metz, M.V.; Stern, C.L.; Marks, T.J. *Organometallics* **2000**, *19*, 1625-1627. (q) Metz, M.V.; Schwartz, D.J.; Stern, C.L.; Nickias, P.N.; Marks, T.J. *Angew. Chem., Int. Ed. Engl.* **2000**, *39*, 1312-1316.

3. (a) Sinn, H.; Kaminsky, W. *Adv. Organomet. Chem.* **1980**, *18*, 99-149. (b) Sinn, H.; Kaminsky, W.; Vollmer, H.-J.; Woldt, R. *Angew. Chem., Int. Ed. Engl.* **1980**, *19*, 390-392.

tris(perfluorophenyl)borane $B(C_6F_5)_3$; (**3**),⁴ and related perfluoroarylboranes,⁵ ammonium or trityl salts of $B(C_6F_5)_4^-$ (**5**)⁶ and related perfluoroarylborates,⁷ and aluminates,⁸ all of which undergo reaction with metallocenes to generate highly active “cationic” complexes as the actual agents for olefin polymerization (**A**; Eq. 1). Over the past two decades, numerous



elegant efforts have been directed at "engineering" the cationic portion of such catalysts,^{1c}

4. (a) Yang, X.; Stern, C. L.; Marks, T. J. *J. Am. Chem. Soc.* **1994**, *116*, 10015-10031. (b) Yang, X.; Stern, C. L.; Marks, T. J. *J. Am. Chem. Soc.* **1991**, *113*, 3623-3625. (c) Ewen, J. A.; Elder, M. J. *Chem. Abstr.* **1991**, *115*, 136998g.

5. (a) Li, L.; Stern, C. L.; Marks, T. J. *Organometallics* **2000**, *19*, 3332-3337. (b) Li, L.; Marks, T. J. *Organometallics* **1998**, *17*, 3996-4003. (c) Chen, Y.-X.; Stern, C. L.; Yang, S.; Marks, T. J. *J. Am. Chem. Soc.* **1996**, *118*, 12451-12452.6. (d) also see Refs. 2c and 2d. (e) For a recent chelating borane review, see: Piers, W. E.; Irvine, G. J.; Williams, V. C. *Eur. J. Inorg. Chem.* **2000**, 2131-2142.

6. (a) Chien, J. C. W.; Tsai, W.-M.; Rausch, M. D. *J. Am. Chem. Soc.* **1991**, *113*, 8570-8571. (b) Yang, X.; Stern, C. L.; Marks, T. J. *Organometallics* **1991**, *10*, 840-842. (c) Ewen, J. A.; Elder, M. J. *Eur. Pat. Appl.* 426637, **1991**; *Chem. Abstr.* **1991**, *115*, 136987c, 136988d.

7. For related fluorinated tetraarylborates, see: (a) Kaul, F. A. R.; Puchta, G. T.; Schneider, H.; Grosche, M.; Mihalios, D.; Herrmann, W. A. *J. Organomet. Chem.* **2001**, *621*, 184-189. (b) also see Refs. 2g, 2h, and 2k. (c) Jia, L.; Yang, X.; Stern, C. L.; Marks, T. J. *Organometallics* **1997**, *16*, 842-857. (d) Jia, L.; Yang, X.; Ishihara, A.; Marks, T. J. *Organometallics* **1995**, *14*, 3135-3137.

8. (a) Chen, Y.-X.; Metz, M. V.; Li, L.; Stern, C. L.; Marks, T. J. *J. Am. Chem. Soc.* **1998**, *120*, 6287-6305. (b) Chen, Y. X.; Stern, C. L.; Marks, T. J. *J. Am. Chem. Soc.* **1997**, *119*, 2582-2583. (c) Elder, M. J.; Ewen, J. A. *Eur. Pat. Appl.* EP 573,403, 1993; *Chem. Abstr.* **1994**, *121*, 0207d.

(d) also see Ref. 2o.

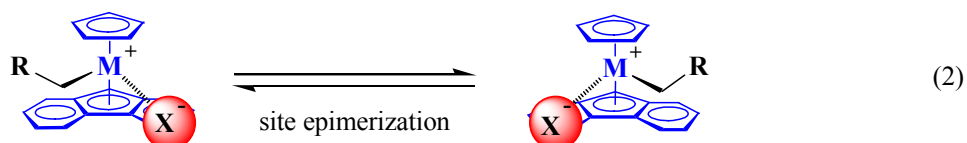
however only recently has the charge-compensating anion (X^-) begun to receive attention in regard to understanding and optimizing the role of the ion pairing dynamics in catalyst system performance. Strong evidence now suggests that the activator and the structures of the resulting ion pairs can have a profound influence on single-site polymerization catalyst activity, lifetime, stability, chain-transfer characteristics, and possibly stereoregulation.^{1,2} As part of our continuing efforts to characterize cocatalyst-related structure-reactivity relationships for such catalysts, we are particularly interested in fluoroarylborate and -aluminate anions and the ion pairing behavior of complexes derived from them. Recently, we communicated some preliminary observations on counteranion effects on propylene enchainment stereochemistry by the archetypal C_s -symmetric precatalyst $[Me_2C(Cp)(Flu)]ZrMe_2$ (**1**; Cp = C_5H_4 ; Flu = fluorenyl),⁹ using a series of structurally/coordinatively diverse cocatalysts/counteranions.¹⁰ In principle, the established pathway¹¹ for syndiospecific propylene enchainment by C_s -symmetric catalysts should be a sensitive probe of the importance of cocatalyst/counteranion^{1,2} interactions since olefin enchainment must occur in concert with "chain swinging" (Eq. 2, R = polypropylene fragment). It is known that rates of similar reorganization/symmetrization processes are sensitive to ion

9. (a) Razavi, A.; Thewalt, U. *J. Organomet. Chem.* **1993**, *445*, 111-114. (b) Razavi, A.; Ferrara, J. *J. Organomet. Chem.* **1992**, *435*, 299-310.

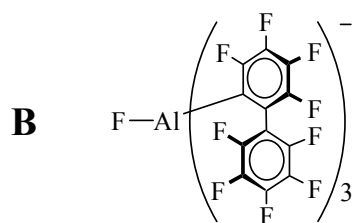
10. Chen, M. -C.; Marks, T. J. *J. Am. Chem. Soc.* **2001**, *123*, 11803-11804.

11. (a) Resconi, L.; Cavallo, L.; Fait, A.; Piemontesi, F. in ref. 1c, pp 1253-1345. (b) Coates, G. W. in Ref. 1c, pp 1223-1252. (c) Veghini, D.; Henling, L. M.; Burkhardt, T. J.; Bercaw, J. E. *J. Am. Chem. Soc.* **1999**, *121*, 564-573. (d) Ewen, J. A.; Jones, R. L.; Razavi, A.; Ferrara, J. D. *J. Am. Chem. Soc.* **1988**, *110*, 6255-6256.

pairing strength in model metallocenium systems ($R = H$, alkyl group),¹² and thought that analogous "back-skip" processes without concomitant enchainment are a major source of polypropylene stereodefects in C_s -symmetric systems (Site Epimerization, Scheme 1B). These stereodefects, in particular m -type stereodefects, have distinct spectroscopic signatures and can be quantified, as has been established.^{11,13}



In the preliminary work¹⁰ it was observed that counteranion effects are strikingly large, and to a significant degree qualitatively understandable, in terms of established trends in ion pairing strength and dynamics. The results at that stage suggested a mechanistic picture in which anion-specific ion pairing effects modulate not only the enchainment and chain transfer rates, but more importantly, the *relative rates* of enchainment versus m stereodefect generation. This suggested that the strong coordinative characteristic of $\text{FAl}(o\text{-C}_6\text{F}_5\text{C}_6\text{F}_4)_3^-$ (**B**)^{8a,b} leads to more tightly bound, stereochemically immobile ion pairs, accounting both for the decrease in polymerization activity, and for the enhancement in stereoselectivity. A solvent effect was



12. (a) Beswick, C. L.; Marks, T. J. *J. Am. Chem. Soc.* **2000**, *122*, 10358-10370. (b) Deck, P. A.; Beswick, C. L.; Marks, T. J. *J. Am. Chem. Soc.* **1998**, *120*, 1772-1784. (c) Luo, L.; Marks, T. J. in Ref. 1d, pp. 97-106. (d) also see Refs. 7c and 8a.

13. (a) See Ref. 2a. (b) Busico, V.; Cipullo, R. *Prog. Polym. Sci.* **2001**, *26*, 443-533. (c) Farina, M.; Terragni, A. *Makromol. Chem., Rapid Commun.* **1993**, *14*, 791-798. (d) Such techniques are reviewed in Ref 11a.

also observed: in low-polarity toluene, polymerization activity, product syndiotacticity, and product molecular weight are sensitively dependent on counteranion identity. In contrast, a "leveling effect" on product stereoregularity is observed in polar 1,3-dichlorobenzene, i.e. the anion dependence is strongly attenuated.

These findings and the questions raised by the apparent significance of ion pairing in C_3 -symmetric polymerization systems motivate the present broader and more quantitative investigation of solution-phase catalyst structure and dynamics, and correlation of these results with polymerization activity, chain transfer pathways, and tacticity/microstructure, as well as detailed determination of ion pair structures in the solid state. Ion pairing effects are found to manifest differently for different processes occurring during polymerization, allowing non-systematic effects on directly observable product polymer properties (e.g., on syndiotacticity or average molecular weight) to emerge from *systematic* effects on individual processes (propagation, site epimerization, chain release, etc.).

Furthermore, recent reports of concentration-dependent ion pair aggregation and anion exchange processes in zirconocenium $\text{MeB}(\text{C}_6\text{F}_5)_3^-$ systems and their sensitivity to Li^+ $\text{MeB}(\text{C}_6\text{F}_5)_3^-$ addition¹⁴ prompt questions about potential ion pair aggregation effects on enchainment in this system. Thus, catalyst concentration effects are also examined here, as are possible influences of counteranion exchange and added Li^+ $\text{MeB}(\text{C}_6\text{F}_5)_3^-$ on propylene polymerization. To further detail and elucidate solvent polarity effects on ion pairing during polymerization, cocatalyst effects in an even less polar solvent, octane, are compared to previous results. In addition, the spectrum of cocatalysts studied has been expanded to include MAO, to compare ion-pairing effects in this broadly utilized cocatalyst to the previously investigated

14. Beck, S.; Lieber, S.; Schaper, F.; Geyer, A.; Brintzinger, H. H. *J. Am. Chem. Soc.* **2001**, *123*, 1483-1489.

species. Propylene polymerization catalyzed by **1**+MAO is carried out over a range of temperatures and propylene pressures, and in the various solvents, and these results are compared to those obtained with the other cocatalysts. In addition, X-ray crystallographic characterization of $[\text{Me}_2\text{C}(\text{Cp})(\text{Flu})]\text{ZrMe}^+ \text{MeB}(\text{C}_6\text{F}_5)_3^-$ (**7**) and $[\text{Me}_2\text{C}(\text{Cp})(\text{Flu})]\text{ZrMe}^+ \text{FAl}(o\text{-C}_6\text{F}_5\text{C}_6\text{F}_4)_3^-$ (**10**), and determination of the solution phase molecular dynamics of these complexes, lead to a description of the molecular basis for catalytic activity and selectivity. Compared to $\text{B}(\text{C}_6\text{F}_5)_4^-$, $\text{CH}_3\text{B}(\text{C}_6\text{F}_5)_3^-$, which is commonly accepted as more strongly coordinating, exhibits an expected lower polymerization activity,^{1b,7c,7d} but surprisingly and without precedent, *lower* polypropylene stereoregularity. Using a straightforward kinetic model, we provide here a rationalization of this interesting, counterintuitive result and then generalize it to all of the cocatalyst systems examined here.

EXPERIMENTAL SECTION

Materials and Methods. All manipulations of air-sensitive materials were performed with rigorous exclusion of oxygen and moisture in flamed Schlenk-type glassware on a dual-manifold Schlenk line or interfaced to a high-vacuum line (10^{-6} Torr), or in an N_2 -filled Vacuum Atmospheres glove box with a high capacity recirculator (<1 ppm O_2). Argon (Matheson, pre-purified), and propylene (Matheson, polymerization grade) were purified by passage through a supported MnO oxygen-removal column and an activated Davison 4A molecular sieve column. Hydrocarbon solvents (toluene and pentane) were distilled under nitrogen from Na/K alloy/benzophenone ketyl. All solvents for high-vacuum line manipulations were stored *in vacuo* over Na/K alloy in Teflon-valved bulbs. Deuterated solvents were obtained from Cambridge Isotope Laboratories (all ≥ 99 atom %D), were freeze-pump-thaw degassed, dried over Na/K

alloy, and stored in re-sealable flasks. Other non-halogenated solvents were dried over Na/K alloy, and halogenated solvents were distilled from CaH₂. Methylaluminoxane (MAO, obtained as a toluene solution from Aldrich) was dried under high vacuum for 24 h to remove excess volatile aluminum alkyls before use. [Me₂C(Cp)(Flu)]ZrMe₂ (**1**),⁹ B(C₆F₅)₃ (**3**),¹⁵ B(*o*-C₆F₅C₆F₄)₃ (**4**),^{8a} Ph₃C⁺B(C₆F₅)₄⁻ (**5**),⁶ Ph₃C⁺FAl(*o*-C₆F₅C₆F₄)₃⁻ (**6**)^{8a} were prepared according to literature procedures.

Physical and Analytical Measurements. NMR spectra were recorded on Varian ^{UNITY}Inova-500 (FT, 500 MHz, ¹H; 125 MHz, ¹³C), ^{UNITY}Inova-400 (FT, 400 MHz, ¹H; 100 MHz, ¹³C), Mercury-400 (FT 400 MHz, ¹H; 100 MHz, ¹³C; 377 MHz, ¹⁹F) or Gemini-300 (FT 300 MHz, ¹H; 75 MHz, ¹³C; 282 MHz, ¹⁹F) instruments. Variable-temperature measurements were carried out using the ^{UNITY}Inova-400 instrument with a 5mm inverse probe or 5mm broadband probe. Probehead temperature calibration was conducted using methanol and ethylene glycol standard samples (Varian, Inc.). Chemical shifts for ¹H and ¹³C spectra were referenced using internal solvent resonances and are reported relative to tetramethylsilane. ¹⁹F NMR spectra were referenced to external CFCl₃. NMR experiments on air-sensitive samples were conducted in Teflon valve-sealed NMR tubes (J. Young). For ¹³C NMR analyses of homopolymer microstructures, 300 ~ 400 mg polymer samples were dissolved in 4 mL C₂D₂Cl₄, heated with a heat gun in a 10 mm NMR tube, and transferred to the NMR spectrometer with the probehead pre-equilibrated at 125°C. A 2.0 s acquisition time was used with a pulse delay of 6.0 s. A total of 4000–6000 transients were accumulated for each spectrum. Pentad signals were assigned

15. Massey, A. G.; Park, A. J. *J. Organomet. Chem.* **1964**, 2, 245-250.

according to literature criteria.¹⁶ Melting temperatures of polymers were measured by DSC (DSC 2920, TA Instruments, Inc.) from the second scan with a heating rate of 10°C/min. GPC analyses of polymer samples were performed at the Dow Chemical Co., Chemical Sciences Catalysis Laboratory, Midland, Michigan, on a Waters Alliance GPCV 2000 high temperature instrument. A polystyrene/polypropylene universal calibration was carried out using polystyrene standards.

Propylene Polymerization Experiments. Ambient-pressure propylene polymerizations were carried out on a high vacuum line (10^{-6} Torr) in 250 mL round-bottom three-neck Morton flasks equipped with large magnetic stirring bars, and with rapid stirring (~ 1000 rpm) to minimize mass transfer,¹⁷ and thermocouple probes to monitor exotherm effects.^{2c} In a typical experiment, dry toluene (50 mL) was vacuum transferred into the flask from Na/K, pre-saturated

16. (a) Busico, V.; Cipullo, R.; Monaco, G; Vacatello, M. *Macromolecules* **1997**, *30*, 6251-6263. (b) Pellecchia, C.; Pappalardo, D.; D'Arco, M.; Zambelli, A. *Macromolecules* **1996**, *29*, 1158. (c) Busico, V.; Cipullo, R.; Corradini, P.; Landriani, L.; Vacatello, M.; Segre, A. L. *Macromolecules* **1995**, *28*, 1887. (d) Miyatake, T.; Miaunuma, K.; Kakugo, M. *Macromol. Symp.* **1993**, *66*, 203. (e) Kakugo, M.; Miyatake, T.; Miaunuma, K. *Stud. Surf. Sci. Catal.* **1990**, *56*, 517. (f) Longo, P.; Grassi, A. *Makromol. Chem.* **1990**, *191*, 2387. (g) Randall, J. C. *J. Polym. Sci., Part B: Polym. Phys.* **1975**, *13*, 889.

17. At 20°C, rate of C₃H₆ absorption is estimated 0.029 (mol/min) in toluene at 1.0 atm of C₃H₆, and propylene mass transfer effects (mass transport coefficient) in (2-PhInd)₂ZrCl₂/ MAO system in toluene (100mL) are observed to be insensitive to the presence of up to 4 g of isotactic PP with a maximum stirring speed (1460 rpm), See: Lin, S.; Tagge, C. D.; Waymouth, R. M.; Nele, M.; Collins, S.; Pinto, J. C. *J. Am. Chem. Soc.* **2000**, *122*, 11275-11285. In the present study, the most active ion pair system, **5** (**9**) at 40°C and 1.0 atm of C₃H₆, has a rate of propylene consumption of ~ 0.015 (mol/min) ($0.77/42 \cdot (75/60)$), which should be lower at 20°C since lower activity is observed at lower temperatures. Thus, propylene mass transfer effects should be negligible for all catalysts under the present conditions.

under 1.0 atm of rigorously purified propylene, and equilibrated at the desired reaction temperature using an external water bath. The catalytically-active species was freshly generated in 2–4 mL of dry toluene in the glove box. Control NMR experiments revealed quantitative activation of the catalyst under these conditions (*vide infra*). The catalyst solution was then quickly injected into the rapidly stirred flask using a gas-tight syringe. The temperature of the reaction mixture during polymerization was monitored in real time using a thermocouple thermometer (OMEGA Type K). The temperature rise was invariably less than 3°C during these polymerizations, and temperature was controlled by occasional addition of ice to the external water bath. After a measured time interval, the reaction was quenched by the addition of 10 mL 2% acidified methanol. Another 300–400 mL methanol was then added and the polymer was collected by filtration, washed with methanol, and dried on the high vacuum line to a constant weight.

High pressure polymerization experiments in toluene solutions were carried out in a 350 mL heavy wall glass pressure reactor, (Chemglass Co., maximum pressure, 10 atm) equipped with a septum port, a large magnetic stirring bar (1000 rpm), and an internal thermocouple (OMEGA Type K), and connected to a high-pressure manifold equipped with a gas inlet, diaphragm capacitance pressure gauge (0–200 psig), and gas outlet (Figure 1). *CAUTION: All of these procedures should be performed behind a blast shield.* In a typical procedure, in glove box, the reactor was charged with dry toluene (50 mL) and the apparatus was assembled, removed, and then connected to the high-pressure manifold. Under rapid stirring, rigorously purified propylene was pressurized into the flask to reach ~ 5–6 atm over 5 min and then slowly released to 1.0 atm over 5 min. This fill and release process was repeated five times. The solution was then equilibrated at the desired propylene pressure (1.0–5.0 atm) and reaction temperature adjusted using an external water bath. Preparation of the catalytically-active species, temperature

control, and reaction quenching were performed as described for ambient-pressure reactions. Propylene pressure was then released to 1.0 atm and polypropylene workup was carried out using the procedure described above. Polymerization experiments in 1,3-dichlorobenzene or octane solutions were carried out as described above, but with addition of 50 mL dry 1,3-dichlorobenzene or octane by cannula through the septum port. Ion pair complexes were prepared and introduced as described above.

Microstructural Analysis of Polypropylene ^{13}C NMR Spectra. Polymer methyl resonances were assigned according to established criteria,¹⁶ and were analyzed at the pentad level. All polymer NMR spectra were collected with identical temperature, solvent, instrument field strength, and acquisition and processing parameters. Steric pentad distributions were determined from direct integration of the following regions (ppm): δ 21.91–21.7 (*mmmm*); 21.63–21.46 (*mmmr*); 21.43–21.24 (*rmmr*); 21.16–20.94 (*mmrr*); 20.94–20.74 (*xrmx*); 20.74–20.58 (*rmmr*); 20.58–19.74 (*rrrr* + *rrrm* + *mrrm*). Pentad distributions were modeled using the syndiospecific Bernoullian model outlined in Table 16 of Ref. 11a (p. 1316), having probability parameters P_m and P_{mm} of formation for *m* and *mm* stereodeflects, respectively. These probabilities were determined by successive nonlinear least-squares minimization of the function,

$$\text{wR}^2 = \frac{\sum (I_{\text{exp}} - I_{\text{calc}})^2 (1 + I_{\text{exp}})^w}{\sum I_{\text{exp}}^2} \quad (3)$$

where I_{exp} and I_{calc} are experimental and calculated integral values (normalized to $\sum I_{\text{exp}} = 1$) with weighting factor $w = 25$ for all regions, with the exception of the *rrrr* + *rrrm* + *mrrm* integral, for which $w = 0$. This weighting scheme increases the contribution to wR^2 of stronger signals (having greater S/N ratios), while ensuring that the *rrrr* + *rrrm* + *mrrm* integral, which is substantially larger than the rest, does not dominate the refinement. Agreement factors calculated

according to the standard method, $R^2 = \Sigma(I_{\text{exp}} - I_{\text{calc}})^2 / \Sigma(I_{\text{exp}})^2$,^{13c} are less than 0.001 in all but two cases, with 0.0022 the highest value. I_{exp} , I_{calc} , and weighting multipliers $(1 + I_{\text{exp}})^w$, for each experiment, along with P_m , P_{mm} , wR^2 and R^2 for each set, are given in the Supporting Information.

Reaction of [Me₂C(Cp)(Flu)]ZrMe₂ with B(C₆F₅)₃, B(*o*-C₆F₅C₆F₄)₃, Ph₃C⁺B(C₆F₅)₄⁻, or Ph₃C⁺FAl(*o*-C₆F₅C₆F₄)₃⁻. [Me₂C(Cp)(Flu)]ZrMe₂ (**1**) and cocatalysts (**3–6**) were loaded into a J. Young NMR tube and 0.5 mL of toluene-*d*₈ was transferred in via pipette. Each sample was then shaken vigorously and removed directly to the NMR spectrometer. Reagents **1** (3.9 mg, 10 μmol) and **3** (B(C₆F₅)₃, 5.1 mg, 10 μmol) were combined, and complete reaction with rapid formation of [Me₂C(Cp)(Flu)]ZrMe⁺MeB(C₆F₅)₃⁻ (**7**) was observed (NMR data are presented below). Reagents **1** (3.9 mg, 10 μmol) and **4** (B(*o*-C₆F₅C₆F₄)₃, 4.8 mg, 5.0 μmol) were combined, and complete reaction with rapid formation of {[Me₂C(Cp)(Flu)]ZrMe₂(μ-Me)}⁺MeB(*o*-C₆F₅C₆F₄)₃⁻ (**8**) was observed. ¹H and ¹⁹F NMR data for **8** are given in a previous report.^{8a} Reagents **1** (1.0 mg, 2.5 μmol) and **5** (Ph₃C⁺B(C₆F₅)₄⁻, 2.3 mg, 2.5 μmol) were combined, and complete reaction with rapid formation of [Me₂C(Cp)(Flu)]ZrMe⁺B(C₆F₅)₄⁻ (**9**) and Ph₃CCH₃ was observed. The C₆H₄ signals of the fluorenyl region could not be assigned completely due to overlap of the signals with the solvent. ¹H NMR for **9** (C₇D₈, 23°C): δ 7.8 (d, 1 H, C₆H₄), 7.6 (d, 1 H, C₆H₄), 5.742 (m, 1 H, C₅H₄), 4.824 (m, 1 H, C₅H₄), 4.435 (m, 1 H, C₅H₄), 3.813 (m, 1 H, C₅H₄), 1.667 (s, 3 H, CMe₂), 1.477 (s, 3 H, CMe₂), -1.142 (s, 3 H, Zr-CH₃). ¹⁹F NMR (C₇D₈, 23°C): δ -132.06 (m, *o*-F), -132.49 (m, *o*-F), -162.77 (t, ³J_{F-F} = 21.5 Hz, *p*-F), -163.0 (m, *p*-F), -166.72 (m, *m*-F), -166.96 (m, *m*-F). Prolonged standing of complex **9** results in a red-brown oily residue, and the solution gradually turns brown-green. In a reaction of **1** with **5** at a fourfold higher concentration, the red-brown oily residue forms immediately, and generates

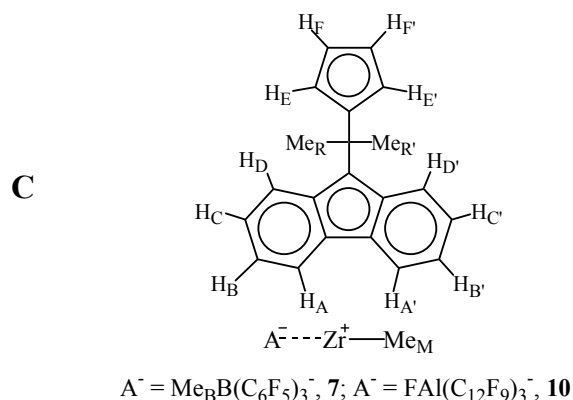
mixtures of unidentified complexes. Reagents **1** (2.0 mg, 0.005 mmol) and **6** ($\text{Ph}_3\text{C}^+\text{FAl}(\text{o-C}_6\text{F}_5\text{C}_6\text{F}_4)_3^-$, 6.5 mg, 0.0050 mmol) were combined and complete reaction of **1** with rapid formation of $[\text{Me}_2\text{C}(\text{Cp})(\text{Flu})]\text{ZrMe}^+\text{FAl}(\text{o-C}_6\text{F}_5\text{C}_6\text{F}_4)_3^-$ (**10**) and Ph_3CCH_3 was observed (NMR data are presented below).

***In Situ* Generation of Ion Pairs 7–10 for Polymerization Studies.**

$[\text{Me}_2\text{C}(\text{Cp})(\text{Flu})]\text{ZrMe}_2$ (**1**) and the required cocatalyst in a 1:1 ratio (**3**, **5**, **6**) or a 0.5:1 ratio (**4**) were loaded in the glove box into a vial equipped with a septum, and 2–4 mL of toluene was added. The mixture was shaken vigorously at room temperature for 10 min (**3**, **4**, **6**) or 2 min (**5**) before use. Total amounts used were chosen/refined as required for temperature control and are reported herein (see Tables 7, 8, and 12–14).

Synthesis of $[\text{Me}_2\text{C}(\text{Cp})(\text{Flu})]\text{ZrMe}^+\text{MeB}(\text{C}_6\text{F}_5)_3^-$ (7**).** In the glovebox, $[\text{Me}_2\text{C}(\text{Cp})(\text{Flu})]\text{ZrMe}_2$ (**1**, 97.5 mg, 0.250 mmol), $\text{B}(\text{C}_6\text{F}_5)_3$ (**3**, 128 mg, 0.250 mmol), and 50 mL toluene were loaded into a 100 mL reaction flask having a filter frit and stirred for 2 h at room temperature. The solvent was next reduced *in vacuo* to 10 mL, and 50 mL pentane was condensed into the flask. The resulting suspension was filtered, and the collected solid was washed with 5 mL of pentane and dried under vacuum to afford 174 mg of the title complex; yield, 77%. ^1H NMR peak assignments are determined from combined 1-D and 2-D NMR techniques, and are as follows (labeling outlined in C): ^1H NMR (C_7D_8 , 23°C): δ 7.65 (d, $J_{\text{H-H}} = 8.5$ Hz, 1 H, H_A), 7.60 (d, $J_{\text{H-H}} = 8.5$ Hz, 1 H, H_A'), 7.12 (d, $J_{\text{H-H}} = 6.3$ Hz, 1 H, H_B), 7.05 (d, $J_{\text{H-H}} = 8.2$ Hz, 1 H, H_D), 6.92 (d, $J_{\text{H-H}} = 8.3$ Hz, 1 H, H_D'), 6.74 (t, $J_{\text{H-H}} = 7.7$ Hz, 1 H, H_C), 6.63 (t, $J_{\text{H-H}} = 7.1$ Hz, 1 H, H_C'), 6.41 (t, $J_{\text{H-H}} = 8.2$ Hz, 1 H, H_B'), 5.93 (d, $J_{\text{H-H}} = 3.0$ Hz, 1 H, H_F), 5.55 (d, $J_{\text{H-H}} = 3.0$ Hz, 1 H, H_F), 5.20 (d, $J_{\text{H-H}} = 3.0$ Hz, 1 H, H_E), 4.45 (d, $J_{\text{H-H}} = 3.0$ Hz, 1 H, H_E'), 1.50 (s, 3 H, Me_R), 1.46 (s, 3 H, Me_R'), -0.53 (s, br, 3 H, Me_B), -0.92 (s, 3 H, Me_M). ^{19}F NMR (C_7D_8 ,

23°C): δ -133.39 (d, $^3J_{F-F} = 22.60$ Hz, 6 F, *o*-F), -159.60 (t, $^3J_{F-F} = 20.6$ Hz, 3 F, *p*-F), -164.62 (t, $^3J_{F-F} = 18.3$ Hz, 6 F, *m*-F). Anal. Calc'd for C₄₁H₂₄BF₁₅Zr: C, 54.49; H, 2.68. Found: C, 54.37; H, 2.84.



Synthesis of [Me₂C(Cp)(Flu)]ZrMe⁺ FAl(*o*-C₆F₅C₆F₄)₃⁻ (10**).** In the glovebox, [Me₂C(Cp)(Flu)]ZrMe₂ (**1**, 97.5 mg, 0.250 mmol), Ph₃C⁺FAl(*o*-C₆F₅C₆F₄)₃⁻ (**6**, 328 mg, 0.250 mmol), and 100 mL toluene were loaded into a 250 mL reaction flask having a filter frit, and stirred for 2 h at room temperature. The solvent was next reduced in *vacuo* to 10 mL, and 100 mL pentane was condensed into the flask. The resulting suspension was filtered, and the collected solid was washed with 20 mL of pentane and dried under vacuum to afford 280 mg of the title complex; yield, 82%. As measured from ¹H spectra, a pair of diastereomers is evident in a 1.6:1 ratio at 23°C. Assignment of the ¹H NMR spectrum was accomplished with combined NOE, EXSY, and COSY techniques; atom labeling is described in **C**. Major and minor diastereomers are differentiated with upper- and lower-case subscripts, respectively. Certain of the C₆H₄ signals of the fluorenyl region could not be clearly assigned due to overlap between the signals of the two isomers. ¹H NMR (C₇D₈, 23°C) for major diastereomer: δ 7.99 (d, $J_{H-H} = 8.0$ Hz, 1 H, H_{A'}), 7.90 (dm, $J_{H-H} = 4.0$ Hz, 1 H, H_A), 7.20 (m, 2 H, H_{B'} and H_D), 7.00 (1 H, H_{D'}), 6.78 (m, 2 H, H_C and H_{C'}), 6.20 (s, 1 H, H_F), 6.08 (t, $J_{H-H} = 8.0$ Hz, 1 H, H_B), 5.44 (m, 1 H, H_E), 4.85

(s, 1 H, H_F), 4.61 (m, 1 H, H_{E'}), 1.61 (s, 3 H, Me_R), 1.44 (s, 3 H, Me_{R'}), -1.03 (s, 3 H, Me_M).

Minor diastereomer: δ 7.65 (d, $J_{\text{H-H}} = 8.4$ Hz, 1 H, H_{a'}), 7.55 (dm, $J_{\text{H-H}} = 8.0$ Hz, 1 H, H_a), 7.20 (m, 1 H, H_d), 7.09 (1 H, H_b), 7.00 (2 H, H_c and H_{d'}), 6.74 (m, 1 H, H_c), 6.32 (s, 1 H, H_f), 5.99 (t, $J_{\text{H-H}} = 8.0$ Hz, 1 H, H_b), 5.44 (m, 1 H, H_e), 5.00 (s, 1 H, H_f), 4.58 (m, 1 H, H_{e'}), 1.65 (s, 3 H, Me_R), 1.50 (s, 3 H, Me_{R'}), -1.07 (s, 3 H, Me_M). ¹⁹F NMR (C₇D₈, 23°C) for major diastereomer: δ -113.62 (s, br, 3F), -133.90 (m, 3F), -134.60 (s, br, Al-F), -138.04 (m, 3F), -139.24 (t, $^3J_{\text{F-F}} = 21.5$ Hz, 3F), 153.27 (t, $^3J_{\text{F-F}} = 19.8$ Hz, 6F), 154.87 (m, 3F), 161.38 (m, 3F), 163.03 (t, $^3J_{\text{F-F}} = 21.2$ Hz, 3F). Minor diastereomer: δ 116.01 (s, br, 3F), -132.42 (s, br, Al-F), -133.90 (m, 3F), -138.68 (m, 3F), -139.55 (t, $^3J_{\text{F-F}} = 18.9$ Hz, 3F), 153.52 (t, $^3J_{\text{F-F}} = 21.2$ Hz, 3F), 153.68 (t, $^3J_{\text{F-F}} = 23.7$ Hz, 3F), 153.89 (m, 3F), 161.22 (dd, $J_{\text{F-F}} = 21.2, 7.6$ Hz, 3F), 162.84 (t, $^3J_{\text{F-F}} = 23.7$ Hz, 3F). Anal. Calc'd for C₅₈H₂₁AlF₂₈Zr: C, 50.92; H, 1.55. Found: C, 50.64; H, 1.73.

X-Ray Crystal Structure Determinations of [Me₂C(Cp)(Flu)]ZrMe⁺ MeB(C₆F₅)₃⁻ (7) and [Me₂C(Cp)(Flu)]ZrMe⁺ FAl(*o*-C₆F₅C₆F₄)₃⁻ (10). Crystals of the title complexes suitable for X-ray diffraction were obtained by slow diffusion of pentane into toluene solutions at 0°C. Crystals were selected and mounted under Infineum V8512 oil, and held under a nitrogen cold-stream at 153(2) K for data collection. Diffraction data were obtained using a Bruker SMART 1000 CCD area detector diffractometer with a fine-focus, sealed tube Mo K α radiation source ($\lambda = 0.71073$ Å) and graphite monochromator. For both **7** and **10**, the initial crystal structure solution was obtained via Patterson synthesis, refined through successive least-squares cycles, and subjected to a face-indexed absorption correction. The refinements were carried to convergence, with hydrogen atoms placed in idealized positions and refined isotropically with fixed U_{eq} under standard riding model constraints, with the following exception: in complex **7**, hydrogen atoms H₃C–B were refined isotropically with group thermal, H–C distance, and H–H

distance parameters. Crystal data collection and refinement parameters are summarized in Table 1 and can be found in the Crystallographic Information File (CIF, see Supporting Information).

2D EXSY NMR Studies of Ion Pair Reorganization/Symmetrization in **7** and **10**.

Toluene-*d*₈ solutions of pure [Me₂C(Cp)(Flu)]ZrMe⁺ MeB(C₆F₅)₃⁻ (**7**, 4.0 mg, 5.5 μM) or [Me₂C(Cp)(Flu)]ZrMe⁺ FAl(*o*-C₆F₅C₆F₄)₃⁻ (**10**, 7.0 mg, 6.4 μM) were prepared in the glove box, and filtered directly into J. Young NMR tubes. Spectra were collected using the NOESY pulse sequence,¹⁸ with acquisition parameters optimized to resolve peaks of interest. Mixing times $\tau_m = 40\text{--}800$ ms, were chosen to minimize the error in calculated exchange rates, according to $\tau_m = (T_1^{-1} + k_{AB} + k_{BA})^{-1}$, where k_{AB} and k_{BA} are estimates of the A→B and B→A exchange rate constants, respectively.¹⁹ Data were zero-filled to 2×np and 4×ni in the *t*₂ and *t*₁ dimensions, respectively, and apodized using appropriate Gaussian weighting in the *t*₂ dimension and combined Gaussian weighting and 1 Hz line-broadening in the *t*₁ dimension, unless otherwise noted. Rate constant calculations are described in the discussion.¹⁹ For **7** ($\tau_m = 600\text{ms}$, 20.5°C), quadrupolar relaxation of the ¹¹B- and ¹⁰B-coupled Me_B protons precludes accurate determination of rates for exchange involving these resonances using this technique. For **10**, exchange rates between resonances H_A and H_a and between H_{A'} and H_{a'} were averaged to determine anion racemization rates at 87.5°C ($\tau_m = 185\text{ms}$) and 117.5°C ($\tau_m = 40\text{ms}$). Anion racemization rate constants calculated from EXSY data are in good agreement with values obtained from lineshape analysis (*vide infra*). At 127°C, τ_m was optimized to determine, or to place a higher limit on, the rate of ion pair reorganization ($\tau_m = 800\text{ms}$). In this case, 14,000 real

18. Macura, S.; Ernst, R. R. *Mol. Phys.* **1980**, *41*, 95-117.

19. Perrin, C. L.; Dwyer, T. J. *Chem. Rev.* **1990**, *90*, 935-967. and also see Ref. 14.

points in the t_2 dimension and 256 points in the t_1 dimension were collected, and the data were processed with no zero-filling and 1 Hz line broadening in t_2 , and with linear prediction to 512 points, zero-filling to 8192 points, 1 Hz line broadening, and 0.036 sec Gaussian weighting in t_1 . With **10**, cross-peaks corresponding to ion pair reorganization are absent at all temperatures measured, invariantly with mixing time and data processing parameters. An upper limit for ion pair reorganization is established as described in the Discussion Section.

DNMR Studies of Ion Pair Reorganization/Symmetrization in 7 and 10 in Toluene- d_8 . Pure $[\text{Me}_2\text{C}(\text{Cp})(\text{Flu})]\text{ZrMe}^+ \text{MeB}(\text{C}_6\text{F}_5)_3^-$ (**7**, 8.0 mg, 8.8 μmol) or $[\text{Me}_2\text{C}(\text{Cp})(\text{Flu})]\text{ZrMe}^+ \text{FAl}(\text{o-C}_6\text{F}_5\text{C}_6\text{F}_4)_3^-$ (**10**, 7.0 mg, 5.1 μmol) were loaded in the glove box into capped vials, and 0.80 mL of a stock solution of $\text{CH}_3\text{Si}(\text{C}_6\text{H}_5)_3$ (internal standard, 11 mM for **7** and 6.4 mM for **10**) in toluene- d_8 was transferred into each vial. The resultant solutions were filtered and transferred into J. Young NMR tubes. Temperatures were varied over the range, 0°–92.5°C for **7**, and over 23° – 132.5°C for **10**. Prior to each acquisition, the NMR probehead was pre-equilibrated at the desired temperature for 10 min. Each acquisition consisted of 65536 points spanning 4360 Hz (resolution 0.067 Hz), and 4908 Hz (resolution 0.075 Hz), for **7** and **10**, respectively. The raw data were zero-filled to $2 \times \text{np}$. Unweighted transforms for both **7** and **10** were phased carefully and subjected to reference deconvolution on the methyl resonance of triphenylmethylsilane as the internal lineshape standard using the Hilbert algorithm,²⁰ along with baseline and drift corrections, such that the final standard peak width was 1.500 Hz in all spectra. Modeling of the ^{29}Si satellites of the reference signal was included in the reference deconvolution ($^2J_{\text{Si-H}} = 6.633$ Hz). Application of reference deconvolution was found to significantly improve variances, both for borane migration and for ion pair reorganization,

20. Rutledge, D. N., ed. *Signal Treatment and Signal Analysis in NMR*; Elsevier Science, 2003, Ch. 16.

compared to line fits generated from use of the approximation for half-height signal widths, $W_{\text{signal}} = W_{\text{real}} + \Delta W_{\text{natural}} + \Delta W_{\text{exchange}}$. For **7**, broadening of the proton signals of the diastereotopic *i*-Pr methyl groups (Me_R , Me_R') and of the zirconocenium methyl group (Me_M) were monitored over the temperature range, 57.8°C–92.3°C. Rate constants at each temperature were calculated from the half-height widths of these signals (measured using the VNMR command, dres) as compared to their widths in the slow-exchange limit (0°C).²¹ Values and confidence intervals for ΔH^\ddagger , ΔS^\ddagger , and ΔG^\ddagger were determined from linear regression analysis of $\ln(k/T)$ vs. $1/T$, and are reported at the 90% confidence level (Table 6).

For complex **10**, spectra were recorded over the temperature range, 78.5°C to 132.5°C, and referenced to a spectrum collected at 23°C. Complete lineshape analysis (CLSA)²² of these spectra converged for an exchange protocol including only diastereomer interconversion via anion racemization (Scheme 2), but failed to converge at all temperatures when a rate parameter for ion pair reorganization was included. Coalescence of the *i*-Pr bridge methyl signals at δ 1.61 (Me_R) and δ 1.65 (Me_R') of the two diastereomers was observed at 127.5°C.

DNMR Studies of Ion Pair Reorganization/Symmetrization in 8, 9. Ion pairs **8** and **9** were prepared *in situ* from $[\text{Me}_2\text{C}(\text{Cp})(\text{Flu})]\text{ZrMe}_2$ (**1**, 3.9 mg, 10 μmol for **8**, or 1.0 mg, 2.5 μmol for **9**) and $\text{B}(o\text{-C}_6\text{F}_5\text{C}_6\text{F}_4)_3$ (**4**, 4.8 mg, 5.0 μmol) or $\text{Ph}_3\text{C}^+\text{B}(\text{C}_6\text{F}_5)_4^-$ (2.3 mg, 2.5 μmol) with 0.5 mL of *o*-xylene-*d*₁₀. Decomposition of **8** begins at \sim 80°C. Complex **8** also decomposes rapidly in toluene at 115°C on a time scale of \sim 10 min to give a deep blue-purple precipitate.

21. (a) Sandstrom, J. *Dynamic NMR Spectroscopy*; Academic Press: New York, 1982; pp 77-92. and also see Ref.

4a. (b) Here k is the rate constant in s^{-1} ; $\Delta W = W_2 - W_1$, where W_2 is line width at half-height of the exchange broadened peak in Hz, and W_1 is the line width in the absence of exchange (the no-exchange limit, 0°C for **7** and 23°C for **10**). The corresponding free energies of activation can also be derived using $\Delta G^\ddagger = -RT[\ln(k/T) + \ln(h/k)]$.

22. Budzelaar, P.H.M. *gNMR v. 4.1.0*; Adept Scientific plc, 1999

Immediate decomposition of **9** was detected at 80°C and broadening of the diastereotopic methyl signals on the *i*-Pr bridge could not be clearly observed.

Concentration Dependence Study of Propylene Polymerization Catalyzed by 1 + 3.

Polymerization experiments were carried out in 100 mL toluene solutions in the high-pressure reaction vessel as described above. The catalytically-active species was freshly generated in 2–10 mL of dry toluene using [Me₂C(Cp)(Flu)]ZrMe₂ samples (**1**, 1.0 mg, 2.5 μmol; 2.0 mg, 5.1 μmol; 4.0 mg, 10 μmol; 8.0 mg, 20 μmol; 16.0 mg, 40.8 μmol; 32.0 mg, 81.6 μmol) activated with 1.0 equivalents of B(C₆F₅)₃ (**3**).

Propylene Polymerization Catalyzed by 1 + 3 with Added Li⁺ MeB(C₆F₅)₃⁻.

Polymerization experiments were carried out in 100 mL toluene solutions in the high-pressure reaction vessel described above. Li⁺ MeB(C₆F₅)₃⁻ was prepared *in situ* by mixing a 1:1 molar ratio of dry LiMe powder and B(C₆F₅)₃ in toluene, and the mixture was shaken vigorously at room temperature for 30 min before use. ¹H NMR (C₇D₈, 23°C): δ 0.79 (s, 3 H, Me). ¹⁹F NMR (C₇D₈, 23°C): δ -136.84 (d, br, *J*_{F-F} = 23.0 Hz, 6 F), -159.39 (t, *J*_{F-F} = 19.6 Hz, 3 F), -163.03 (t, *J*_{F-F} = 19.6 Hz, 6 F). The catalytically-active species was freshly generated in 2 ~ 4 mL toluene, as described above. The mixture was then combined with the corresponding Li⁺ MeB(C₆F₅)₃⁻ solution in toluene, shaken vigorously at room temperature for 3 min, and then injected immediately into the polymerization reactor.

Propylene Polymerization Catalyzed by 1 + MAO (2). Polymerization experiments were carried out in the high-pressure reaction vessel described above. In a typical polymerization, [Me₂C(Cp)(Flu)]ZrMe₂ (**1**, 3.9 mg) and MAO (**2**, 40 mg) were loaded in the glove box into a septum-capped vial, to which 4 mL of toluene was added. The mixture was shaken vigorously at room temperature for 20 min before use. In the polymerization reaction

flask, MAO (**2**, 80 mg) was loaded with 50 mL of toluene. The solution was then equilibrated at the desired polymerization temperature and pressure as described above.

RESULTS AND DISCUSSION

The following analysis couples complementary methods for studying ion pairing effects in polymerization systems, and is presented in three parts. First, a description of the preparation and characterization of the *in situ* generated and isolated active catalytic species is presented, with detailed structural and solution/dynamic characterization of **7** and **10**, with a discussion extending these results to polymerization behavior. Second, a detailed examination is presented of the effects of varying the cocatalyst/counteranion on polymerization dynamics and product polymer characteristics, as functions of temperature, monomer concentration, and solvent. Using these results, a comparative kinetic treatment is derived which provides a self-consistent model for the effects of ion pairing/counteranion identity on polymerization behavior and product polymer attributes. Finally, we present an examination of putative catalyst and counteranion concentration effects on syndioselection and other product polymer characteristics.

This Discussion focuses on the importance of ion pairing dynamics. The cation-anion interaction is recognized to have both electrostatic and covalent components;^{23,24} thus the *potential barrier* to ion pair reorganization in the isolated catalyst systems discussed below, or analogous site epimerization processes operative during polymerization, may have both

23. Strauss, S.H. *Chem. Rev.* **1993**, *93*, 927-942.

24. (a) Lanza, G.; Fragala, I. L.; Marks, T. J. *Organometallics* **2002**, *21*, 5594-5612. (b) Lanza, G.; Fragala, I. L.; Marks, T. J. *Organometallics* **2001**, *20*, 4006-4017. (c) Lanza, G.; Fragala, I. L.; Marks, T. J. *J. Am. Chem. Soc.* **2000**, *122*, 12764-12777.

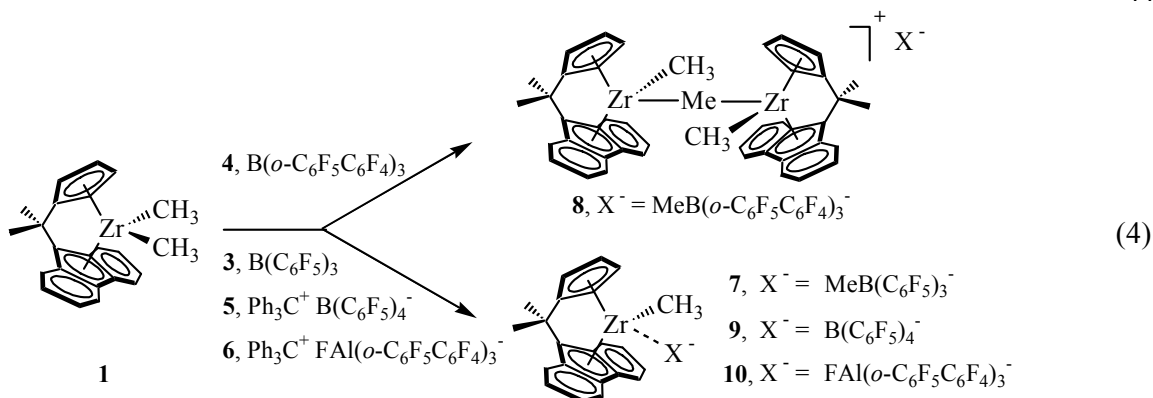
electrostatic and covalent/coordinative components. While there are doubtless differences in the relative magnitudes of the coordinative/covalent and electrostatic contributions to the ion pair reorganization barrier among the various ion pair complexes studied here, we do not distinguish between these components using the present experimental results, and refer to kinetic inertness of the ion pair toward reorganization as "ion pairing strength," or "coordinative tendency."

I. Zirconocenium Cations Generated via Reaction of $[\text{Me}_2\text{C}(\text{Cp})(\text{Flu})]\text{ZrMe}_2$ with Cocatalysts 3–6.

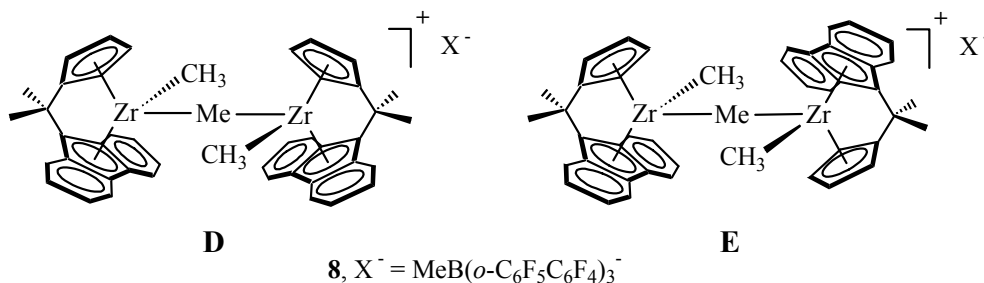
The substantial body of available structural and spectroscopic data on complexes **7–10** permits qualitative and quantitative evaluation of cation-anion interactions. These interactions exhibit diverse structural/dynamic behavior, which is quantified using X-ray diffraction and dynamic NMR spectroscopy. The purpose of the following discussion is to highlight key structural and kinetic features of these systems, and to set the stage for correlation with polymerization characteristics.

A. Synthesis and Spectroscopy. Under rigorously anhydrous/anaerobic conditions, $[\text{Me}_2\text{C}(\text{Cp})(\text{Flu})]\text{ZrMe}_2$ (**1**) undergoes reaction with $\text{B}(\text{C}_6\text{F}_5)_3$ (**3**), $\text{B}(o\text{-C}_6\text{F}_5\text{C}_6\text{F}_4)_3$ (**4**),^{8a} $\text{Ph}_3\text{C}^+\text{B}(\text{C}_6\text{F}_5)_4^-$ (**5**), and $\text{Ph}_3\text{C}^+\text{FAl}(o\text{-C}_6\text{F}_5\text{C}_6\text{F}_4)_3^-$ (**6**)^{8a} to generate the corresponding ion pairs (**7–10**; Eq. 4) and to afford highly active olefin polymerization catalysts.²⁵ Except for **9**, these

25. NMR-scale reaction of **1** with MAO is not amenable to interpretation, thus will not be discussed here.



ion pairs can be isolated and characterized by standard 1-D and 2-D $^1H/^{19}F$ NMR, and analytical techniques (see Experimental Section for details); **7** and **10** have been further characterized by single-crystal X-ray diffraction (*vide infra*). The reaction of cocatalyst $B(C_6F_5)_3$ (**3**) or $Ph_3C^+FAl(o-C_6F_5C_6F_4)_3^-$ (**6**) with **1** cleanly generates the monomeric ion pairs **7** and **10** in good isolated yield. In contrast, $B(o-C_6F_5C_6F_4)_3$ (**4**) preferentially yields cationic μ -Me bridged dinuclear complex **8** as diastereomers in a ratio of 1.8:1 (**D** and **E**, depicted below), even with



stoichiometric excesses of reagent **4** and long reaction times.^{8a} The reaction of cocatalyst $Ph_3C^+B(C_6F_5)_4^-$ (**5**) with **1** affords ion pair **9** as suggested by 1H NMR (along with 1.0 stoichiometric equivalent of Ph_3CCH_3), with **9** being the least stable of the present four ion pairs. Attempts to isolate or crystallize this complex have been unsuccessful, and have resulted in dark oily residues and a yellow-green solution (similar behavior is observed for most known group 4 metallocenium $B(C_6F_5)_4^-$ complexes).^{7c}

Interactions between the cationic and anionic portions of ion-pair complexes **7-10** can be evaluated qualitatively from ambient temperature 1-D 1H and ^{19}F NMR spectroscopy. The 1H

NMR spectra of these compounds are straightforward, with four distinct resonances at δ 4–6 ppm for the C_5H_4 ring and two methyl signals at δ 1.5–2.0 ppm for the *ansa*-isopropyl group, in accord with the dissymmetry generated by the ion pairing. The Zr–CH₃ proton signals in **7**, **9**, and **10** invariably appear at $\sim \delta$ -1 ppm; in contrast, the Zr–CH₃ signals of **8** appear at -1.21 and -1.27 (for major and minor diastereomers, respectively), and the μ -Me (bridging Zr–CH₃–Zr) proton resonance of **8** appears in the region typical of this chemical environment (δ 3.33 ppm). As previously shown, metallocenium cation–MeB(*o*-C₆F₅C₆F₄)₃[−] interactions are considerably weaker than those involving MeB(C₆F₅)₃[−], and the equilibrium solution structure of **8** argues that neutral [Me₂C(Cp)(Flu)]ZrMe₂ has a greater affinity for the cation than does MeB(*o*-C₆F₅C₆F₄)₃^{−5a,8a}. Thus, the relative coordinative tendency of these methyl fluoroarylborate anions versus neutral [Me₂C(Cp)(Flu)]ZrMe₂ with respect to the [Me₂C(Cp)(Flu)]ZrMe⁺ cation follows the order MeB(C₆F₅)₃[−] > [Me₂C(Cp)(Flu)]ZrMe₂ > MeB(*o*-C₆F₅C₆F₄)₃[−].

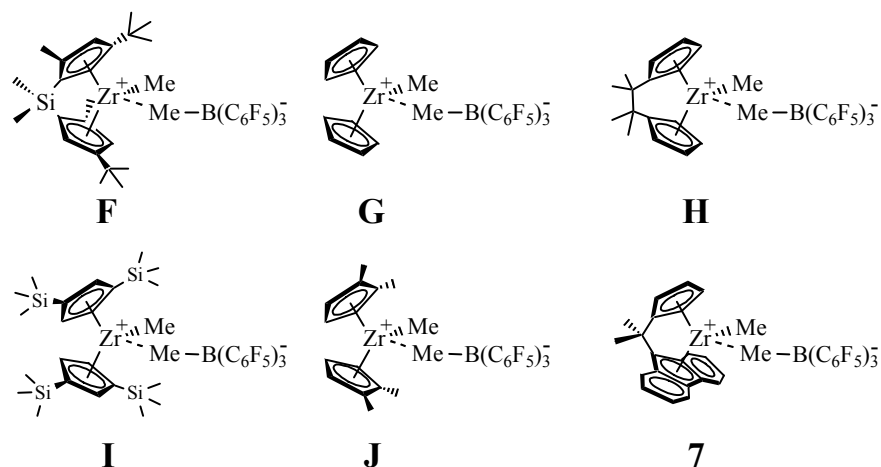
In a prior communication, we observed that ion pairing interactions between metallocenium cations and fluoroaryl counteranions significantly influence fluoroaryl ¹⁹F NMR chemical shifts.^{8a} Thus, the ¹⁹F spectrum of complex **9** shows no substantial chemical shift differences from that of Ph₃C⁺ B(C₆F₅)₄[−] (**5**) at room temperature, suggesting that B(C₆F₅)₄[−] coordination to Zr⁺ is weak and labile. Conversely, chemical shift evidence for strong cation-anion interactions in **10** in solution is readily detected in the ¹⁹F NMR spectra. While Ph₃C⁺ FAl(*o*-C₆F₅C₆F₄)₃[−] (**6**) exhibits seven ¹⁹F signals (1:1:1:1:1:2:2), **10** exhibits nine fluoroaryl signals, indicative of restricted internal C₆F₅ rotation but free anion rotation about the Zr–F–Al linkage. The existence of **10** as diastereomers in toluene-*d*₈ solution, together with other structural and dynamic data, demonstrates that the mutual *o*-perfluorobiphenyl group orientations impart chirality to the Al center in solution, as seen in the solid state (*vide infra*).

The ^{19}F NMR spectrum of **10** exhibits a characteristic broad $\text{F}-\text{Al}$ resonance at δ -132.2 ppm, which, compared to the $\text{F}-\text{Al}$ chemical shift of $\text{Ph}_3\text{C}^+ \text{FAl}(\text{o}-\text{C}_6\text{F}_5\text{C}_6\text{F}_4)_3^-$ (δ . -175.60 ppm), demonstrates a strong $\text{M}^+\cdots\text{F}-\text{Al}^-$ interaction, and is consistent with a (time-averaged) preferred orientation of the fluoroaluminate ion with respect to the cation. Diffraction data clearly confirm the coordination of the $\text{FAl}(\text{o}-\text{C}_6\text{F}_5\text{C}_6\text{F}_4)_3^-$ anion via the $\text{Zr}-\text{F}-\text{Al}$ bridge in the solid-state structure of **10**.

B. X-Ray Crystal Structures of $[\text{Me}_2\text{C}(\text{Cp})(\text{Flu})]\text{ZrMe}^+ \text{MeB}(\text{C}_6\text{F}_5)_3^-$ (7**), and $[\text{Me}_2\text{C}(\text{Cp})(\text{Flu})]\text{ZrMe}^+ \text{FAl}(\text{o}-\text{C}_6\text{F}_5\text{C}_6\text{F}_4)_3^-$ (**10**).** Attempts were made during the course of this study to grow single crystal samples of complexes **7–10**, and crystals of more stable ion pairs **7** and **10** suitable for X-ray analysis were obtained.²⁶ The structure of **7** shows the $[\text{Me}_2\text{C}(\text{Cp})(\text{Flu})]\text{ZrMe}^+$ cation in contact with the counteranion through the $\text{MeB}(\text{C}_6\text{F}_5)_3^-$ methyl group (Figure 2). Important bond distances and angles for **7** are summarized in Table 2. The $\text{Zr}-\text{Me}_\text{B}-\text{B}$ bridge is nearly linear (bond angle $165.5(3)^\circ$). This interaction has been shown by *ab initio* calculations to be predominantly electrostatic in nature.²⁴ The $\text{Me}_\text{B}-\text{Zr}-\text{Me}_\text{M}$ bond angle is $94.15(17)^\circ$, with the $\text{Zr}-\text{Me}_\text{M}$ distance ($2.248(4)\text{\AA}$), significantly shorter than the $\text{Zr}-\text{Me}_\text{B}$ distance ($2.521(4)\text{\AA}$). In comparison with the non-coordinating $\text{Me}_\text{B}\text{B}(\text{C}_6\text{F}_5)_3^-$ anion in previously reported structure $\{([\text{Me}_2\text{C}(\text{Cp})(\text{Flu})]\text{Zr}(\text{C}_6\text{F}_5)_2(\mu-\text{F})\}^+ \text{MeB}(\text{C}_6\text{F}_5)_3^-$,^{8a} the slightly longer $\text{Me}_\text{B}-\text{B}$ bond distance ($1.652(7)\text{\AA}$ vs. $1.64(2)\text{\AA}$) and smaller mean $\text{C}(\text{C}_6\text{F}_5)-\text{B}-\text{Me}_\text{B}$ angle ($108.7(4)^\circ$ vs. $111.4(9)^\circ$) show the effect on anion structure in **7** due to cation-anion interaction. This observed coordination-induced lengthening of the $\text{B}-\text{Me}_\text{B}$ bond and flattening of the

26. When a toluene solution of complex **7** was left standing at room temperature for two weeks, crystals of decomposition product $\{[\text{Me}_2\text{C}(\text{Flu})(\text{Cp})\text{Zr}(\text{C}_6\text{F}_5)_2(\mu-\text{F})\}^+ \text{MeB}(\text{C}_6\text{F}_5)_3^-$ were obtained, as reported previously, see Ref. 8a.

$B(C_6F_5)_3$ substructure (compared to uncoordinated $MeB(C_6F_5)_3^-$) possibly reflect the degree to which the cation and anion share the Me_B moiety, hence the degree of covalent character of the $Zr-Me_B$ interaction. In comparison with reported analogous zirconocenium $MeB(C_6F_5)_3^-$ ion pair crystal structures (**F–J**),^{27a-e} the present result affords the shortest $B-Me_B$ (0.024Å shorter than the average of **F–I**)^{27f}



and $Zr-Me_B$ bond distances observed to date (0.047Å shorter than the average), and the largest mean $C(C_6F_5)-B-Me_B$ angle (1.8° larger than the average; Table 3), suggesting that the covalent character of the action-anion interaction, while evident, is least in the present case. The observed $Cp(\text{centroid})-Zr-Cp(\text{centroid})$ angle (bite angle) for **7** (118.6°), as compared with **F** (127.0°),^{27a} may be correlated with closer proximity of the bridging methyl carbon and counteranion boron atoms to the metal in structure **7**. However, the steric bulk of the ancillary ligand structure and

27. (a) **F**, $[Me_2Si(Cp')_2]ZrMe^+ MeB(C_6F_5)_3^-$; $Cp' = C_5H_2(Me)(t-Bu)$, Ref. 14. (b) **G**, $(Cp)_2ZrMe^+$

$MeB(C_6F_5)_3^-$, Guzei, I. A.; Stockland, R. A.; Jordan, R. F. *Acta Crystallogr., Sect. C (Cryst. Str. Comm.)* **2000**, C56,

635-636. (c) **H**, $[Me_4C_2(Cp)_2]ZrMe^+ MeB(C_6F_5)_3^-$, Beck, S.; Prosenc, M. H.; Brintzinger, H. H.; Goretzki, R.;

Herfert, N.; Fink, G. *J. Mol. Catal. A: Chem.* **1996**, 111, 67-79. (d) **I**, $[(1,3-C_5H_3R_2)_2]ZrMe^+ MeB(C_6F_5)_3^-$; R =

$SiMe_3$, ref. 4a, also see: Bochmann, M.; Lancaster, S. J.; Hursthouse, M. B.; Malik, K. M. A. *Organometallics*

1994, 13, 2235-2243. (e) **J**, $[(1,2-C_5H_3Me_2)_2]ZrMe^+ MeB(C_6F_5)_3^-$, ref. 4a. (f) Average of the five complexes, **F–J**.

difference in backbone composition in **F** also possibly contribute to the observed differences in Zr–Me_B–B(C₆F₅)₃ geometry.

The crystal structure of **10** shows the [Me₂C(Cp)(Flu)]ZrMe⁺ moiety in close contact with sterically congested FAl(*o*-C₆F₅C₆F₄)₃[−] through a Zr–F–Al bridge (Figure 3). Important bond distances and bond angles of **10** are summarized in Table 4. For **10**, the Zr–F–Al (162.21(10)°) and F–Zr–Me (92.65(10)°) bond angles, as well as the Zr–Me (2.245(3)Å) and Al–F (1.7858(17)Å) bond distances are reminiscent of those in [*rac*-Me₂Si(Ind)₂ZrMe]⁺ FAl(*o*-C₆F₅C₆F₄)₃[−] (166.5(8)°, 90.8(6)°, 2.24(2)Å, 1.81(1)Å, respectively).^{8a} The anion in **10** adopts a pseudotetrahedral geometry, with the C₆F₅–C₆F₄ torsion angles substantially divergent from 90° (72.3° on average; ranging from 70.6° to 79.0°). In comparison with trityl salt **6**, which shows no cation-anion coordinative interaction in the solid state,^{8a} **10** exhibits a much longer Al–F bond distance (1.786(2)Å vs. 1.682(5)Å) and much smaller average of the three F–Al–C₁₂F₉ bond angles (103.0(1)° vs. 107.7(3)°), demonstrating that the impact of the zirconocenium cation on the structure of the fluoroaluminate anion is large in comparison to the cation influence on the anion structure in **7**.

Direct comparison of the cation structures in complexes **7** and **10** shows a subtle relationship between counteranion identity and Zr environment. In **10**, the larger Cp(centroid)–Cp(flu, centroid) distance (3.796(11)Å vs. 3.763(14)Å), greater metal-ligand distances (Zr–Cp(centroid), 2.176(3)Å vs. 2.157(4)Å; Zr–C(*i*-Pr bridging), 3.124(3)Å vs. 3.109(4)Å), and greater C(bridgehead, Cp)–C(*i*-Pr bridging) bond distance (1.530(5)Å vs. 1.512(6)Å) in **10**, reveal: a) that the Zr center is displaced slightly out of the [Me₂C(Cp)(Flu)]^{2−} ligand pocket in **10** as compared to **7**, and b) that the [Me₂C(Cp)(Flu)]^{2−} ligand is pried open by FAl(*o*-C₆F₅C₆F₄)₃[−]. The above observations indicate a stronger coordinative interaction with the bulkier but more

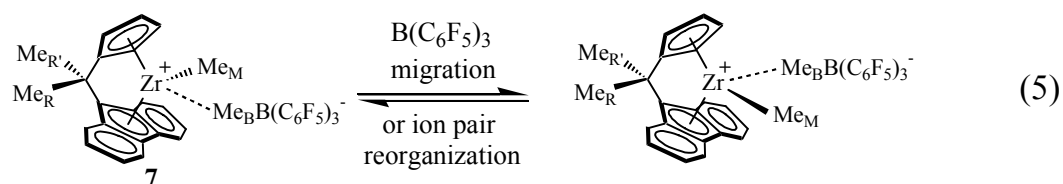
strongly donating $\text{FAl}(o\text{-C}_6\text{F}_5\text{C}_6\text{F}_4)_3^-$ anion (Table 5). Note that in **10**, π - π stacking is also observed among the C_{12}F_9 groups of the anion, where the C_6F_4 rings bound to the Al center engage in stacking with the end C_6F_5 rings on adjacent C_{12}F_9 groups. The sense of the corkscrew motif described by the C_{12}F_9 groups determines the stereochemical configuration at the Al center. In contrast, this π - π stacking interaction is conspicuously absent in the solid-state structure of trityl salt **6**. This, together with the observed interconversion of diastereomers of **10** in solution (*vide infra*), suggests a subtle reciprocation between ancillary ligand architecture and structural dynamics.^{8a}

C. Solution Dynamics of Ion Pair Reorganization/Symmetrization in $[\text{Me}_2\text{C}(\text{Cp})(\text{Flu})]\text{ZrMe}^+\text{MeB}(\text{C}_6\text{F}_5)_3^-$ (7**) and $[\text{Me}_2\text{C}(\text{Cp})(\text{Flu})]\text{ZrMe}^+\text{FAl}(o\text{-C}_6\text{F}_5\text{C}_6\text{F}_4)_3^-$ (**10**).**

Exchange processes available to ion pairs **7** and **10** in the absence of olefin can be correlated with polymerization behavior of these catalyst systems. The principal structural reorganization process of interest in each of these systems is migration of the anionic portion of the catalyst-cocatalyst system from one side of the zirconocenium-methyl metal center to the other (ion pair reorganization). This process mirrors the site epimerization of the zirconocenium-polymeryl-anion ensemble thought to occur during polymerization and to give rise to product *m* stereodeflects in the absence of synchronous propylene enchainment (Eq. 2; Scheme 1B). In the absence of olefin, both **7** and **10** undergo background exchange processes as well, and ion pair reorganization must be studied in the context of all extant reorganization processes.

The ^1H EXSY spectrum of ion pair **7** at 23°C shows NOE contact between protons Me_B and H_F (see atom labeling scheme **C** in Experimental Section), with sufficient intensity to indicate that the time-averaged solution structure of **7** is a dissymmetric contact ion pair, with a

preferred orientation of the anion with respect to the cation.²⁸ This spectrum reveals exchange between Me_B and Me_M signals (methyl-methide exchange), arising from borane migration (dissociation of $\text{B}(\text{C}_6\text{F}_5)_3$ from Me_B and subsequent transfer to Me_M) and also permutation of diastereotopic Me_R and $\text{Me}_{R'}$ resonances and exchange between corresponding fluorenyl and cyclopentadienyl ring proton pairs (ligand side-side exchange, arising from both borane migration and ion pair reorganization, Eq. 5). Relative rates of borane migration and ion pair reorganization are sensitively dependent on metal identity and ligand architecture, as shown in previous studies of archetypal Group 4 metallocene dimethyl precatalysts activated with $\text{B}(\text{C}_6\text{F}_5)_3$.^{4a,12,29}



1-D ^1H NMR spectral data collected for **7** over a 40° temperature range afford kinetic parameters for both of these processes. Broadening of the *i*-Pr methyl (Me_R and $\text{Me}_{R'}$) and methide resonances (Me_M) can be used to determine the rates of both processes using the standard modified Bloch two-site exchange line-broadening formalism, $k = \pi(\Delta W)$.^{21b} At a given temperature, the ion pair reorganization rate is taken as the difference between total side-side exchange rate, taken from broadening in the Me_R and $\text{Me}_{R'}$ resonances, and the rate of borane migration, determined from broadening of Me_M .³⁰ Kinetic results are summarized in Table 6.

28. Zuccaccia, C.; Stahl, N. G.; Macchioni, A.; Marks, T. J., manuscript in preparation.

29. Line broadening is found to be independent of concentration over an 8-fold range for **7**, arguing that an intramolecular exchange process is prevalent.

30. Temperature-dependent quadrupolar broadening of the Me_B resonance precludes measurement of exchange broadening on this signal, which is instead assumed to be equal to that of the Me_M resonance. The detection limit for

Confidence intervals for ΔH^\ddagger and ΔS^\ddagger are determined using standard error values from linear regression analysis on the data used to generate the Eyring plot.

Exchange-broadening observed in variable-temperature 1-D ^1H spectra of **10** arises from two discrete processes: ion pair reorganization, and interconversion between stereochemical configurations at the chiral Al center (anion racemization, see Scheme 2 for both processes). Both processes interconvert major and minor diastereomers, however ion pair reorganization does so with ligand side-side exchange, whereas anion racemization does not. Thus EXSY can be used to differentiate between them. EXSY spectra collected at 23°C, 87.5°C, and 117.5°C ($\tau_m = 1200\text{ms}$, 185ms, 40ms, respectively) exhibit cross-peaks corresponding to interconversion between diastereomers, but no cross-peak intensity indicative of ligand side exchange. This observation motivated EXSY data collection at 127.5°C ($\tau_m = 800\text{ms}$) specifically to examine the possibility of very slow ion pair reorganization. This spectrum also reveals no apparent side-side exchange cross-peak intensity (Figure 4), and is analyzed to establish a lower limit for the ion pair reorganization rate at this temperature. In Figure 4, Aa and aA, or collectively [Aa], refer to the pair of $\text{H}_A\text{-H}_a$ exchange peaks (see atom labeling scheme C in the Experimental Section), and $I_{Aa} = I_{aA}$ refers to the cross-peak intensity at these positions.³¹ Cross-peaks at [Aa], and at [A'a'] arise exclusively from anion racemization. Intensity at [Aa'], [A'a], [AA'], and [aa'] is expected from ion pair reorganization + rapid anion racemization, with only the former process permuting ligand sides. Any cross-peak intensity from ion pair reorganization is distributed over these eight locations by the background anion racemization (for which the

broadening is determined by the digital resolution (0.067 Hz, corresponding to $k = 0.21\text{ s}^{-1}$), thus the site exchange rate at 23°C ($k \sim 0.2\text{ s}^{-1}$) as determined from EXSY data demonstrates that 0°C is a suitable temperature to take as the zero-exchange limit for the purposes of lineshape analysis.

31. Signal overlap precludes use of other sets of signals for this determination.

present conditions represent the saturation regime, with $k = 28 \text{ s}^{-1}$ at 127.5°C from dynamic NMR).

For two-site exchange, a suitable model for the proposed ion pair reorganization under saturation conditions for anion racemization, rates is given by Eq. 6.¹⁹

$$k = \frac{1}{\tau_m} \ln\left(\frac{r+1}{r-1}\right) \text{ with } r = \frac{\sum I_{\text{diag}}}{\sum I_{\text{cross}}} \quad (6)$$

A lower limit for r , r_{ll} , can be established using extant diagonal peak intensities and a suitable higher limit for the corresponding cross-peak intensities I_{cross} . What follows is a general method for estimating r_{ll} for systems undergoing two-site exchange *without* distribution of cross-peak intensity by background, saturation-regime processes:

$$r > r_{ll} \approx \frac{\sum_i^q I_{d,i}}{qI_n} = \frac{\sum_i^q \phi_{d,i}n}{q\phi_n n} = \frac{\sum_i^q \phi_{d,i}}{q\phi_n} \quad (7)$$

for some q extant diagonal signals $S_{d,i}$ with intensities $I_{d,i}$ and cross-peak intensity limit I_n , where $\Phi_{d,i}$ is the measured signal-to-noise ratio of signal $S_{d,i}$ over the (noise) region where a corresponding cross-peak is sought, and Φ_n is the arbitrary signal-to-noise ratio limit below which real intensity might be mistaken for background noise. Not all observed diagonal peaks need be employed, but for each pair of cross-peaks sought, both corresponding diagonal peaks are measured, pairing each cross-peak region with a diagonal peak, as dictated by the F2 dimension direction, when the exchange interconverts species that are present in unequal concentrations. The above formulation effectively averages the noise intensity for the q regions measured and is valid inasmuch as the noise intensity is constant across the noise regions used to measure the $\Phi_{d,i}$'s.

In the present case, diagonal peaks A' and a give intensities $I_{A'}$ and I_a with respective signal-to-noise ratios $\Phi_{A'}$ (over region aA') and Φ_a (over A'a), respectively, and $q = 2$. We extend the above general formulation to the present system using a factor D representing distribution of cross-peak intensity due to background saturation-regime exchange. Anion racemization distributes expected total cross-peak intensity such that the summed intensity of the *interdiastereomer* cross-peaks is one half of the total expected cross-peak intensity arising from ion pair reorganization, thus $D = 1/2$. We set the arbitrary but reasonable criterion, that a cross-peak having intensity $I_{\text{cross}} < 2I_n$, may be extant but indistinguishable from background noise, thus setting $\Phi_n = 2$. Supposing such a peak exists, r_{ll} is then:

$$r > r_{ll} \approx D \frac{\sum_i^q \phi_{d,i}}{q\phi_n} = \frac{\phi_{A'} + \phi_a}{8} \quad (8)$$

The signal-to-noise ratios $\Phi_{A'}$ and Φ_a (33.4 and 64.4, respectively, see Figure 4) are determined from F_2 slices passing through the highest points in A' and a, setting $r > r_{ll} = 12.2$ and thereby giving a higher limit, $k < 0.25 \text{ s}^{-1}$ at 127.5°C for ion pair reorganization, including a correction for implicit NOE intensity.³²

Ion pair complexes formed by activation of metallocene precatalysts with $\text{Ph}_3\text{C}^+ \text{B}(\text{C}_6\text{F}_5)_4^-$ are found to be insoluble and very unstable, excepting $\text{Cp}_2^*\text{ThMe}^+ \text{B}(\text{C}_6\text{F}_5)_4^-$.^{7c} For complex **9**, determining the rate of a putative dynamic reorganization/symmetrization process

32. RMS signal-to-noise ratios for specific signals over specific noise regions are obtained from the VNMR command, `dsn`. Scant NOE intensity detected in the EXSY spectrum of **10** at 127.5°C at locations [A'B'], [a'b'], [A'b'], and [B'a'] (distributed by rapid anion racemization) is measured, and used together with the crystal data of **10** to estimate the expected NOE intensity at A'a and aA' (accompanied by intensities at [Aa'], [A'A], and [a'a]) and increases the higher limit for the ion pair reorganization rate constant by 0.05 s^{-1} , assuming total cancellation of NOE and exchange cross-peak intensity at these positions.

analogous to that observed with **7** was unsuccessful, with extensive decomposition occurring at much lower temperatures ($\sim 50^\circ\text{C}$) compared to complexes **7** and **10**. Similarly, decomposition of complex **8** is observed upon heating (above $\sim 80^\circ\text{C}$) and results in an insoluble, blue-purple product in toluene. It will be seen from evidence derived from polymerization results, that the site epimerization rate constant for **9** is $11.1(11) \text{ s}^{-1}$ at 60°C , the highest value for all systems studied, suggesting that the ion pairing interaction is weakest for $\text{B}(\text{C}_6\text{F}_5)_4^-$ as compared to the other systems (see discussion below). The structure of the active species corresponding to **8** during polymerization is unknown, however results discussed below allow an estimation of $k = 10.9(10) \text{ s}^{-1}$ at 60°C for a putative site epimerization in this species.

The assembled NMR-derived kinetic data (Table 6) indicate a fundamental and substantial difference in the lability of $\text{MeB}(\text{C}_6\text{F}_5)_3^-$ and $\text{FAl}(o\text{-C}_6\text{F}_5\text{C}_6\text{F}_4)_3^-$ as counteranions for the zirconocenium fragment.³³ Indeed, the lower limit derived for the barrier to ion pair reorganization in **10** is conservative, and considering that this interaction may be even stronger, it is remarkable that **10** produces polymer at all, inviting speculation on the pathway for monomer enchainment. Multiple pathways for insertion have been postulated in computational studies where the catalyst-cocatalyst interaction is included,²⁴ and the collection of systems presented here may serve to differentiate among these possibilities: specifically, an enchainment pathway with concerted anion displacement may be favored in the $\text{FAl}(o\text{-C}_6\text{F}_5\text{C}_6\text{F}_4)_3^-$ system, in contradistinction to the $\text{B}(\text{C}_6\text{F}_5)_4^-$ system, for example. Also, considering that monomer enchainment is in general impeded by stronger ion pairing/increasing counteranion coordinative tendencies,^{12c} and that in similar systems ion pairing strength has been shown to diminish with

33. Dynamic NMR experiments with **7** and **10** 1,2-dichlorobenzene-*d*₄ as solvent reveal that in this more polar medium, the barrier to ion pair reorganization in **7** is lowered, whereas with **10** such a process is still undetectable.

increasing zirconocenium alkyl steric bulk,^{12a} it is possible that this latter differential effect may diminish more rapidly with more strongly binding counteranions.

Independent of mechanistic considerations, differences in counteranion coordinative ability manifest themselves measurably in the rate constants for propylene insertion relative to those of competing processes believed to occur during polymerization. It is the goal of the following sections to examine these effects.

II. Catalytic Propylene Polymerization Mediated by Complexes 7–10.

It will be seen that substantial counteranion effects are evident in the polymerization characteristics and polypropylene microstructures obtained using the present catalyst systems. The following sections examine cocatalyst, temperature, monomer concentration, and solvent polarity effects on stereodeflect production, polymerization activity, termination/chain-transfer kinetics. These effects represent an interplay of structural, kinetic, and thermodynamic influences, among which the dominant factor is argued to be the lability of the catalyst cation-anion interaction.

A. Counteranion and Temperature Effects on Propylene Polymerization. Under rigorously anhydrous/anaerobic conditions, complex **1** was activated with MAO (**2**) or perfluoroaryl cocatalysts **3–6** to generate catalytically-active ion pairs *in situ*.³⁴ Polymerizations were carried out under 1.0 atm propylene pressure in toluene solution over the temperature range of -10° to 60°C using conditions minimizing mass transfer¹⁷ and exotherm effects (see

34. For experiments using MAO (**2**) as cocatalyst, an Al:Zr ratio of 60:1 is employed, to improve comparability with results collected using molecular cocatalysts. Control experiments in which the Al:Zr ratio is varied across a 30-fold range show no significant dependence of the pentad distribution on this ratio. These results are presented in Table 2 of the Supporting Information.

Experimental Section for details),^{2c,10} product isolation and characterization utilized standard techniques.¹¹ The results of these propylene polymerization experiments are summarized in Table 7. The data are analyzed with a view toward discerning cocatalyst-dependent effects on polymerization activity, molecular weight characteristics, and microstructure, and how these may reflect the coordinative component of anion interaction with the cationic metal center.^{7c} Several trends are immediately evident in the data. Product polydispersities are consistent with well-defined single-site processes and are rather temperature- and anion-insensitive. Polymer production rates, however, are highly anion-sensitive — the intrinsic steric and electronic characteristics of the anions appearing to have a major influence on monomer activation and enchainment. The most strongly (FAI(*o*-C₆F₅C₆F₄)₃⁻) and weakly (MeB(*o*-C₆F₅C₆F₄)₃⁻, B(C₆F₅)₄⁻) coordinating anions generally exhibit the lowest and highest polymerization rates, respectively (Table 7). Not surprisingly,^{1,11} product molecular weights fall with rising reaction temperature, in all cases (Figure 5). FAI(*o*-C₆F₅C₆F₄)₃⁻ affords the highest M_w product polymer at all temperatures (*vide infra* for pressure effects). Most interesting, however, is the striking pattern in polypropylene stereodeflect probabilities³⁵ (P_m, generally attributed to site epimerization,³⁶ Scheme 1B, and P_{mm}, from propylene enantiofacial misinsertion or chain epimerization, Schemes 1D, 1E, respectively) as a function of anion and temperature (Figure 6).

35. For **1**+MAO, syndiotacticity falls with increasing polymerization temperature, Ref. 11, while for C₁-symmetric catalysts, isotacticity sometimes increases with increasing polymerization temperature: (a) Kleinschmidt, R.; Reffke, M.; Fink, G. *Macromol. Rapid Commun.* **1999**, *20*, 284-288. (b) Grisi, F.; Longo, P.; Zambelli, A.; Ewen, J. A. *J. Mol. Catal. A: Chem.* **1999**, *140*, 225-233. (c) For example of a C₂-symmetric catalyst propylene polymerization temperature dependent study, see: Resconi, L.; Piemontesi, F.; Camurati, I.; Sudmeijer, O.; Nifant'ev, I. E.; Ivchenko, P. V.; Kuz'mina, G. K. *J. Am. Chem. Soc.* **1998**, *120*, 2308-2321.

36. See Ref. 11. Other proposed processes giving rise to *m* stereodeflects are discussed below. See Ref. 2c.

It can be seen that the $\text{FAl}(o\text{-C}_6\text{F}_5\text{C}_6\text{F}_4)_3^-$ -based catalyst exhibits far higher syndiospecificity, with far lower m and somewhat lower mm stereodeflect production. All systems exhibit a not unprecedented erosion in syndiospecificity with increasing temperature,¹¹ likely due to acceleration of m steric dyad production vs. enchainment, least prevalent in the $\text{FAl}(o\text{-C}_6\text{F}_5\text{C}_6\text{F}_4)_3^-$ -based catalyst. The NMR-derived ion pair reorganization/symmetrization kinetic results and the comparatively low polymerization activity temperature dependence for **10** argue that tighter ion pairing raises the activation energy for site epimerization. Interestingly, mm stereodeflects are far less temperature-sensitive for all catalysts, with the $\text{FAl}(o\text{-C}_6\text{F}_5\text{C}_6\text{F}_4)_3^-$ catalyst again slightly superior. In contrast, the $\text{MeB}(\text{C}_6\text{F}_5)_3^-$ catalyst exhibits the lowest syndiotacticity with greatest increase of m and mm stereodeflect production with rising polymerization temperature (*vide infra* for detailed explanation). In general, as the temperature is increased, polymerization activities increase, except near 60°C, where activities decrease for all ion pairs. Not only lower ion pair thermal stability, but also decreased propylene solubility at higher temperatures doubtless contributes to the lower activity observed in all systems at 60°C (in toluene, [propylene] = 0.36 M at 60°C vs. 0.83 M at 25°C, at 1.0 atm system pressure).³⁷ In addition, the $\text{B}(\text{C}_6\text{F}_5)_4^-$ -derived catalyst exhibits the most significant erosion in performance, likely reflecting the poor thermal stability of this complex as noted above. In comparison to the $\text{FAl}(o\text{-C}_6\text{F}_5\text{C}_6\text{F}_4)_3^-$ -based polymerization system, lower product syndiotacticities but higher polymerization activities are observed in the **1** + MAO system. In agreement with previous polymerization studies using $[\text{Me}_2\text{C}(\text{Cp})(\text{Flu})]\text{ZrCl}_2 + \text{MAO}$ (% *rrrr* = 93.1 at 10°C),^{35a}

37. An empirical model for calculation of solution-phase composition of propylene in toluene and isododecane under relevant conditions is presented in (a) Dariva, C.; Lovisi, H.; Santa Mariac, L. C.; Coutinho, F. M. B.; Oliveira, J. V.; Pinto, J. C. *Can. J. Chem. Eng.* **2003**, *81*, 147-152. (b) also see Ref. 17.

comparable *rrrr* pentad contents (93.6%, Table 7, entry 3) are obtained in the present work.

The temperature dependence of derived kinetic parameters will be addressed below.

B. Monomer Concentration Effects. Polymerization series in which [propylene] is systematically varied reveal anion dependences that are subtle compared to the anion sensitivity of the temperature effects described above. These experiments were carried out with $T = 60^{\circ}\text{C}$, to maximize signal-to-noise ratios for dilute pentad signals. The mechanistic consequences of increasing [propylene] can be ascribed to increased rates of bimolecular reactions such as insertion or enantiofacial misinsertion vs. those of competing unimolecular processes such as site epimerization and β -hydrogen elimination to Zr (resulting in either chain epimerization or termination and reasonably assumed to be zero-order in monomer). Generally, any observed [propylene] effect on a measurable polymer feature can be interpreted as arising from a combination of processes having proposed rate laws that differ in their [propylene] dependence.^{11,38} This approach is used for analyzing product molecular weight and the abundance of *m* and *mm* stereodeflects, always against the background of chain propagation,

38. (a) For C_3 -symmetric catalysts, lower propylene concentrations correlate with lower product molecular weights and tacticities (mostly *m* stereodeflects), Ref. 13c. (b) In contrast, declining isotacticity with increasing monomer concentration is observed in C_1 -symmetric catalysts: Kukral, J.; Lehmus, P.; Feifel, T.; Troll, C.; Rieger, B. *Organometallics* **2000**, *19*, 3767-3775. (c) For C_2 -symmetric catalyst propylene concentration studies, see Ref. 17, and also (d) Busico, V.; Cipullo, R.; Cuttillo, F.; Vacatello, M. *Macromolecules*, **2002**, *35*, 349-354, (e) Busico, V.; Brita, D.; Caporaso, L.; Cipullo, R.; Vacatello, M. *Macromolecules* **1997**, *30*, 3971-3977, and (f) Resconi, L.; Fait, A.; Piemontesi, F.; Colonesi, M. *Macromolecules* **1995**, *28*, 6667-6676.

reasonably assumed to be first-order in monomer.³⁹ The present work reveals that these effects are particularly sensitive to counteranion identity.

Limited, but anion-dependent increases in product molecular weights (Table 8) are observed with increasing monomer pressure, arguing that [monomer]-dependent termination processes are significant.^{11,38} The sensitivity of M_n to propylene pressure change is markedly higher in the $\text{MeB}(\text{C}_6\text{F}_5)_3^-$ polymerization system (7), suggesting that the ratio of rates for unimolecular termination (v_{t1}) vs. [monomer]-dependent termination ($v_{t2,\text{propylene}}$) is higher in this case.¹⁷ This is illustrated in Figure 7: assuming negligible chain transfer involving species other than propylene, the slope and intercept from a linear fit of $1/P_n$ vs. $1/[\text{propylene}]$ (P_n is the number-averaged degree of polymerization; see Eq. 9) are equal to k_{t1}/k_p , and $k_{t2,\text{propylene}}/k_p$,

$$\frac{1}{P_n} = \frac{v_{t2,\text{propylene}} + v_{t1}}{v_p} = \frac{k_{t2,\text{propylene}}}{k_p} + \frac{k_{t1}}{k_p} \left(\frac{1}{[\text{propylene}]} \right) \quad (9)$$

respectively (v_p being the rate of polymerization, assumed to be first order in [propylene]).¹⁷ The other catalyst-cocatalyst systems studied here, including MAO (2, for which chain transfer to aluminum alkyls cannot be ruled out), are indistinguishable in this respect, in particular exhibiting a general suppression of unimolecular termination (Figure 7). However, the variance in GPC-determined M_w values propagates to substantial uncertainties in the quantitation of k_{t1}/k_p ,

39. Examination of insertion rate vs. propylene concentration from Table 8 reveals an approximately linear correlation in several systems, thus insertion is assumed to be first-order in monomer in the present model. This was also observed for the polymerization of 1-hexene catalyzed by $[\text{rac}-(\text{C}_2\text{H}_4(1\text{-indenyl})_2)\text{ZrMe}] [\text{MeB}(\text{C}_6\text{F}_5)_3]$ over the temperature range of -10° to 50°C , see Ref. 40. However, for C_2 -symmetric catalyst propylene studies, there is debate in the literature as to the exact order of monomer in production of isotactic polypropylene. See Refs. 17, 38d-f. Ref. 38d contains a model reconciling observed apparent propagation [propylene] dependences using a rigorous model that holds propagation to be first order in monomer.

and $k_{t2,prp}/k_p$.^{11c} ¹H NMR end-group analysis of the product polymers reveals that in these systems, 2,1-misinsertion followed by β -hydrogen transfer to Zr is not significant (less than 10%),⁴⁰ also arguing that chain transfer to monomer is the preferred bimolecular termination route, in these systems.

Increased monomer concentrations are accompanied by increases in syndiotacticity in all systems studied (Figure 6). Statistical techniques for modeling polymer ¹³C NMR pentad distributions have been described for C_s -symmetric catalyst systems, in particular for simultaneous estimation of probabilities (relative to propagation) for events that produce m steric dyads and mm steric triads in the product polymer.¹³ These models have the advantage of accounting for steric pentads (or any n -ads) containing multiple stereodefects ('shared pentads' e.g. $mrmr$, or $mrmr$). We apply here a standard statistical model^{13c,d} to extract the probability P_{mm} of mm -generating processes and P_m of m -generating processes, that takes into account their contributions to shared pentad intensity. This model is based on the assumption of perfect enantiomorphic site control, as has been justified in several previous examples for this class of catalysts.¹³ Experimental and calculated pentad distributions for both pressure- and temperature-dependence polymerization series appear in the Supporting Information.

Catalyst site epimerization, having the proposed rate law, $v_{se} = k_{se}[\text{catalyst}]$, leads to the formation of m steric dyads as stereodefects in the product polymer when followed by "normal" chain-migratory insertion, but *is not necessarily* the most significant factor in degradation of syndiotacticity at the temperature maintained for this set of experiments (60°C). In another possible scenario, β -hydrogen transfer to the catalyst metal center is followed by *re-si* interconversion of the resulting π -macroolefin complex, and reinsertion (chain epimerization,

40. Liu, Z.; Somsook, E.; White, C. B.; Rosaaen, K. A.; Landis, C. R. *J. Am. Chem. Soc.* **2001**, *123*, 11193-11207.

Scheme 1E). Concomitant stereoinversion at the metal (ion-pair reorganization, Scheme 1E, pathway i) also generates an *m* stereodeflect. This process would then have the same stereosequence *and* rate law as site epimerization. It is possible that in certain systems, ion-pair reorganization of the π -macroolefin complex proceeds rapidly compared to the reinsertion step (the macroolefin being 1,1'-disubstituted). Chain epimerization without stereoinversion of the metal generates an *mm* stereodeflect (Scheme 1E, pathway ii).^{11a,41} As Busico *et al.* have recently observed,^{2a} *m* stereodeflects can in principle also arise from insertion without chain migration ("back-side attack," opposite the anion, rather than same-side attack). In fact, any 1,2-insertion in which no net stereochemical inversion of the catalyst occurs, if followed by a "normal" chain-migratory insertion, will give rise to an isolated *m* stereodeflect, either as an *mrr* or *rmr* tetrad, depending on the enantiofacial orientation of the back-side misinserted monomer (Scheme 1D). If we assume $v_{\text{bsa}} = k_{\text{bsa}}[\text{catalyst}][\text{propylene}]$ for such a process, then the *m* stereodeflect probability can be expressed as in Eq. 10:

$$P_m = \frac{v_{\text{bsa}} + v_{\text{se}}}{v_p} = \frac{k_{\text{bsa}}}{k_p} + \frac{k_{\text{se}}}{k_p} \left(\frac{1}{[\text{propylene}]} \right) \quad (10)$$

A linear fit of P_m vs $1/[\text{propylene}]$ then gives estimates for k_{bsa}/k_p and k_{se}/k_p (as intercept and slope, respectively, Eq. 10; see Figure 8, Table 9). In this and subsequent models, v_p , the rate of polymerization, represents the sum of rates for chain migratory insertion, misinsertion via back-side attack, and enantiofacial misinsertion, all assumed to be first order in [propylene]. The present results indicate that k_{bsa} is detectably nonzero at 60°C with $\text{MeB}(\text{C}_6\text{F}_5)_3^-$ as the anion (**7**, in agreement with Ref. 2a), and indeed for all activators treated in the present report. The observed anion ordering in k_{se}/k_p is $\text{FAI}(\text{o-C}_6\text{F}_5\text{C}_6\text{F}_4)_3^-$ (counteranion in **10**) < MeMAO^- (**2**) <

41. Sillars, D. R.; Landis, C. R. *J. Am. Chem. Soc.* **2003**, *125*, 9894-9895.

MeB(*o*-C₆F₅C₆F₄)₃⁻ (**8**) < B(C₆F₅)₄⁻ (**9**) < MeB(C₆F₅)₃⁻ (**7**). This ordering does not track ion pairing strength, but there is no reason to expect it should.^{2a,b} It is possible that ion pairing dynamics and counteranion structure/electronics influence the propagation and site epimerization processes to different degrees. The anion ordering in $k_{\text{bsa}} / k_{\text{p}}$, **10** ~ **2** < **9** ~ **8** < **7**, also fails to adhere to a specific trend.

This analysis employs the assumptions that back-side attack and site epimerization occur according to the above rate laws and are the *only* processes giving rise to *m* stereodeflects. Independent evidence supporting a back-side reaction pathway is desired. Also, structure/function relationships are meaningful only when determined for elementary processes; the product polymer features analyzed herein are each derivative phenomena. Estimates for k_{p} using available activity data are required to extract approximate values for k_{se} and k_{bsa} ; the results of this analysis, along with a discussion of its inherent limitations, are presented below. The decrease in *m* stereodeflect abundance with increasing monomer concentration is found here to be greater than that of the *mm* stereodeflect abundance, this latter decline being largest with MeB(C₆F₅)₃⁻ system but undetectable for the FAl(*o*-C₆F₅C₆F₄)₃⁻-derived catalyst **10**. Rate constants for chain epimerization ($v_{\text{ce}} = k_{\text{ce}}[\text{catalyst}]$) and enantiofacial misinsertion ($v_{\text{em}} = k_{\text{em}}[\text{catalyst}][\text{propylene}]$) vs. propagation can be calculated from P_{mm} for each catalyst (Eq. 11, with v_{p} as defined above), by analyzing the plots of P_{mm} vs. $1/[\text{propylene}]$ for each system

$$P_{\text{mm}} = \frac{v_{\text{em}} + v_{\text{ce}}}{v_{\text{p}}} = \frac{k_{\text{em}}}{k_{\text{p}}} + \frac{k_{\text{ce}}}{k_{\text{p}}} \left(\frac{1}{[\text{propylene}]} \right) \quad (11)$$

(Figure 9, Table 10). The present collected results suggest that enantiofacial misinsertion is the prevailing process for the generation of *mm* stereodeflects in all systems studied here. Similar evaluation of the data for (1,2-SiMe₂)₂{C₅H₂-4-R}{C₅H-3,5-(CHMe₂)₂}ZrCl₂ (R = H, CHMe₂, SiMe₃) activated by MAO at 24°C suggests that in this case,^{11c} the relative contribution of

enantiofacial misinsertion is small. This distinction is likely due to metallocene structural differences, and possibly also to differences in reaction temperature.

C. Anion Mobility during Propylene Polymerization Probed *In Situ* by Enchainment Syndioselection. Considering the large observed counteranion effects on M_w , m , and mm stereodefects, it is important to inquire into their origin;⁴² as indicated above, counteranion effects, or any effects, are best analyzed against the rates for individual processes. However, use of polymerization analytical yields for determination of k_p values, necessary for determination of k_{se} , k_{bsa} , k_{ce} , and k_{em} , can be relied on only in certain cases. Propagation rates are systematically underrepresented owing to reversible and irreversible catalyst deactivation and catalyst induction, each of which is likely both cocatalyst- and temperature-dependent.⁴³ Correcting for such effects would have the effect of inflating $k_{p,apparent}$, thus increasing the estimates for elementary rate constants k_{se} , k_{bsa} , k_{ce} , and k_{em} from the relative quantities derived using Eqs. 10 and 11. However, reaction of catalysts with adventitious stoichiometric poisons can be

42. For general kinetic models, see: (a) Nele, M.; Mohammed, M.; Xin, S.; Collins, S.; Dias, M. L.; Pinto, J. C. *Macromolecules* **2001**, *34*, 3830-3841. (b) Grisi, F.; Longo, P.; Zambelli, A.; Ewen, J. A. *J. Mol. Catal. A: Chem.* **1999**, *140*, 225. (c) Ewen, J. A. *J. Mol. Catal. A: Chem.* **1998**, *128*, 103

43. Whereas the thermal instability of group IV metallocenium salts of $B(C_6F_5)_4^-$ is well known (Refs. 1b,2,7c) previous work (Ref. 7c) indicates that $B(C_6F_5)_4^-$ -based systems are to some degree stabilized in the presence of olefin, and extant literature finds catalyst activity during polymerization to be more or less constant: (a) Wester, T. S.; Johnsen, H.; Kittilsen, P.; Rytter, E. *Makromol. Chem. Phys.* **1998**, *199*, 1989-2004. Negligible catalyst deactivation is observed in 1-hexene polymerizations using [*rac*- C_2H_4 (indenyl) $_2$ ZrMe][MeB(C₆F₅)₃], see: (b) Liu, Z.; Somsok, E.; Landis, C. R. *J. Am. Chem. Soc.* **2001**, *123*, 2915-2916. For relevant ethylene homopolymerization results using mononuclear and binuclear constrained geometry catalysts see: (c) Abramo, G. P.; Li, L.; Marks, T. J. *J. Am. Chem. Soc.* **2002**, *124*, 13966-13967, and also see Ref. 2c. (d) Landis, C. R.; Rosaaen, K. A.; Sillars, D. R.; *J. Am. Chem. Soc.* **2003**, *125*, 1710-1711.

reasonably assumed to proceed to completion in all cases. Thus the depression of $v_{p,\text{apparent}}$ due to unintentional contamination should be statistical and independent of catalyst and temperature, and can be safely ignored when comparing $k_{p,\text{apparent}}$ among the present catalyst systems, with the exception of **1 + 2**, wherein large quantities of excess alkylaluminoxanes introduce a further systematic uncertainty. Catalyst thermal decomposition is clearly both temperature- and catalyst-dependent (and possibly also [catalyst]-dependent), and will thus introduce systematic errors into estimates of the elementary rate constants k_{se} , k_{bsa} , k_{ce} , and k_{em} for each system. However, we observe that greater polymerization rates ($v_{p,\text{apparent}}$, see Table 7) are generally associated with greater thermal instability, thus suggesting a greater underrepresentation of these elementary rate constants with systems that are more active.⁴⁴ It has been observed by Landis *et al.* that the fraction of catalytically-active states in isospecific 1-hexene polymerizations is moderately higher with $\text{B}(\text{C}_6\text{F}_5)_3$ as activator than with $[\text{PhNH}(\text{Me}_2)]^+\text{B}(\text{C}_6\text{F}_5)_4^-$, suggesting that the actual propagation rate constant is indeed higher in the latter case. Thus, underrepresentation of rate constants k_{se} , k_{bsa} , k_{ce} , and k_{em} can reasonably be expected to be larger with $\text{B}(\text{C}_6\text{F}_5)_4^-$ than with $\text{MeB}(\text{C}_6\text{F}_5)_3^-$ in the present case. Also, in both cases, the fraction of active catalysts at any given time is approximately the same as the fraction of catalysts that were active at some time, suggesting that the formation of dormant states on the timescale of their experiments (0.01-1000 s) is not significant.^{43b} Subsequent direct NMR observation of catalyst polymeryl species has shown that accumulation of dormant states is insignificant.^{43d} Assuming this holds in the present systems, the above findings on active site count and activity provide the following condition for comparability: in comparing two catalysts of different activity, if the more active catalyst gives

the larger apparent value for some elementary rate constant, the *difference* in this value for the two catalysts is thus underrepresented, and the ordering is reliably given by the data. The ordering can be established, in any comparison for which this condition is satisfied. Estimates for k_p , k_{se} , k_{bsa} , k_{ce} , and k_{em} among the present series of catalysts are summarized in Table 11.⁴⁵ Values for k_p at 60°C were determined by extrapolation of activity Arrhenius plots established from the temperature-dependence data (Figure 10), excluding experiments in which k_p is obviously underrepresented by $k_{p,apparent}$ (see Table 7). Confidence intervals for these projected k_p values are given at the 90% confidence level, as determined from linear regression analysis of $\ln(k_{p,apparent})$ vs. $1/T$ for each system. Confidence intervals for k_{se}/k_p and k_{bsa}/k_p were determined from linear regression analysis of P_m vs. $1/[\text{propylene}]$, and for k_{ce}/k_p and k_{em}/k_p , from P_{mm} vs. $1/[\text{propylene}]$; these are also given at the 90% confidence level. Confidence intervals k_{se} , k_{bsa} , k_{ce} , and k_{em} are derived from those of the parent quantities. Due to the presence of large excesses of aluminoxanes in reactions using **2** as cocatalyst, and the large confidence interval associated with k_p for this system ($402(44) \text{ s}^{-1}$) these data are excluded from the present discussion. Also, lack of detailed information on the structure(s) of the catalyst system obtained using this cocatalyst impedes interpretation of rate data from a mechanistic standpoint; data for **2** are presented for consideration in Table 11.

The trends in propagation and site epimerization rates both track ion pairing strength. For k_p ($\text{L}\cdot\text{mol}^{-1}\cdot\text{s}^{-1}$), the observed anion ordering is as follows: $\text{FAl}(o\text{-C}_6\text{F}_5\text{C}_6\text{F}_4)_3^-$ (**10**, 33.7(16)) <

44. For example, in NMR study of the freshly generated ion pairs, we observe systems **8** and **9** to undergo rapid decomposition (with **9** faster than **8**), while **7** decomposes slowly and **10** exhibits comparatively high thermal stability.

45. See Table 1 in Supporting Information for additional polymerization results used together with those in Table 7 to generate rate constants k_p for Table 11.

MeB(C₆F₅)₃⁻ (**7**, 41.8(8)) << B(C₆F₅)₄⁻ (**9**, 297(4)) < MeB(*o*-C₆F₅C₆F₄)₃⁻ (**8**, 321(12)). For k_{se} (s⁻¹), the ordering is the same: **10** (0.474(47)) < **7** (1.85(26)) << **8** (10.9(10)) ~ **9** (11.1(11)).

These general trends are consistent with the anion coordinating metrics developed on the basis of dynamic NMR-derived ion pair reorganization barriers and anion displacement equilibria.^{1b,4a,7c,8a,12} Surprisingly, the observed trend in k_{bsa} (L·mol⁻¹·s⁻¹) also tracks ion pairing strength: FAl(*o*-C₆F₅C₆F₄)₃⁻ (**10**, 0.486(65)) < MeB(C₆F₅)₃⁻ (**7**, 3.61(38)) < B(C₆F₅)₄⁻ (**9**, 9.5(16)) ~ MeB(*o*-C₆F₅C₆F₄)₃⁻ (**8**, 10.9(14) s⁻¹). If this trend accurately reflects selectivity for same-side approach of the olefin with respect to the counteranion, it seems counterintuitive from the standpoint of steric factors: certainly a more intimately bound anion would be more likely to suppress same-side attack. However, it is possible that a strongly coordinating anion stabilizes the distribution of positive charge at the catalyst metal center such that same side attack (as with "normal" chain-migratory insertion) is favored.²⁸ Considering that anion stereochemical mobility, catalyst stability, and reactivity all seem to depend strongly on the coordinative contribution to the cation-anion interaction, it seems likely that charge distribution and stabilization of the cationic moiety is highly anion-dependent, and that the anion is intimately involved in the insertion reaction (and in competing processes). The formal charge of the cationic olefin π -adduct fragment (assuming one exists) is the same as the isolated catalyst, and it is likely that such species also persist as contact ion pairs in solution.²⁸ Interaction between the anion and a π -adduct may indeed *involve* the olefin (inasmuch as the anion's charge is itself localized), the anion possibly assisting in olefin activation.²⁴ This would explain the remarkable fact that the fluoroaluminate system yields polymer at all, given the remarkable kinetic inertness of the anion as a ligand in this system. Further evidence of ion pairing influences can be seen in the trend in enantiofacial misinsertion (k_{em} , L·mol⁻¹·s⁻¹), with **10** (0.807(74)) << **7** (1.09(11)) < **9**

(7.75(62)) < **8** (9.36(65)). This trend in particular suggests a complex dependence on both electronic and steric factors.

Chain epimerization is observable in all systems with the notable exception of catalyst system **10** ($k_{ce} = 0.03(44)$, indistinguishable from zero, as with **8**, having $k_{ce} = 0.29(37)$, a rather large confidence interval; see Table 11) and is also suppressed, but to a lesser extent, with **7** ($k_{ce} = 0.239(75)$).⁴⁶ Conversely, the weakly coordinating $B(C_6F_5)_4^-$ exhibits a chain epimerization rate constant of 0.69(42), $\sim 20 \times$ greater than that of the $FAI(o-C_6F_5C_6F_4)_3^-$ anion (although indistinguishable from **10** at the 90% confidence level). The diminished chain epimerization channel observed with **10**, if well-represented by the present data, is possibly due to suppression of β -hydrogen transfer to Zr (Scheme 1E). A tightly bound counteranion would *a priori* be expected to destabilize the 4-center transition state generally considered necessary for β -hydrogen transfer (termination via β -hydrogen transfer is undetectable with **10**, but also with **8** and **9**).^{11a,41} This possibility is not inconsistent with (but by no means conclusively demonstrates) the ideas of i) intimate involvement of the counteranion in polymerization events, and ii) multiple available, counteranion-differentiated pathways for monomer activation and enchainment.

The above observed trends mirror ion pairing strength quite well, and since these orderings arise from estimates of k_p , which we also observe to track ion pairing strength, it is worthwhile to entertain the possibility that errors in the k_p estimates, rather than systematic chemical structure/function relationships, dominate the analysis. The present findings, if valid,

46. Absolute rates for chain epimerization and enantiofacial misinsertion for each catalyst at each pressure can be roughly gauged using Eq. 11 (P_{mm}) and insertion rates. The chain epimerization rates follow the ordering: **3** > **5** > **2** > **4** > **6**. It is likely in any event that the various steps involved in chain epimerization are subject to anion-dependent steric and electronic influences in a complex manner.

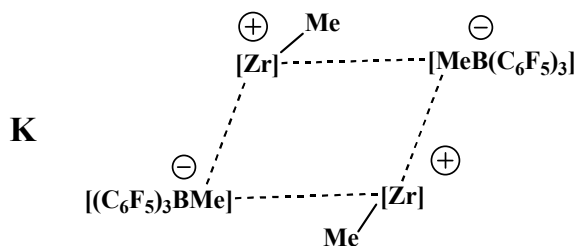
do shed light on some interesting observations¹⁰ that have also received attention in recent literature:^{2a,b} for example, $\text{B}(\text{C}_6\text{F}_5)_4^-$ (**9**) is found to produce a higher-syndiotacticity polymer than $\text{MeB}(\text{C}_6\text{F}_5)_3^-$ (**7**) at all temperatures, even though it is thought to be more weakly bound to the cation. At $[\text{propylene}] = 0.36 \text{ M}$ (1 atm. system pressure, $T = 60^\circ\text{C}$), the present results give $P_{m,7}/P_{m,9}$ ranging from 1.5 to 2.8, as determined directly from NMR analysis of the product polymers from these two catalysts. The aforementioned observations are consistent with a scenario in which $P_{m,7}/P_{m,9} < v_{p,9}/v_{p,7}$ (see Eq. 10 above). Thus at 25°C , for example, relative insertion rates $v_{p,9}/v_{p,7} > 2.8$ would give $v_{m,9} > v_{m,7}$, as expected ($P_m \times v_p = v_m = v_{\text{bsa}} + v_{\text{se}}$). In such a scenario, m stereodeflect generation proceeds more rapidly in **9** than **7**, but by a smaller margin than propagation. In fact, activity measurements give an estimated $v_{p,9}/v_{p,7} = 25.9(79)$, at 25°C , suggesting that this is indeed the case. A similar argument explains comparative polymer M_w values: whereas attenuated β -hydrogen elimination with $\text{MeB}(\text{C}_6\text{F}_5)_3^-$ and $\text{FAl}(o\text{-C}_6\text{F}_5\text{C}_6\text{F}_4)_3^-$ does contribute to increased polymer M_w values, $\text{B}(\text{C}_6\text{F}_5)_4^-$ produces a higher M_w product due to its much greater propagation rate.

D. Solvent Effects on Polymerization Stereocontrol. In non-polar hydrocarbon solvents such as toluene ($\epsilon = 2.15$), which are commonly used for olefin polymerization, strong cation-anion interactions¹² are doubtless an important modulator of reactivity in the present class of catalysts.²

To probe the effects of polar solvation-induced ion pair weakening on enchainment stereochemistry, polymerizations were also carried out in more polar 1,3-dichlorobenzene ($\epsilon = 5.04$; Table 12). The net result is dramatic compression in the dispersion of polymerization rates and collapse of $rrrr$, m , and mm stereosequence percentages to the experimentally indistinguishable values of 50, 17.5, and 4%, respectively, for all cocatalysts studied, indicating

that polar solvents significantly weaken ion pairing effects on stereocontrol in this system (Figure 11).⁴⁷ In contrast, polymerizations in less polar octane ($\epsilon = 2.08$; Table 12) evidence trends similar to those in toluene, but with more dramatic decreases in polymerization activity and slightly lower to negligible changes in product syndiotacticities. Although stronger ion pairing effects in octane vs. toluene can be used to explain the observed decrease in activity in **9** and **10** (95% and 25% respectively), the lower solubility of these ion pair complexes in octane is a tenable explanation for the reduced productivity.^{43a}

E. Catalyst Concentration and Added $\text{Li}^+ \text{MeB}(\text{C}_6\text{F}_5)_3^-$ Effects on Syndiospecific Polymerizations Mediated by **7.** Increased zirconocenium ion pair concentrations and the addition of $\text{Li}^+ \text{MeB}(\text{C}_6\text{F}_5)_3^-$ (**11**) have recently been reported to accelerate anion exchange/catalyst symmetrization processes (c.f., Eq. 2).¹⁴ An ion quadruple (**K**) or higher aggregate was proposed to be the key intermediate in such acceleration. To test the possible



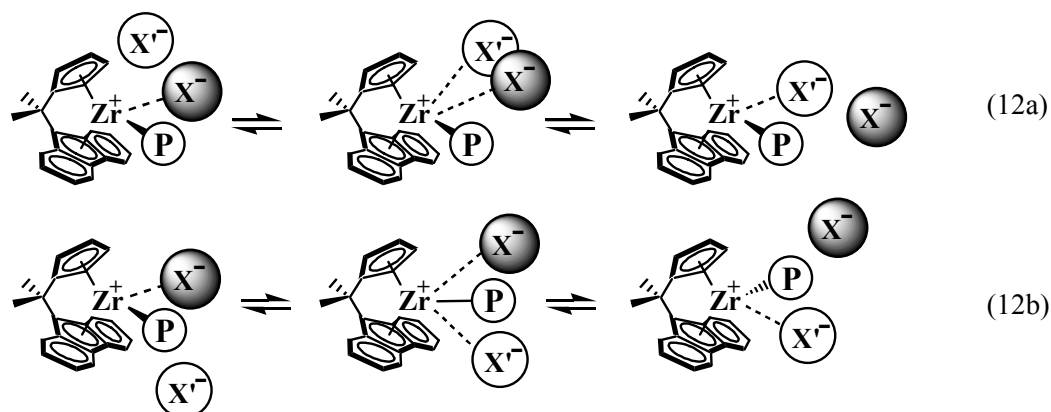
effects of putative ion pair aggregation and the introduction of lithium counteranion salts on the

47. (a) Propylene solubilities at 1 atm can be expected to vary somewhat with solvent. However, with 1,3-dichlorobenzene as solvent we observe that whereas activity (hence insertion rate) increases, so also does the rate of *xmrx* steric pentad formation, *relative to insertion*. Based on what we have demonstrated here from the propylene concentration study, we would expect the opposite, were the effect exclusively a concentration effect. (b) Herfert, N.; Fink, G. *Makromol. Chem.* **1992**, *193*, 773-778. (c) Coevoet, D.; Cramail, H.; Deffieux, A. *Makromol. Chem. Phys.* **1999**, *200*, 1208-1214. (d) For solvent effects in C_2 -symmetric catalyst system, Forlini, F.; Tritto, I.; Locatelli, P.; Sacchi, M. C.; Piemontesi, F. *Makromol. Chem. Phys.* **2000**, *201*, 401-408. (d) For CGC catalyst systems, see: Kleinschmidt, R.; Griebenow, Y.; Fink, G. *J. Mol. Catal. A-Chem.* **2000**, *157*, 83-90.

present polymerization system, experiments in which the concentration of **7** was varied, and experiments examining the effect of added $\text{Li}^+ \text{MeB}(\text{C}_6\text{F}_5)_3^-$ on propylene polymerizations catalyzed by **1** + **3**, were carried out. *A priori*, structures such as **K** might be expected to exhibit enhanced degrees of stereochemical mobility, which would consequently erode product syndiotacticity. Indeed, evidence for¹⁴ and against^{12,14} increased catalyst site epimerization rates (Eq. 2) with increasing catalyst concentration in the absence of olefin has been presented in the literature. However, in the present experiments with **7**, catalyst activity and product syndiotacticity were found to be essentially concentration-invariant over a 32-fold catalyst concentration range, while product M_w data decline only modestly at the highest concentrations (Table 13). These results argue that under typical polymerization conditions, where $[\text{catalyst}] = 25\text{--}800 \mu\text{M}$ (in contrast with the aggregation experiments, in which $[\text{catalyst}] = 2\text{--}20 \text{mM}$),¹⁴ inter-ion pair exchange via aggregation is not an important factor influencing activity or enchainment stereochemistry. In work presented elsewhere,⁴⁸ ion pair aggregation is shown by cryoscopy and pulsed field gradient spin-echo NMR spectroscopy to be insignificant in benzene or toluene solutions for a broad range of single-site metallocenium $\text{MeB}(\text{C}_6\text{F}_5)_3^-$ or $\text{B}(\text{C}_6\text{F}_5)_4^-$ ion pairs, even at concentrations substantially higher than employed here. Taken together, these findings argue that formation of ion quadruples (**K**) or higher-order aggregates is unlikely to be of importance in the present zirconocene-based catalyst systems for single-site α -olefin polymerization.

48. (a) Stahl, N. G.; Zuccaccia, C.; Jensen, T. R.; Marks, T. J. *J. Am. Chem. Soc.* **2003**, *125*, 5256-5257. (b) Stahl, N. G.; Marks, T. J.; Macchioni, A.; Zuccaccia, C. Presented in part at the 222nd ACS National Meeting, Chicago, IL, August 2001, Abstract INORG 407. (c) Zuccaccia, C.; Stahl, N. G.; Roberts, J. A. S.; Marks, T. J. *J. Am. Chem. Soc.*, in press.

Experiments examining the effects of added $\text{Li}^+ \text{MeB}(\text{C}_6\text{F}_5)_3^-$ (**11**) on propylene polymerizations catalyzed by **1+3** reveal at most a minor increase in product M_w , syndiotacticity, or melting point with increased **11** concentrations over a broad range (Table 14). This observation suggests that under the present conditions, either the ion exchange rate (if exchange occurs at all) is dictated by a slow dissociative step, and is thus invariant with $[\text{Li}^+ \text{MeB}(\text{C}_6\text{F}_5)_3^-]$, or that exchange occurs associatively but without stereoinversion, i.e. through same-side attack (compare Eqs. 12a and 12b), as proposed by Brintzinger *et al.*⁴⁹ As in the concentration-



dependence studies of **7**, catalyst activity and product syndiotacticity are modestly to negligibly invariant to added $\text{Li}^+ \text{MeB}(\text{C}_6\text{F}_5)_3^-$ while product M_w may be more sensitive.

CONCLUSIONS

A series of stable, structurally well-characterized, highly reactive C_s -symmetric zirconocenium ion pair propylene polymerization catalysts has been studied with regard to the molecular and ion pair structure and structural dynamics, both in the solid state and in solution. Ion pairing differences are evaluated on the basis of detailed spectroscopic/crystallographic characterization and ion pair reorganization/symmetrization kinetics, and reveal strongly anion-

49. $\text{Li}^+ \text{MeB}(\text{C}_6\text{F}_5)_3^-$ is not assumed to be a solvent-separated or dissociated ion pair.

dependent correlations with product polypropylene molecular weight and microstructural features. A distinctive signature of the catalyst-cocatalyst interaction emerges: polymerization activity, polymer microstructure, and molecular weight, in particular the relative rates of termination pathways and stereodeflect-generating side reactions relative to syndiospecific propylene enchainment, are all highly sensitive to the sterics and energetics of cocatalyst binding.

Comparison of solid-state structures demonstrates that the tightly bound $\text{FAl}(o\text{-C}_6\text{F}_5\text{C}_6\text{F}_4)_3^-$ counteranion actually draws the $[\text{Me}_2\text{C}(\text{Cp})(\text{Flu})]\text{ZrMe}^+$ Zr center slightly further out of the ligand pocket than does $\text{MeB}(\text{C}_6\text{F}_5)_3^-$. Reciprocal effects on anion structure are larger: differences in flattening of the Group 13 atom geometry and lengthening of this atom's bond to the bridging moiety with coordination of the anion, demonstrate strong differences in the cation-anion interaction in **7** and **10**. These counteranion differences are further manifested in the rate constants of dynamic unimolecular reorganization processes in isolated $[\text{Me}_2\text{C}(\text{Cp})(\text{fluorenyl})]\text{ZrMe}^+\text{X}^-$ ion pairs; from NMR kinetic analysis, we find that the fluoroaluminate ion pair has a far higher barrier to reorganization: $\Delta G^\ddagger > 24.8$ kcal/mol vs. 21.3(36) kcal/mol for $\text{MeB}(\text{C}_6\text{F}_5)_3^-$ at 127.5°C. Ion pair reorganization is herein assumed to be kinetically accessible to the metallocene Group 4 olefin polymerization catalysts as a class, but possibly requires the presence of olefin in the fluoroaluminate system (**10**). This is consistent with the commonly accepted chain-swinging model developed in conjunction with metallocene polymerization catalysts for stereoregular propylene polymerization.^{11,50}

50. (a) Cossee, P. *Tetrahedron Lett.* **1960**, 17, 12. (b) Cossee, P. *Tetrahedron Lett.* **1960**, 17, 17. (c) Arlman, E. J.; Cossee, P. *J. Catal.* **1964**, 3, 99. Cossee, P. *J. Catal.* **1964**, 3, 80. Cossee, P.

The above observations and conclusions help to reconcile the present accumulated evidence for appreciable counteranion/cocatalyst influences on product polymer features with the complex manifold of processes proposed to be kinetically accessible during polymerization. Stereodeflect frequencies and molecular weights examined as a function of polymerization temperature and monomer concentration across the entire cocatalyst series allow quantitation of anion effects on a collection of processes, and by extension, comparison of $\text{FAl}(o\text{-C}_6\text{F}_5\text{C}_6\text{F}_4)_3^-$, $\text{MeB}(\text{C}_6\text{F}_5)_3^-$, $\text{B}(\text{C}_6\text{F}_5)_4^-$, $\text{MeB}(o\text{-C}_6\text{F}_5\text{C}_6\text{F}_4)_3^-$, and MAO. Comparing $\text{FAl}(o\text{-C}_6\text{F}_5\text{C}_6\text{F}_4)_3^-$ and $\text{MeB}(\text{C}_6\text{F}_5)_3^-$, we find that the latter exhibits a greater proclivity toward unimolecular reorganization/symmetrization and termination processes than does the former, suggesting not only that the difference in ion pairing strength persists during polymerization, but that the fluoroaluminate anion suppresses β -hydrogen transfer to Zr more strongly than the methylborate. The catalytic activities and polymer syndiotacticities exhibited by $\text{MeB}(o\text{-C}_6\text{F}_5\text{C}_6\text{F}_4)_3^-$ lie between those of $\text{MeB}(\text{C}_6\text{F}_5)_3^-$ and $\text{B}(\text{C}_6\text{F}_5)_4^-$, in accord with previous evidence suggesting that, as compared with the former, the bulkier ancillary structure of $\text{MeB}(o\text{-C}_6\text{F}_5\text{C}_6\text{F}_4)_3^-$ reduces the ion pairing interactions, all else being equal. However, due to its tendency to form $[\text{Zr}-(\mu\text{-Me})\text{-Zr}]^+$ structures, the latter system is more complex. It is evident, however, that the $\text{B}(\text{C}_6\text{F}_5)_4^-$ counteranion is the most weakly bound, exhibiting the most rapid production of *m* and *mm* stereodeflects, and by a greater margin, the most rapid chain propagation. Consistently across the present series, polymerization activity decreases and the rate of catalyst site epimerization decreases, as the ion pairing strength is increased. Estimation of absolute rates for propagation, site epimerization, back-side misinsertion, enantiofacial misinsertion, and chain epimerization for each of these cation-anion systems provides a complete and self-consistent explanation for the relative syndiotacticities of product polymers from each system. Spectroscopic,

theoretical,^{24,51} and polymerization studies argue that polar solvents significantly weaken ion pairing, and in accord with a picture in which ion pairing modulates syndiospecific enchainment, we find here that differential anion effects on propagation rates diminish and those on stereodefects *completely vanish* in a more polar solvent. While the present results serve to elucidate the importance of catalyst-cocatalyst interactions in the production of syndiotactic polypropylene, they also reveal a unique new feature of the $\text{FAl}(o\text{-C}_6\text{F}_5\text{C}_6\text{F}_4)_3^-$ counteranion. This remarkable species, showing the greatest affinity for the cationic zirconocenium fragment, exhibits the highest, least temperature-dependent syndioselectivity. This unprecedented, cocatalyst-derived stabilization suggests completely new strategies for selectivity enhancement in single-site polymerization processes.

Acknowledgements. Financial support by DOE (DE-FG02-86ER1351) is gratefully acknowledged. M.-C. C. thanks Dow Chemical for a postdoctoral fellowship and Dr. P. Nickias of Dow for GPC measurements. We also thank Dr. L. Li, Dr. H. Ahn, Dr. C. Zuccaccia, Dr. T. R. Jensen, and Mr. N. G. Stahl for helpful discussions.

Supporting Information. Additional polymerization results as an extension to results in Table 11 above, and a full-page, low peak-threshold EXSY spectrum for **10** at 127.5°C, $\tau_m = 800\text{ms}$ are presented in Appendix I. Complete X-ray experimental details and tables of bond lengths,

51. (a) Beswick, C. L.; Marks, T. J. *Organometallics* **1999**, *18*, 2410-2412. (b) Deck, P. A.; Beswick, C. L.; Marks, T. J. *J. Am. Chem. Soc.* **1998**, *120*, 12167-12167. (c) and also see ref. 12.

angles, and positional parameters for the crystal structures of **7** and **10** are available via the ACS website, <http://pubs.acs.org>, document number ja036288k.

Figure 1. High-pressure polymerization reaction system.

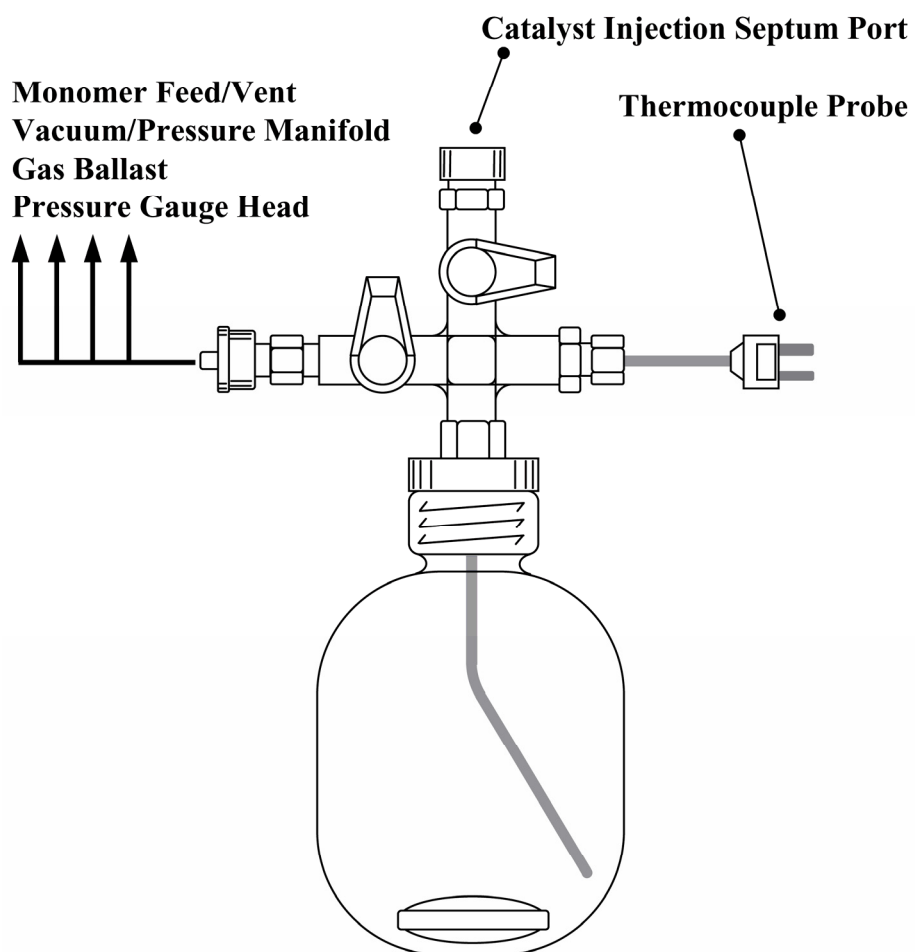


Figure 2. Perspective ORTEP drawing of the molecular structure of the complex $[\text{Me}_2\text{C}(\text{Cp})(\text{Flu})]\text{ZrMe}^+ \text{MeB}(\text{C}_6\text{F}_5)_3^-$ (**7**). Thermal ellipsoids are drawn at the 30% probability level.

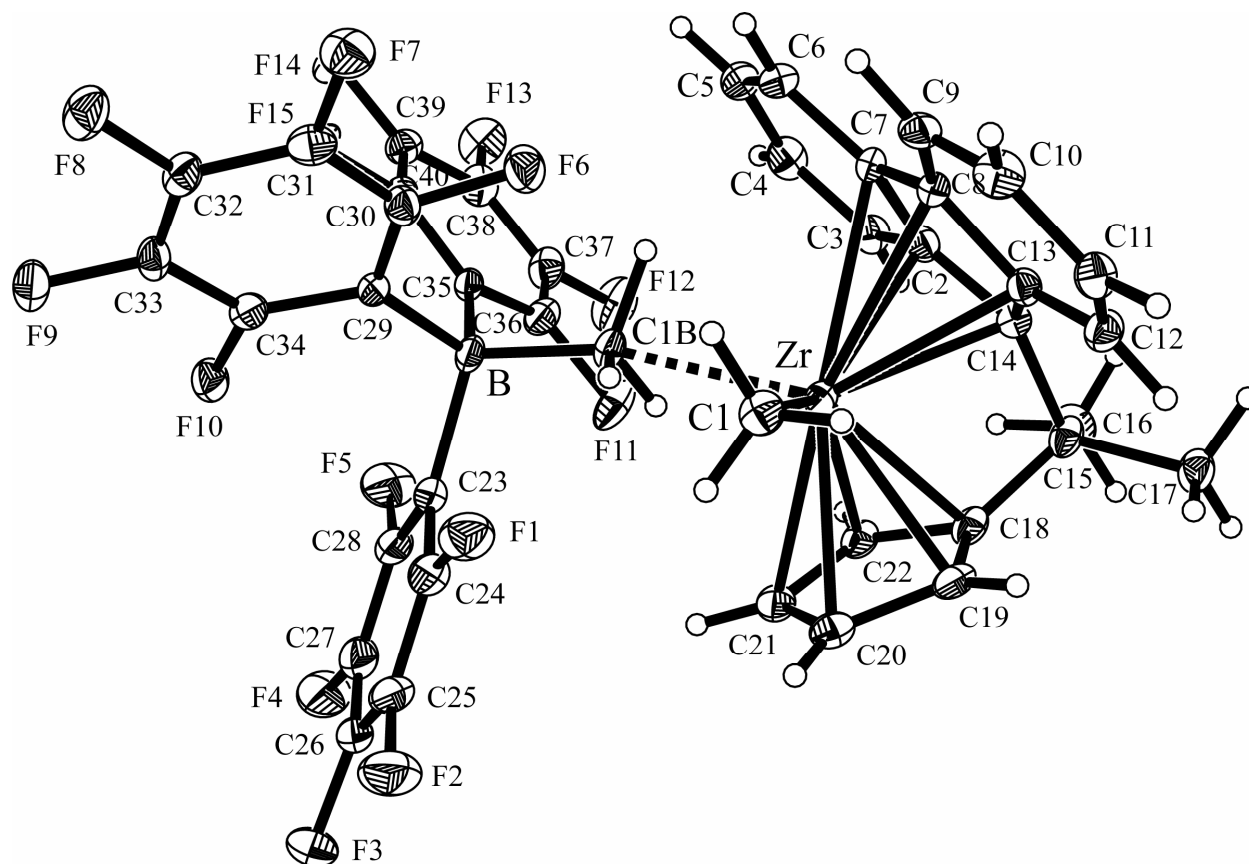


Figure 3. Perspective ORTEP drawing of the molecular structure of the complex $[\text{Me}_2\text{C}(\text{Cp})(\text{Flu})]\text{ZrMe}^+ \text{FAl}(\text{C}_6\text{F}_5\text{C}_6\text{F}_4)_3^-$ (**10**). Thermal ellipsoids are drawn at the 30% probability level. The terminal C_6F_5 groups not only twist out of coplanarity with connected C_6F_4 fragments but also exhibit π - π interactions with the C_6F_4 groups on adjacent C_{12}F_9 ligands.

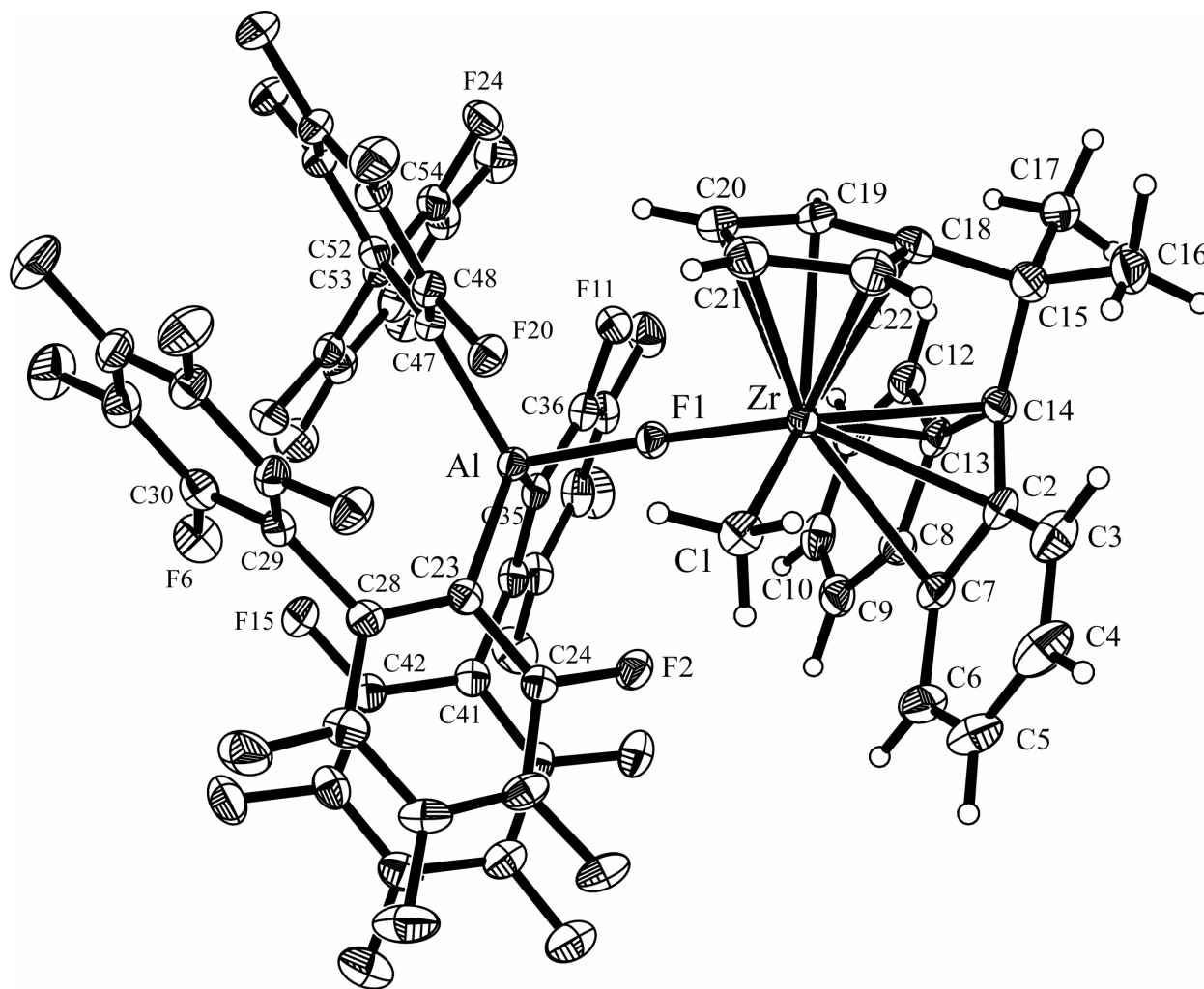


Figure 4. EXSY spectrum (in toluene- d_8) of complex 10, 127.5°C, $\tau_m = 800$ ms. Diagonal peaks, lower-left to upper-right, correspond to resonances $H_{A'}$, H_A , $H_{a'}$, and H_a , respectively. Spectra *a.* and *b.* are F2 slices passing through the points of greatest intensity in resonances H_a and $H_{A'}$, respectively.

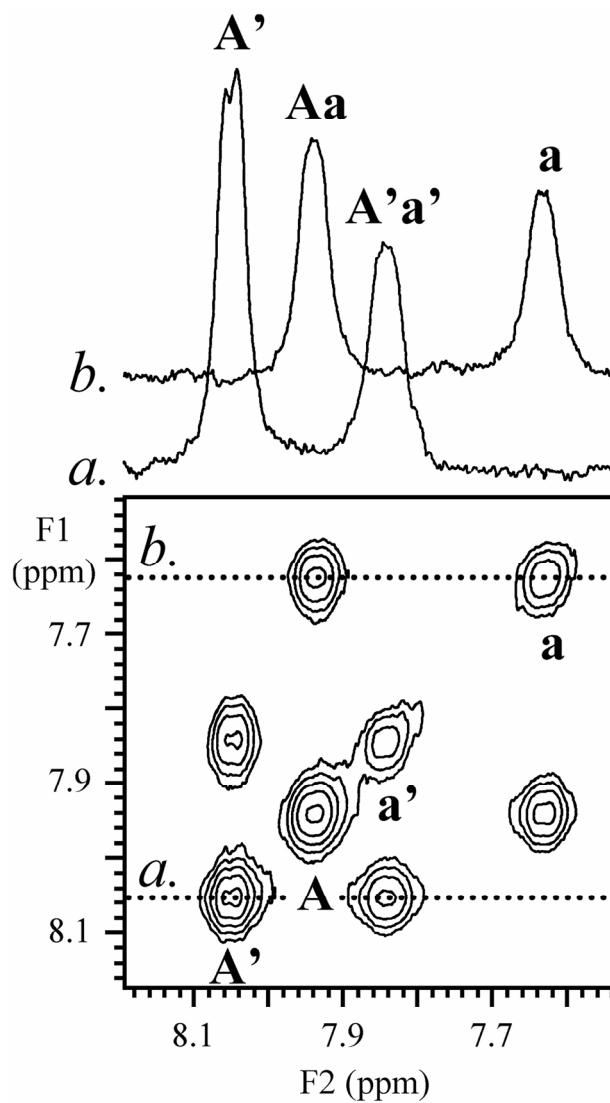


Figure 5. Product molecular weight (M_w) data for polypropylenes produced by **1** + the indicated cocatalysts over the temperature range of -10° – $+60^\circ\text{C}$ under 1.0 atm of propylene.

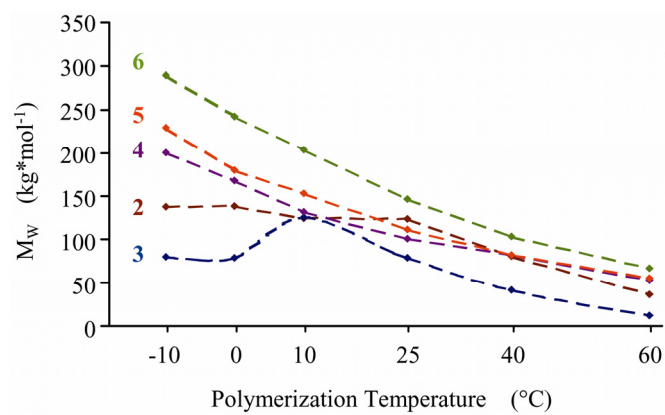


Figure 6. Syndiotacticity (%*rrrr*) data and calculated *m* and *mm* stereodeflect production probabilities (relative to insertion, P_m and P_{mm} respectively, discussed below) for polypropylenes produced by **1** + indicated cocatalysts under 1.0 atm of propylene over the temperature range of -10° – +60°C (A) and using propylene concentrations varying over the range 0.36M – 2.05M at 60°C (B).

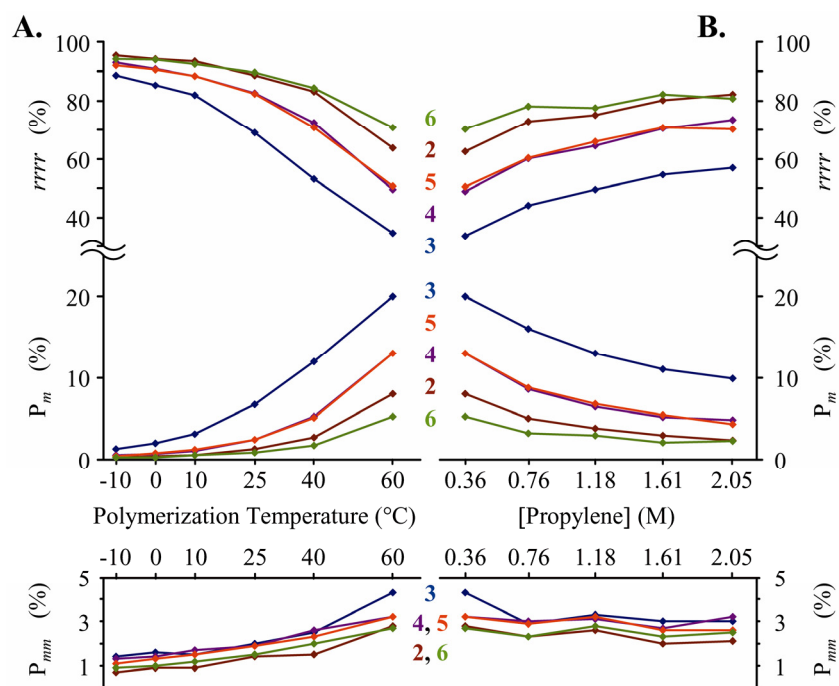


Figure 7. Product $1/P_n$ at 60°C plotted vs. $1/[\text{propylene}]$ for **1** + indicated cocatalysts (Table 8).

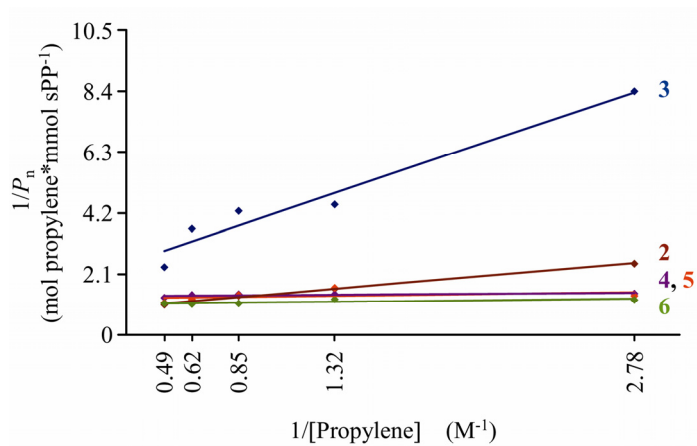


Figure 8. Product P_m at 60°C plotted vs. $1/[\text{propylene}]$ for **1** + indicated cocatalysts (Table 8).

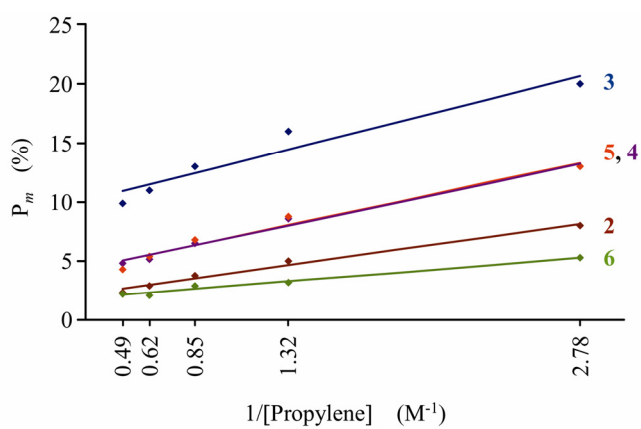


Figure 9. Product P_{mm} at 60°C plotted vs. $1/[\text{propylene}]$ for **1** + indicated cocatalysts (Table 8).

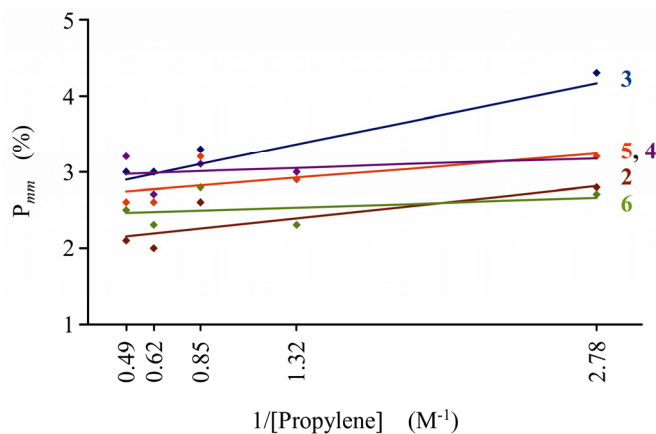


Figure 10. Plots of $-\ln(k_p)$ vs. $1/(\text{polymerization temperature})$ for **1** + indicated cocatalysts under 1.0 atm propylene over the temperature range of $-10^\circ - +60^\circ\text{C}$ in toluene (Table 7; k_p values corrected for $[\text{propylene}]$ temperature dependence).

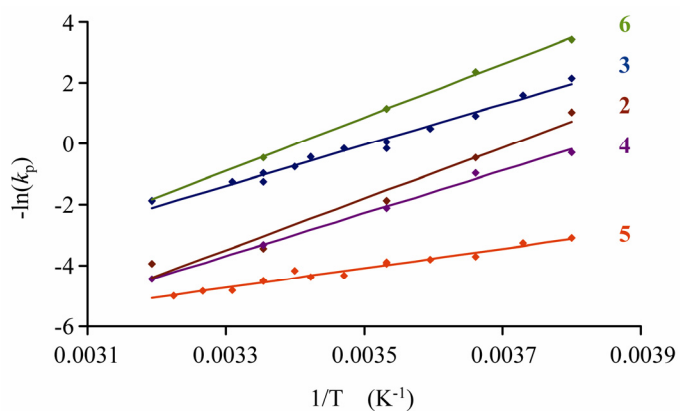


Figure 11. **A.** $\log(\text{polymerization activity})$, **B.** Polypropylene M_w , **C.** *rrrr* pentad intensity (%), and **D.** *xmrx* pentad intensity (%) data for polypropylenes produced by 1 + indicated cocatalysts under 1.0 atm of propylene at 25°C in octane, toluene, and 1,3-dichlorobenzene solutions.

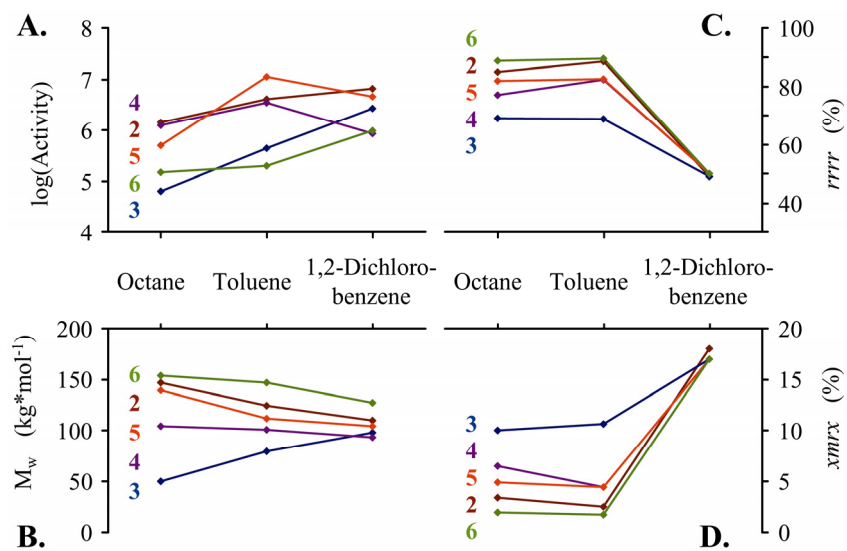


Table 1. Summary of the Crystal Structure Data for Complexes [Me₂C(Cp)(Flu)]ZrMe⁺ MeB(C₆F₅)₃⁻ (**7**) and [Me₂C(Cp)(Flu)]ZrMe⁺ FAl(2-C₆F₅C₆F₄)₃⁻ (**10**).

complex	7	10
formula	C ₄₈ H ₃₂ BF ₁₅ Zr	C ₅₈ H ₂₁ AlF ₂₈ Zr
formula weight	995.77	1367.95
crystal color, habit	red, plate	red, block
crystal dimensions (mm)	0.284 x 0.178 x 0.044	0.194 x 0.174 x 0.166
crystal system	Monoclinic	Monoclinic
space group	<i>P</i> 2 ₁ / <i>c</i>	<i>P</i> 2 ₁ / <i>c</i>
<i>a</i> , Å	13.5302 (18)	16.4939 (10)
<i>b</i> , Å	26.815 (4)	19.6187 (12)
<i>c</i> , Å	12.4684 (16)	16.9722 (10)
β, deg	116.673 (2)	112.4710 (10)
<i>V</i> , Å ³	4042.3 (9)	5075.0 (5)
<i>Z</i>	4	4
<i>d</i> (calc), g/cm ³	1.636	1.790
μ, mm ⁻¹	0.378	0.380
T _{min} -T _{max}	0.91577-0.98342	0.92539-0.95286
Measured reflections	35835	46570
Independent reflections	9692	12346
Reflections > 2σ(<i>I</i>)	4357	8033
R _{int}	0.1409	0.0705
R[<i>F</i> ² > 2σ(<i>F</i> ²)]	0.0548	0.0503
wR(<i>F</i> ²)	0.1344	0.1374
<i>S</i>	0.880	0.981
no. of parameters	601	796

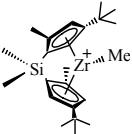
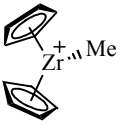
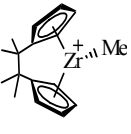
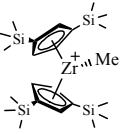

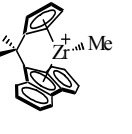
^a CCD area detector diffractometer; phi and omega scans; temperature for data collection, 153 (2) K; Mo Kα radiation; λ = 0.71073 Å.

Table 2. Selected Bond Distances (Å) and Angles (deg) for Complex $[\text{Me}_2\text{C}(\text{Cp})(\text{Flu})]\text{ZrMe}^+ \text{MeB}(\text{C}_6\text{F}_5)_3^-$ (7).

Bond Distances (Å)							
B-C1B	1.652(7)	Zr-C1B	2.521(4)	C1-Zr	2.248(4)	C2-Zr	2.480(4)
C7-Zr	2.615(4)	C8-Zr	2.652(4)	C13-Zr	2.524(4)	C14-Zr	2.414(4)
C18-Zr	2.429(4)	C19-Zr	2.446(4)	C20-Zr	2.521(4)	C21-Zr	2.515(4)
C22-Zr	2.433(4)	C14-C15	1.553(6)	C15-C18	1.512(6)	B-C35	1.650(7)
B-C29	1.651(7)	B-C23	1.669(7)	C24-F2	1.366(6)		

Bond Angles (deg)					
B-C1B-Zr	165.5(3)	C1-Zr-C1B	94.15(17)	C1B-B-C23	108.2(4)
C1B-B-C35	107.7(4)	C1B-B-C29	110.1(4)	C29-B-C23	107.1(4)
C35-B-C23	112.8(4)	C35-B-C29	111.0(3)	C14-C15-C18	99.5(3)
C16-C15-C17	106.2(4)	C14-Zr-C18	57.76(15)		

Table 3. Comparison of Selected Bond Distances (Å) and Angles (deg) in Complex [Me₂C(Cp)(Flu)]ZrMe⁺ MeB(C₆F₅)₃⁻ (**7**) to those of Analogous Zirconocenium-MeB(C₆F₅)₃⁻ Ion Pairs.²⁶

Complex	F ^{26a}	G ^{26b}	H ^{26c}	I ^{26d}	J ^{26e}	Average ^a	7	
Cation Structure								
Zr–Me _M	2.294(8)	2.251(3)	2.258(9)	2.260(4)	2.252(4)	2.263(20)	2.248(4)	
Zr–Me _B	2.550(8)	2.556(2)	2.516(8)	2.667(5)	2.549(3)	2.568(60)	2.521(4)	
B–Me _B	1.688(13)	1.667(3)	1.678(12)	1.684(7)	1.663(5)	1.676(10)	1.652(7)	
B–(C ₆ F ₅) ₃ ^b	1.657(12)	1.656(8)	1.648(11)	1.704(14)	1.652(11)	1.664(23)	1.657(11)	
Zr–Me _B –B	162.7(6)	169.1(2)	171.5(5)	170.5(3)	161.8(2)	167.1(45)	165.5(3)	
Me _M –Zr–Me _B	92.4(3)	87.7(9)	91.8(3)	97.1(1)	92.0(1)	92.2(33)	94.2(2)	
Me _B –B–(C ₆ F ₅) ₃ ^c	109.0(49)	108.8(44)	107.8(44)	109.0(27)	108.0(50)	108.5(6)	110.3(29)	
Cp–Zr–Cp ^d	127.0	131.1	125.1	132.4	131.3	129.4	118.6	

^a Average of structures **F** - **J**. ^b Mean B–C(C₆F₅) distance. ^c Mean Me_M–B–C(C₆F₅) angle. ^d Bite angle.

Table 4. Selected Bond Distances (Å) and Angles (deg) for Complex [Me₂C(Cp)(Flu)]ZrMe⁺ FAl(2-C₆F₅C₆F₄)₃⁻ (**10**).

Bond Distances (Å)							
Al-F1	1.7858(17)	F1-Zr	2.1165(15)	C1-Zr	2.245(3)	C2-Zr	2.531(3)
C7-Zr	2.621(3)	C8-Zr	2.594(3)	C13-Zr	2.498(3)	C14-Zr	2.419(3)
C18-Zr	2.444(3)	C19-Zr	2.451(3)	C20-Zr	2.530(3)	C21-Zr	2.538(3)
C22-Zr	2.460(3)	C14-C15	1.554(4)	C15-C18	1.530(5)	Al-C23	2.014(3)
Al-C35	2.012(3)	Al-C47	2.025(3)	C28-C29	1.497(4)	C24-F2	1.369(3)
Bond Angles (deg)							
Al-F1-Zr	162.21(10)	F1-Zr-C1	92.65(10)	F1-Al-C23	103.52(10)		
F1-Al-C35	100.14(10)	F1-Al-C47	105.32(10)	C35-Al-C23	116.00(12)		
C35-Al-C47	115.34(12)	C23-Al-C47	113.98(12)	C18-C15-C14	99.5(2)		
C16-C15-C17	106.5(3)	C14-Zr-C18	57.89(10)	C23-C28-C29	123.2(3)		

Table 5. Comparative Bond Distances (Å) and Angles (deg) for Complexes [Me₂C(Cp)(Flu)]ZrMe⁺ MeB(C₆F₅)₃⁻ (**7**), and [Me₂C(Cp)(Flu)]ZrMe⁺ FAI(2-C₆F₅C₆F₄)₃⁻ (**10**).

	Zr-C _{Flu} ^a	Zr-C _{Cp} ^b	Zr-C ₁₅	C _{Cp} -Zr-C _{Flu}	C ₁₅ -C ₁₄	C ₁₅ -C ₁₈	C ₁₄ -C ₁₅ -C ₁₈
7	2.221(4)	2.157(4)	3.109(4)	118.6(2)	1.553(4)	1.512(6)	99.5(3)
10	2.221(3)	2.176(3)	3.124(3)	119.0(1)	1.554(4)	1.530(5)	99.5(2)

^a Centroid of C₁₃H₈ ligand. ^b Centroid of C₅H₄ ligand.

Table 6. NMR-Derived Rate Constants and Free Energies of Activation for Solution Dynamic Processes of Complexes $[\text{Me}_2\text{C}(\text{Cp})(\text{Flu})]\text{ZrMe}^+ \text{MeB}(\text{C}_6\text{F}_5)_3^-$ (**7**). and $[\text{Me}_2\text{C}(\text{Cp})(\text{Flu})]\text{ZrMe}^+ \text{FAI}(\text{2-C}_6\text{F}_5\text{C}_6\text{F}_4)_3^-$ (**10**) in toluene- d_8 . Confidence Intervals Presented at the 90% Confidence Level.

Cocat. (Cat.)	Temp. (°C)	$k_{\text{total}}^{\text{a}}$ (s^{-1})	k_1 (s^{-1})	$\Delta\text{G}_1^{\ddagger}$ (kcal/mol)	$k_{\text{reorg}}^{\text{d}}$ (s^{-1})	$\Delta\text{G}_{\text{reorg}}^{\ddagger}$ (kcal/mol)
3(7) ^e	77.5	6.0	5.2 ^b	19.6(10)	0.8(4)	20.6(36)
3(7) ^e	92.5	18.6	16.4 ^b	19.4(10)	2.2(4)	20.8(36)
6(10) ^e	87.5	1.1	1.1 ^c	21.2(6)	~ 0 ^g	n.d.
6(10) ^f	87.5	2.8	2.8 ^c	20.5	~ 0 ^g	n.d.
6(10) ^h	117.5	8.4	8.4 ^c	21.4(6)	~ 0 ^g	n.d.
6(10) ^f	117.5	18.3	18.3 ^c	20.8	~ 0 ^g	n.d.
6(10) ^e	127.5	15.0	15.0 ^c	21.5(6)	~ 0 ^g	n.d.
6(10) ^f	127.5	n.d. ⁱ	n.d. ⁱ	n.d. ⁱ	< 0.25	> 24.8

^a $k_{\text{total}} = k_1 + k_{\text{reorg}}$ ^b For **7**, k_1 = rate constant for $\text{B}(\text{C}_6\text{F}_5)_3$ migration. ^c For **10**, k_1 = rate constant for anion racemization. ^d k_{reorg} = rate constant of ion pair reorganization. ^e Taken from line-broadening analysis. ^f From 2D-EXSY NMR. ^g Assumed based on EXSY results at 127.5°C. ^h Projected values from line-broadening analysis. ⁱ Anion racemization saturation regime, see discussion.

Table 7. Propylene Polymerization Results for the Reactions Mediated by [Me₂C(Cp)(Flu)]ZrMe₂ (**1**) + Indicated Cocatalysts under 1.0 atm of Propylene over the Temperature Range of -10° – +60°C.^a

Cocat. (Cat.)	Exp. No.	T _p (°C)	Cat. (μmol)	[C ₃ H ₆] ^b (M)	Time (s)	Yield ^c (g)	v _{p,apparent} ^d (M*s ⁻¹)	k _p ^e (M ⁻¹ *s ⁻¹)	T _m (°C)	M _w ^f (kg*mol ⁻¹)	P.D.I. ^f	P _m ^g (%)	P _{mm} ^g (%)	r ^h (%)	rrrr ⁱ (%)
2	1	-10	10	2.83	1,800	0.77	0.188	0.36	156.0	138	1.88	0.3	0.7	98.2	95.3
	2	0	5.0	1.87	1,200	0.75	0.278	1.6	151.0	139	1.85	0.4	0.9	97.8	94.1
	3	10	3.3	1.31	600	0.73	0.535	6.6	148.9	125	1.83	0.5	0.9	97.6	93.6
	4	25	3.3	0.83	600	2.20	1.61	32	141.5	124	1.88	1.3	1.4	96.1	88.7
	5	40	2.5	0.56	600	1.80	1.32	51	129.5	80.8	1.87	2.7	1.5	94.3	83.1
	6	60	2.5	0.36	1,200	1.24	0.459	27 ^j	N.O. ^k	36.7	2.16	8.0	2.8	87.6	63.8
3(7)^l	7	-10	20	2.83	1,800	0.50	0.122	0.12	147.0	79.8	1.75	1.3	1.4	95.8	88.6
	8	0	20	1.87	1,800	1.14	0.279	0.40	140.4	78.8	1.56	2.0	1.6	94.7	85.2
	9	10	20	1.31	3,600	4.68	0.572	1.2	127.3	126	1.87	3.1	1.5	93.9	81.8
	10	25	20	0.83	1,800	4.40	1.08	3.5	101.4	79.0	1.81	6.7	2.0	89.7	69.0
	11	40	10	0.56	600	0.94	0.689	6.6	69.0	41.6	1.92	12	2.5	83.9	53.1
	12	60	20	0.36	1,800	2.48	0.606	4.5 ^j	N.O. ^k	11.9	2.38	20	4.3	74.7	34.6
4(8)	13	-10	7.6	2.83	720	0.88	0.538	1.4	150.9	201	1.83	0.5	1.3	97.3	92.9
	14	0	5.0	1.87	600	0.62	0.455	2.6	147.4	168	1.83	0.7	1.4	96.6	90.8
	15	10	5.0	1.31	300	0.69	1.01	8.4	143.2	132	1.92	1.0	1.7	95.8	88.5
	16	25	10	0.83	300	2.92	4.28	28	130.3	101	1.85	2.4	1.9	94.1	82.7
	17	40	6.2	0.56	300	3.71	5.44	84	108.2	82.8	1.78	5.3	2.6	90.6	72.4
	18	60	10	0.36	600	1.74	1.28	19 ^j	N.O. ^k	53.1	1.82	13	3.2	82.0	49.5
5(9)^l	19	-10	1.5	2.83	300	1.18	1.73	22	151.5	229	1.95	0.4	1.1	97.0	92.1
	20	0	1.3	1.87	180	0.74	1.81	40	147.6	180	1.93	0.8	1.3	96.5	90.7
	21	10	1.3	1.31	120	0.42	1.54	49	143.5	153	1.98	1.2	1.5	95.6	88.3
	22	25	1.3	0.83	180	0.73	1.78	90	130.7	112	1.95	2.4	1.9	93.8	82.4
	23	40	2.6	0.56	75	0.77	4.52	167	110.3	82.6	1.96	5.1	2.3	89.9	70.8
	24	60	10	0.36	600	1.27	0.932	14 ^j	N.O. ^k	55.8	1.82	13	3.2	82.4	50.8
6(10)	25	-10	20	2.83	10,800	0.85	0.035	0.030	156.5	290	1.86	0.3	0.9	97.8	94.3
	26	0	20	1.87	3,600	0.54	0.066	0.10	154.5	242	2.04	0.3	1.0	97.6	93.9
	27	10	20	1.31	4,500	1.58	0.155	0.32	151.2	204	1.96	0.5	1.2	97.1	92.6
	28	25	20	0.83	4,500	5.00	0.489	1.6	145.7	147	1.85	0.9	1.5	96.1	89.5
	29	40	20	0.56	3,600	0.51	0.062	0.30 ^j	136.0	104	2.09	1.7	2.0	94.1	84.2
	30	60	20	0.36	1,800	0.25	0.061	0.45 ^j	N.O. ^k	66.5	1.95	5.3	2.7	89.8	70.8

^a In 54 mL of toluene. ^b See Ref. 37a. ^c After workup (see Experimental). ^d As calculated from polymerization yield. ^e As calculated from v_{p,apparent}. ^f Determined from GPC analysis relative to polystyrene standards; polydispersity index = M_w / M_n. ^g Determined from polymer ¹³C NMR pentad analysis. ^h fractional dyad content, $r = (\sum_{x,y} xmr_y + \sum_{x,y} xrm_y + 2\sum_{x,y} xrry) / 2$, with x, y ∈ {r, m}. ⁱ Calculated rrrr signal integral; see Supporting Information for experimental and calculated pentad distributions. ^j Not used for estimating k_p at 60°C ^k Not observed. ^l This data supplemented with additional results for estimation of k_p at 60°C (see Supporting Information).

Table 8. Propylene Polymerization Results for the Reactions Mediated by [Me₂C(Cp)(Flu)]ZrMe₂ (**1**) + Indicated Cocatalysts at 60°C over the Pressure Range of 1 – 5 atm of Propylene.^a

Cocat. (Cat.)	Exp. No.	P (atm)	Cat. (μmol)	[C ₃ H ₆] ^b (M)	Time (s)	Yield ^c (g)	$v_{p,apparent}$ ^d (M*s ⁻¹)	k_p ^e (M ⁻¹ *s ⁻¹)	T _m (°C)	M _w ^f (kg*mol ⁻¹)	P.D.I. ^f	P _m ^g (%)	P _{mm} ^g (%)	r ^h (%)	rrrr ⁱ (%)
2	1	1.0	2.5	0.36	1,200	1.24	0.454	27	N.O. ^j	36.7	2.16	8.0	2.8	87.0	62.7
	2	2.0	1.5	0.76	240	0.92	1.69	80	113.8	48.8	1.87	5.0	2.3	90.8	72.9
	3	3.0	1.5	1.18	120	1.03	3.79	116	122.2	56.7	1.84	3.8	2.6	91.1	75.2
	4	4.0	1.5	1.61	180	1.88	4.60	103	125.4	63.2	1.81	2.9	2.0	93.2	80.2
	5	5.0	1.5	2.05	120	2.19	8.03	141	131.6	71.2	1.80	2.3	2.1	93.6	82.2
3(7)	6	1.0	20	0.36	1,800	2.48	0.606	4.5	N.O. ^j	11.9	2.38	20	4.3	74.6	33.6
	7	2.0	6.6	0.76	1,200	1.18	0.433	4.6	N.O. ^j	19.0	2.03	16	2.9	79.8	43.9
	8	3.0	5.9	1.18	1,200	2.41	0.884	6.9	N.O. ^j	25.0	2.55	13	3.3	81.7	49.5
	9	4.0	5.9	1.61	1,200	2.82	1.03	5.9	N.O. ^j	29.5	2.57	11	3.0	83.9	54.5
	10	5.0	5.1	2.05	1,200	1.52	0.560	2.9	N.O. ^j	33.9	1.89	9.9	3.0	84.9	57.1
4(8)	11	1.0	10	0.36	600	1.74	1.28	19	N.O. ^j	53.1	1.82	13	3.2	81.7	48.9
	12	2.0	2.9	0.76	1,200	1.31	0.480	12	N.O. ^j	53.5	1.80	8.6	3.0	86.2	60.2
	13	3.0	2.5	1.18	1,200	1.88	0.689	13	99.0	55.8	1.89	6.5	3.1	87.5	64.6
	14	4.0	2.9	1.61	600	1.19	0.873	10	106.0	56.6	1.86	5.2	2.7	89.9	70.5
	15	5.0	2.5	2.05	1,200	1.25	0.458	4.8	109.6	58.6	1.81	4.8	3.2	90.7	73.5
5(9)	16	1.0	10	0.36	600	1.27	0.932	14	N.O. ^j	55.8	1.82	13	3.2	82.4	50.5
	17	2.0	5.1	0.76	1,200	1.21	0.444	6.2	N.O. ^j	57.1	2.23	8.8	2.9	86.1	60.3
	18	3.0	2.6	1.18	1,200	1.01	0.370	6.5	105.8	59.3	1.97	6.8	3.2	87.9	65.9
	19	4.0	2.6	1.61	1,200	1.62	0.594	7.7	106.4	61.2	1.82	5.4	2.6	90.0	70.8
	20	5.0	2.6	2.05	1,200	1.56	0.572	5.8	109.7	63.2	1.68	4.3	2.6	89.2	70.2
6(10)	21	1.0	20	0.36	1,800	0.25	0.061	0.45	N.O. ^j	66.5	1.95	5.3	2.7	89.6	70.4
	22	2.0	40	0.76	1,800	2.09	0.511	0.91	119.4	68.6	2.04	3.2	2.3	92.4	78.1
	23	3.0	60	1.18	1,200	3.54	1.30	0.99	124.5	71.2	1.88	2.9	2.8	91.6	77.5
	24	4.0	60	1.61	1,800	6	1.47	0.82	130.0	73.3	1.87	2.1	2.3	93.6	82.1
	25	5.0	20	2.05	1,800	2.92	0.714	0.94	127.2	70.8	1.86	2.2	2.5	93.0	80.8

^a In 54 mL of toluene. ^b See Ref. 37a. ^c After workup (see Experimental). ^d As calculated from polymerization yield. ^e As calculated from $v_{p,apparent}$. ^f Determined from GPC analysis relative to polystyrene standards; polydispersity index = M_w / M_n . ^g Determined from polymer ¹³C NMR pentad analysis. ^h fractional dyad content, $r = (\sum_{x,y} xmry + \sum_{x,y} xmy + 2\sum_{x,y} xrry) / 2$, with $x, y \in \{r, m\}$. ⁱ Calculated rrrr signal integral; see Supporting Information for experimental and calculated pentad distributions. ^j Not observed.

Table 9. Slopes, Intercepts, and Rate Ratios (%) of *m* Stereodefects Originating from Site Epimerization vs. "Back-Side" Misinsertion Obtained from P_m vs. $1/[\text{Propylene}]$ Plots for Polymerizations Mediated by $[\text{Me}_2\text{C}(\text{Cp})(\text{Flu})]\text{ZrMe}_2$ (**1**) + Indicated Cocatalysts under 1.0 – 5.0 atm Propylene at 60°C. Confidence Intervals Presented at the 90% Confidence Level.

Cocat. (Cat)	$k_{\text{se}}/k_{\text{p}}^{\text{a}}$ (slope)	$k_{\text{bsa}}/k_{\text{p}}^{\text{a}}$ (intercept)	$v_{\text{se}}/v_{\text{p}}^{\text{b}}$	$\frac{v_{\text{se}}}{v_{\text{se}} + v_{\text{bsa}}}$ ^b
2	0.0243(19)	0.0146(28)	0.067	0.82
3(7)	0.0442(62)	0.0863(90)	0.12	0.58
4(8)	0.034(29)	0.034(43)	0.1	0.76
5(9)	0.0374(37)	0.0319(55)	0.093	0.73
6(10)	0.0141(12)	0.0144(18)	0.039	0.73

^a k_{p} , k_{se} , and k_{bsa} are as defined in Eq. 10. ^b At 60°C, 1.0 atm, $[\text{propylene}] = 0.364 \text{ M}$, see Ref. 37a for conversion. $v_{\text{se}} / v_{\text{p}} = (k_{\text{se}} / k_{\text{p}}) * (1 / [\text{propylene}])$; $v_{\text{se}} / (v_{\text{se}} + v_{\text{bsa}})$ represents the fraction of *m* stereodefects attributable to site epimerization at 60°C, 1.0 atm.

Table 10. Slopes, Intercepts, and Rate Ratios (%) of *mm* Stereodefects Originating from Chain Epimerization vs. Enantiofacial Misinsertion Obtained from P_{mm} vs. $1/[\text{Propylene}]$ Plots for Polymerizations Mediated by $[\text{Me}_2\text{C}(\text{Cp})(\text{Flu})]\text{ZrMe}_2$ (**1**) + Indicated Cocatalysts under 1.0 – 5.0 atm Propylene at 60°C. Confidence Intervals Presented at the 90% Confidence Level.

Cocat. (Cat)	k_{ce}/k_p^a (slope)	k_{em}/k_p^a (intercept)	v_{ce}/v_p^b	$\frac{v_{ce}}{v_{ce} + v_{em}}^b$
2	0.0026(13)	0.0204(20)	0.0071	0.26
3(7)	0.0057(18)	0.026(26)	0.016	0.38
4(8)	0.0009(11)	0.0291(17)	0.0063	0.19
5(9)	0.0023(14)	0.0261(20)	0.0025	0.078
6(10)	0.0009(13)	0.0239(19)	0.0025	0.094

^a k_p , k_{ce} , and k_{em} are as defined in Eq. 11. ^b At 60°C, 1.0 atm, $[\text{propylene}] = 0.364 \text{ M}$, see Ref. 37a for conversion. $v_{ce}/v_p = (k_{ce}/k_p) * (1/[\text{propylene}])$; $v_{ce}/(v_{ce} + v_{em})$ represents the fraction of *mm* stereodefects attributable to site epimerization at 60°C, 1.0 atm.

Table 11. Estimated Absolute Rate Constants For Propagation, Site Epimerization, "Back-Side" Misinsertion, Chain Epimerization, and Enantiofacial Misinsertion Obtained from Activities, P_m vs. $1/[\text{Propylene}]$ Plots, and P_{mm} vs. $1/[\text{Propylene}]$ Plots for Polymerizations Mediated by $[\text{Me}_2\text{C}(\text{Cp})(\text{Flu})]\text{ZrMe}_2$ (**1**) + Indicated Cocatalysts under 1.0 – 5.0 atm Propylene at 60°C. Confidence Intervals Presented at the 90% Confidence Level; k_p , k_{se} , k_{bsa} , k_{ce} , and k_{em} as Defined in Eqs. 10 and 11

Cocat. (Cat)	k_p^a ($\text{M}^{-1}\cdot\text{s}^{-1}$)	k_{se}^b (s^{-1})	k_{bsa}^b ($\text{M}^{-1}\cdot\text{s}^{-1}$)	k_{ce}^c (s^{-1})	k_{em}^c ($\text{M}^{-1}\cdot\text{s}^{-1}$)
2	402(44)	9.8(13)	5.9(13)	1.04(55)	8.2(12)
3(7)	41.8(8)	1.85(26)	3.61(38)	0.239(75)	1.09(11)
4(8)	321(12)	10.9(10)	10.9(14)	0.29(37)	9.36(65)
5(9)	297(4)	11.1(11)	9.5(16)	0.69(42)	7.75(62)
6(10)	33.7(16)	0.474(47)	0.486(65)	0.03(44)	0.807(74)

^a k_p values are extrapolated from plots of $\ln(k_{p,\text{apparent}})$ vs. $1/T$ (see text). ^b From plots using Eq. 10.
^c From plots using Eq. 11.

Table 12. Propylene Polymerization Results for the Reactions Mediated by $[\text{Me}_2\text{C}(\text{Cp})(\text{Flu})]\text{ZrMe}_2$ (**1**) + Indicated Cocatalysts in 1,3-dichlorobenzene^a or Octane^a under 1.0 atm of Propylene at 25°C

Solvent ^a	Exp. No.	Cocat. (Cat.)	Cat. (μmol)	Time (s)	Yield ^b (g)	Act-ivity ^c ($\times 10^6$)	T _m (°C)	M _w ^d (kg/mol)	P.D.I. ^d	<i>mmmr</i> ^e (%)	<i>mmrr</i> ^e (%)	<i>rrmr</i> ^e (%)	<i>rrrr</i> ^e (%)
1,3-Dichloro-benzene	1	2	2.5	120	0.56	6.5	N.O. ^f	110	1.85	1.6	4.3	18	49
	2	3(7)	10	360	2.67	2.67	113.8	97.6	1.76	2.3	4.6	17	49
	3	4(8)	3.8	900	0.82	0.86	122.2	93.3	2.24	2.4	4.4	17	50
	4	5(9)	8.0	120	1.21	4.53	125.4	104	1.92	2.3	4.3	17	50
	5	6(10)	10	900	2.4	0.96	131.6	127	1.78	2.3	4.3	17	50
Octane	6	2	3.6	600	0.83	1.4	N.O. ^f	147	1.86	1.3	2.8	3.4	85
	7	3(7)	20	9,000	3.16	0.063	N.O. ^f	49.7	2.01	1.6	3.4	10	69
	8	4(8)	5.0	1,200	2.09	1.256	N.O. ^f	104	1.82	1.9	4.0	6.5	77
	9	5(9)	10	1,800	2.45	0.49	N.O. ^f	139	1.83	1.5	3.2	4.9	82
	10	6(10)	40	1,500	2.47	0.148	N.O. ^f	154	1.89	1.4	2.8	1.9	89

^a 50 mL, 4 mL toluene injected with catalyst solution. ^b After workup (see Experimental). ^c Units: g polymer/(mol cat.*atm*h). ^d Determined from GPC analysis relative to polystyrene standards; polydispersity index = M_w/M_n . ^e Pentad integrals from polymer ¹³C NMR. ^f Not observed.

Table 13. Concentration Effects on Propylene Polymerization Results for the Reactions Mediated by $[\text{Me}_2\text{C}(\text{Cp})(\text{Flu})]\text{ZrMe}_2$ (**1**) + $\text{B}(\text{C}_6\text{F}_5)_3$ (**3**) in Toluene under 1.0 atm of Propylene at $25^\circ\text{C}^{\text{a}}$

Exp. No.	Cat. (μmol)	Time (s)	Yield ^b (g)	Activity ^c ($\times 10^6$)	T_{m} ($^\circ\text{C}$)	M_{w}^{d} ($\text{kg}\cdot\text{mol}^{-1}$)	P.D.I. ^d	<i>rrmmr</i> ^e (%)	<i>mmrr</i> ^e (%)	<i>rrmr</i> ^e (%)	<i>rrrr</i> ^e (%)
1	800	600	4.92	0.37	102.5	56.9	1.66	1.6	3.3	11.0	68.1
2	400	900	2.30	0.46	102.5	66.4	1.7	1.5	3.1	10.5	69.5
3	200	2,400	5.90	0.44	101.4	79.4	1.81	1.5	3.1	10.6	69.4
4	100	2,400	2.59	0.39	102.5	77.5	1.85	1.6	3.1	10.5	69.6
5	50	3,600	0.86	0.17	101.0	76.0	1.78	1.5	3.1	10.8	69.2
6	25	7,200	2.10	0.42	101.3	81.9	1.83	1.7	3.2	10.9	68.7

^a In 104 mL toluene. ^b After workup (see Experimental). ^c Units: g polymer/(mol cat.*atm*h). ^d Determined from GPC analysis relative to polystyrene standards; polydispersity index = $M_{\text{w}} / M_{\text{n}}$. ^e Pentad integrals from ^{13}C NMR.

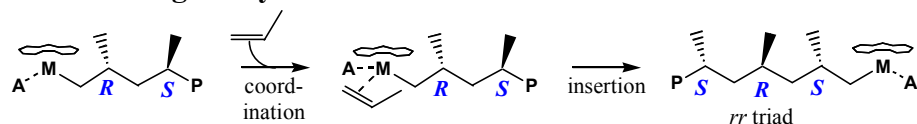
Table 14. Propylene Polymerization Results for the Reactions Mediated by **1** + **3** with Addition of $\text{Li}^+ \text{MeB}(\text{C}_6\text{F}_5)_3^-$ (**11**) in Toluene under 1.0 atm of Propylene at 25°C^a

Exp. No.	Cat. (μmol)	Added 11 (μmol)	Time (s)	Yield ^b (g)	Activity ^c ($\times 10^6$)	T _m (°C)	M _w ^d ($\text{kg}\cdot\text{mol}^{-1}$)	P.D.I. ^d	<i>rmmr</i> ^e (%)	<i>mmrr</i> ^e (%)	<i>rrmr</i> ^e (%)	<i>rrrr</i> ^e (%)
1	20	0	2,400	5.90	0.44	101.4	79.0	1.81	1.5	3.1	10.6	69.4
2	20	20	2,400	2.21	0.17	109.5	84.6	1.78	1.7	3.1	9.2	72
3	20	40	1,800	4.02	0.40	108.5	83.6	1.84	1.8	3.3	9.4	70.9
4	20	60	1,200	3.45	0.52	114.5	86.6	1.8	1.5	2.9	8	75.6
5	20	80	1,200	4.43	0.67	112.2	84.5	1.82	1.6	3	8.9	73.2
6	20	100	1,200	4.90	0.74	114.6	93.0	1.84	1.5	2.9	7.8	76

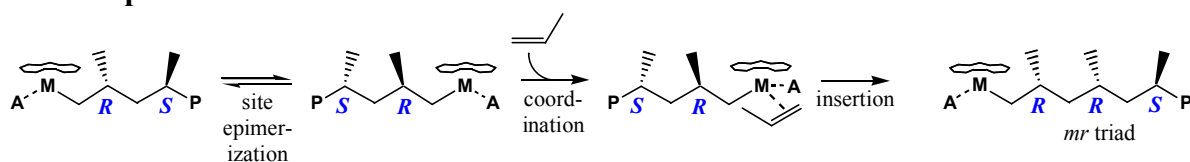
^a In 104 mL toluene. ^b After workup (see Experimental). ^c Units: g polymer/(mol cat.*atm*h). ^d Determined from GPC analysis relative to polystyrene standards; polydispersity index = M_w / M_n . ^e Pentad integrals from ¹³C NMR.

Scheme 1. Syndiospecific Propylene Polymerization and Stereodeflect Mechanisms – C_s -Symmetric Precatalyst

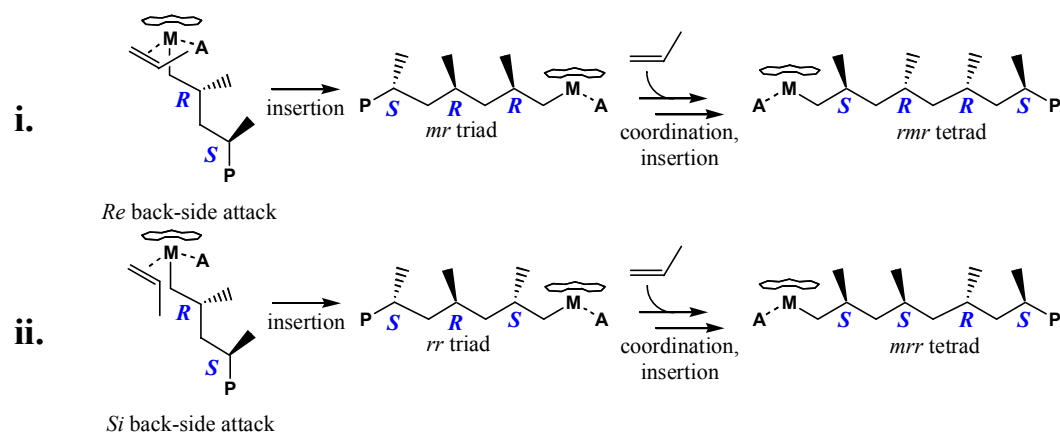
A. Chain-Migratory Insertion



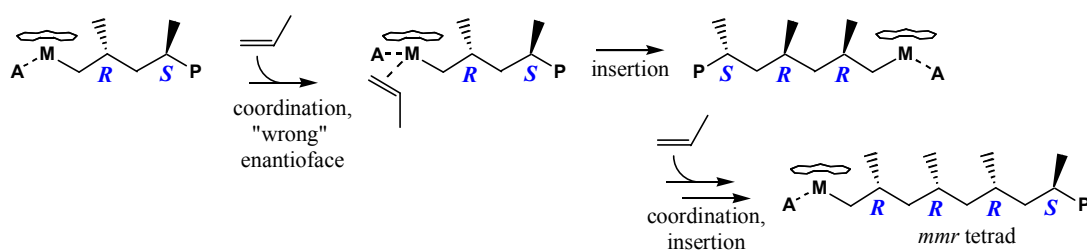
B. Site Epimerization



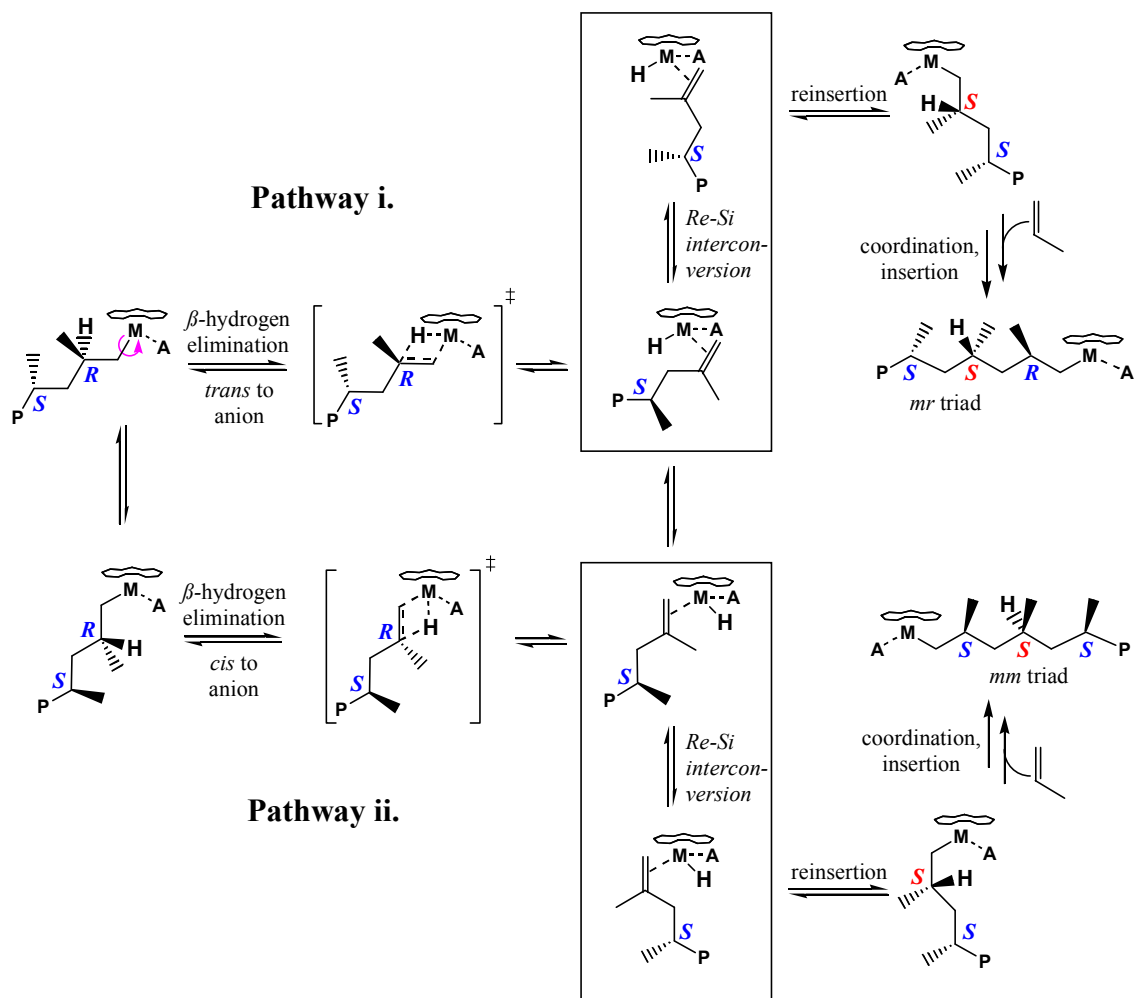
C. "Back-Side" Misinsertion



D. Enantiofacial Misinsertion

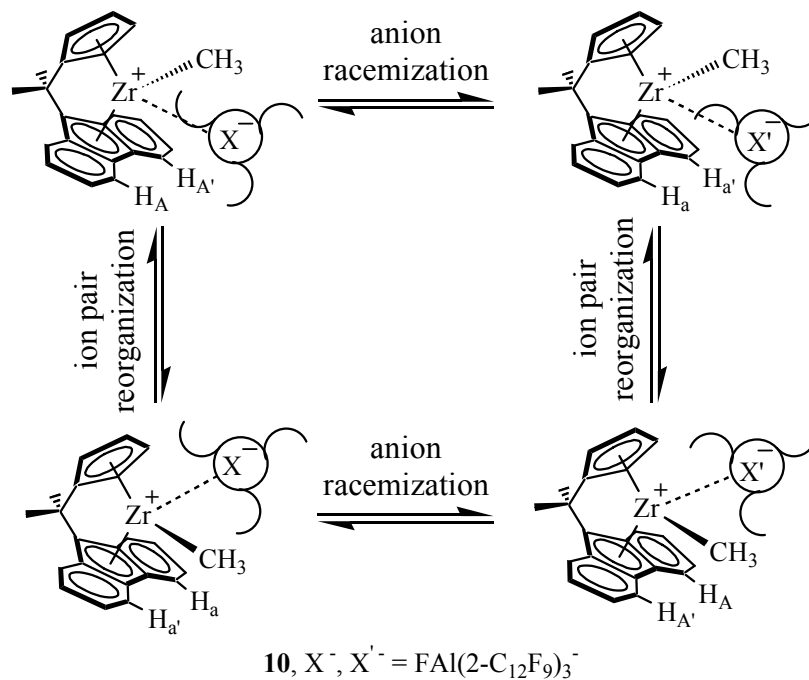


E. Multiple Pathways for Chain Epimerization



Scheme 2. Solution-Phase Reorganization Pathways in $[\text{Me}_2\text{C}(\text{Cp})(\text{Flu})]\text{ZrMe}^+$

$\text{FAI}(2\text{-C}_6\text{F}_5\text{C}_6\text{F}_4)_3^-$ (**10**).



X^-, X'^- represent alternate stereochemical configurations at Al.
The symbols used to represent these configurations are intended to convey a qualitative picture of anion racemization (see Fig. 4).

Diversity in Weakly Coordinating Anions. Mono- and Polynuclear Halo-Perfluoroarylmatalates as Cocatalysts for Stereospecific Olefin Polymerization: Synthesis, Structure, and Reactivity.

Ming-Chou Chen, John A. S. Roberts, Afif M. Seyam, Liting Li, Cristiano Zuccaccia, Nicholas

G. Stahl, and Tobin J. Marks*

Department of Chemistry, Northwestern University

Evanston, Illinois 60208-3113

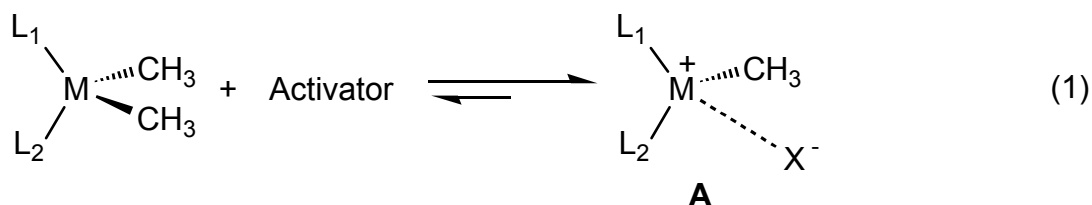
ABSTRACT

A series of mononuclear and polynuclear trityl perfluoroarylborate, -aluminate, and -gallate reagents, potential cocatalysts/activators for metallocene-mediated olefin polymerization have been synthesized via fluoride abstraction from trityl fluoride (Ph_3CF) by the organo-Lewis acid reagents $\text{B}(\text{C}_6\text{F}_5)_3$ (**1**), $\text{B}(o\text{-C}_6\text{F}_5\text{C}_6\text{F}_4)_3$ (**2**), and $\text{Al}(\text{C}_6\text{F}_5)_3$ (**3**), by derivitization of Ph_3C^+ $\text{FAl}(o\text{-C}_6\text{F}_5\text{C}_6\text{F}_4)_3^-$ (**4**), and by reaction of trityl fluoride with *in-situ* generated $\text{Ga}(\text{C}_6\text{F}_5)_3$ (**5**). Reaction of trityl fluoride with tris(perfluoroaryl)boranes **1** and **2** yields trityl tris(perfluoroaryl)fluoroborates $\text{Ph}_3\text{C}^+ \text{FB}(\text{C}_6\text{F}_5)_3^-$ (**6**) and $\text{Ph}_3\text{C}^+ \text{FB}(o\text{-C}_6\text{F}_5\text{C}_6\text{F}_4)_3^-$ (**7**), respectively. Three trityl tris(perfluorophenyl)fluoroaluminates $(\text{Ph}_3\text{C}^+)_x \text{F}_x[\text{Al}(\text{C}_6\text{F}_5)_3]_y^{x-}$ ($x = 1$, $y = 1$, **8**; $x = 1$, $y = 2$, **9**; $x = 2$, $y = 3$, **10**) can be isolated from reaction of trityl fluoride with tris(perfluoroaryl)alane **3** in appropriate molar ratios. Reaction of trityl tris(perfluoroaryl)fluoroaluminate **4** with **3** affords the asymmetric fluoro-bridged trityl bis[tris(perfluoroaryl)]aluminate $\text{Ph}_3\text{C}^+ (\text{C}_6\text{F}_5)_3\text{AlFAl}(o\text{-C}_6\text{F}_5\text{C}_6\text{F}_4)_3^-$ (**11**), while reaction of trityl halides Ph_3CCl and Ph_3CBr with **3** gives the corresponding trityl

tris(perfluorophenyl)haloaluminates $\text{Ph}_3\text{C}^+ \text{XAl}(\text{C}_6\text{F}_5)_3^-$ ($\text{X} = \text{Cl}$, **12**; $\text{X} = \text{Br}$, **13**). Isolable, symmetric fluoro-bridged trityl bis[tris(perfluoroaryl)]gallate $\text{Ph}_3\text{C}^+ \text{F}[\text{Ga}(\text{C}_6\text{F}_5)_3]_2^-$ (**14**) is derived from a "one pot" reaction of trityl fluoride with $\text{Ga}(\text{C}_6\text{F}_5)_3$, generated *in situ* from **4** + $\text{Ga}(\text{CH}_3)_3$. Of these new species, compounds **7** and **10-14** were characterized by single-crystal X-ray diffraction. Trityl salts **6** – **13** react with C_S -symmetric metallocene precatalyst $\text{Me}_2\text{C}(\text{Cp})(\text{Flu})\text{ZrMe}_2$ (**15**; $\text{Cp} = \text{C}_5\text{H}_4$; $\text{Flu} = \text{C}_{13}\text{H}_8$, fluorenyl) to form isolable ion-pair complexes or characterizable mixtures. Species **6** reacts with **15** to generate known ion-pair $\text{Me}_2\text{C}(\text{Cp})(\text{Flu})\text{ZrMe}^+ \text{MeB}(\text{C}_6\text{F}_5)_3^-$ (**16**), and reaction of **7** with **15** gives fluoro-bridged dimeric diastereomers $[\text{Me}_2\text{C}(\text{Cp})(\text{Flu})\text{ZrMe}]_2(\mu\text{-F})^+ \text{FB}(o\text{-C}_6\text{F}_5\text{C}_6\text{F}_4)_3^-$ (**17**). Trityl tris(perfluorophenyl)fluoroaluminates **8**, **9**, and **10** all react with **15** to afford mixtures of $\text{Me}_2\text{C}(\text{Cp})(\text{Flu})\text{ZrMe}^+ \text{FAl}(\text{C}_6\text{F}_5)_3^-$ (**18**) and diastereomeric $[\text{Me}_2\text{C}(\text{Cp})(\text{Flu})\text{ZrMe}]_2(\mu\text{-Me})^+ (\text{C}_6\text{F}_5)_3\text{AlFAl}(\text{C}_6\text{F}_5)_3^-$ (**19**). Asymmetric species **11** cleanly affords diastereomeric $[\text{Me}_2\text{C}(\text{Cp})(\text{Flu})\text{ZrMe}]_2(\mu\text{-Me})^+ (\text{C}_6\text{F}_5)_3\text{AlFAl}(o\text{-C}_6\text{F}_5\text{C}_6\text{F}_4)_3^-$ (**20**) in reaction with metallocene **15**. Adducts of **12** and **13** with metallocene **15** afford decomposition products $\text{Me}_2\text{C}(\text{Cp})(\text{Flu})\text{ZrCl}(\text{C}_6\text{F}_5)$ (**21**) and $[\text{Me}_2\text{C}(\text{Cp})(\text{Flu})\text{Zr}(\mu_2\text{-Br})]_2^{2+} [\text{Al}(\text{C}_6\text{F}_5)_4]_2^-$ (**22**), respectively. Complexes **17** - **22** were characterized by single-crystal X-ray diffraction.

INTRODUCTION

Recent developments in understanding cation-anion interactions in metallocenium/single-site ion-pair polymerization catalyst systems (**A**, produced via reaction of neutral metallocenes with neutral or ionic organometalloid activators; eq. 1) reveal that the



nature of the cation-anion interaction has a profound influence on catalyst lifetime and stability, polymerization activity, chain-transfer pathways, and stereoregulation.^{1,2} Well-known

¹ For recent reviews, see: (a) Gibson, V. C.; Spitzmesser, S. K. *Chem. Rev.*, **2003**, 103 (1), 283-315. (b) Pédeutour, J.-N.; Radhakrishnan, K.; Cramail, H.; Deffieux, A. *Macromol. Rapid Commun.* **2001**, 22, 1095-1123. (c) Chen, Y.-X.; Marks, T. J. *Chem. Rev.*, **2000**, 100 (4), 1391-1434. (d) Gladysz, J. A., Ed. *Chem. Rev.* **2000**, 100, 1167-1682. (e) Marks, T. J.; Stevens, J. C., Eds. *Topics in Catalysis*, **1999**, 7, 1-208. (f) Britovsek, G. J. P.; Gibson, V. C.; Wass, D. F. *Angew. Chem., Int. Ed. Engl.* **1999**, 38, 428-447.

² For recent cocatalyst studies, see: (a) Busico, V.; Cipullo, R.; Cutillo, F.; Vacatello, M.; Castelli, V. V. *Macromolecules* **2003**, 36, 4258-4261. (b) Mohammed, M.; Nele, M.; Al-Humydi, A.; Xin, S.; Stapleton, R. A.; Collins, S. *J. Am. Chem. Soc.* **2003**, 125, 7930-7941. (c) Abramo, G. P.; Li, L.; Marks, T. J. *J. Am. Chem. Soc.* **2002**, 124, 13966-13967. (d) Li, L.; Metz, M. V.; Li, H.; Chen, M.-C.; Marks, T. J. *J. Am. Chem. Soc.* **2002**, 124, 12725-12741. (e) Metz, M. V.; Schwartz, D. J.; Stern, C. L.; Marks, T. J.; Nickias, P. N. *Organometallics*, **2002**, 21, 4159-4168. (f) Metz, M. V.; Sun, Y. M.; Stern, C. L.; Marks, T. J. *Organometallics*, **2002**, 21, 3691-3702. (g) Wilmes, G. M.; Polse, J. L.; Waymouth, R. M. *Macromolecules* **2002**, 35, 6766-6772. (h) Lancaster, S. J.; Rodriguez, A.; Lara-Sanchez, A.; Hannant, M. D.; Walker, D. A.; Hughes, D. H.; Bochmann, M. *Organometallics*, **2002**, 21, 451-453. (i) Rodriguez, G.; Brant, P. *Organometallics*, **2001**, 20, 2417-2420. (j) Kaul, F. A. R.; Puchta, G. T.; Schneider, H.; Grosche, M.; Mihalios, D.; Herrmann, W. A. *J. Organometal. Chem.* **2001**, 621, 177-183. (k) Chen, Y.-X.; Kruper, W. J.; Roof, G.; Wilson, D. R. *J. Am. Chem. Soc.* **2001**, 123, 745-746. (l) Zhou, J.; Lancaster,

activator/cocatalyst classes include alkylaluminoxanes (e.g. MAO and MMAO),³ tris(perfluorophenyl)borane ($B(C_6F_5)_3$; **1**)⁴ and related perfluoroarylboranes,⁵ ammonium or trityl salts of $B(C_6F_5)_4^-$ ⁶ and related perfluoroarylborates,⁷ perfluoroarylalanes (e.g. $Al(C_6F_5)_3$; **7**),⁸ and perfluoroaryl-fluoroaluminate salts.⁹ Systems with single-molecule activators exhibiting

S. J.; Walker, D. A.; Beck, S.; Thornton-Pett, M.; Bochmann, M. *J. Am. Chem. Soc.* **2001**, *123*, 223-237. (m) Kehr, G.; Roesmann, R.; Fröhlich, R.; Holst, C.; Erker, G. *Eur. J. Inorg. Chem.* **2001**, 535-538. (n) Mager, M.; Becke, S.; Windisch, H.; Denninger, U. *Angew. Chem., Int. Ed. Engl.* **2001**, *40*, 1898-1902.

³ (a) Sinn, H.; Kaminsky, W. *Adv. Organomet. Chem.* **1980**, *18*, 99-149. (b) Sinn, H.; Kaminsky, W.; Vollmer, H.-J.; Woldt, R. *Angew. Chem., Int. Ed. Engl.* **1980**, *19*, 390-392.

⁴ (a) Yang, X.; Stern, C. L.; Marks, T. J. *J. Am. Chem. Soc.* **1994**, *116*, 10015-10031. (b) Yang, X.; Stern, C. L.; Marks, T. J. *J. Am. Chem. Soc.* **1991**, *113*, 3623-3625.

⁵ (a) Li, L.; Stern, C. L.; Marks, T. J. *Organometallics* **2000**, *19*, 3332-3337. (b) Li, L.; Marks, T. J. *Organometallics* **1998**, *17*, 3996-4003. (c) Chen, Y.-X.; Stern, C. L.; Yang, S.; Marks, T. J. *J. Am. Chem. Soc.* **1996**, *118*, 12451-12452. (d) also see refs. 2c, 2d, and 2e. (e) For a recent chelating borane review, see: Piers, W. E.; Irvine, G. J.; Williams, V. C. *Eur. J. Inorg. Chem.* **2000**, 2131-2142.

⁶ (a) Chien, J. C. W.; Tsai, W.-M.; Rausch, M. D. *J. Am. Chem. Soc.* **1991**, *113*, 8570-8571. (b) Yang, X.; Stern, C. L.; Marks, T. J. *Organometallics* **1991**, *10*, 840-842. (c) Ewen, J. A.; Elder, M. J. *Eur. Pat. Appl.* 426637, **1991**; *Chem. Abstr.* **1991**, *115*, 136987c, 136988d.

⁷ For related fluorinated tetraarylborates, see: (a) refs 2h, 2i, 2j, and 2l. (b) Jia, L.; Yang, X.; Stern, C. L.; Marks, T. J. *Organometallics* **1997**, *16*, 842-857. (c) Jia, L.; Yang, X.; Ishihara, A.; Marks, T. J. *Organometallics* **1995**, *14*, 3135-3137.

⁸ (a) ref 2f. (b) Bochmann, M.; Sarsfield, M. J. *Organometallics* **1998**, *17*, 5908-5912. (c) Biagini, P.; Lugli, G.; Abis, L.; Andreussi, P. U.S. Pat. 5,602,269, **1997**.

⁹ (a) Chen, Y.-X.; Metz, M. V.; Li, L.; Stern, C. L.; Marks, T. J. *J. Am. Chem. Soc.* **1998**, *120*, 6287-6305. (b) Chen, Y.-X.; Stern, C. L.; Marks, T. J. *J. Am. Chem. Soc.* **1997**, *119*, 2582-2583. (c) Elder, M. J.; Ewen, J. A. *Eur. Pat. Appl.* EP 573,403, **1993**; *Chem. Abstr.* **1994**, *121*, 0207d.

clean activation chemistry and affording characterizable active catalysts (e.g. with $B(C_6F_5)_3$ and trityl salts of $B(C_6F_5)_4^-$)^{1, 4, 6} allow correlation of catalyst ion-pair structural and dynamic features with polymerization behavior. These catalyst systems exhibit varying modes of cation-anion interaction and are found to be 1:1 contact ion-pairs at typical polymerization concentrations in low- ϵ media.^{10, 11}

In general, product polymer M_w , polydispersity, and (with prochiral propylene as monomer) the relative abundances of various stereosequences in the polymer backbone are sensitive to counteranion identity in a systematic way.¹² For C_S -symmetric precatalysts, these observables reflect the rate of propylene insertion *relative to* the rates of competing stereodeflect generation and chain termination processes, according to the established mechanism for syndiospecific propylene enchainment.¹³ The strength and nature of the ion pairing is found to play a key role in determining the *absolute* rates of these individual processes. These systematic correlations, explored in detail in recently published work,¹² are briefly summarized here. In

¹⁰ (a) Stahl, N. G.; Zuccaccia, C.; Jensen, T. R.; Marks, T. J. *J. Am. Chem. Soc.* **2003**, *125*, 5256-5257. (b) Stahl, N. G.; Marks, T. J.; Macchioni, A.; Zuccaccia, C. Presented in part at the 222nd ACS National Meeting, Chicago, IL, August 2001, Abstract INORG 407. (c) Zuccaccia, C.; Stahl, N. G.; Macchioni, A.; Chen, M.-C.; Roberts, J. A. S.; Marks, T. J. *J. Am. Chem. Soc.* **2004**, *126*, 1448-1464.

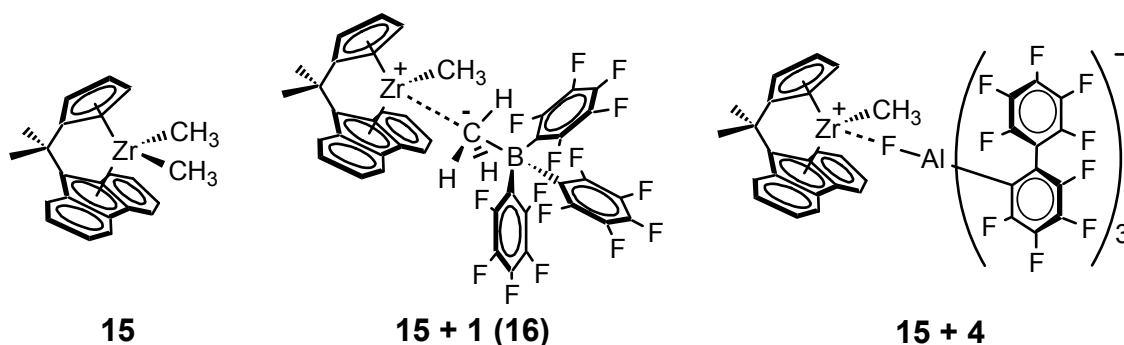
¹¹ Song, F.; Lancaster, S. J.; Cannon, R. D.; Schormann, M.; Humphrey, S. M.; Zuccaccia, C.; Macchioni, A.; Boehmann, M. *Organometallics* **2005**; ASAP Article.

¹² Chen, M.-C.; Roberts, J. A. S.; Marks, T. J. *J. Am. Chem. Soc.* **2004**, *126*, 4605-4625.

¹³ (a) Resconi, L.; Cavallo, L.; Fait, A.; Piemontesi, F. *Chem. Rev.*, **2000**, *100*, 1253-1345. (b) Coates, G. W. *Chem. Rev.*, **2000**, *100*, 1223-1252. (c) Veghini, D.; Henling, L. M.; Burkhardt, T. J.; Bercaw, J. E. *J. Am. Chem. Soc.* **1999**, *121*, 564-573. (d) Ewen, J. A.; Jones, R. L.; Razavi, A.; Ferrara, J. D. *J. Am. Chem. Soc.* **1988**, *110*, 6255-6256.

isolated ion-pair complexes formed by reaction of C_S -symmetric metallocene **15** with a collection of cocatalyst reagents/activators of the present class, the cation-anion contact is apparently dictated by the structure of the anion, and exhibits a diverse variety of motifs.

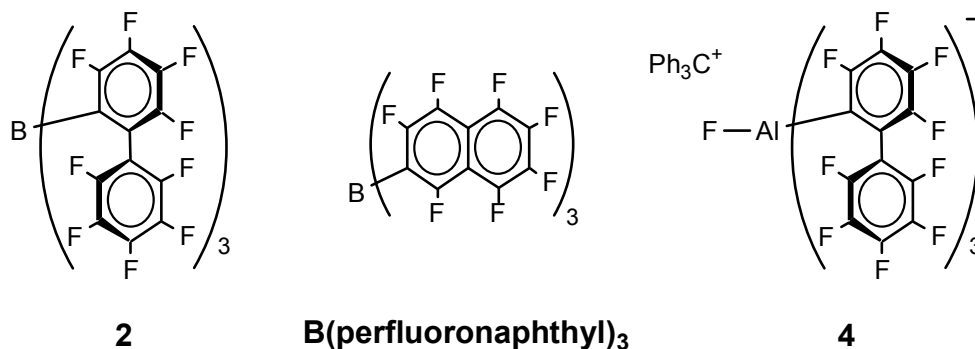
Complex **15** + **1**, for example, exhibits a largely electrostatic cation-anion interaction,¹⁴ with the $\text{MeB}(\text{C}_6\text{F}_5)_3^-$ anionic fragment bound at the available coordination site of the cationic Zr center, the anion methide group acting as a bridge between the Zr and B atoms. The cation-anion interaction is observed by NMR to be rather labile, and monomer insertion proceeds rapidly in polymerization experiments with this catalyst system.¹² However, for the catalyst derived from **15** + **4**, the anion is coordinated via the Al-bound fluorine atom, this interaction being



significantly more inert. Insertion is dramatically attenuated, as are (to a greater degree) chain termination and stereodeflect-forming reorganization processes. In stark contrast to these results, with **15** + $\text{Ph}_3\text{C}^+ \text{B}(\text{C}_6\text{F}_5)_4^-$ (irreversibly and quantitatively releasing Ph_3CCH_3), the highly symmetric, charge-dispersed $\text{B}(\text{C}_6\text{F}_5)_4^-$ anion binds rather loosely with no obviously dominant preferred interatomic contact, and all polymerization-related processes proceed much more rapidly, particularly propylene enchainment.¹² As with $\text{B}(\text{C}_6\text{F}_5)_4^-$, the anions in catalyst systems

¹⁴ (a) Lanza, G.; Fragala, I. L.; Marks, T. J. *Organometallics* **2002**, 21, 5594-5612. (b) Lanza, G.; Fragala, I. L.; Marks, T. J. *Organometallics* **2001**, 20, 4006-4017. (c) Lanza, G.; Fragala, I. L.; Marks, T. J. *J. Am. Chem. Soc.* **2000**, 122, 12 764-12 777.

15 + **2** and **15** + B(perfluoronaphthyl)₃ appear to be more weakly bound to the cationic fragment



than is the anion generated by reaction of precatalyst **15** with **1**, based on polymerization reactivity data. Room-temperature polymerization data do not alone provide direct evidence that these specific cation-anion interactions persist during catalytic turnover. However, the observed systematic dependence of the absolute rates of observed polymerization-related processes on anion identity and the nature of the cation-anion interaction in the isolated catalyst ion-pairs inferred from crystallographic and solution-phase dynamic NMR analysis suggests that this is likely the case. Indeed, early observations of anion effects in polymerization experiments stimulated efforts to develop new single-molecule cocatalysts, leading to the development of the sterically encumbered perfluoroaryl group 13 cocatalysts B(*o*-C₆F₅C₆F₄)₃ (**2**),^{5c} B(perfluoronaphthyl)₃,^{5b} and the trityl tris(perfluoroaryl)fluoroaluminate salt Ph₃C⁺ FAl(*o*-C₆F₅C₆F₄)₃⁻ (**4**).^{9a} This research represents a facet of the important continuing search for weakly coordinating anionic species.¹⁵ The catalyst systems afforded by these new cocatalysts and their antecedents exhibit a broad range of thermal stabilities, with the more active systems being in general less stable. These collected observations have therefore motivated and directed

¹⁵ (a) Juhasz, M.; Hoffmann, S.; Stoyanov, E.; Kim, K.-C.; Reed, C. A. *Angew. Chem., Int. Ed.* **2004**, *43*, 5352-5355.

(b) Reed, C. A. *Acc. Chem. Res.* **1998**, *31*, 133-139. (c) Seppelt, K. *Angew. Chem., Int. Ed.* **1993**, *32*, 1025-1027.

the development of single-site catalyst systems that are both highly active and more thermally robust.

Recently we communicated several new classes of mononuclear and polynuclear fluoro-perfluoroarylborate, -aluminate, and -gallate cocatalysts.¹⁶ These more sterically encumbered and charge-dispersing cocatalysts afford thermally stable active catalyst systems that can produce highly stereoregular polypropylenes with very high polymerization activities.¹⁷ In the present report, we extend our preliminary findings,¹⁶ discuss the syntheses of new and previously reported species in detail, and describe observed spectroscopic, structural, and reactivity trends of these new cocatalysts. We also discuss the chemistry of these new cocatalysts as activators for metallocene precatalyst **15** as well as the spectroscopic and structural properties of ion-pair complexes produced in these activation reactions. In a complementary account¹⁷ we compare/contrast the propylene polymerization behavior of the active catalyst systems derived from this new series of cocatalysts in combination with the archetypal C_5 -symmetric precatalyst **15**, and with C_1 -symmetric precatalyst $\text{Me}_2\text{Si}(\text{CpR}^*)(\text{octahydrofluorenyl})\text{ZrMe}_2$ ($\text{R}^* = (1R,2S,5R)\text{-trans-5-methyl-cis-2-(2-propyl)cyclohexyl}$; (-)-menthyl). In certain interesting and instructive cases, we observe high stereoselectivities in conjunction with high polymerization activities with both of these precatalysts.¹⁷

¹⁶ Preliminary communication: Chen, M. -C.; Roberts, J. A. S.; Marks, T. J. *Organometallics* **2004**, *23*, 932-935.

¹⁷ Polymerization results using the present series of cocatalysts with metallocenes **15** and $\text{Me}_2\text{Si}(\text{CpR}^*)(\text{octahydrofluorenyl})\text{ZrMe}_2$ (**2**, $\text{R}^* = (1R,2S,5R)\text{-trans-5-methyl-cis-2-(2-propyl)cyclohexyl}$; (-)-menthyl) are presented in a separate report.

EXPERIMENTAL SECTION

Materials and Methods. All manipulations of air-sensitive materials were performed with rigorous exclusion of oxygen and moisture in flamed Schlenk-type glassware on a dual-manifold Schlenk line or interfaced to a high-vacuum line (10^{-6} Torr), or in an N₂-filled Vacuum Atmospheres or MBraun glove box with a high capacity recirculator (<1 ppm O₂). Argon (Matheson, pre-purified) was purified by passage through a supported MnO-packed oxygen removal column and a column packed with activated Davidson 4A molecular sieves. Hydrocarbon solvents (toluene and pentane) were distilled under nitrogen from Na/benzophenone ketyl or passed through columns packed with molecular sieves and supported Cu(0) deoxygenating agent. These solvents were subsequently stored under vacuum over Na/K alloy in Teflon-valved bulbs and distilled using a high-vacuum line immediately prior to use. Deuterated solvents were obtained from Cambridge Isotope Laboratories (all ≥ 99 atom %D), were freeze-pump-thaw degassed, dried over Na/K alloy, and stored in resealable flasks. Other nonhalogenated solvents were dried over Na/K alloy, and halogenated solvents were distilled from CaH₂. Trityl fluoride (Ph₃CF),¹⁸ B(C₆F₅)₃ (**1**),¹⁹ B(*o*-C₆F₅C₆F₄)₃ (**2**),^{5c} Al(C₆F₅)₃·0.5(C₇H₈) (**3**),²⁰ Ph₃C⁺ FAl(*o*-C₆F₅C₆F₄)₃⁻ (**4**),^{9a} and Me₂C(Cp)(Flu)ZrMe₂ (**15**)²¹ were prepared according

¹⁸ Oishi, M.; Yamamoto, H. *B. Chem. So. Jpn.* **2001**, 74(8), 1445-1454.

¹⁹ Massey, A. G.; Park, A. J. *J. Organomet. Chem.* **1964**, 2, 245-250.

²⁰ This compound was prepared as a toluene adduct, see refs 8b and 8c. **CAUTION:** Al(C₆F₅)₃ has been reported to detonate on attempted sublimation at elevated temperatures. Pohlmann, J. L. W.; Brinckmann, F. E. *Z. Naturforsch. B* **1965**, 20b, 5. Chambers, R. D. *Organomet. Chem. Rev.* **1966**, 1, 279.

²¹ (a) Razavi, A.; Thewalt, U. *J. Organomet. Chem.* **1993**, 445, 111-114. (b) Razavi, A.; Ferrara, J. *J. Organomet. Chem.* **1992**, 435, 299-310.

Physical and Analytical Measurements. NMR spectra were recorded on Varian ^{UNITY}Inova-500 (FT, 500 MHz, ¹H; 125 MHz, ¹³C), ^{UNITY}Inova-400 (FT, 400 MHz, ¹H; 100 MHz, ¹³C), Mercury-400 (FT 400 MHz, ¹H; 100 MHz, ¹³C; 377 MHz, ¹⁹F) instruments. Chemical shifts for ¹H and ¹³C spectra were referenced using internal solvent resonances and are reported relative to tetramethylsilane. ¹⁹F NMR spectra were referenced to external CFCl₃. NMR experiments on air-sensitive samples were conducted in Teflon valve-sealed NMR tubes (J. Young).

Synthesis of Ph₃C⁺ ClAl(C₆F₅)₃⁻ (12). In the glovebox, Ph₃CCl (70 mg, 0.25 mmol), Al(C₆F₅)₃·0.5(C₇H₈) (**3**, 114 mg, 0.200 mmol),²² and 5 mL toluene were loaded into a 50 mL reaction flask having a filter frit, and then the flask was reattached to the vacuum line. The mixture was stirred for 1.0 h at room temperature, and 20 mL pentane was next condensed into the flask. The resulting suspension was filtered, and the collected orange solid was washed three times with 10 mL of pentane. This recrystallization procedure from toluene/pentane was repeated until the pure title compound was obtained, 133 mg; yield, 83%. ¹H NMR (C₇D₈, 23°C): δ 6.8 – 7.4 (br, Ph). ¹⁹F NMR (C₇D₈, 23°C): δ -122.354 (m, 6 F, *o*-F), -156.706 (m, 3 F, *p*-F), -163.79 (m, 6 F, *m*-F). Anal. Calc'd for C₃₇H₁₅AlClF₁₅: C, 55.07; H, 1.87. Found: C, 54.72; H, 2.12.

²² Al-Humydi, A.; Garrison, J.C.; Youngs, W.J.; Collins, S. *Organometallics* **2005**, 24(2), 193-196. (b) Lancaster, S. J.; Bochmann, M. *J. Organomet. Chem.* **2002**, 654(1-2), 221-223.

Synthesis of $\text{Ph}_3\text{C}^+ \text{BrAl}(\text{C}_6\text{F}_5)_3^-$ (13**).** In a procedure similar to that described above but using Ph_3CBr (80 mg, 0.25 mmol) in place of Ph_3CCl , the title compound was obtained; 121 mg yield, 71%. ^1H NMR (C_7D_8 , 23°C): δ 6.8 – 7.4 (br, Ph). ^{19}F NMR (C_7D_8 , 23°C): δ -122.44 (m, 6 F, *o*-F), -156.85 (m, 3 F, *p*-F), -163.73 (m, 6 F, *m*-F). Anal. Calc'd for $\text{C}_{37}\text{H}_{15}\text{AlBrF}_{15}$: C, 52.20; H, 1.78. Found: C, 52.05; H, 2.01. Orange crystals of the title complex suitable for X-ray diffraction were obtained by slow diffusion of pentane into toluene solutions. Similar to the previous reaction, with a 1:2 ratio of Ph_3CBr and $\text{Al}(\text{C}_6\text{F}_5)_3 \cdot 0.5(\text{C}_7\text{H}_8)$, three new ^{19}F resonances were observed. Crystals suitable for X-ray diffraction, isolated by slow diffusion of pentane into toluene solutions of this reaction mixture, were found to be **13**.

General Procedure for Reaction of $\text{Me}_2\text{C}(\text{Cp})(\text{Flu})\text{ZrMe}_2$ (15**) with Cocatalysts Studied by *In-Situ* NMR.** In a typical procedure, in the glove box, $\text{Me}_2\text{C}(\text{Cp})(\text{Flu})\text{ZrMe}_2$ (**15**) and the required cocatalyst in a 1:1 stoichiometric ratio were loaded into a J. Young NMR tube, and 0.5 mL of toluene-*d*₈ was transferred in. Each sample was then shaken vigorously and transferred directly to the NMR spectrometer probe. In all cases, complete consumption of complex **1** was observed by ^1H and ^{19}F NMR, along with the formation of Ph_3CCH_3 and the corresponding ion-pair complex.

Experimental descriptions and chemical shift data for *in-situ* NMR study of $\text{Me}_2\text{C}(\text{Cp})(\text{Flu})\text{ZrMe}_2$ (**15**) activation by $\text{Ph}_3\text{C}^+ \text{FB}(\text{C}_6\text{F}_5)_3^-$ (**6**), $\text{Ph}_3\text{C}^+ \text{FB}(\text{o-C}_6\text{F}_5\text{C}_6\text{F}_4)_3^-$ (**7**), $\text{Ph}_3\text{C}^+ \text{FAl}(\text{C}_6\text{F}_5)_3^-$ (**8**), $\text{Ph}_3\text{C}^+ \text{F}[\text{Al}(\text{C}_6\text{F}_5)_3]_2^-$ (**9**), $(\text{Ph}_3\text{C}^+)_2 \text{F}_2[\text{Al}(\text{C}_6\text{F}_5)_3]_3^{2-}$ (**10**), $\text{Ph}_3\text{C}^+ (\text{C}_6\text{F}_5)_3\text{AlFAl}(\text{o-C}_6\text{F}_5\text{C}_6\text{F}_4)_3^-$ (**11**) are presented in the Supporting Information accompanying Ref. 16.

***In-Situ* NMR Study of $\text{Me}_2\text{C}(\text{Cp})(\text{Flu})\text{ZrMe}_2$ (**15**) Activation by $\text{Ph}_3\text{C}^+ \text{ClAl}(\text{C}_6\text{F}_5)_3^-$ (**12**), or $\text{Ph}_3\text{C}^+ \text{BrAl}(\text{C}_6\text{F}_5)_3^-$ (**13**).** $\text{Me}_2\text{C}(\text{Cp})(\text{Flu})\text{ZrMe}_2$ (**15**, 3.9 mg, 0.010 mmol) and one of the above cocatalysts were loaded into two NMR tubes as described in the above procedure. Rapid methide abstraction from **15** by both of these cocatalysts to form Ph_3CCH_3 was observed, and multiple products were detected in the three reaction mixtures. However, due to overlap of the fluorenyl signals in the ^1H NMR, complete and unambiguous identification of the derived species was not possible. Nevertheless, orange crystals of $\text{Me}_2\text{C}(\text{Cp})(\text{Flu})\text{ZrCl}(\text{C}_6\text{F}_5)$ (**21**, from reaction of **15** + **12**) and doubly bridged $[\text{Me}_2\text{C}(\text{Cp})(\text{Flu})\text{Zr}(\mu\text{-Br})]_2^{2+} [\text{Al}(\text{C}_6\text{F}_5)_4]_2^-$ (**22**, from reaction of **15** + **13**) suitable for X-ray diffraction were obtained by slow diffusion of pentane into toluene solutions of the above reaction mixtures at 0°C .

X-Ray Crystal Structure Determinations of $\text{Ph}_3\text{C}^+ \text{ClAl}(\text{C}_6\text{F}_5)_3^-$ (12**), $\text{Ph}_3\text{C}^+ \text{BrAl}(\text{C}_6\text{F}_5)_3^-$ (**13**), $[\text{Me}_2\text{C}(\text{Cp})(\text{Flu})\text{ZrMe}]_2(\mu\text{-F})^+ \text{FB}(\text{o-C}_6\text{F}_5\text{C}_6\text{F}_4)_3^-$ (**17**), $[\text{Me}_2\text{C}(\text{Cp})(\text{Flu})\text{ZrMe}]_2(\mu\text{-Me})^+ \text{F}[\text{Al}(\text{C}_6\text{F}_5)_3]_2^-$ (**19**), $[\text{Me}_2\text{C}(\text{Cp})(\text{Flu})\text{ZrMe}]_2(\mu\text{-Me})^+ [(\text{C}_6\text{F}_5)_3\text{AlFAl}(\text{2-C}_6\text{F}_5\text{C}_6\text{F}_4)_3]^-$ (**20**), $\text{Me}_2\text{C}(\text{Cp})(\text{Flu})\text{ZrCl}(\text{C}_6\text{F}_5)$ (**21**), and $[\text{Me}_2\text{C}(\text{Cp})(\text{Flu})\text{Zr}(\mu\text{-Br})]_2^{2+} [\text{Al}(\text{C}_6\text{F}_5)_4]_2^-$ (**22**).** Crystals of the title complexes suitable for X-ray diffraction were obtained as described above by slow diffusion of pentane into toluene solutions, either at room temperature or at 0°C . Inside the

glove box, the crystals were placed on a glass slide and covered with dry Infineum V8512 oil.

The crystals were then removed from the box and a suitable crystal was chosen under a microscope using plane-polarized light. The crystal was mounted on a glass fiber and transferred to a Bruker SMART 1000 CCD area detector diffractometer in a nitrogen cold-stream at 153(2) K. Twenty frames (20 sec exposures, 0.3° slices) were collected in three areas of space to determine the orientation matrix. The parameters for data collection were determined by the peak intensities and widths from the 60 frames used to determine the orientation matrix. The faces of the crystal were then indexed and data collection was begun. After data collection, the frames were integrated, the initial crystal structure solved by direct methods, the structure solution was expanded through successive least-squares cycles, absorption corrections were applied, and the final solution was determined. Crystal, data collection, and refinement parameters are summarized in Table 1. Data for the previously reported structures $\text{Ph}_3\text{C}^+\text{FB}(o\text{-C}_6\text{F}_5\text{C}_6\text{F}_4)_3^-$ (7), $(\text{Ph}_3\text{C}^+)_2\text{F}_2[\text{Al}(\text{C}_6\text{F}_5)_3]_3^{2-}$ (10), $\text{Ph}_3\text{C}^+(\text{C}_6\text{F}_5)_3\text{AlFAl}(o\text{-C}_6\text{F}_5\text{C}_6\text{F}_4)_3^-$ (11), and $\text{Ph}_3\text{C}^+\text{F}[\text{Ga}(\text{C}_6\text{F}_5)_3]_2^-$ (14), has been reprocessed to ensure consistency with the newly reported structures.

RESULTS AND DISCUSSION

In the following sections, we discuss the syntheses, solid state structural, and solution structural/dynamic features of perfluoroarylmethyl complexes **6 – 14**, their reaction chemistry with $\text{Me}_2\text{C}(\text{Cp})(\text{Flu})\text{ZrMe}_2$ (**15**), and the products generated in these reactions.

The discussion is presented in five parts: in the first we provide an overview of the syntheses and general features of new cocatalysts **6 – 14**; in the second, we briefly survey the activation chemistry of group 4 metallocene dimethyl precatalysts with the single-molecule

cocatalysts/anion precursors and give an overview of activation reactions between cocatalysts **6 – 14** with precatalyst **15**; the third, fourth, and fifth sections are devoted to B-, Al- and Ga-containing species, respectively: in each, we detail the syntheses, spectroscopic, and structural features of the cocatalysts, and then describe the activation chemistry of these cocatalyst species with metallocene **15** and the spectroscopic and structural features of the resultant metallocenium ion-pair complexes. The collected spectroscopic, structural, and reactivity data are examined independently and as parts of the whole, to provide a complete picture of these interesting and complex systems.

I. Synthesis and Characterization of Cocatalysts 6 – 14. General Considerations.

The species presented herein constitute a new class of sterically encumbered, highly charge-delocalized perfluoroarylmethylate cocatalysts/counteranions, offering a variety of substituents with differing coordinative tendencies, classified by the general synthetic route by which they are accessed: under oxygen- and moisture-free conditions, trityl halides are combined with known neutral and ionic perfluoroaryl complexes of boron, aluminum, and gallium in varying stoichiometries to yield trityl salt species featuring metalloid-halogen linkages. Specific isolable mono- and polymeric trityl perfluoroarylmethyl halide salts are accessible in this way and in some cases exhibit remarkable performance as cocatalysts in propylene polymerization with zirconocene dialkyls $\text{Me}_2\text{C}(\text{Cp})(\text{Flu})\text{ZrMe}_2$ (**15**) and $\text{Me}_2\text{Si}(\text{Cp}(-)\text{-menthyl})(\text{octahydrofluorenyl})\text{ZrMe}_2$; these polymerization results and their mechanistic implications are presented in detail elsewhere.¹⁷

The common structural theme across this series of cocatalysts is the presence of one or more metalloid-bound halogen atoms found in either M–X or M–X–M bonding configurations;

the synthetic and metallocene activation chemistry typically involves formation or cleavage of these metalloid-halogen bonds. The group 13 atoms of these species also bear strongly electron-withdrawing perfluoroaryl substituents that impart considerably heightened Lewis acidity to the corresponding neutral tris(perfluoroaryl)metalloid analogs and are thought to play a key role in anion charge delocalization in addition to providing steric bulk. In the present series, these substituents are either simple perfluorophenyl (C_6F_5) groups or *ortho*-perfluorobiphenyl ($o-C_6F_5C_6F_4$) groups, the latter capable of sterically encapsulating *or* exposing the metalloid-bound halogen or C atoms, depending on the steric context of these potentially bridging moieties (*vide infra*).

The new cocatalysts described below have been isolated and characterized by standard 1-D $^1H/^{19}F$ NMR and analytical techniques (see Experimental Section for details). Scheme 1 illustrates the general synthetic route by which cocatalyst reagents **6** - **10** and **14** are obtained. Of these, six have been further characterized by single-crystal X-ray diffraction. Comparison of the structures of cocatalysts **4**, **7**, and **11** - **14** (Table 2) reveals, not surprisingly, that: a) the M–X bond distances increase with increasing summed ionic radii: $B-F < Ga-(\mu-F) < Al-Cl < Al-Br$; b) the M–C_{aryl} bond distances increase with increasing metalloid covalent radius: as $B-C_{aryl} < Al-C_{aryl} \sim Ga-C_{aryl}$; c) the unassociated Ph_3C^+ cations are virtually identical in all cocatalyst crystal structures. The breadth of available species and combined ^{19}F NMR, solid-state structural, and reactivity data present a unique opportunity for an in-depth comparative analysis of these metalloid-halogen interactions.

II. Activation of Metallocene $\text{Me}_2\text{C}(\text{Cp})(\text{Flu})\text{ZrMe}_2$ (**15**) with Cocatalysts **6 – 14**. General

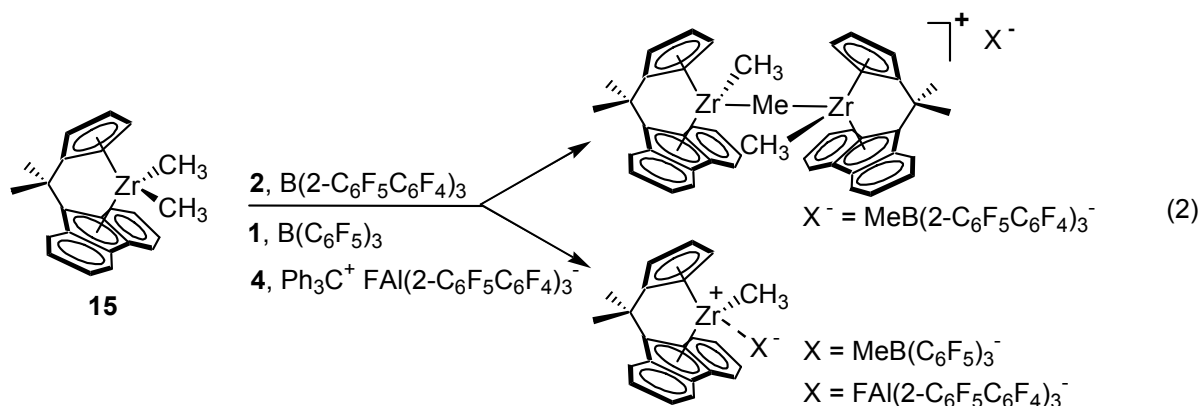
Considerations.

Activation of typical group 4 metallocene dimethyls with methide-abstrating cocatalyst reagents is observed to generate highly reactive metallocenium perfluoroarylmethyl complexes that typically exist as contact ion-pairs in nonpolar media, even at catalytic ($<10^{-4}$ M) concentrations.^{10, 11} Complex mixtures and decomposition products are often observed as well, especially with highly active polymerization catalyst systems studied in the absence of olefin.

Study of activation reactions using a broad array of preactylst and cocatalyst species has led to the identification of a number of different modes of cation-anion interaction. These observations, coupled with profound observed anion-dependent effects on the relative rates of various enchainment, misinsertion, reorganization, and termination processes, have led to an emergent picture in which the mode and strength of ion pairing plays a significant role in determining polymerization activity and stereoselectivity.

Metallocene-derived cations have been observed in both mononuclear or dinuclear configurations (e.g., having single μ -methyl linkages between metal centers, see Eq. 2).¹ In some cases, either product or a mixture of both is possible — as with cocatalyst $\text{Ph}_3\text{C}^+\text{B}(\text{C}_6\text{F}_5)_4^-$ — depending on the reaction conditions, stoichiometry, metallocene ancillary ligation, solvent, etc.²² Both mononuclear and dinuclear monocations have been reported in the reactions of **15** with various cocatalyst reagents. The anion may also be mono- or polynuclear, and can interact with the cation either via specific interatomic contacts, or in the absence of any dominant low-energy interatomic contact. For example, the cocatalyst reagents $\text{B}(\text{C}_6\text{F}_5)_3$ (**1**) and $\text{Ph}_3\text{C}^+\text{FAl}(\text{o-C}_6\text{F}_5\text{C}_6\text{F}_4)_3^-$ (**4**) afford contact ion-pairs having a mononuclear zirconocenium cation with the anion occupying a vacancy in the Zr coordination sphere and interacting with the cationic Zr

center via a μ -methyl or μ -fluoro linkage,¹² while the sterically encumbered mononuclear cocatalyst $B(o\text{-C}_6\text{F}_5\text{C}_6\text{F}_4)_3$ (**2**) yields a contact ion-pair having a dinuclear bridged monocation with the μ -methyl group completing the coordination spheres of both Zr centers, and a nonspecific cation-anion contact (Eq. 2).^{9a} The exact fates of such alkyl-bridged dinuclear species during olefin polymerization processes remains unclear.²³



The persistence of particular modes of cation-anion interaction during polymerization reactions remains an area of intensive study. Interestingly, the cation-anion interaction can be quite kinetically inert and still mediate polymerization: whereas in complex **16** the cation-anion interaction is observed to be rather labile, in mononuclear $Me_2C(Cp)(Flu)ZrMe^+ FAI(o\text{-C}_6\text{F}_5\text{C}_6\text{F}_4)_3^-$ (generated from **15** + **4**), the $FAI(o\text{-C}_6\text{F}_5\text{C}_6\text{F}_4)_3^-$ anionic fragment coordinates to the metal center via an exceptionally robust Zr-F-Al linkage, strongly attenuating or shutting down solution-phase unimolecular catalyst epimerization as observed in isolation, while still permitting propylene enchainment under polymerization conditions.¹²

²³ Direct NMR observation of mononuclear and dinuclear catalyst polymeryl species suggests that the concentration of μ -methyl bridged dinuclear species can diminish in the presence of olefin, and that such species may constitute resting states under certain conditions, see Tritto, I.; Donetti, R.; Sacchi, M. C.; Locatelli, P.; Zannoni, G. *Macromolecules* **1999**, 32(2), 264-269.

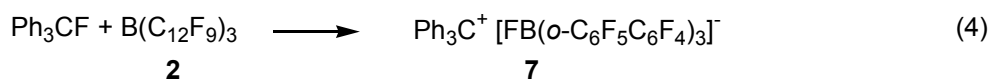
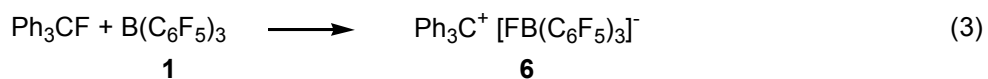
Halide linkages of this type have also been observed in the reaction of AlR_3 reagents with metallocene halides.²⁴ The possibility of accessing new variants of this bonding motif, and entirely new ion-pair structures, has motivated synthesis/development of new cocatalysts **6 - 14** and the study of their reactions with archetypal $\text{Me}_2\text{C}(\text{Cp})(\text{Flu})\text{ZrMe}_2$ (**15**).

Beyond differences in spectroscopic and structural characteristics, the present B-, Al-, and Ga-based systems can be differentiated by their activation chemistry. Cocatalysts **6 - 14** all react with metallocene **15**, in some cases generating highly active olefin polymerization catalyst ion-pairs; polymerization results are presented in a companion report.¹⁷ As monitored by *in-situ* NMR spectroscopy, reaction via trityl cation abstraction of one metallocene methide ligand is rapid in all cases and appears to proceed to completion, based on observed evolution of 1.0 stoichiometric equivalent triphenylethane. Many of the resultant mixtures are complicated, with multiple products observed; spectroscopically identified products are shown in Scheme 2. Exhaustive attempts were made to isolate single-crystal samples from each of these reaction mixtures, and three new ion-pair complexes and two decomposition products have been characterized by single-crystal X-ray diffraction.

²⁴ (a) Activation of $(\text{Cp}^*\text{TiOF})_4$ with AlMe_3 affords $(\text{Cp}^*\text{TiO})_4(\text{FAlMe}_3)_4$. Yu, P. H.; Roesky, H. W.; Demsar, A.; Albers, T.; Schmidt, H. G.; Noltemeyer, M. *Angew. Chem., Int. Ed. Engl.* **1997**, *36*, 1766-1767. (b) Activation with $\text{Al}(\text{CH}_2\text{Ph})_3$ $(\text{Cp}^*\text{TiO})_4(\text{F})_3[\text{FAl}(\text{CH}_2\text{Ph})_3]$. Yu, P.; Pape, T.; Usón, I.; Said, M. A.; Roesky, H.W.; Montero, M.L.; Schmidt, H. -G.; Demsar, A. . *Inorg. Chem.*,**1998**, *37*, 5117-5124. (c) Reaction of Cp_2TiF_2 with AlEt_3 gives $[\text{Cp}_2\text{Ti}(\mu_2\text{-F})_2\text{AlEt}_2]_2$; Yu, P.; Montero, M. L.; Barnes, C. E.; Roesky, H. W.; Usón, I. *Inorg. Chem.*,**1998**, *37*, 2595-2597. (d) For reaction of Cp_2ZrMe_2 with $[(\text{Me}_3\text{Si})_3\text{CALF}_2]_3$ and Me_3SnF , see Hatop, H.; Roesky, H. W.; Labahn, T.; Fischer, A.; Schmidt, H. G.; Noltemeyer, M. *Organometallics* **2000**, *19*, 937-940.

III. Trityl Perfluoroaryl Fluoroborates $\text{Ph}_3\text{C}^+ \text{FB}(\text{C}_6\text{F}_5)_3^-$ (6**) and $\text{Ph}_3\text{C}^+ \text{FB}(o\text{-C}_6\text{F}_5\text{C}_6\text{F}_4)_3^-$ (**7**).**

The reaction of trityl fluoride¹⁸ with $\text{B}(\text{C}_6\text{F}_5)_3$ (**1**) and $\text{B}(o\text{-C}_6\text{F}_5\text{C}_6\text{F}_4)_3$ (**2**)^{5a} yields the corresponding trityl fluorometallate salts, trityl tris(perfluorophenyl)fluoroborate (**6**; 68%; eq. 3)²⁵ and trityl tris(2,2',2''-nonafluorobiphenyl)fluoroborate (**7**; 63%; eq. 4). Bridged B–F–B species are not observed. In addition to sharp fluoroaryl signals, the ¹⁹F NMR spectra of both



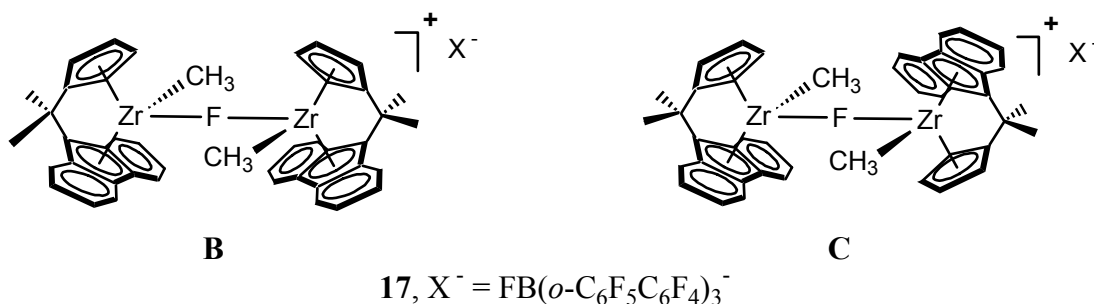
fluoroborates exhibit characteristic broad, upfield B–F resonances at δ -186.99 (**6**) and -185.00 ppm (**7**). Integration of these resonances versus the fluoroaryl resonances is consistent with the molecular structures proposed for **6** and **7**.

The crystal structure of complex **7** has also been confirmed by X-ray diffraction and features an unassociated trityl cation and a sterically congested chiral, essentially C_3 -symmetric borate anion, as shown in Fig. 1. Selected bond distances and angles are summarized in Table 3. The anion in **7** adopts a pseudotetrahedral geometry and the B–F distance (1.437(6) Å) and average B–C_{aryl} distances (1.654(6) Å) are not unexpectedly shorter than the corresponding Al–F (1.682(5) Å) and Al–C_{aryl} (2.018 (9) Å) distances in homologous Al cocatalyst **4**.^{9a} The Al–F and B–F bond distances are within 3% of the summed Shannon ionic radii but considerably smaller than the summed covalent radii, whereas the B–C_{aryl} and Al–C_{aryl} distances closely match the

²⁵ The similar fluoroborate $\text{Li}^+ \text{FB}(\text{C}_6\text{F}_5)_3^-$ has been claimed previously. See, Klemann, L. P.; Newman, G. H.; Stogryn, E. L. *U.S. Pat.* 4139681, **1979**.

corresponding summed covalent radii.²⁶ As with **4**, the biphenyl groups of **7** encapsulate the metalloid-bound fluorine atom, and the fluoroaryl rings in the biphenyl groups are substantially twisted out of coplanarity (-84.7° (average); *vide infra* for a discussion of perfluorobiphenyl configuration effects).

The activation reactions of metallocene Me₂C(Cp)(Flu)ZrMe₂ (**15**) with cocatalysts **6** and **7** are rapid, with B–F bond cleavage observed in both cases: **6** + **15** affords Me₂C(Cp)(Flu)ZrMe⁺ MeB(C₆F₅)₃⁻ (**16**, also produced via reaction of **15** with **1**) in 30% yield,²⁷ implying formation of an insoluble zirconocene fluoride side-product (putatively, [Me₂C(Cp)(Flu)ZrMeF]_n, see Eq. 5). No ¹⁹F signal consistent with a B–F or Zr–F environment is observed. For cocatalyst reagent Ph₃C⁺ FB(*o*-C₆F₅C₆F₄)₃⁻ (**7**), dinuclear [Me₂C(Cp)(Flu)ZrMe]₂(μ-F)⁺ FB(*o*-C₆F₅C₆F₄)₃⁻ diastereomers (**17**) form in a 2:1 ratio by NMR (**B** and **C**, depicted below). The sequence outlined in eq. 6 below suggests possible pathways for

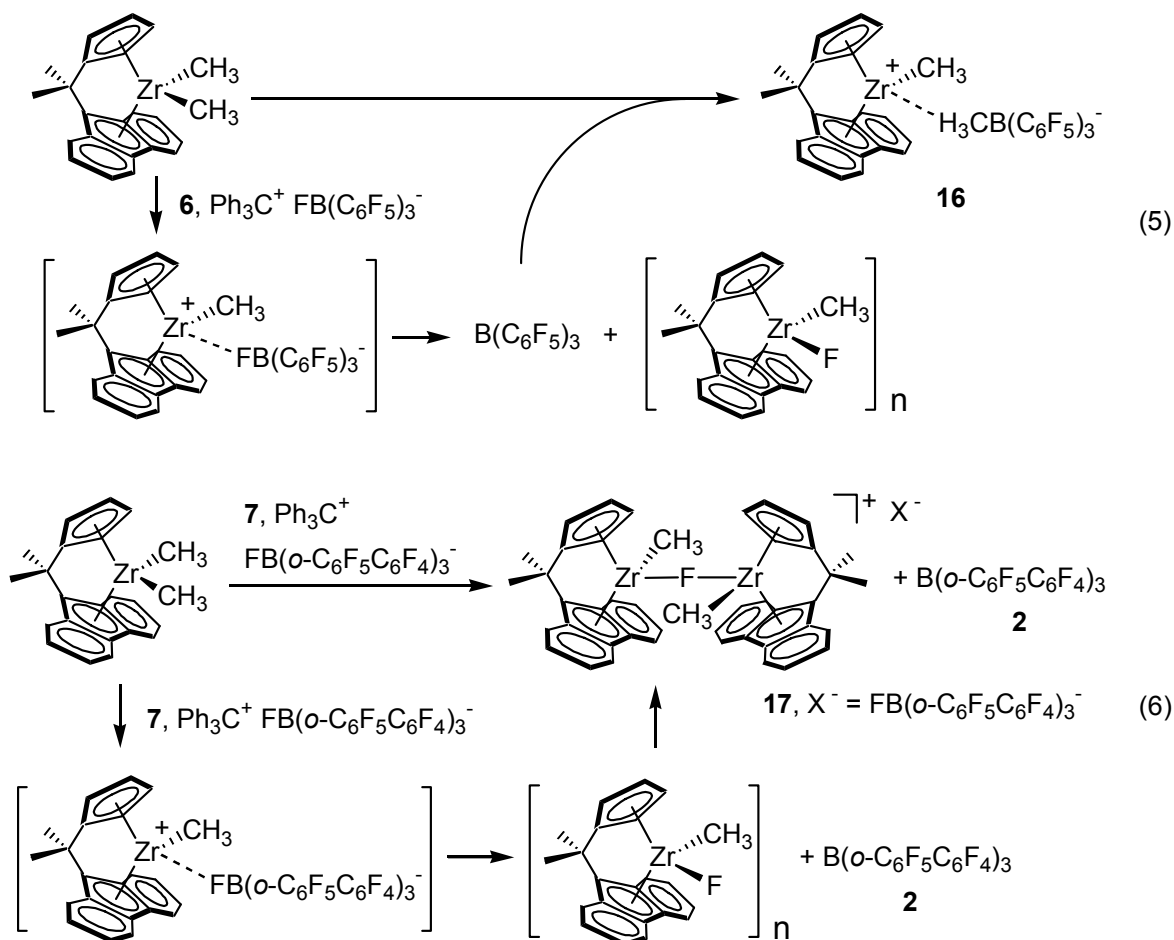


the formation of **17**. In the ¹⁹F NMR, nine distinct fluoroaryl ¹⁹F signals are observed, indicating

²⁶ For ionic radii, see: (a) Shannon, R. D. *Acta Cryst.* **1976**, *A32*, 751-767. For covalent radii, see: (b) Huheey, J. E.; Keiter, E. A.; Keiter R. L. in *Inorganic Chemistry: Principles of Structure and Reactivity*, 4th edition, HarperCollins, New York, USA, **1993**.

²⁷ The other product is an unidentified precipitate which exhibits very broad peaks in the ¹H NMR (CD₂Cl₂), and structural identification is ambiguous. However, examples of Zr-F formation in catalyst deactivation processes have been observed previously. See refs 1c, 9a, and 24.

restricted internal fluoroaryl ring rotation. The Zr–F–Zr and F–B ^{19}F signals of ion-pair **17** appear as broad singlets at δ -77.97 and -184.47 ppm respectively, the latter being similar to the F–B signal in **7** (δ -185.00 ppm). These signals exhibit a 1:1 integral ratio, and a 1:3 ratio versus the sum of fluoroaryl signal integrals, consistent with the proposed solution structures for diastereomers **17**.¹⁶ The zirconocene dimethyl and cocatalyst trityl salt are combined in a 1:1 ratio to generate **17**; free $\text{B}(\text{o-C}_6\text{F}_5\text{C}_6\text{F}_4)_3$ is also observed in ~50% yield in the crude reaction mixture, again indicating a B–F bond cleavage event (eq. 6) and suggesting a source for the bridging fluoride in the cationic fragments of **17**. Added cocatalyst **7** beyond 1.0 equivalent remains unreacted at room temperature.



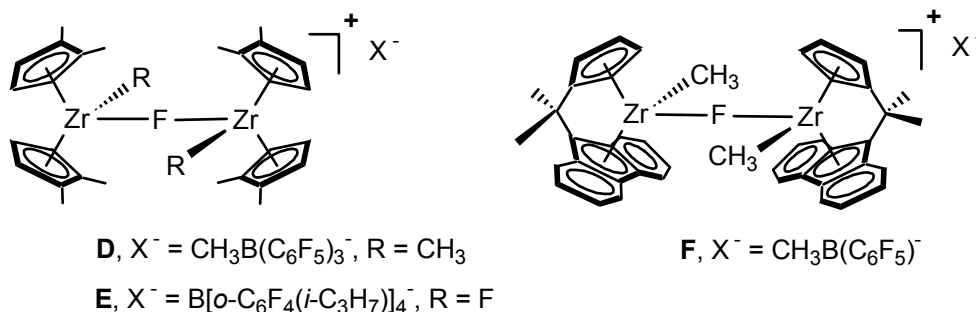
The crystal structure of complex **17** has been confirmed by X-ray diffraction and features an unassociated, F-bridged dinuclear Zr–F–Zr cation and a sterically congested pseudotetrahedral fluoroborate anion (Fig. 6). Selected bond distances and angles are summarized in Table 4. The overall structure of the anion in **17** is quite similar to that of trityl salt **7**: in particular, the B–F distances for **7** and **17** are quite close (1.424(5) Å and 1.437(6) Å, respectively), and the averaged B–C_{aryl} distances are indistinguishable (1.661(5) vs. 1.654(6) Å). The perfluorobiphenyl substituents again encapsulate the F atom (*vide infra*, and see Table 8 for a detailed comparison of observed perfluorobiphenyl ligand arrangements). The marked similarity in ¹⁹F spectra for **7** and **17** suggest that these similarities persist in solution, i.e. that the cation-anion interaction is not mediated by a Zr–F–B linkage (a profound Zr-induced ¹⁹F chemical shift effect is seen in the analogous zirconium fluoroaluminates having Zr–F–Al linkages, *vide infra*).

The observed B–F bond cleavage chemistry, along with an absence of any structural or NMR evidence for Zr–F–B or B–F–B species suggests that: a) such a bridging structure may be unstable in the present context²⁸ and that b) the Zr–F–Zr linkage is stronger than a possible Zr–F–B linkage — the neutral Me₂C(Cp)(Flu)ZrMeF moiety can be viewed as outcompeting the anion for coordination to the Me₂C(Cp)(Flu)ZrMe⁺ moiety in this case. In contrast, F–Al bond

²⁸ B–F–B linkages are seen in three solid-state structures containing a F[BF₃]₂⁻ anion: a) Watanabe, M.; Sato, M.; Nagasawa, A.; Kai, M.; Motoyama, I.; Takayama, T. *Bull. Chem. Soc. Jpn.*, **1999**, 72, 715. b) Akiba, K.; Yamashita, M.; Yamamoto, Y.; Nagase, S. *J. Am. Chem. Soc.*, **1999**, 121, 10644. c) Braunstein, P.; Douce, L.; Fischer, J.; Craig, N.C.; Goetz-Grandmont, G.; Matt, D. *Inorg. Chim. Acta*, **1992**, 194, 151. A neutral, structurally asymmetric (fluoro)borabicyclononane dimer with one tetrahedral B and one planar B atom has also been reported: Koster, R.; Schussler, W.; Boese, R. *Chem. Ber.*, **1990**, 123, 1945.

cleavage is not observed in the reaction of **15** with fluoroaluminate reagent **4**, the perfluorobiphenyl ligands rearranging to accommodate a Zr–F–Al linkage.^{12a}

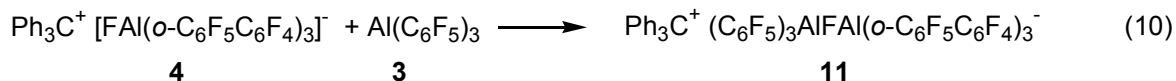
Diffraction data for **17** are of sufficient quality to unambiguously identify the bridging moiety as μ -F rather than μ -CH₃ in this structure, with bond lengths consistent with the suggested atom assignment. The cation in **17** has a bent Zr–F–Zr configuration with the F atom equidistant from both Zr atoms (see Table 4). Three similar fluoride-bridged dinuclear Zr–F–Zr cationic structures, [(Cp''₂ZrMe)₂(μ -F)]⁺ MeB(C₆F₅)₃⁻ (**D**),^{4a} [(Cp''₂ZrF)₂(μ -F)]⁺ B[*o*-C₆F₄(*i*-C₃H₇)]₄⁻ (**E**),^{7b} and [Me₂C(Cp)(Flu)Zr(C₆F₅)₂(μ -F)]⁺ MeB(C₆F₅)₃⁻ (**F**)^{9a} have been



previously reported, all obtained as decomposition products from metallocene-borane ion-pairs. Table 5 compares relevant bond distances and angles for these four Zr–F–Zr cations. Among these, complex **17** presents the shortest Zr–(μ -F) bond distance (2.099(4) Å, average) and the most acute Zr–(μ -F)–Zr bond angle (155.57(13)^o), thus having the shortest Zr⋯Zr distance (4.103 Å).

IV. A. Trityl Perfluoroaryl Fluoroaluminates (Ph_3C^+)_x F_x[Al(C₆F₅)₃]_y^{x-} (x = 1, y = 1, **8; x = 1, y = 2, **9**; x = 2, y = 3, **10**) and Ph_3C^+ (C₆F₅)₃AlFAl(o-C₆F₅C₆F₄)₃⁻ (**11**).**

Natta *et al.* have shown that the bimetallic, fluorine-bridged F[AlEt₃]₂⁻ anion can be generated as a potassium salt using a 1:2 ratio of KF and AlEt₃.²⁹ Combining trityl fluoride and Al(C₆F₅)₃ (**3**) gives similar results: depending on the reagent molar ratio, any of three trityl tris(perfluorophenyl) fluoroaluminates (Ph_3C^+)_x F_x[Al(C₆F₅)₃]_y^{x-} (x = 1, y = 1, **8**; x = 1, y = 2, **9**; x = 2, y = 3, **10**) can be isolated in good yield (Eqs. 7-10). Fluoroaluminate **10** was characterized by single-crystal X-ray diffractometry (Fig. 2; see below).



The ¹⁹F NMR spectra of complexes **8** - **10** exhibit broad singlets at δ -168.61, -167.30, and -166.49, respectively. Compared to the F–Al signal of Ph₃C⁺ FAl(C₆F₅)₃⁻ (**8**), the Al–F–Al resonance of dinuclear Ph₃C⁺ F[Al(C₆F₅)₃]₂⁻ (**9**) is shifted slightly downfield by the additional F-coordinated Al(C₆F₅)₃ moiety. In this case, it appears that any diamagnetic shielding of the bridging F nucleus due to heightened steric congestion in **9** is outweighed by the electron-withdrawing effect of the added, strongly Lewis-acidic fragment. Similarly, the Al(F–Al)₂ signal in trinuclear **10** appears slightly downfield of the Al–F–Al resonance dinuclear **9**.

²⁹ For the first structural study of a fluoro-bridged organoaluminum complex, K⁺ F[AlEt₃]₂⁻, with F–Al = 1.80(6) Å, see: Natta, G.; Allegra, G.; Perego, G.; Zambelli, A. J. Am. Chem. Soc. 1961, 83, 5033 – 5033.

Perfluorophenyl ^{19}F chemical shift differences between **8** and **9** are small ($\Delta\delta = +0.14$, $+1.77$, and $+0.38$ ppm for *o*-, *m*-, and *p*-F atoms, respectively). The perfluorophenyl ^{19}F NMR signals for **10** are also quite similar to those of **8** and **9**. Notably, the terminal and bridging $\text{Al}(\text{C}_6\text{F}_5)_3$ ^{19}F resonances are all within ± 0.09 and ± 0.94 ppm of corresponding values for **9**, respectively.

The solid state structure of complex **10** features two unassociated trityl cations and a sterically congested pseudo- C_3 -symmetric trinuclear anion where the three Al centers are connected by two $\mu\text{-F}$ atoms in a nearly linear Al–F–Al–F–Al configuration (Fig. 2; selected bond distances and angles are summarized in Table 6).³⁰ The average F–Al_{terminal} distance (1.738(3) Å) is noticeably shorter than the average F–Al_{internal} distance (1.965(2) Å), and the bridging Al atom has a trigonal bipyramidal coordination geometry, whereas the terminal Al atoms exhibit a distorted tetrahedral coordination geometries. The Al–C_{aryl} distances for bridging and terminal Al atoms in **10** are indistinguishable (1.999(4) Å and 2.003(4) Å, respectively) and comparable to Al–C_{aryl} distances in cocatalysts **4** and **11** - **14** (see Table 2 for detailed comparison of the seven cocatalysts). The three sets of fluoroaryl rings are substantially eclipsed, and in each set the fluoroaryl moieties are twisted out of the equatorial plane (Fig. 2A), suggesting strong π - π or steric interactions among the three sets of fluoroaryl rings (Fig. 2B).

The previously isolated monometallic trityl salt $\text{Ph}_3\text{C}^+ \text{FAl}(\textit{o}\text{-C}_6\text{F}_5\text{C}_6\text{F}_4)_3^-$ (**4**)^{9a} undergoes reaction with $\text{Al}(\text{C}_6\text{F}_5)_3$ to afford the fluoro-bridged mixed aluminate $\text{Ph}_3\text{C}^+ (\text{C}_6\text{F}_5)_3\text{AlFAl}(\textit{o}\text{-C}_6\text{F}_5\text{C}_6\text{F}_4)_3^-$; **11**, eq. 7). Neutral $\text{Al}(\textit{o}\text{-C}_6\text{F}_5\text{C}_6\text{F}_4)_3$ and thus the symmetrically bridged $\text{Ph}_3\text{C}^+ \text{F}[\text{Al}(\textit{o}\text{-C}_6\text{F}_5\text{C}_6\text{F}_4)_3]_2^-$ are synthetically inaccessible by the present methods.

³⁰ A similar M–F–M–F–M arrangement has been observed in a Bi system. For a recent review of such metal fluorides, see: Roesky, H. W.; Haiduc, I. *J. Chem. Soc., Dalton Trans.*, **1999**, 2249-2264.

Fluoroaluminate **11** was also characterized by single-crystal X-ray diffractometry (Fig. 3; see below).

The effect of $\text{Al}(\text{C}_6\text{F}_5)_3$ coordination to the $\text{FAl}(o\text{-C}_6\text{F}_5\text{C}_6\text{F}_4)_3^-$ anion in trityl salt **4** is quite significant compared to that of $\text{Al}(\text{C}_6\text{F}_5)_3$ coordination to the $\text{FAl}(\text{C}_6\text{F}_5)_3^-$ anion in trityl salt **8**, according to the ^{19}F NMR data: the chemical shift difference between the Al-bound F atoms of mononuclear **4** (δ -175.02 ppm)³¹ and asymmetric dinuclear adduct $\text{Ph}_3\text{C}^+(\text{C}_6\text{F}_5)_3\text{AlFAl}(o\text{-C}_6\text{F}_5\text{C}_6\text{F}_4)_3^-$ (**11**; δ -169.38, $\Delta\delta = +5.64$ ppm) is very large by comparison to the difference between Al–F and Al–F–Al shifts in **8** and **9** ($\Delta\delta = +1.31$ ppm). The Al–F chemical shift in mononuclear **4** is displaced dramatically upfield of that in mononuclear perfluorophenyl analog **8**, whereas the Al–F–Al resonance of asymmetric $\text{Ph}_3\text{C}^+(\text{C}_6\text{F}_5)_3\text{AlFAl}(o\text{-C}_6\text{F}_5\text{C}_6\text{F}_4)_3^-$ (**11**) is shifted only slightly upfield of the symmetric dinuclear analog **9**. Furthermore, the perfluorobiphenyl ^{19}F shifts change drastically upon reaction of $\text{Al}(\text{C}_6\text{F}_5)_3$ with **4** (c.f. $\Delta\delta = +5.34$ ppm for the Al-vicinal F atom). Signals for the two *o*-F atoms of the C_6F_5 fragment of the perfluorobiphenyl ligand are magnetically equivalent in **4** but inequivalent in **11**, the same being true of the *m*-F resonances, indicating that rotation about the medial $\text{C}_{\text{Ph}}\text{--C}_{\text{Ph}}$ bond is facile in **4**, but restricted in **11**. The perfluorophenyl ^{19}F NMR signals of **11** are quite similar to those of both **8** and **9**.

The Al-bound perfluorobiphenyl ligands can assume two quite different conformations, according to the crystallographic evidence from **4**^{9b} and **11** (Fig. 4; selected bond distances and

³¹ See Ref. 9b, Supporting Information preparation and characterization of **4**. Previously unreported ^{19}F NMR chemical shift data for **4** in C_7D_8 at 23°C is as follows: δ -120.72 (s, 3 F, F-3), -139.52 (s, 3 F, F-6), -141.48 (s, 6 F, F-2'/F-6'), -156.55 (t, 3 F, F-4), -157.22 (s, 3 F, F-4'), -158.46 (t, 3 F, F-5), -165.20 (s, 6 F, F-3'/F-5'), -175.02 (s, br, 1 F, Al–F).

angles are summarized in Table 7): in **4**, the the biphenyl ligands are oriented along the Al–F axis and sterically encapsulate the Al-bound F atom, whereas in **11** the biphenyl ligands are oriented away from the Al-bound F atom, assuming a mutual stacking arrangement that exposes the Al-bound F atom and imparts a corkscrew motif to the anionic fragment, with each Al-bound C₆F₄ ring lying in close proximity to, and parallel with, the C₆F₅ ring of one adjacent *o*-perfluorobiphenyl ligand. This motif is also seen in the solid-state structure of the ion-pair complex Me₂C(Cp)(Flu)ZrMe⁺ FAl(*o*-C₆F₅C₆F₄)₃⁻ (obtained from reaction of **4** with **15**), in this case featuring a Zr–F–Al linkage.¹² The observed profound effect of the added Al(C₆F₅)₃ unit upon the ¹⁹F chemical shift values of both the Al-bound F atom and perfluorophenyl ligands of **4** may derive from a solution-phase rearrangement process that converts the sterically encapsulated, terminal Al–F configuration observed in **4** to the exposed, bridging Al–F–Al configuration observed in **11** (see Table 8 for a detailed comparison of the six anions containing *o*-C₆F₅C₆F₄ substituents). The nearly linear Al–F–Al core (\angle Al–F–Al = 176.91(16)^o) present in the structure of **11** is much like those of previously reported F[AlMe₃]₂⁻^{32a} and F[AlEt₃]₂⁻.^{32b} However, whereas the alkyl moieties in these latter two anion structures occupy a staggered conformation,³² the two sets of Al-bound fluoroaryl rings in **11** are substantially eclipsed as in the case of **10** above, suggesting a pronounced π - π or steric interaction between the two sets of fluoroaryl rings. The two F–Al bonds in **11** differ slightly in length (F–Al(C₆F₅)₃ = 1.770(3) Å and F–Al(*o*-C₆F₅C₆F₄)₃ = 1.797(3) Å), but are similar to the F–Al bond distances in F[AlMe₃]₂⁻

³² The Al–F–Al bond angle in both complexes is ~180°. (a) For R = Me; G. Allegra, G.; Perego, G. *Acta Crystallogr.* **1963**, *16*, 185. (b) For R= Et; J.L. Atwood, J. L.; Newberry III, W.R. *J. Organomet. Chem.* **1974**, *66*, 15.

(1.783 Å)^{32a} while shorter than in F[AlEt₃]₂⁻ (1.835 Å), likely due to alkyl-alkyl repulsions in the latter.^{32b}

In the reactions of metallocene dimethyl **15** with cocatalysts **8** - **10**, each instance affords Me₂C(Cp)(Flu)ZrMe⁺ FAl(C₆F₅)₃⁻ (**18**) together with varying amounts of diastereomeric [Me₂C(Cp)(Flu)ZrMe]₂(μ-Me)⁺ F[Al(C₆F₅)₃]₂⁻ (**19**; see Scheme 2). These systems do not undergo rapid equilibration: mixtures of **18** and **19** slowly decompose to pure **18**, suggesting either: a) conversion of **19** to **18** together with slow formation and subsequent comparatively rapid decomposition of Me₂C(Cp)(Flu)ZrMe⁺ MeAl(C₆F₅)₃⁻, or b) direct decomposition of **19** to form some insoluble product. Mononuclear **18** is robust with respect to decomposition. Despite the complexity of these reactions, it is found that the catalytically-active species generated via reaction *in situ* are effective agents for highly syndiospecific propylene polymerization.¹⁷ In the reaction of **15** with Ph₃C⁺ FAl(C₆F₅)₃⁻ (**8**), ion-pair complexes **18** and **19** are initially formed in a ~1:1 ratio (as assayed from *in-situ* NMR experiments), implying a Zr-mediated Al-F bond cleavage reaction: mononuclear trityl salt **8** is isolable in pure form, suggesting that the Al-F cleavage process likely involves reaction of Me₂C(Cp)(Flu)ZrMe⁺ FAl(C₆F₅)₃⁻ (**18**) with FAl(C₆F₅)₃⁻ salts **8** or **18** to generate an ion-pair complex containing the dinuclear F[Al(C₆F₅)₃]₂⁻ anion, together with unidentified insoluble fluoromethylzirconium species. When metallocene **15** is combined with cocatalyst Ph₃C⁺ F[Al(C₆F₅)₃]₂⁻ (**9**), metallocenium complexes **18** and **19** are initially formed in a 1:2 ratio, demonstrating that the dinuclear F[Al(C₆F₅)₃]₂⁻ anion can indeed undergo conversion to the mononuclear FAl(C₆F₅)₃⁻ anion in **18**. Trinuclear cocatalyst (Ph₃C⁺)₂ F₂[Al(C₆F₅)₃]₃⁻ (**10**) reacts with **15** to form **18** and **19** in a 2:3 ratio, suggesting that **10** behaves much like a 1:1 mixture of **8** and **9** in the activation of metallocene **15**. In the reaction of **15** with cocatalyst **11** we observe by NMR the exclusive formation of μ-methyl bridged

$[\text{Me}_2\text{C}(\text{Cp})(\text{Flu})\text{ZrMe}]_2(\mu\text{-Me})^+ (\text{C}_6\text{F}_5)_3\text{AlFAl}(o\text{-C}_6\text{F}_5\text{C}_6\text{F}_4)_3^-$ (**20**; as diastereomers in a 3:2 ratio) with no detectable mononuclear species (Scheme 2).³³ The $\text{Al}(o\text{-C}_6\text{F}_5\text{C}_6\text{F}_4)_3$ moiety, insoluble by itself, confers added stability with no observed formation of complex **18** or $\text{Me}_2\text{C}(\text{Cp})(\text{Flu})\text{ZrMe}^+ \text{FAl}(o\text{-C}_6\text{F}_5\text{C}_6\text{F}_4)_3^-$.

The Al-F-Al ^{19}F chemical shifts in complexes **19** and **20** are much like those of the corresponding cocatalysts, whereas coordination to Zr induces a considerable downfield shift in the Zr-F-Al signal of **18** compared with that in cocatalyst **8** (δ -168.61 vs -140.33 ppm). There is an interesting correlation between increasing Al-F ^{19}F chemical shift and increasing average Al-F bond distance that obtains regardless of F atom coordination number (1 or 2) or anion nuclearity (1, 2, or 3 Al atoms), across the series **4**, **10**, **11**, **19**, and **20**. This trend does not extend to systems having a Zr-F contact.

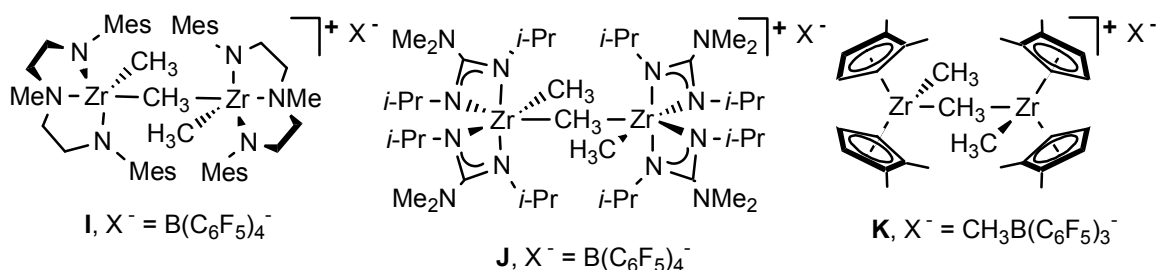
The crystal structures of metallocenium complexes **19** and **20** each feature a μ -methyl-bridged dinuclear Zr-Me-Zr cation and an unassociated, sterically congested F-bridged dinuclear aluminate anion (Figs. 7 and 8, respectively). Selected bond distances and angles are summarized in Tables 9 and 10, respectively. The $(\text{C}_6\text{F}_5)_3\text{AlFAl}(o\text{-C}_6\text{F}_5\text{C}_6\text{F}_4)_3^-$ anions in **11** and **20** are metrically similar, with some interesting differences: in **11**, the bridging F atom is nearer the $\text{Al}(\text{C}_6\text{F}_5)_3$ group (1.770(3) Å vs 1.797(3) Å) whereas in **20**, it is equidistant from the Al centers (1.786(7) Å vs 1.785(7) Å). In **11**, **19**, and **20**, the Al coordination tetrahedra are distorted toward $\text{Al}(\text{fluoroaryl})_3$ planarity. Interestingly, the $\text{Al}(\text{C}_6\text{F}_5)_3$ moiety of **20** is more planarized than that of **11** (average $\angle\text{F-Al-C} = 101.7(5)^\circ$ vs $104.01(16)^\circ$), and the $(\text{C}_6\text{F}_5)_3\text{Al-F}$ bond is

³³ Pure orange complex **20** can be isolated, however thermal decomposition in the solid state slowly occurs at room temperature.

correspondingly longer (1.786(7) in **20** vs 1.770(3) Å in **11**). We suggest that these differences are largely due to packing forces, and in any case they indicate a certain degree of conformational flexibility about the Al atoms in these structures, with Al(fluoroaryl)₃ flattening correlated with a lengthening of the Al–F bond. Similar to the F-bridged polynuclear aluminate cocatalysts **10** and **11**, the sets of Al-bound fluoroaryl rings **19** and **20** are substantially eclipsed.

As in the perfluorobiphenyl groups of cocatalyst **11** and ion-pair complex $\text{Me}_2\text{C}(\text{Cp})(\text{Flu})\text{ZrMe}^+ \text{FAl}(\text{o-C}_6\text{F}_5\text{C}_6\text{F}_4)_3^-$, the perfluorobiphenyl groups of the anion in complex **20** stack together in a corkscrew structure that exposes the bridging F atom. In contrast, the anionic components of cocatalyst $\text{Ph}_3\text{C}^+ \text{FB}(\text{o-C}_6\text{F}_5\text{C}_6\text{F}_4)_3^-$ (**7**) and ion-pair complex $[\text{Me}_2\text{C}(\text{Cp})(\text{Flu})\text{ZrMe}]_2(\mu\text{-F})^+ \text{FB}(\text{o-C}_6\text{F}_5\text{C}_6\text{F}_4)_3^-$ (**17**) feature B-bound F atoms in terminal, encapsulated configurations in both cases and do not exhibit this corkscrew conformational motif. Also, whereas the structure of $\text{Me}_2\text{C}(\text{Cp})(\text{Flu})\text{ZrMe}^+ (\mu\text{-Me})\text{B}(\text{C}_6\text{F}_5)_3^-$ exhibits a B–C–Zr linkage, previously reported ion-pair complex $[\text{Me}_2\text{C}(\text{Cp})(\text{Flu})\text{ZrMe}]_2(\mu\text{-Me})^+ \text{MeB}(\text{o-C}_6\text{F}_5\text{C}_6\text{F}_4)_3^-$ does not,¹² and only the dinuclear Zr– μ -Me–Zr cation is obtained upon reaction of $\text{Me}_2\text{C}(\text{Cp})(\text{Flu})\text{ZrMe}_2$ with $\text{B}(\text{o-C}_6\text{F}_5\text{C}_6\text{F}_4)_3$ in toluene-*d*₈ solution. These data appear to suggest that the cost in degrees of conformational freedom of forming a rigid, corkscrew-packed perfluorobiphenylborate anion outweighs the benefits of forming a B–C–Zr linkage. It is possible that the B-based systems cannot achieve the corkscrew packing at all, possibly due to the smaller covalent radius of boron and comparative closeness of the C_{aryl}–B contacts. In comparing torsion angles among the collected perfluorobiphenyl Al and B anions (C_a–C_b–C_c–C_d or F–M–C_a–C_b; see Table 8), it can be seen that the nonbridging, encapsulated forms **G** (see Fig. 7) exhibit relatively wide variations in conformation, whereas forms **H** (see Fig. 7) are remarkably similar, suggesting that this corkscrew motif is uniquely stable.

The cationic fragments of metallocenium structures **19** and **20** also exhibit some degree of conformational flexibility: For complex **19**, the μ -methyl bridged dinuclear cation has a crystallographically enforced linear Zr–Me–Zr configuration ($\angle \text{Zr1–Me–Zr2} = 180^\circ$) and the two zirconocene fragments are essentially identical. For complex **20**, the Me-bridged dinuclear cation has a markedly bent Zr–Me–Zr configuration ($\angle \text{Zr1–Me–Zr2} = 161.1(6)^\circ$) with the two zirconocene fragments having rather different coordination environments (e.g., $\text{Zr1}-(\mu\text{-Me}) = 2.443(12) \text{ \AA}$, $\text{Zr2}-(\mu\text{-Me}) = 2.393(12) \text{ \AA}$, $\text{Zr1–Me}_{(\text{terminal})} = 2.278(13) \text{ \AA}$, $\text{Zr2–Me}_{(\text{terminal})} = 2.228(13) \text{ \AA}$ (see Table 10). Three other methyl-bridged dinuclear Zr–Me–Zr cation structures, $[(\text{N}_3)_2\text{ZrMe}]_2(\mu\text{-Me})^+ \text{B}(\text{C}_6\text{F}_5)_4^-$ (**I**; $\text{N}_3 = \text{MesN}(\text{CH}_2\text{CH}_2)_2\text{NMe}$),³⁴ $\{[(\text{guan})_2\text{ZrMe}]_2(\mu\text{-Me})\}^+ \text{B}(\text{C}_6\text{F}_5)_4^-$ (**J**),³⁵ and $[(\text{Cp}''_2\text{ZrMe})_2(\mu\text{-Me})]^+ \text{MeB}(o\text{-C}_6\text{F}_4\text{C}_6\text{F}_5)_3^-$ (**K**)^{9a} have been reported, and relevant bond distances and angles are presented in Table 11.



³⁴ Mes = mesityl; see Schrock, R. R.; Casado, A. L.; Goodman, J. T.; Liang, L. -C.; Bonitatebus, Jr. P. J.; Davis, W. M. *Organometallics* **2000**, *19*, 5325-5341.

³⁵ Guan = $\eta^2\text{-}(\text{i-PrN})_2\text{C}(\text{NMe}_2)$, see Duncan, A. P.; Mullins, S. M.; Arnold, J.; Bergman, R. G. *Organometallics* **2001**, *20*, 1808-1819.

IV. B. Trityl Perfluoroaryl Haloaluminates $\text{Ph}_3\text{C}^+ \text{XAl}(\text{C}_6\text{F}_5)_3^-$ (X = Cl, **12**; X = Br, **13**).

The reaction of trityl chloride or trityl bromide with **3** in 1:1 ratio yields trityl tris(perfluorophenyl) chloro- or bromoaluminates ($\text{Ph}_3\text{C}^+ \text{XAl}(\text{C}_6\text{F}_5)_3^-$, X = Cl, 78% yield, **12**; X = Br, yield **13**; eq. 9), evidenced by the appearance of three new fluoroaryl resonances in the ^{19}F NMR spectra of these reaction mixtures. Both complexes were further characterized by X-ray diffractometry (Fig. 8) and are, to the authors' knowledge, the first reported triarylchloro-³⁶ and triarylbromoaluminate³⁷ complexes. Selected bond distances and angles are summarized in Table 12. Both structures feature a noncoordinating trityl cation and pseudotetrahedral perfluoroarylmethylate anion. The Al–Cl bond distance in **12** (2.1676(7) Å) is shorter than that in $\text{PPN}^+ \text{ClAl}(t\text{-Bu})_3^-$ (2.251(3) Å).^{36a} Similarly, the present Al–Br distance (2.332(2) Å) is considerably shorter than in the first reported BrAlR_3^- anion (2.439(3) Å, R = 1-adamantyl, $\text{C}_{10}\text{H}_{15}$).³⁷

³⁶ The structure of $\text{PPN}^+ \text{ClAlR}_3^-$ has been characterized (PPN = bis(triphenylphosphine)nitrogen). See, for example: (a) R = *t*-butyl, see Harlan, C. J.; Bott, S. G.; Barron, A. R. *J. Am. Chem. Soc.* **1995**, *117*, 6465-6474. (b) R = *t*-amyl (CMe_2Et), see Harlan, C. J.; Gillan, E. G.; Bott, S. G.; Barron, A. R. *Organometallics* **1996**, *15*, 5479-5488. (c) The structure of chloro-bridged dinuclear aluminate $\text{K}^+ \text{Cl}[\text{AlMe}_3]_2^-$ has also been characterized crystallographically, see Atwood, J. L.; Rodgers, R. D.; Hrnčir, D. C.; Zaworotko, M. J.; Hunter, W. E. *Acta Crystallogr., Sect. A: Cryst. Phys., Diffr., Theor. Crystallogr.* **1981**, C83. (d) structure of chloroalane ($\mu_2\text{-Cl}$)₂[Al(C₆F₅)₂]₂ generated via reaction of Al(C₆F₅)₃ with CH₂Cl₂ has also been reported, see Chakraborty, D.; Chen, E. Y.-X. *Inorg. Chem. Commun.* **2002**, *9*, 698-701.

³⁷ $\text{Mg}_3\text{BrCl}_3(\text{OEt})(\text{Et}_2\text{O})_6^+$ is the counteranion, see: Vohs, J. K.; Downs, L. E.; Barfield, M. E.; Latibeaudiere, K. L.; Robinson, G. H. *J. Organomet. Chem.* **2003**, *666*, 7-13.

In reaction of metallocene **15** with chloroaluminate **12** or bromoaluminate **13**, formation of a mononuclear ion-pair is expected (examples of $M^+ ClAlR_3^-$ ³⁸ and $M^+ BrAlR_3^-$ ³⁹ species are well known). However, in each of these three reactions, rapid methide abstraction is observed by *in-situ* NMR along with the formation of complex mixtures, precluding further unambiguous characterization of the products. Attempts to isolate individual species as single crystals from these mixtures yielded decomposition products $Me_2C(Cp)(Flu)ZrCl(C_6F_5)$ (**21**; Fig. 9; from **15** + **12**) and $[Me_2C(Cp)(Flu)Zr(\mu_2-Br)]_2^{2+} [Al(C_6F_5)_4]_2^-$ (**22**; Fig. 10; from **15** + **13**), which were characterized by X-ray diffractometry. Selected bond distances and angles are summarized in Tables 13 (for **21**) and 14 (for **22**). Formation of these decomposition products suggests that the Br–Al and Cl–Al interactions are considerably less robust than analogous Al–F linkages.

V. Trityl Perfluoroaryl Fluorogallate $Ph_3C^+ F[Ga(C_6F_5)_3]_2^-$ (**14**).

Trityl fluorobis[tris(perfluorophenyl)gallate] ($Ph_3C^+ F[Ga(C_6F_5)_3]_2^-$; **14**) is derived from a "one-pot" reaction of trityl fluoride with $Ga(C_6F_5)_3$ (**5**), in turn generated *in situ* via alkyl-aryl

³⁸ (a) For [Ti]-ClAlMe₃, see Coles, M.P.; Hitchcock, P. B. *J. Chem. Soc. Dalton. Trans.* **2001**, 1169-1171. and (b) Kelly, D. G.; Toner, A.J.; Walker, N. M.; Coles, S. J.; Hursthouse, M. B. *Polyhedron*, **1996**, *15*, 4307-4310. (c) For [Zr]-ClAl(*t*-Bu)₃, see ref. 36a. (d) for [Ta]-ClAlMe₃ see: Churchill, M. R.; Wasserman, H. J.; Turner, H. W.; Schrock, R. R. *J. Am. Chem. Soc.* **1982**, *104*, 1710-1716. (e) For ([Cr]-Me-[Cr])⁺ ClAlMe₃⁻, see Wei, P.; Stephan, D. W. *Organometallics* **2003**, *22*, 1712-1717. (f) For [Cr]-ClAlMe₃, see Sugiyama, H.; Aharonian, G.; Gambarotta, S.; Yap, G. P. A.; Budzelaar, P. H. M. *J. Am. Chem. Soc.* **2002**, *124*, 12268-12274.

³⁹ For the only characterized structure, [Ti]-BrAlMe₃, see Coles, S.J.; Hursthouse, M. B.; Kelly, D. G.; Walker, N. M. *J. Organomet. Chem.* **1999**, *580*, 304.

metathesis of $\text{B}(\text{C}_6\text{F}_5)_3$ with $\text{Ga}(\text{CH}_3)_3$ (eq. 8).⁴⁰ Several products are observed in this reaction; however, pure **14** can be isolated in good yield (67%) by fractional crystallization. In addition to three fluoroaryl ^{19}F signals, the ^{19}F NMR spectrum of **14** exhibits a characteristic broad upfield resonance at δ -210.11 ppm, indicative of Ga-F bond formation. Furthermore, the 12:6:12:1 integral ratio of these resonances reveals that one F atom is bound to two Ga moieties. The structure of **14** was confirmed by X-ray diffraction as the first linear fluoro-bridged organogallium complex,⁴¹ as shown in Fig. 11. Selected bond distances and angles are summarized in Table 15. Similar to **10**, the two Ga centers are connected by one F atom with a nearly linear Ga-F-Ga configuration ($173.37(12)^\circ$). This bridged Ga-F bond distance (1.907(11) Å, average) is longer (0.069 Å) than the terminal Ga-F bond distances in both $\text{GaF}(\text{Bz})_2(\text{Bu}^t\text{NH}_2)$ ^{41c} and $\text{GaF}(\text{Mes})_2(\text{Bu}^t\text{NH}_2)$ ^{41d} (1.828 Å and 1.838 Å, respectively). The six fluoroaryl rings attached to the two Ga centers are substantially eclipsed as in **11**, again reflecting possible π - π stacking or steric interactions between sets of fluoroaryl rings.

In the reaction of metallocene **15** with dinuclear, fluoro-bridged dinuclear gallate **14**, a pair of diastereomeric μ -methyl complexes similar to **19** or **20** would be expected, *a priori*. However, in this reaction as well, rapid methide abstraction is observed by NMR along with the formation of multiple unidentifiable, insoluble species.

⁴⁰ (a) Klosin, J.; Roof, G. R.; Chen, E. Y.-X.; Abboud, K. A. *Organometallics* **2000**, *19*, 4684-4684. (b) Hair, G. S.; Cowley, A. H.; Gorden, J. D.; Jones, J. N.; Jones R. A.; Macdonald, C. L. B. *Chem. Commun.*, **2003**, *3*, 424-425.

⁴¹ For recent examples of organogallium-F complexes, see: (a) Werner, B.; Kräuter, T.; Neumüller, B. *Organometallics* **1996**, *15*, 3746-3751. (b) See ref. 30a for examples of nonlinear fluoro-bridged Ga complexes. (c) Kopp, M. R.; Neumüller, B. *Z. Anorg. Allg. Chem.* **1999**, *625*, 1413. (d) Kräuter, T.; Neumüller, B. *Z. Anorg. Allg. Chem.* **1995**, *621*, 597-606.

CONCLUSIONS

The evolution of metallocene-catalyzed olefin polymerization chemistry has led to development of a wide array of group 4 metallocene dihalides and dialkyls — structure-function relationships based on differences among these metallocenes are generally well-understood, aided in part by the development of molecular activators allowing correlations between active catalyst system structural and electronic properties and polymerization performance. Recent advances in understanding the relationship between ion pairing dynamics and polymerization properties has underscored the significance of the cocatalyst/activator and the resulting anionic fragment in determining polymerization activity, active catalyst thermal stability, as well as product polymer molecular weight and microstructure. The possibility that cocatalyst research can lead to improvements not only in catalyst system performance but also in our mechanistic understanding of polymerization processes provides impetus for the directed expansion of the library of viable activator species.

With findings on the synthesis, chemical properties, and remarkable polymerization behavior of first-generation perfluoroaryl fluoroaluminate cocatalyst **7** as a starting point, a broad new family of mono- and polynuclear trityl salts featuring one or more group 13–halide linkages has been developed,¹⁶ and is expanded and discussed in the present contribution, with detailed syntheses and characterization, and with X-ray crystallographic analysis in most cases. Beyond development of new cocatalyst species, this work constitutes a complete survey of the chemical behavior of species **1** - **5** as synthons, leading to a general understanding of the interaction between trityl halides and very strong Lewis-acid perfluoroarylmetailloid species of the class represented by $B(C_6F_5)_3$. Trityl salts **6** - **14** constitute a new class of synthetically accessible cocatalysts for single-site olefin polymerization. Their behavior as activators for the archetypal

C_s -symmetric zirconocene dialkyl **15** has been explored in detail and demonstrates efficient and rapid activation by these new cocatalysts, again with structural analysis of products in most cases. In a companion report,¹⁷ we present a detailed mechanistic study of polymerization behavior with these new cocatalysts with respect to both C_s -symmetric precatalyst **15** and C_1 -symmetric precatalyst $\text{Me}_2\text{Si}(\text{CpR}^*)(\text{octahydrofluorenyl})\text{ZrMe}_2$ ($\text{R}^* = (1R,2S,5R)\text{-trans-5-methyl-cis-2-(2-propyl)cyclohexyl}$; (-)-menthyl). In certain noteworthy cases, we observe *both* enhancements in stereoselectivity *and* in polymerization activity, in contrast to the selectivity-reactivity pattern that has generally been observed thus far in catalytic metallocene olefin polymerization systems.^{1,2} These findings represent a significant advancement in overall catalyst system performance derived from cocatalyst development.

Acknowledgements. Financial support by DOE (DE-FG02-86ER1351) is gratefully acknowledged. M.-C. C. thanks Dow Chemical for a postdoctoral fellowship, Dr. M. Oishi for helpful discussions, and Dr. P. Nickias of Dow for GPC measurements. C. Z. thanks the Italian CNR for a postdoctoral fellowship, and A. M. S. thanks the University of Jordan for a sabbatical leave.

Supporting Information Available. Complete X-ray experimental details and tables of bond lengths, angles, and positional parameters for the above eleven crystal structures are available via the ACS website, <http://pubs.acs.org>, document number om0508334.

Figure 1. Perspective ORTEP drawing of the molecular structure of cocatalyst reagent

$\text{Ph}_3\text{C}^+ \text{FB}(\text{o-C}_6\text{F}_5\text{C}_6\text{F}_4)_3^-$ (**7**). Thermal ellipsoids are drawn at the 30% probability level.

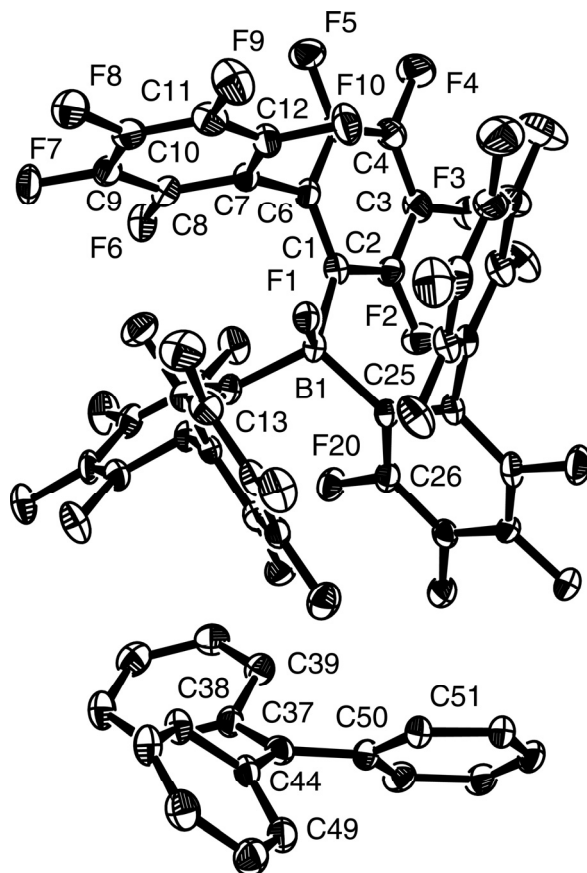


Figure 2. Perspective ORTEP drawings of the molecular structure of dinuclear Zr-(μ -F)-Zr complex $[\text{Me}_2\text{C}(\text{Cp})(\text{Flu})\text{ZrMe}]_2(\mu\text{-F})^+ \text{FB}(\text{o-C}_6\text{F}_5\text{C}_6\text{F}_4)_3^-$ (**17**). Thermal ellipsoids are drawn at the 30% probability level.

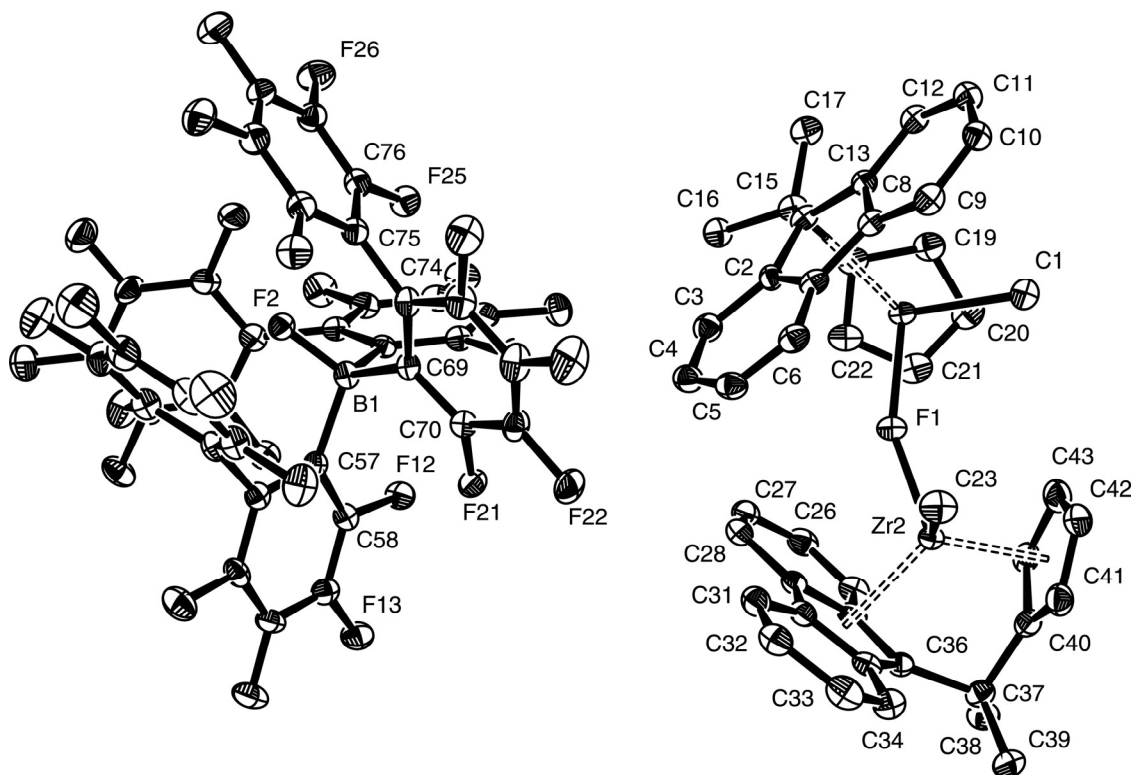


Figure 3. Perspective ORTEP drawings of the molecular structure of cocatalyst reagent $(\text{Ph}_3\text{C}^+)_2\text{F}_2[\text{Al}(\text{C}_6\text{F}_5)_3]_3^{2-}$ (**10**) viewed perpendicular the (noncrystallographic) Al–F–Al–F–Al axis (A), and viewed along this axis (B). Thermal ellipsoids are drawn at the 30% probability level.

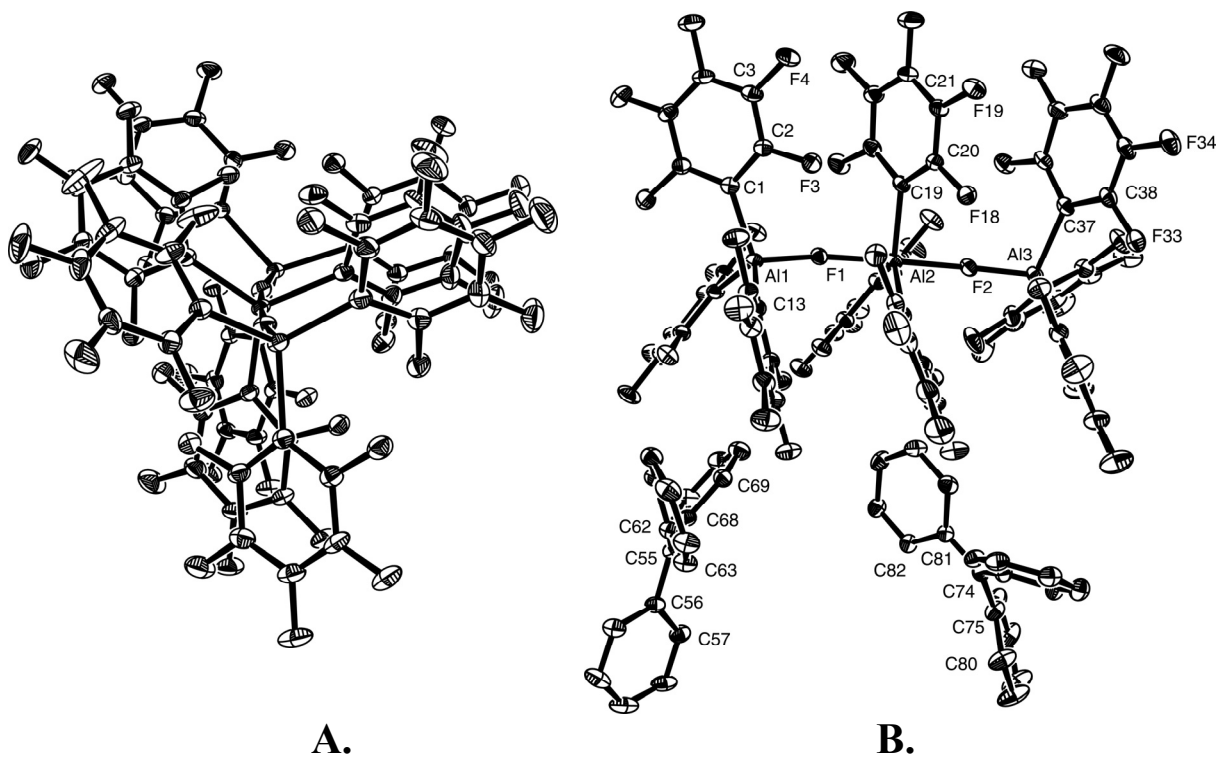


Figure 4. Perspective ORTEP drawings of the molecular structure of cocatalyst reagent $\text{Ph}_3\text{C}^+ (\text{C}_6\text{F}_5)_3\text{AlFAl}(\text{o-C}_6\text{F}_5\text{C}_6\text{F}_4)_3^-$ (**11**) viewed abroad the Al–F–Al axis (A), and showing mutual π - π or steric stacking among the *o*- $\text{C}_6\text{F}_5\text{C}_6\text{F}_4$ groups (B). Thermal ellipsoids are drawn at the 30% probability level.

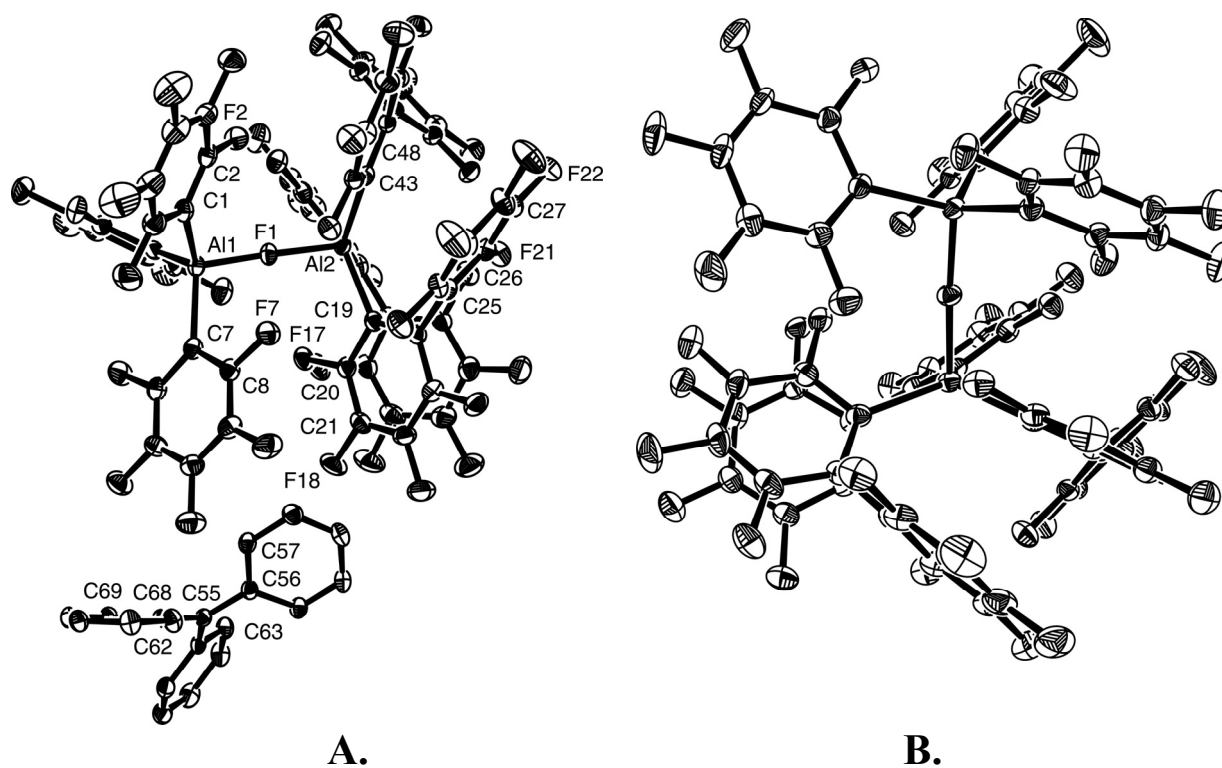


Figure 5. Perspective ORTEP drawings of the molecular structure of dinuclear Zr-(μ -Me)-Zr complex $[\text{Me}_2\text{C}(\text{Cp})(\text{Flu})\text{ZrMe}]_2(\mu\text{-Me})^+ (\text{C}_6\text{F}_5)_3\text{AlFAl}(\text{C}_6\text{F}_5)_3^-$ (**19**). Thermal ellipsoids are drawn at the 30% probability level.

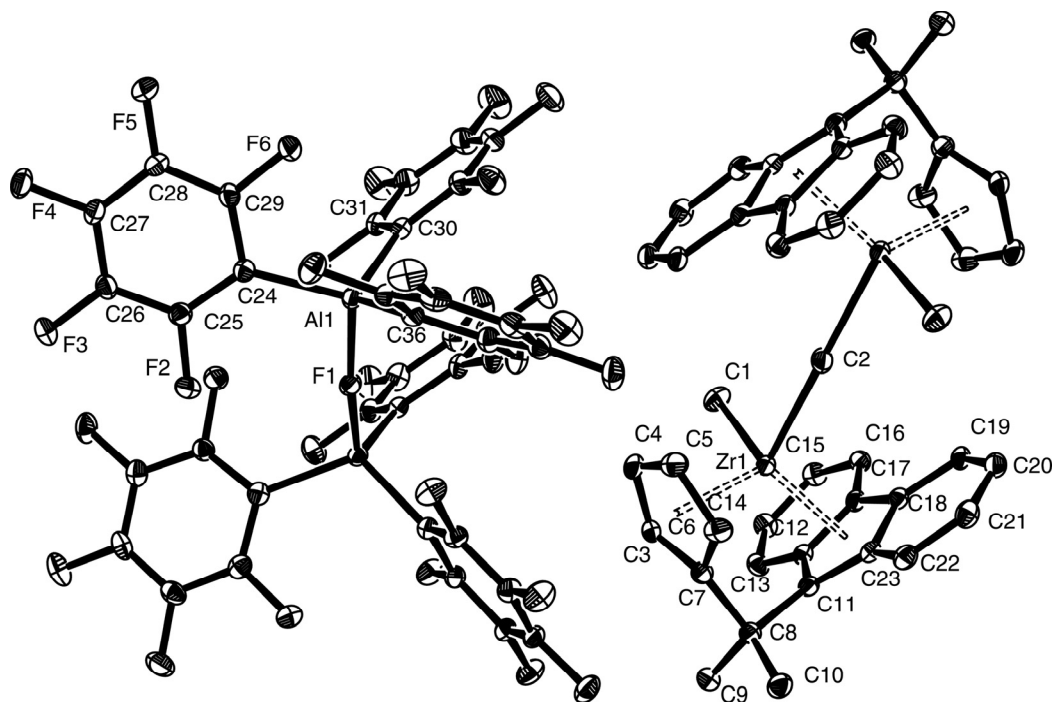


Figure 6. Perspective ORTEP drawings of the molecular structure of dinuclear Zr-(μ -Me)-Zr complex $[\text{Me}_2\text{C}(\text{Cp})(\text{Flu})\text{ZrMe}]_2(\mu\text{-Me})^+$ $(\text{C}_6\text{F}_5)_3\text{AlFAl}(o\text{-C}_6\text{F}_5\text{C}_6\text{F}_4)_3^-$ (**20**; A), and of the anion in **20** (B). Thermal ellipsoids are drawn at the 30% probability level.

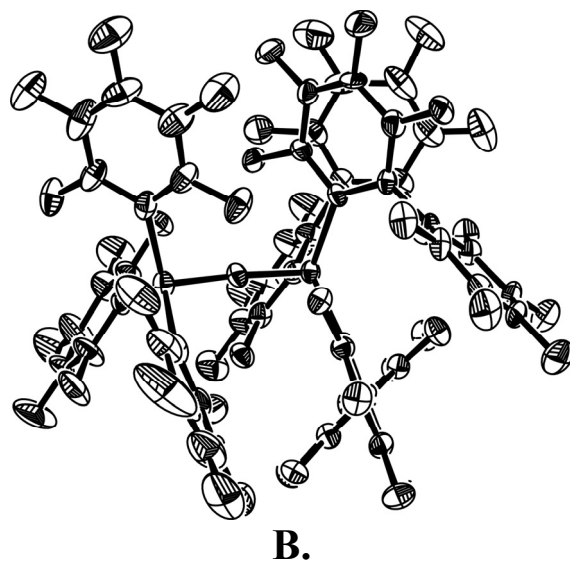
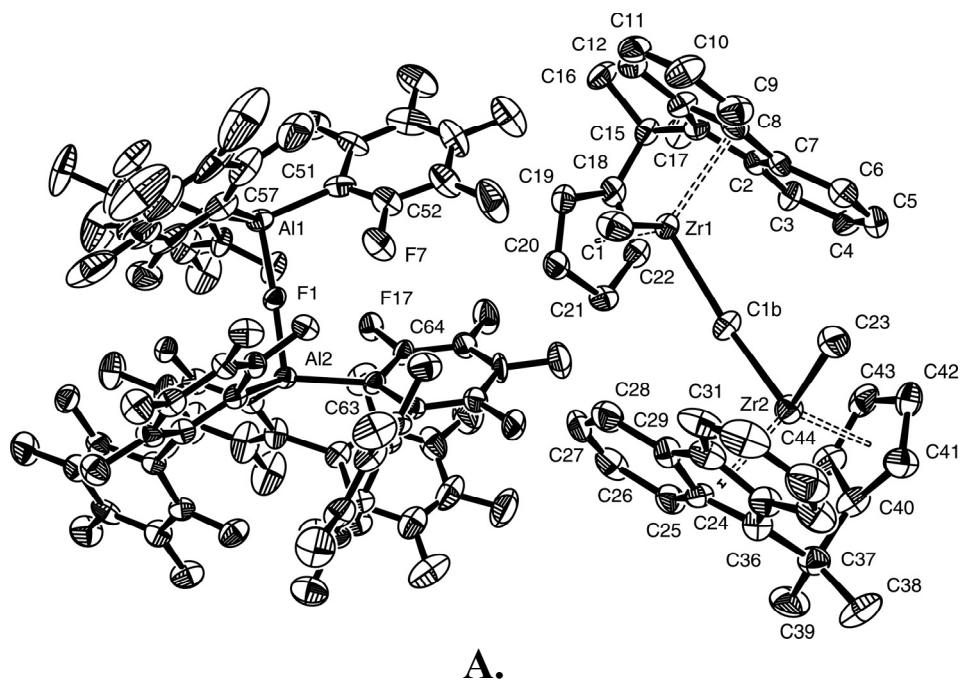


Figure 7. Perspective drawings of free (**G**) and associated (**H**) (tris)perfluorobiphenyl fluorometallate ligands.

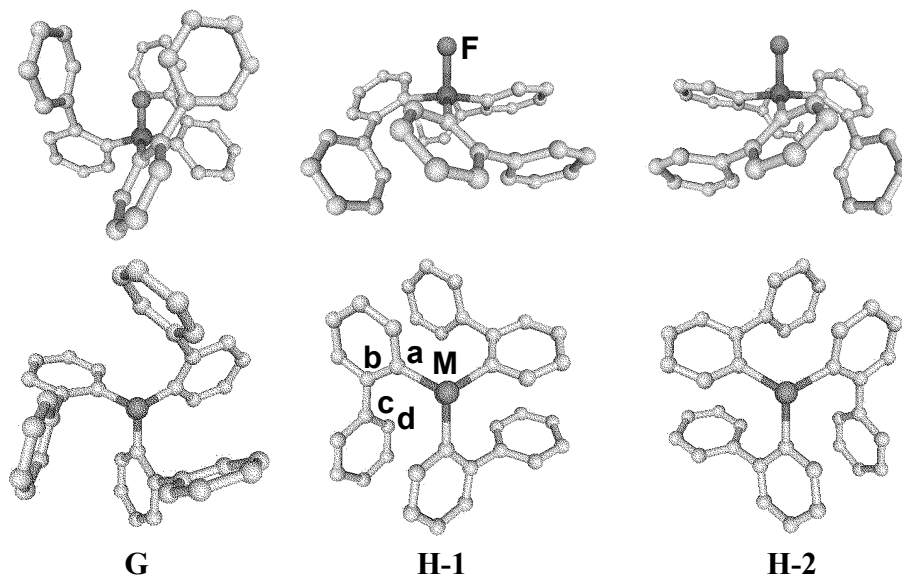


Figure 8. Perspective ORTEP drawings of the molecular structures of cocatalyst reagents $\text{Ph}_3\text{C}^+ \text{ClAl}(\text{C}_6\text{F}_5)_3^-$ (**12**; A) and $\text{Ph}_3\text{C}^+ \text{BrAl}(\text{C}_6\text{F}_5)_3^-$ (**13**; B). Thermal ellipsoids are drawn at the 30% probability level.

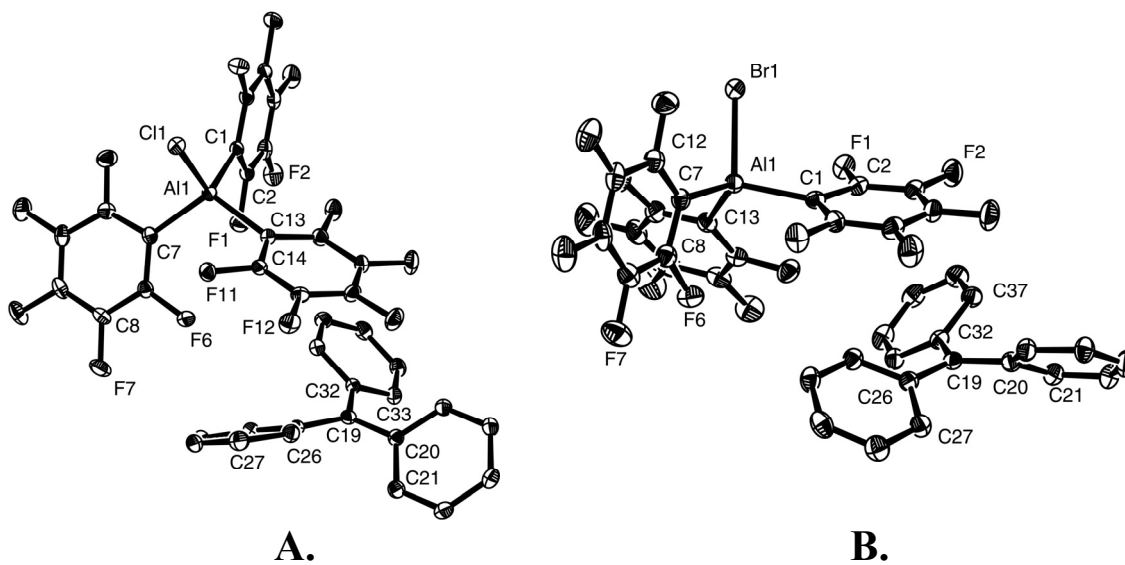


Figure 9. Perspective ORTEP drawings of the molecular structure of $\text{Me}_2\text{C}(\text{Cp})(\text{Flu})\text{ZrCl}(\text{C}_6\text{F}_5)$ (**21**). Thermal ellipsoids are drawn at the 50% probability level.

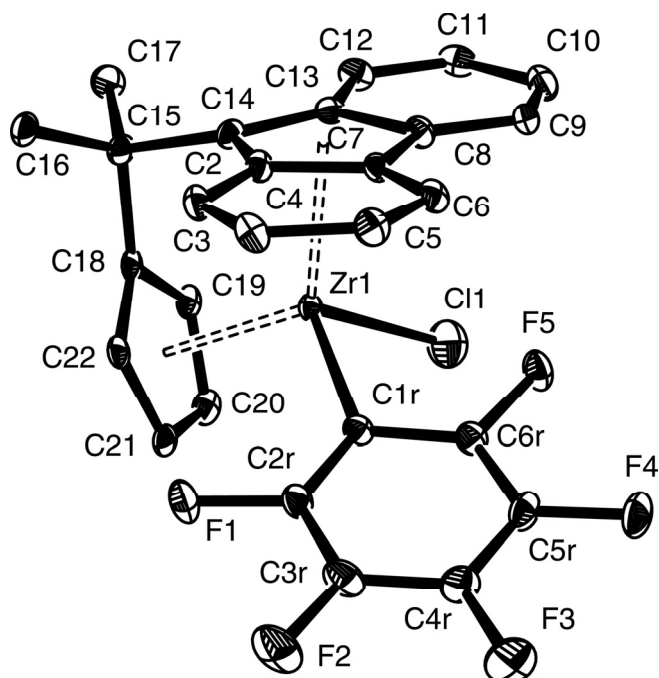


Figure 10. Perspective ORTEP drawings of the molecular structure of the $[\text{Me}_2\text{C}(\text{Cp})(\text{Flu})\text{Zr}(\mu_2\text{-Br})_2]^{2+}$ dication in complex $[\text{Me}_2\text{C}(\text{Cp})(\text{Flu})\text{Zr}(\mu_2\text{-Br})_2]^{2+} [\text{Al}(\text{C}_6\text{F}_5)_4]^{-}_2$ (**22**; A), and the $\text{Al}(\text{C}_6\text{F}_5)_4^-$ monoanion (B). Thermal ellipsoids are drawn at the 30% probability level.

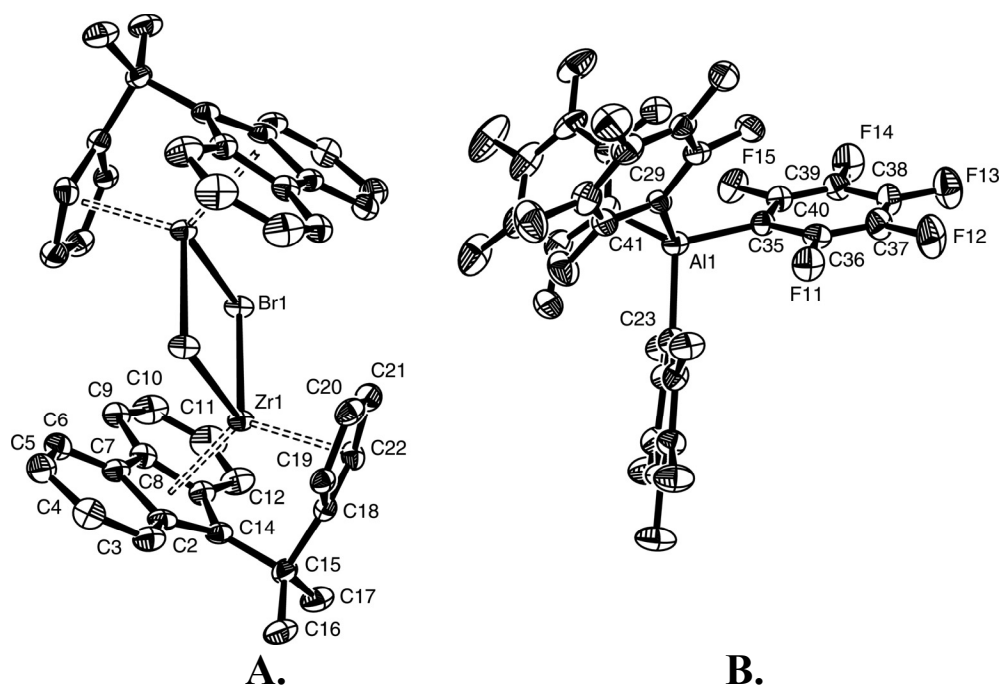


Figure 11. Perspective ORTEP drawing of the molecular structure of the cocatalyst reagent $\text{Ph}_3\text{C}^+\text{F}[\text{Ga}(\text{C}_6\text{F}_5)_3]_2^-$ (**14**). Thermal ellipsoids are drawn at the 30% probability level.

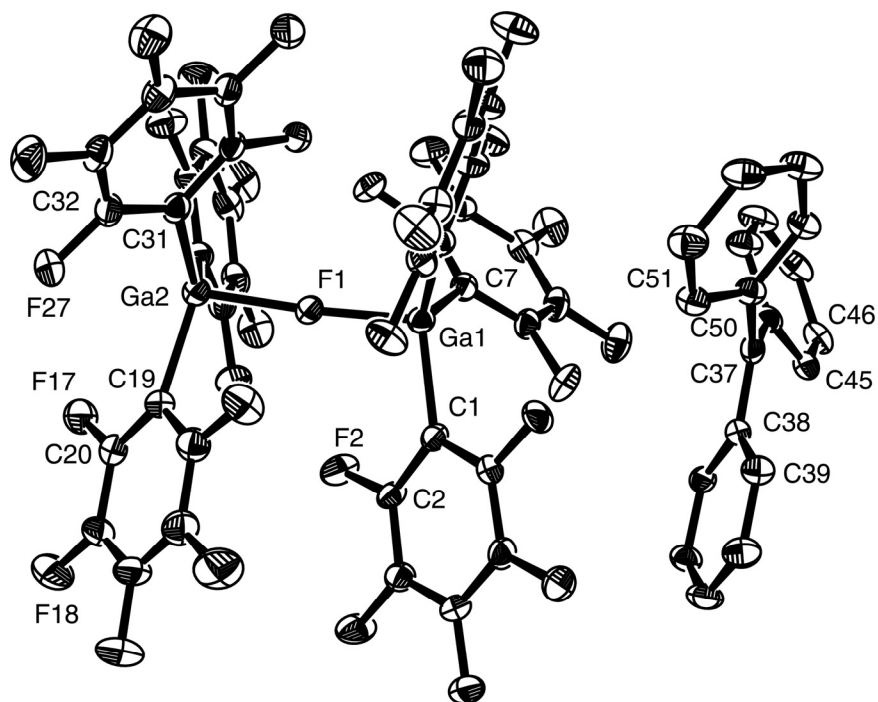


Table 1. Summary of Crystal Structure Data for Cocatalysts **7** and **10 – 14** and Complexes **17, 19,** and **20 – 22.**^a

complex	7	10	11	12	13	14
formula	C _{57.5} H ₁₈ BF ₂₈	C ₁₀₅ H ₃₀ Al ₃ F ₄₇	C _{83.5} H ₁₉ Al ₂ F ₄₃	C ₃₇ H ₁₅ AlClF ₁₅	C ₃₇ H ₁₅ AlBrF ₁₅	C ₅₅ H ₁₅ Ga ₂ F ₃₁
formula wt.	1251.53	2265.23	1892.95	806.92	851.38	1404.11
crystal color, habit	yellow, needle	orange, plate	yellow, plate	yellow, block	yellow, plate	yellow, needle
crystal dimensions (mm)	0.454 × 0.104 × 0.070	0.442 × 0.158 × 0.128	0.310 × 0.200 × 0.066	0.248 × 0.142 × 0.104	0.488 × 0.104 × 0.074	0.508 × 0.104 × 0.084
crystal system	Triclinic	Triclinic	Triclinic	Monoclinic	Monoclinic	Monoclinic
space group	P $\bar{1}$	P $\bar{1}$	P $\bar{1}$	P2 ₁ /c	P2 ₁ /c	P2 ₁ /c
A, Å	9.718(3)	12.6562(11)	13.3346(13)	12.3098(8)	12.510(9)	15.975(2)
B, Å	14.501(4)	13.2621(12)	14.3315(14)	7.8476(5)	7.896(5)	14.134(2)
C, Å	18.768(5)	30.7946(27)	21.134(2)	33.702(2)	33.79(2)	23.140(3)
α , deg	85.523(4)	85.8182(15)	90.371(2)	90	90	90
β , deg	82.419(4)	87.6169(16)	104.966(2)	97.732(10)	97.512(14)	101.368(2)
γ , deg	74.328(4)	76.1506(15)	94.913(2)	90	90	90
V, Å ³	2521.8(11)	5003.6(13)	3885.7(7)	3226.1(4)	3309(4)	5122.5(12)
Z	2	2	2	4	4	4
d(calc), g/cm ³	1.648	1.504	1.618	1.661	1.709	1.821
μ , mm ⁻¹	0.168	0.173	0.188	0.262	1.382	1.206
T _{min} - T _{max}	0.95072 - 0.98877	0.9377 - 0.9789	0.95208 - 0.98757	0.94486 - 0.97504	0.67736 - 0.90708	0.69567 - 0.90904
measd. reflns.	22657	46426	35713	28960	20514	45529
indep. reflns.	11546	23459	18073	7880	7855	12345
reflns.>2 σ (I)	4419	12242	8474	5488	4050	6283
R _{int}	0.1749	0.1399	0.1505	0.0688	0.1278	0.1278
R[F ² >2 σ (F ²)]	0.0678	0.0815	0.0750	0.0450	0.0484	0.0490
wR(F ²)	0.2292	0.2808	0.2660	0.1249	0.1402	0.1401
S	0.879	1.018	1.028	1.034	0.932	0.961
no. of params.	777	1433	1135	487	487	793

^a CCD area detector diffractometer; phi and omega scans; temperature for data collection, 153(2) K; Mo K α radiation; λ = 0.71073 Å. ^b Estimated from crystal diffraction data, with T_{min}/T_{max} calculated using SADABS

Table 1, Cont'd. Summary of Crystal Structure Data for Cocatalysts **7** and **10 – 14** and Complexes **17, 19,** and **20 – 22.**^a

complex	17	19	20	21	22
formula	C ₉₄ H ₅₈ BF ₂₉ Zr ₂	C _{43.25} H _{16.5} AlF _{15.5} Zr	C ₁₁₁ H ₅₀ Al ₂ F ₄₃ Zr ₂	C ₅₄ H ₃₆ Cl ₂ F ₁₀ Zr ₂	C _{48.5} H ₁₈ AlBrF ₂₀ Zr
formula wt.	1931.65	948.76	2436.91	1128.17	1178.74
crystal color, habit	red, block	red, plate	red, needle	red, needle	green/yel- low, plate
crystal dimensions (mm)	0.280 × 0.124 × 0.094	0.438 × 0.252 × 0.026	0.382 × 0.080 × 0.036	0.324 × 0.044 × 0.038	0.868 × 0.300 × 0.024
crystal system	Triclinic	Monoclinic	Triclinic	Monoclinic	Triclinic
space group	<i>P</i> $\bar{1}$	<i>C</i> 2/ <i>c</i>	<i>P</i> $\bar{1}$	<i>P</i> 2 ₁ / <i>c</i>	<i>P</i> $\bar{1}$
A, Å	16.0202(16)	11.9646(8)	12.947(2)	8.7197(15)	14.145(4)
B, Å	16.9357(17)	21.1165(14)	17.518(3)	15.908(3)	14.570(4)
C, Å	17.3241(17)	30.680(2)	23.134(4)	15.612(3)	15.542(4)
α , deg	112.792(2)	90	84.617(3)	90	111.423(5)
β , deg	106.482(2)	101.237(1)	79.768(3)	91.030(3)	100.320(5)
γ , deg	101.012(2)	90	84.966(3)	90	112.691(5)
V, Å ³	3907.0(7)	7602.8(9)	5127.1(17)	2165.3(6)	2552.9(13)
Z	2	8	2	4	2
d(calc), g/cm ³	1.642	1.671	1.579	1.73	1.533
μ , mm ⁻¹	0.387	0.422	0.348	0.689	1.12
T _{min} - T _{max}	0.89868 - 0.96938	0.727662 - 0.989 ^b	0.90579 - 0.98720	0.89011 - 0.97367	0.7043 - 0.9685
measd. reflns.	36465	35163	46991	19679	15514
indep. reflns.	18343	9362	23912	5285	11048
reflns.>2 σ (<i>I</i>)	10461	6755	5929	3021	5220
R _{int}	0.1045	0.0747	0.3386	0.1234	0.1687
R[F ² >2 σ (F ²)]	0.0507	0.0463	0.1069	0.0615	0.089
wR(F ²)	0.1476	0.136	0.2752	0.1814	0.3004
S	0.973	1.089	0.877	0.981	0.967
no. of params.	1143	582	1406	309	659

^a CCD area detector diffractometer; phi and omega scans; temperature for data collection, 153(2) K; Mo K α radiation; λ = 0.71073 Å. ^b Estimated from crystal diffraction data, with T_{min}/T_{max} calculated using SADABS

Table 2. Comparison of Selected Bond Distances (Å) for Cocatalysts $\text{Ph}_3\text{C}^+ \text{FAl}(o\text{-C}_6\text{F}_5\text{C}_6\text{F}_4)_3^-$ (**4**), $\text{Ph}_3\text{C}^+ \text{FB}(o\text{-C}_6\text{F}_5\text{C}_6\text{F}_4)_3^-$ (**7**), $\text{Ph}_3\text{C}^+ (\text{C}_6\text{F}_5)_3\text{AlFAl}(o\text{-C}_6\text{F}_5\text{C}_6\text{F}_4)_3^-$ (**11**), $\text{Ph}_3\text{C}^+ \text{ClAl}(\text{C}_6\text{F}_5)_3^-$ (**12**) $\text{Ph}_3\text{C}^+ \text{BrAl}(\text{C}_6\text{F}_5)_3^-$ (**13**), and $\text{Ph}_3\text{C}^+ \text{F}[\text{Ga}(\text{C}_6\text{F}_5)_3]_2^-$ (**14**).

complex	halometallate fragment	M–X	M–C _{aryl} ^b	C–C _{phenyl} ^c
4	FAl (<i>o</i> -C ₆ F ₅ C ₆ F ₄) ₃	1.682(5)	2.018(6)	1.44(1)
7	FB (<i>o</i> -C ₆ F ₅ C ₆ F ₄) ₃	1.437(6)	1.654(6)	1.443(6)
10	Al–F–Al–F–Al	1.738(3) ^{b,d}	1.999(4) ^d	1.447(6)
		1.965(2) ^e	2.003(4) ^e	
11	(C ₆ F ₅) ₃ AlFAl (<i>o</i> -C ₆ F ₅ C ₆ F ₄) ₃	1.770(3) ^f	1.983(5) ^f	1.439(6)
		1.797(3) ^g	2.008(4) ^g	
12	ClAl(C ₆ F ₅) ₃	2.1676(7)	2.007(4)	1.445(3)
13	BrAl(C ₆ F ₅) ₃	2.3317(18)	2.006(8)	1.440(6)
14	Ga–F–Ga	1.907(2) ^b	1.990(4)	1.447(5)

^a X = F, Cl, or Br, ^b Average of bond distance. ^c Average of bond distance in trityl cation. ^d F–Al_{Terminal}. ^e F–Al_{internal}. ^f FAl(C₆F₅)₃. ^g FAl(*o*-C₆F₅C₆F₄)₃.

Table 3. Selected Bond Distances (Å) and Angles (deg) for Cocatalyst Ph_3C^+ $\text{FB}(o\text{-C}_6\text{F}_5\text{C}_6\text{F}_4)_3^-$ (**7**).

Bond Distances (Å)							
B1–F1	1.437(6)	B1–C25	1.655(6)	C30–C31	1.477(6)	C37–C44	1.442(6)
B1–C1	1.649(7)	C6–C7	1.504(6)	C37–C38	1.425(6)	C37–C50	1.463(6)
B1–C13	1.659(6)	C18–C19	1.495(6)				
Bond Angles (deg)							
F1–B1–C1	105.3(4)	F1–B1–C13	106.8(3)	F1–B1–C25	107.2(3)		
C1–B1–C13	114.4(4)	C1–B1–C25	112.2(3)	C25–B1–C13	110.4(4)		
C38–C37–	121.8(4)	C38–C37–	120.6(4)	C44–C37–	117.4(4)		
C1–C6–C7	123.4(4)	C13–C18–	123.4(4)	C25–C30–	123.4(4)		
Torsion Angles (deg)							
C1–C6–C7–C8	-77.9	C13–C18–C19–C24	-94.9	C25–C30–C31–C36	-81.4		

Table 4. Selected Bond Distances (Å) and Angles (deg) for Dinuclear MetalloceneComplex $[\text{Me}_2\text{C}(\text{Cp})(\text{Flu})\text{ZrMe}]_2(\mu\text{-F})^+ \text{FB}(\text{o-C}_6\text{F}_5\text{C}_6\text{F}_4)_3^-$ (**17**).

Bond Distances (Å)			
C1–Zr1 2.257(4)	C23–Zr2 2.248(4)	B1–F2 1.424(5)	C62–C63 1.487(5)
F1–Zr1 2.095(2)	F1–Zr2 2.103(2)	B1–C45 1.666(5)	Zr–Cp _(cent) ^a 2.166
C14–C15 1.555(5)	C36–C37 1.546(6)	B1–C57 1.653(6)	Zr1–Flu _(cent) ^a 2.231
C15–C18 1.541(6)	C37–C40 1.523(6)	B1–C69 1.664(5)	Zr2–Cp _(cent) ^a 2.175
Zr1–C15 3.137	Zr2–C37 3.107	C50–C51 1.501(6)	Zr2–Flu _(cent) ^a 2.225
Bond Angles (deg)			
Zr1–F1–Zr2 155.57(12)	C45–B1–C57 112.0(3)	C57–C62–C63 122.0(3)	
F2–B1–C45 106.5(3)	C45–C50–C51 123.5(3)	Cp _(cent) ^a –Zr1–Flu _(cent) ^a 118.6	
F2–B1–C57 108.0(3)	C18–C15–C14 98.6(3)	Cp _(cent) ^a –Zr2–Flu _(cent) ^a 119.0	
F2–B1–C69 107.7(3)	C40–C37–C36 99.8(3)	C57–B1–C69 109.1(3)	
F1–Zr1–C1 98.35(13)	C45–B1–C69 113.4(3)	C69–C74–C75 124.3(3)	
F1–Zr2–C23 92.60(13)			
Torsion Angles (deg)			
C45–C50–C51–C52 -94.4	C–57–C62–C63– -97.9	C69–C74–C75–C76 -59.7	

^a Centroid of C₅ ligand.

Table 5. Comparison of Selected Bond Distances (Å) and Angles (deg) for Dinuclear Metallocene Cations Containing Zr–F–Zr Linkages.

[Zr]–F–[Zr]	D ^{4a}	E ^{7b}	F ^{9a}	17
[Zr]	1,2-Me ₂ CpZrMe	1,2-Me ₂ CpZrF	Me ₂ C(Cp)(Flu) Zr(C ₆ F ₅)	Me ₂ C(Cp)(Flu) ZrMe
Anion	MeB(C ₆ F ₅) ₃ ⁻	B(C ₆ F ₄ (C ₃ H ₇)) ₄ ⁻	MeB(C ₆ F ₅) ₃ ⁻	FB(<i>o</i> -C ₆ F ₅ C ₆ F ₄) ₃ ⁻
Zr–(μ-F) ^a	2.113(5)	2.111(2)	2.152(2)	2.099(4)
Zr–R ^b	2.222(3)	1.934(13)	2.306(2)	2.253(5)
Zr–(μ-F)–Zr ^c	173.3(1)	158.0(6)	174.3(3)	155.57(13)
R–Zr–(μ-F) ^d	93.8(20)	94.0(13)	106.3(6)	95.5(31)
Cp _(cent) ^e –Zr–Cp _(cent) ^e	131.3(5)	131.4(5)	118.1(1)	118.8(2)
R–Zr–Zr–R ^f	99.9	96.4	89.2	67.1
Zr–Zr ^g	4.219	4.144	4.300	4.103

^a Mean bond distance. ^b Mean Zr–R bond distance, R = Me, C₆F₅ (in **F**) or F (in **E**). ^c Bond angle.

^d Mean R–Zr–(μ-F) bond angle. ^e Centroid of C₅ ligand. ^f Torsion angle. ^g Metal distance.

Table 6. Selected Bond Distances (Å) and Angles (deg) for Cocatalyst (Ph₃C⁺)₂F₃[Al(C₆F₅)₃]₃²⁻ (**10**).

Bond Distances (Å)			
Al1–F1 1.741(2)	Al2–F2 1.965(2)	Al3–C37 1.999(4)	C55–C68 1.440(6)
Al1–C1 2.000(4)	Al2–C19 1.996(4)	Al3–C43 1.995(4)	C74–C75 1.446(6)
Al1–C13 1.986(4)	Al2–C25 2.009(4)	Al3–C49 2.003(5)	C74–C81 1.449(6)
Al1–C7 2.008(4)	Al2–C31 2.004(4)	C55–C56 1.443(5)	C74–C87 1.438(6)
Al2–F1 1.964(2)	Al3–F2 1.734(3)	C55–C62 1.458(6)	
Bond Angles (deg)			
Al1–F1–Al2 168.56(15)	F1–Al2–C31 89.73(14)	C37–Al3–C43 112.04(17)	
Al3–F2–Al2 173.51(15)	F2–Al2–C19 91.16(14)	C37–Al3–C49 113.79(18)	
F1–Al1–C1 106.38(14)	F2–Al2–C25 91.15(14)	C43–Al3–C49 112.26(17)	
F1–Al1–C7 104.85(15)	F2–Al2–C31 87.41(14)	C56–C55–C62 118.0(4)	
F1–Al1–C13 105.36(15)	C19–Al2–C25 117.04(17)	C56–C55–C68 121.9(4)	
C1–Al1–C7 110.36(17)	C19–Al2–C31 120.77(17)	C62–C55–C68 120.1(3)	
C1–Al1–C13 115.48(17)	C25–Al2–C31 122.19(17)	C75–C74–C81 119.8(4)	
F1–Al2–F2 177.03(12)	F2–Al3–C37 104.77(15)	C75–C74–C87 118.7(4)	
F1–Al2–C19 89.62(14)	F2–Al3–C43 105.71(15)		
F1–Al2–C25 91.05(14)	F2–Al3–C49 107.54(15)		

Table 7. Selected Bond Distances (Å) and Angles (deg) for Cocatalyst Ph₃C⁺ $(\text{C}_6\text{F}_5)_3\text{AlFAl}(\text{o-C}_6\text{F}_5\text{C}_6\text{F}_4)_3^-$ (**11**).

Bond Distances (Å)			
Al1–F1 1.770(3)	Al1–C13 1.981(4)	C24–C25 1.485(6)	C55–C62 1.435(6)
Al2–F1 1.797(3)	Al2–C19 2.015(4)	C36–C37 1.489(7)	C55–C68 1.453(6)
Al1–C1 1.977(5)	Al2–C31 1.998(5)	C48–C49 1.486(6)	
Al1–C7 1.992(5)	Al2–C43 2.010(4)	C55–C56 1.430(6)	
Bond Angles (deg)			
Al1–F1–Al2 176.91(16)	F1–Al2–C19 100.18(15)	C31–C36–C37 122.2(4)	
F1–Al1–C1 102.02(16)	F1–Al2–C31 100.60(15)	C43–C48–C49 123.9(4)	
F1–Al1–C13 105.70(16)	F1–Al2–C43 103.28(15)	C56–C55–C68 118.2(4)	
F1–Al1–C7 104.32(16)	C31–Al2–C43 115.21(19)	C62–C55–C68 120.7(4)	
C1–Al1–C7 113.60(19)	C31–Al2–C19 116.73(18)	C56–C55–C62 121.1(4)	
C1–Al1–C13 115.87(19)	C43–Al2–C19 116.73(18)		
C13–Al1–C7 113.51(18)	C19–C24–C25 123.0(4)		
Torsion Angles (deg)			
C19–C24–C25–C26 -71.2	C19–C24–C25–C26 -71.2	C43–C48–C49–C54 -69.6	

Table 8. Comparison of the Torsion Angles (deg) in $\text{FAl}(o\text{-C}_6\text{F}_4\text{C}_6\text{F}_5)_3^-$ and $\text{FB}(o\text{-C}_6\text{F}_4\text{C}_6\text{F}_5)_3^-$ Anions.

	Anion	Structure	$\text{C}_a\text{-C}_b\text{-C}_c\text{-C}_d$ ^a	$\text{F-M-C}_a\text{-C}_b$ ^a
4 ^{9a}	$\text{FAl}(o\text{-C}_6\text{F}_5\text{C}_6\text{F}_4)_3^-$	J	-53.9	-15.0
			-95.3	-38.4
			-98.0	-38.4
4 + 15 ^{12a}	$[\text{Zr}]\text{-FAl}(o\text{-C}_6\text{F}_5\text{C}_6\text{F}_4)_3^-$	K-2	-102.6	+119.6
			-102.7	+120.1
			-109.2	+130.0
7	$\text{FB}(o\text{-C}_6\text{F}_5\text{C}_6\text{F}_4)_3^-$	J	-77.9	-30.5
			-81.4	-32.2
			-94.9	-39.2
17	$\text{FB}(o\text{-C}_6\text{F}_5\text{C}_6\text{F}_4)_3^-$	J	-59.7	-17.9
			-94.4	-40.6
			-97.9	-42.4
11	$[\text{Al}]\text{-FAl}(o\text{-C}_6\text{F}_5\text{C}_6\text{F}_4)_3^-$	K-1	-69.6	-119.0
			-69.7	-120.6
			-71.2	-121.3
20	$[\text{Al}]\text{-FAl}(o\text{-C}_6\text{F}_5\text{C}_6\text{F}_4)_3^-$	K-2	-101.8	+115.9
			-109.9	+119.5
			-118.0	+124.8

^a Torsion angle.

Table 9. Selected Bond Distances (Å) and Angles (deg) for Dinuclear MetalloceneComplex $[\text{Me}_2\text{C}(\text{Cp})(\text{Flu})\text{ZrMe}]_2(\mu\text{-Me})^+ \text{F}[\text{Al}(\text{C}_6\text{F}_5)_3]_3^-$ (**19**).

Bond Distances (Å)			
Zr1–C2 2.4179(3)	Zr1–Flu _(cent) ^a 2.237	Al1–F1 1.7945(9)	Al1–C36 1.986(3)
C1–Zr1 2.248(3)	Zr1–C8 3.126	Al1–C30 1.993(3)	C8–C11 1.553(4)
Zr1–Cp _(cent) ^a 2.178	Zr1–Zr1' 4.836(6)	Al1–C24 1.983(3)	C7–C8 1.530(4)
Bond Angles (deg)			
Zr1–C2–Zr1' 180	F1–Al1–C36 107.23(11)	Al1–F1–Al1' 167.10(12)	
C2–Zr1–C1 92.35(10)	C24–Al1–C30 111.32(13)	C7–C8–C11 99.5(2)	
F1–Al1–C24 105.60(10)	C24–Al1–C36 114.35(13)	Cp _(cent) ^a –Zr1–Flu _(cent) ^a 118.43	
F1–Al1–C30 104.61(12)	C36–Al1–C30 112.88(13)		

^a Centroid of C₅ ligand.

Table 10. Selected Bond Distances (Å) and Angles (deg) for Dinuclear MetalloceneComplex $[\text{Me}_2\text{C}(\text{Cp})(\text{Flu})\text{ZrMe}]_2(\mu\text{-Me})^+ (\text{C}_6\text{F}_5)_3\text{AlFAl}(\text{o-C}_6\text{F}_5\text{C}_6\text{F}_4)_3^-$ (**20**).

Bond Distances (Å)			
C1B–Zr1 2.443(12)	C23–Zr2 2.228(13)	Al1–C51 1.965(15)	Zr2–Flu _(cent) ^a 2.245
C1B–Zr2 2.393(12)	Al1–C45 1.986(12)	Al2–C87 2.018(12)	Zr1–C15 3.097
Al1–F1 1.786(7)	Al2–C63 1.992(12)	Zr2–Cp _(cent) ^a 2.170	Zr2–C37 3.105
Al2–F1 1.785(7)	Zr1–Flu _(cent) ^a 2.251	C15–C18 1.506(14)	C68–C69 1.462(16)
Zr1–Cp _(cent) ^a 2.162	Al1–Al2 3.568	C37–C40 1.520(15)	C80–C81 1.501(15)
Zr1–Zr 2 4.770	C14–C15 1.566(16)	Al1–C57 1.945(14)	C91–C92 1.529(17)
C1–Zr1 2.278(13)	C36–C37 1.545(17)	Al2–C75 2.022(12)	
Bond Angles (deg)			
Zr1–C1B–Zr2 161.1(6)	C51–Al1–C45 115.5(6)	F1–Al2–C87 99.9(4)	
Al1–F1–Al2 175.5(4)	C57–Al1–C45 116.4(6)	C87–C91–C92 122.5(11)	
F1–Al1–C45 102.1(4)	C57–Al1–C51 116.0(6)	Cp _(cent) ^a –Zr1–Flu _(cent) ^a 119.0	
F1–Al1–C51 102.7(5)	C75–C80–C81 123.4(10)	Cp _(cent) ^a –Zr2–Flu _(cent) ^a 118.1	
F1–Al1–C57 100.3(5)	C18–C15–C14 101.2(9)	C63–Al2–C87 114.9(5)	
C69–C68–C63 121.9(11)	C40–C37–C36 101.2(10)	C63–Al2–C75 117.6(5)	
C1–Zr1–C1B 91.0(5)	F1–Al2–C63 101.2(4)	C87–Al2–C75 118.0(5)	
C23–Zr2–C1B 96.3(5)	F1–Al2–C75 100.1(4)		

^a Centroid of C₅ ligand.

Table 11. Comparison of Selected Bond Distances (Å) and Angles (deg) for Dinuclear Metallocene Cations Containing Zr–Me–Zr Linkages.

	G ³⁴	H ³⁵	I ^{9a}	19	20
[Zr]	(N ₃) ₂ ZrMe ^h	(guan) ₂ ZrMe ⁱ	(1,2-Me ₂ Cp) ZrMe	[Me ₂ C(Cp)(Flu)] ZrMe	[Me ₂ C(Cp)(Flu)] ZrMe
Anion	B(C ₆ F ₅) ₄ ⁻	B(C ₆ F ₅) ₄ ⁻	MeB(<i>o</i> - C ₆ F ₅ C ₆ F ₄) ₃ ⁻	(C ₆ F ₅) ₃ AlFAl(C ₆ F ₅) ₃ ⁻	(C ₆ F ₅) ₃ AlFAl(<i>o</i> - C ₆ F ₅ C ₆ F ₄) ₃ ⁻
Zr–(μ–Me) ^a	2.482(25)	2.45(5)	2.424(16)	2.4179(3)	2.418(12)
Zr–Me _t ^b	2.243(13)	2.254(4)	2.242(16)	2.248(3)	2.253(13)
Zr–(μ–Me)– Zr ^c	167.4(4)	170.84(13)	170.9(4)	180	161.1(6)
Me _t –Zr– (μ–Me) ^d	96.0(13)	89.3(8)	93.3(10)	92.35(10)	93.7(5)
Cp _(cent) ^e –Zr– Cp _(cent) ^e			132.41	118.43	118.6
R–Zr–Zr–R ^f	82.0	33.0	108.5	180	-62.8
Zr–Zr ^g	4.933	4.871	4.833	4.836(6)	4.770

^a Mean bond distance. ^b Mean Zr–Me bond distance. ^c Bond angle. ^d Mean R–Zr–(μ–Me) bond angle. ^e Centroid of C₅ ligand. ^f Torsion angle. ^g Metal distance. ^h N₃ = (MesNCH₂CH₂)₂NMe; ref. 34. ⁱ guan = η²-(*i*-PrN)₂C(NMe₂); ref. 35.

Table 12. Selected Bond Distances (Å) and Angles (deg) for Cocatalysts Ph_3C^+ $\text{ClAl}(\text{C}_6\text{F}_5)_3^-$ (**12**) and $\text{Ph}_3\text{C}^+ \text{BrAl}(\text{C}_6\text{F}_5)_3^-$ (**13**).

12		13	
Bond Distances (Å)		Bond Distances (Å)	
Cl1–Al1 2.1676(7)	C19–C20 1.441(3)	Br1–Al1 2.3317(18)	C19–C20 1.448(5)
Al1–C1 2.0043(19)	C19–C26 1.445(2)	Al1–C1 2.019(4)	C19–C26 1.435(5)
Al1–C7 2.0046(19)	C19–C32 1.451(2)	Al1–C7 1.998(4)	C19–C32 1.436(6)
Al1–C13 2.0143(19)		Al1–C13 2.001(5)	
Bond Angles (deg)		Bond Angles (deg)	
Cl1–Al1–C1 112.88(6)	C7–Al1–C13 113.47(8)	Br1–Al1–C1 103.98(11)	C7–Al1–C13 109.00(17)
Cl1–Al1–C7 105.68(6)	C20–C19–C26	Br1–Al1–C7 112.69(12)	C20–C19–C26 119.3(4)
Cl1–Al1–C13 104.56(6)	C20–C19–C32	Br1–Al1–C13 104.90(13)	C20–C19–C32 119.9(4)
C1–Al1–C7 108.88(8)	C26–C19–C32	C1–Al1–C7 111.71(18)	C26–C19–C32 120.8(3)
C1–Al1–C13 111.26(8)		C1–Al1–C13 114.37(17)	

Table 13. Selected Bond Distances (Å) and Angles (deg) for Me₂C(Cp)(Flu)ZrCl(C₆F₅)

(21).

Bond Distances (Å)			
C11–Zr1 2.4225(19)	C3R–C4R 1.373(9)	Zr1–C15 3.1137	C1R–C2R 1.380(7)
C2R–C3R 1.382(8)	Zr1–Flu _(cent) ^a 2.239	C15–C18 1.533(8)	C1R–C6R 1.394(7)
Zr1–Cp _(cent) ^a 2.178	C14–C15 1.556(7)	C5R–C6R 1.362(8)	C6R–F5 1.357(6)
C1R–Zr1 2.351(5)	C4R–C5R 1.386(9)	C2R–F1 1.364(6)	
Bond Angles (deg)			
C1R–Zr1–C11 99.44(14)	C18–C15–C14 98.7(4)	C2R–C1R–C6R 113.2(5)	
C6R–C1R–Zr1 113.8(4)	Cp _(cent) ^a –Zr1–Flu _(cent) ^a 118.2	C2R–C1R–Zr1 133.0(4)	
Torsion Angles (deg)			
Cl–Zr–C1R–C6R 39.4		Cl–Zr–C1R–C2R -138.7	

^a Centroid of C₅ ligand.

Table 14. Selected Bond Distances (Å) and Angles (deg) for[Me₂C(Cp)(Flu)Zr(μ₂-Br)]₂²⁺ [Al(C₆F₅)₄]₂⁻ (**22**).

Bond Distances (Å)			
Br1–Zr1 2.6772(13)	Br1'–Zr1 2.7155(13)	C13–C14 1.459(12)	C15–C18 1.537(13)
Al1–C23 2.027(10)	Al1–C29 2.023(10)	Al1–C35 2.019(10)	Al1–C41 2.023(10)
Zr1–Cp _(cent) ^a 2.135	Zr1–Flu _(cent) ^a 2.197	Zr1–Zr2 3.896	Zr1–C14 3.093

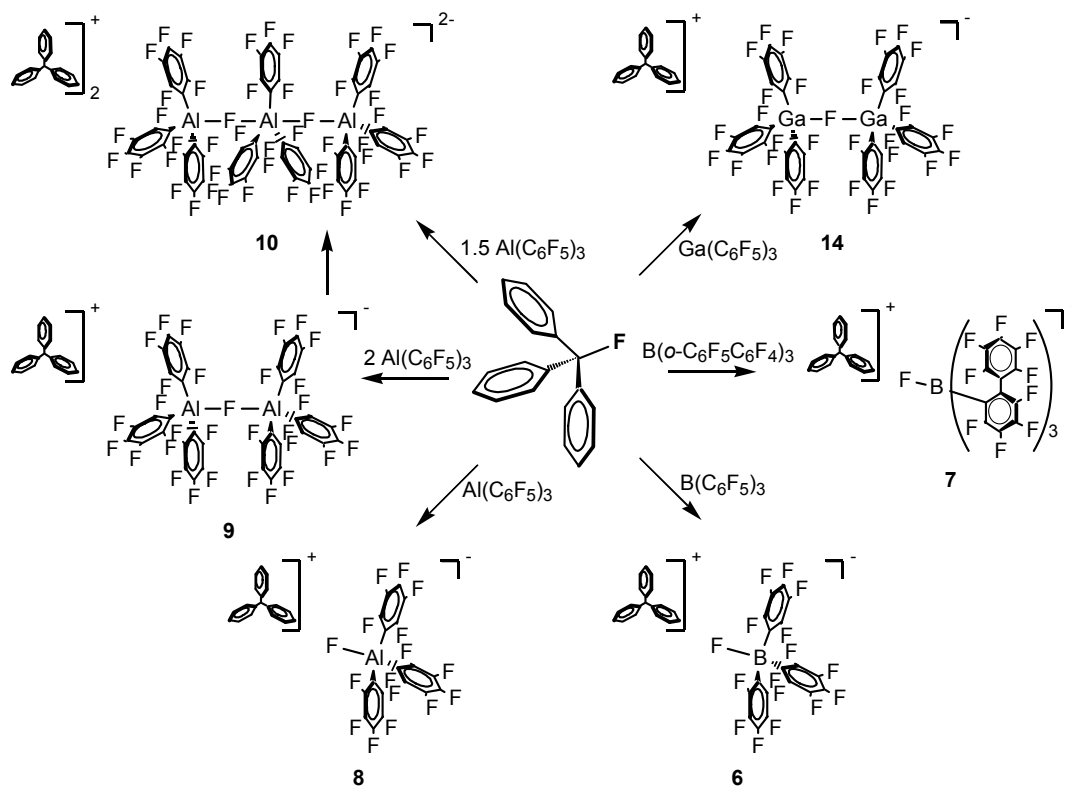
Bond Angles (deg)		
Zr1–Br1–Zr1' 92.52(4)	Br1–Zr1–Br1' 87.48(4)	C23–Al1–C29 109.2(4)
C35–Al1–C23 105.6(4)	C41–Al1–C23 112.9(4)	C35–Al1–C29 111.9(4)
C41–Al1–C29 105.7(4)	C41–Al1–C35 111.5(4)	Cp _(cent) ^a –Zr1–Flu _(cent) ^a 120.2

^a Centroid of C₅ ligand.

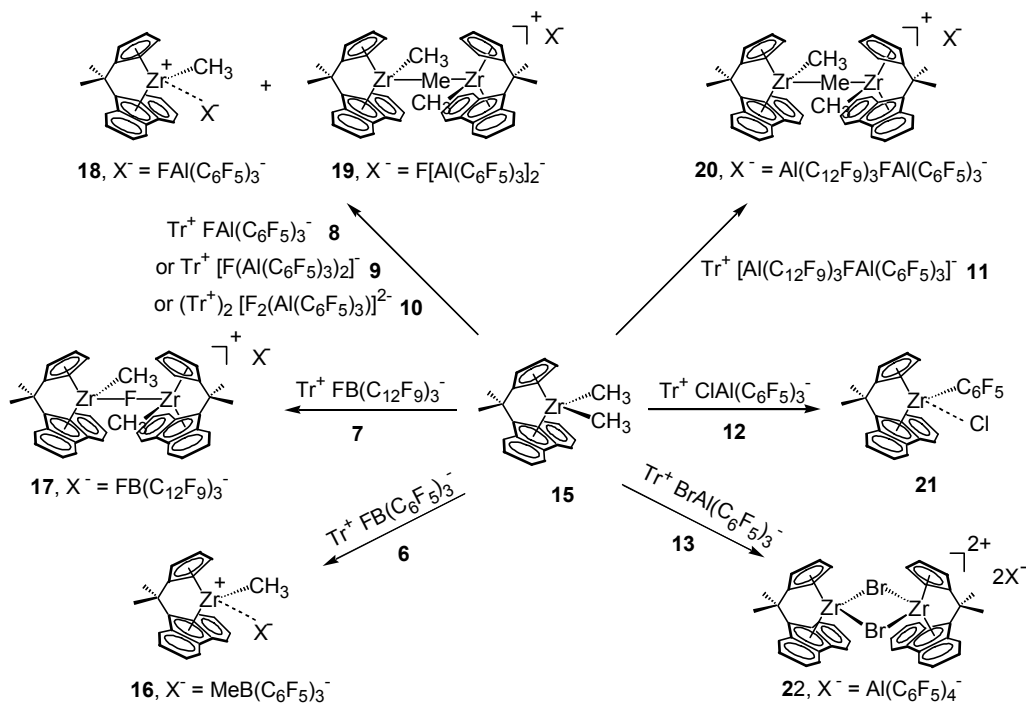
Table 15. Selected Bond Distances (Å) and Angles (deg) for Cocatalyst Ph_3C^+ $\text{F}[\text{Ga}(\text{C}_6\text{F}_5)_3]_2^-$ (**14**).

Bond Distances (Å)			
F1–Ga1 1.896(2)	C7–Ga1 1.994(4)	C25–Ga2 1.988(4)	C37–C44 1.444(6)
F1–Ga2 1.918(2)	C13–Ga1 2.003(4)	C31–Ga2 1.989(4)	
C1–Ga1 1.991(4)	C19–Ga2 1.992(4)	C37–C38 1.436(5)	
Bond Angles (deg)			
F1–Ga1–C1 103.02(13)	C7–Ga1–C13 116.61(16)	C19–Ga2–C31 116.77(16)	
F1–Ga1–C7 101.02(13)	F1–Ga2–C19 97.39(13)	C25–Ga2–C31 117.25(16)	
F1–Ga1–C13 102.78(13)	F1–Ga2–C25 98.11(13)	C38–C37–C44 122.2(3)	
C1–Ga1–C7 113.98(16)	F1–Ga2–C31 100.08(12)	C38–C37–C50 119.7(4)	
C1–Ga1–C13 116.23(16)	C19–Ga2–C25 119.52(16)	C44–C37–C50 118.1(3)	

Scheme 1. New trityl salt species arising from reaction of trityl fluoride with various known neutral cocatalyst species.



Scheme 2. Reactions of $\text{Me}_2\text{C}(\text{Cp})(\text{Flu})\text{ZrMe}_2$ (**15**) with cocatalyst reagents **6** – **13**.



**Diverse Stereocontrol Effects Induced by Weakly Coordinating Anions.
Stereospecific Olefin Polymerization Pathways at Archetypal C_S - and C_1 -
Symmetric Metallocenium Catalysts Using Mono- and Polynuclear
Halo-Perfluoroarylmatalates as Cocatalysts.**

John A. S. Roberts, Ming-Chou Chen, Afif M. Seyam, Liting Li, Cristiano Zuccaccia, Nicholas
G. Stahl, and Tobin J. Marks*

Department of Chemistry, Northwestern University

Evanston, Illinois 60208-3113

ABSTRACT

Counteranion effects on propylene polymerization rates and stereoselectivities are compared using C_S -symmetric $\text{Me}_2\text{C}(\text{Cp})(\text{Flu})\text{ZrMe}_2$ (**1**; Cp = C_5H_4 , η^5 -cyclopentadienyl; Flu = C_{13}H_8 , η^5 -fluorenyl) and C_1 -symmetric $\text{Me}_2\text{Si}(\text{OHf})(\text{CpR}^*)\text{ZrMe}_2$ (**2**; OHf = $\text{C}_{13}\text{H}_{16}$, η^5 -octahydrofluorenyl; CpR* = η^5 -3-(-)-menthylcyclopentadienyl) precatalysts activated with mononuclear and polynuclear perfluoroarylborate, -aluminate, and -gallate cocatalysts/activators $\text{B}(\text{C}_6\text{F}_5)_3$ (**3**), $\text{B}(o\text{-C}_6\text{F}_5\text{C}_6\text{F}_4)_3$ (**4**), $\text{Al}(\text{C}_6\text{F}_5)_3$ (**5**), $\text{Ph}_3\text{C}^+ \text{B}(\text{C}_6\text{F}_5)_4^-$ (**6**), $\text{Ph}_3\text{C}^+ \text{FAl}(o\text{-C}_6\text{F}_5\text{C}_6\text{F}_4)_3^-$ (**7**), $\text{Ga}(\text{C}_6\text{F}_5)_3$ (**8**), and recently reported mono- and polymetallic trityl perfluoroarylhalometallates $\text{Ph}_3\text{C}^+ \text{FB}(\text{C}_6\text{F}_5)_3^-$ (**9**), $\text{Ph}_3\text{C}^+ \text{FB}(o\text{-C}_6\text{F}_5\text{C}_6\text{F}_4)_3^-$ (**10**), $(\text{Ph}_3\text{C}^+)_x \text{F}_x[\text{Al}(\text{C}_6\text{F}_5)_3]_y^{x-}$ ($x = 1, y = 1$, **11**; $x = 1, y = 2$, **12**; $x = 2, y = 3$, **13**), $\text{Ph}_3\text{C}^+ (\text{C}_6\text{F}_5)_3\text{AlFAl}(o\text{-C}_6\text{F}_5\text{C}_6\text{F}_4)_3^-$ (**14**), $\text{Ph}_3\text{C}^+ \text{XAl}(\text{C}_6\text{F}_5)_3^-$ ($X = \text{Cl}$, **15**; $X = \text{Br}$, **16**), and $\text{Ph}_3\text{C}^+ \text{F}[\text{Ga}(\text{C}_6\text{F}_5)_3]_2^-$ (**17**). Temperature, propylene concentration, and solvent polarity

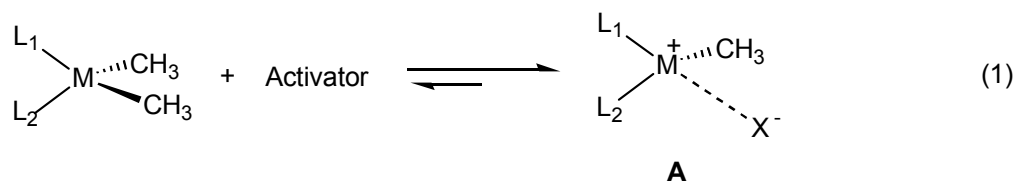
dependence are surveyed in polymerizations catalyzed by **1** activated with cocatalysts **3** - **16** and with a 1:2 ratio of Ph_3CCl and **5** and a 1:2 ratio of Ph_3CBr and **5**, and by **2** activated with **3**, **6**, **7**, **12**, and **14**. Remarkable stereocontrol with high activities is observed for **1** + **12** and **1** + **14**. Polypropylene samples produced using C_1 -symmetric precatalyst **2** are subjected to microstructural analyses using stochastic models describing the relative contributions of enantiofacial misinsertion and backskip processes. A powerful technique is introduced for calculating interparametric correlation matrices for these nonlinear stochastic models. The collected results significantly extend what is known about ion-pairing effects in the case of C_S -symmetric precatalyst **1** and extend these findings to the case of C_1 -symmetric precatalyst **2** as a mediator for isospecific propylene polymerization.

INTRODUCTION

New understanding of the significance of ion pairing interactions in metallocene-based olefin polymerization catalyst systems (**A**, produced via metallocene alkide abstraction by neutral or ionic organometalloid activators; eq. 1) has emerged from recent studies of catalyst system ion pairing dynamics.^{1, 2, 3, 4} Importantly, it is evident that: a) in low- ϵ media at catalyst

¹ For recent reviews of single-site olefin polymerization, see: (a) Gibson, V. C.; Spitzmesser, S. K. *Chem. Rev.*, **2003**, 103 (1), 283-315. (b) Pédeutour, J.-N.; Radhakrishnan, K.; Cramail, H.; Deffieux, A. *Macromol. Rapid Commun.* **2001**, 22, 1095-1123. (c) Chen, Y.-X.; Marks, T. J. *Chem. Rev.*, **2000**, 100 (4), 1391-1434. (d) Gladysz, J. A., Ed. *Chem. Rev.* **2000**, 100, 1167-1682. (e) Marks, T. J.; Stevens, J. C., Eds. *Topics in Catalysis*, **1999**, 7, 1-208. (f) Britovsek, G. J. P.; Gibson, V. C.; Wass, D. F. *Angew. Chem., Int. Ed. Engl.* **1999**, 38, 428-447.

² For recent cocatalyst studies, see: (a) Busico, V.; Cipullo, R.; Cutillo, F.; Vacatello, M.; Castelli, V. V. *Macromolecules* **2003**, 36, 4258-4261. (b) Mohammed, M.; Nele, M.; Al-Humydi, A.; Xin, S.; Stapleton, R. A.;



concentrations typical for olefin polymerization reactions, these catalyst systems exist as stereochemically mobile 1:1 contact ion pairs and exhibit varying modes of cation-anion

Collins, S. *J. Am. Chem. Soc.* **2003**, *125*, 7930-7941. (c) Abramo, G. P.; Li, L.; Marks, T. J. *J. Am. Chem. Soc.* **2002**, *124*, 13966-13967. (d) Li, L.; Metz, M. V.; Li, H.; Chen, M.-C.; Marks, T. J. *J. Am. Chem. Soc.* **2002**, *124*, 12725-12741. (e) Metz, M. V.; Schwartz, D. J.; Stern, C. L.; Marks, T. J.; Nickias, P. N. *Organometallics*, **2002**, *21*, 4159-4168. (f) Metz, M. V.; Sun, Y. M.; Stern, C. L.; Marks, T. J. *Organometallics*, **2002**, *21*, 3691-3702. (g) Wilmes, G. M.; Polse, J. L.; Waymouth, R. M. *Macromolecules* **2002**, *35*, 6766-6772. (h) Lancaster, S. J.; Rodriguez, A.; Lara-Sanchez, A.; Hannant, M. D.; Walker, D. A.; Hughes, D. H.; Bochmann, M. *Organometallics*, **2002**, *21*, 451-453. (i) Rodriguez, G.; Brant, P. *Organometallics*, **2001**, *20*, 2417-2420. (j) Kaul, F. A. R.; Puchta, G. T.; Schneider, H.; Grosche, M.; Mihalios, D.; Herrmann, W. A. *J. Organometal. Chem.* **2001**, *621*, 177-183. (k) Chen, Y.-X.; Kruper, W. J.; Roof, G.; Wilson, D. R. *J. Am. Chem. Soc.* **2001**, *123*, 745-746. (l) Zhou, J.; Lancaster, S. J.; Walker, D. A.; Beck, S.; Thornton-Pett, M.; Bochmann, M. *J. Am. Chem. Soc.* **2001**, *123*, 223-237. (m) Kehr, G.; Roesmann, R.; Fröhlich, R.; Holst, C.; Erker, G. *Eur. J. Inorg. Chem.* **2001**, 535-538. (n) Mager, M.; Becke, S.; Windisch, H.; Denninger, U. *Angew. Chem., Int. Ed. Engl.* **2001**, *40*, 1898-1902. (o) Al-Humydi, A.; Garrison, J.C.; Youngs, W.J.; Collins, S. *Organometallics* **2005**, *24*(2), 193-196. (p) Lancaster, S. J.; Bochmann, M. *J. Organomet. Chem.* **2002**, *654*(1-2), 221-223.

³ (a) Yang, X.; Stern, C. L.; Marks, T. J. *J. Am. Chem. Soc.* **1994**, *116*, 10015-10031. (b) Yang, X.; Stern, C. L.; Marks, T. J. *J. Am. Chem. Soc.* **1991**, *113*, 3623-3625.

⁴ (a) Chien, J. C. W.; Tsai, W.-M.; Rausch, M. D. *J. Am. Chem. Soc.* **1991**, *113*, 8570-8571. (b) Yang, X.; Stern, C. L.; Marks, T. J. *Organometallics* **1991**, *10*, 840-842. (c) Ewen, J. A.; Elder, M. J. *Eur. Pat. Appl.* 426637, **1991**; *Chem. Abstr.* **1991**, *115*, 136987c, 136988d.

interaction;^{2, 5, 6} b) during polymerization reactions, the rates of a host of competing processes, including chain-migratory insertion (chain propagation), various stereodeflect production and polymer chain termination processes and even catalyst deactivation are all profoundly anion-dependent, with strong correlations between the rates of processes occurring during polymerization and active catalyst ion pairing strength as assayed by *ex-situ* solution-phase spectroscopic studies of the catalyst systems.⁷ These findings suggest that polymerization-significant ion pairing must persist under polymerization conditions and that the anion-derived effects on activity, stereoregulation, and chain release are deeply rooted in ion pairing dynamics. This stands to reason: in asymmetric catalysis, the influence of catalyst ancillary moieties on transition state energies generally increases with increasing proximity to the catalyst active site; in the case of ion-paired polymerization catalysts, the counteranion can compete for occupancy of the active site with incoming monomer. The emerging picture then is one in which the interplay between counteranion, cation-polymeryl moiety, and incoming monomer dictates the relative rates of the various processes occurring at the catalytic center during the polymerization process. Cocatalyst/anion effects thus have a direct influence on catalyst performance and product polymer properties such as stereo- and regioregularity and molar mass.

⁵ (a) Stahl, N. G.; Zuccaccia, C.; Jensen, T. R.; Marks, T. J. *J. Am. Chem. Soc.* **2003**, *125*, 5256-5257. (b) Stahl, N. G.; Marks, T. J.; Macchioni, A.; Zuccaccia, C. Presented in part at the 222nd ACS National Meeting, Chicago, IL, August 2001, Abstract INORG 407.

⁶ Song, F.; Lancaster, S. J.; Cannon, R. D.; Schormann, M.; Humphrey, S. M.; Zuccaccia, C.; Macchioni, A.; Bochmann, M. *Organometallics* **2005**; ASAP Article

⁷ Chen, M.-C.; Roberts, J. A. S.; Marks, T. J. *J. Am. Chem. Soc.* **2004**, *126* (14), 4605-4625.

Major advances in the study of metallocene-mediated olefin polymerization have followed from the discovery and development of new activator/cocatalyst classes having distinctive properties: alkylaluminumoxanes (e.g. MAO and MMAO),⁸ tris(perfluorophenyl)borane ($\text{B}(\text{C}_6\text{F}_5)_3$; **3**)³ and related perfluoroarylboranes,⁹ ammonium or trityl salts of $\text{B}(\text{C}_6\text{F}_5)_4^-$ ⁴ and related perfluoroarylborates,¹⁰ perfluoroarylanes (e.g. $\text{Al}(\text{C}_6\text{F}_5)_3$; **7**),¹¹ and perfluoroaryl fluoroaluminate salts.¹² We recently reported new classes of mononuclear and polynuclear fluoro- perfluoroarylborate, -aluminate, and -gallate weakly coordinating anions and cocatalysts having one or more metalloïd-bound halogen atoms in $[\text{M}-\text{X}]^-$, $[\text{M}-\text{X}-\text{M}]^-$, and $[\text{M}-\text{X}-\text{M}-\text{X}-\text{M}]^{2-}$ bonding configurations,^{13, 14} with the synthetic and metallocene activation chemistry of

⁸ (a) Sinn, H.; Kaminsky, W. *Adv. Organomet. Chem.* **1980**, *18*, 99-149. (b) Sinn, H.; Kaminsky, W.; Vollmer, H.-J.; Woldt, R. *Angew. Chem., Int. Ed. Engl.* **1980**, *19*, 390-392.

⁹ (a) Li, L.; Stern, C. L.; Marks, T. J. *Organometallics* **2000**, *19*, 3332-3337. (b) Li, L.; Marks, T. J. *Organometallics* **1998**, *17*, 3996-4003. (c) Chen, Y.-X.; Stern, C. L.; Yang, S.; Marks, T. J. *J. Am. Chem. Soc.* **1996**, *118*, 12451-12452. (d) also see refs. 2c, 2d, and 2e. (e) For a recent chelating borane review, see: Piers, W. E.; Irvine, G. J.; Williams, V. C. *Eur. J. Inorg. Chem.* **2000**, 2131-2142.

¹⁰ For related fluorinated tetraarylborates, see: (a) refs 2h, 2i, 2j, and 2l. (b) Jia, L.; Yang, X.; Stern, C. L.; Marks, T. J. *Organometallics* **1997**, *16*, 842-857. (c) Jia, L.; Yang, X.; Ishihara, A.; Marks, T. J. *Organometallics* **1995**, *14*, 3135-3137.

¹¹ (a) ref 2f. (b) Bochmann, M.; Sarsfield, M. J. *Organometallics* **1998**, *17*, 5908-5912. (c) Biagini, P.; Lugli, G.; Abis, L.; Andreussi, P. U.S. Pat. 5,602,269, **1997**.

¹² (a) Chen, Y.-X.; Metz, M. V.; Li, L.; Stern, C. L.; Marks, T. J. *J. Am. Chem. Soc.* **1998**, *120*, 6287-6305. (b) Chen, Y.-X.; Stern, C. L.; Marks, T. J. *J. Am. Chem. Soc.* **1997**, *119*, 2582-2583. (c) Elder, M. J.; Ewen, J. A. *Eur. Pat. Appl. EP 573,403*, **1993**; *Chem. Abstr.* **1994**, *121*, 0207d. (d) also ref. 2p.

¹³ Chen, M. -C.; Roberts, J. A. S.; Marks, T. J. *Organometallics* **2004**, *23*, 932-935.

these species typically involving formation or cleavage of these metalloid-halogen bonds. These more sterically encumbered and charge-dispersing cocatalysts afford thermally robust active catalyst systems that can produce highly stereoregular polypropylenes with very high polymerization activities.

Herein we compare and contrast the propylene polymerization behavior of active catalyst systems derived from cocatalysts $\text{Al}(\text{C}_6\text{F}_5)_3$ (**5**), *in-situ* generated $\text{Ga}(\text{C}_6\text{F}_5)_3$ (**8**), and the new trityl perfluoroaryl fluoroborates $\text{Ph}_3\text{C}^+ \text{FB}(\text{C}_6\text{F}_5)_3^-$ (**9**)¹⁵ and $\text{Ph}_3\text{C}^+ \text{FB}(\text{o-C}_6\text{F}_5\text{C}_6\text{F}_4)_3^-$ (**10**), a homologous series of mono- and polynuclear perfluoroaryl fluoroaluminates $(\text{Ph}_3\text{C}^+)_x \text{F}_x[\text{Al}(\text{C}_6\text{F}_5)_3]_y^{x-}$ ($x = 1, y = 1$, **11**; $x = 1, y = 2$, **12**; $x = 2, y = 3$, **13**)^{16, 17} $\text{Ph}_3\text{C}^+ (\text{C}_6\text{F}_5)_3 \text{AlFAl}(\text{o-C}_6\text{F}_5\text{C}_6\text{F}_4)_3^-$ (**14**), the haloaluminates $\text{Ph}_3\text{C}^+ \text{XAl}(\text{C}_6\text{F}_5)_3^-$ ($\text{X} = \text{Cl}$, **15**; $\text{X} = \text{Br}$, **16**), and binuclear fluorine-bridged gallate $\text{Ph}_3\text{C}^+ \text{F}[\text{Ga}(\text{C}_6\text{F}_5)_3]_2^-$ (**17**)¹⁸ in combination with archetypal C_s -symmetric precatalyst $\text{Me}_2\text{C}(\text{Cp})(\text{Flu})\text{ZrMe}_2$ (**1**; $\text{Cp} = \text{C}_5\text{H}_4, \eta^5\text{-cyclopentadienyl}$;

¹⁴ Syntheses and characterization of the present series of cocatalysts, and details of their stoichiometric reaction with metallocene **15**, are presented in a separate report: Chen, M.-C.; Roberts, J. A. S.; Seyam, A. M.; Li, L.; Zuccaccia, C.; Stahl, N. G.; Marks, T. J. *Organometallics* **2006**, *25*, 2833-2850.

¹⁵ A similar fluoroborate, $\text{Li}^+ [\text{FB}(\text{C}_6\text{F}_5)_3]^-$ has been claimed previously. See Klemann, L. P.; Newman, G. H.; Stogryn, E. L. *U.S. Pat.* 4139681, **1979**.

¹⁶ For the first structural study of a fluoro-bridged organoaluminum complex, $\text{K}^+ [(\text{Et})_3\text{Al-F-Al}(\text{Et})_3]^-$, with $\text{F-Al} = 1.80(6) \text{ \AA}$, see: Natta, G.; Allegra, G.; Perego, G.; Zambelli, A. *J. Am. Chem. Soc.* **1961**, *83*, 5033 – 5033.

¹⁷ A similar M-F-M-F-M arrangement is seen in a Bi system. For a recent review of metal fluorides, see: Roesky, H. W.; Haiduc, I. *J. Chem. Soc., Dalton Trans.*, **1999**, 2249-2264.

¹⁸ For recent examples of organogallium-F complexes, see: (a) Werner, B.; Kräuter, T.; Neumüller, B. *Organometallics* **1996**, *15*, 3746-3751. (b) See ref. 17a for examples of nonlinear fluoro-bridged Ga complexes. (c) Kräuter, T.; Neumüller, B. *Z. Anorg. Allg. Chem.* **1995**, *621*, 597-606.

Flu = C₁₃H₈, η⁵-fluorenyl) and also with the C₁-symmetric precatalyst Me₂Si(OHF)(CpR*)ZrMe₂, (**2**; OHF = C₁₃H₁₆, η⁵-octahydrofluorenyl; CpR* = η⁵-3-(-)-menthylcyclopentadienyl; structures of precatalysts **1** and **2** and cocatalysts **3** - **17** are depicted in Scheme 1). We also describe polymerization results using precatalyst **1** activated with cocatalyst preparations in which Al(C₆F₅)₃ (**5**) is combined with reagent Ph₃CCl in a 2:1 ratio (“Ph₃C⁺ Cl[Al(C₆F₅)₃]⁻”), and in which **5** is combined with Ph₃CBr in a 2:1 ratio (“Ph₃C⁺ Br[Al(C₆F₅)₃]⁻”).¹⁹

Our detailed mechanistic picture of counteranion effects in syndiospecific propylene polymerization arises in part from polypropylene microstructural analysis,^{1d} a quantitative treatment in which the relative abundances of certain defects in an otherwise stereoregular polymer backbone are modeled according to a collection of proposed stereodeflect-producing mechanisms, whose relative rates can then be estimated. Application of this this approach to catalytic systems based on C₁-symmetric precatalyst Me₂Si(OHF)(CpR*)ZrMe₂ (**2**) plus the present cocatalysts should in principle allow a similar level of detail to be achieved. To this end, the substantially isotactic polypropylene samples produced using C₁-symmetric precatalyst **2** are subjected to microstructural analyses using a standard parameterization describing the relative contributions of proposed enantiofacial misinsertion and backskip mechanisms (*vide infra*). This model is presented along with a series of submodels based on some reasonable simplifying assumptions, and a powerful new technique for calculating matrices of correlation coefficients among the parameters of these nonlinear stochastic models. This particular analysis affords a clear picture of the strength of the stochastic approach as applied in the case of isospecific

¹⁹ These latter cocatalyst preparations do not contain isolable molecular species, but do produce polymerization-active catalyst systems when combined with metallocene precatalyst **1**.

propylene polymerization. While the level of detail ascribable to the microstructural analysis of the present isotactic polypropylenes is found to be reduced in comparison to the syndiotactic case, observations on the overall stereoregularity of polymers produced using C_1 -symmetric precatalyst **2** plus the present cocatalysts are consistent with the hypothesis demonstrated using C_S -symmetric precatalyst **1**, that ion pairing strength is a key factor in determining the relative rates of individual processes available during polymerization.

Perfluoroarylmethyl complexes **9 - 16** are accessed by combining trityl halides with known neutral and ionic perfluoroaryl complexes of boron, aluminum, and gallium in varying stoichiometries. In a companion report,¹⁴ we discuss the syntheses, solid state structural, and solution structural/dynamic features of these new cocatalysts and describe the products generated in their reactions with metallocene **1**. In the present series of polymerization experiments, active catalyst systems are prepared by combining the C_S - or C_1 -symmetric precatalyst and cocatalyst of choice and are used without further purification according to the Experimental Section. We represent the catalyst system prepared by combining, for example, precatalyst **1** and cocatalyst **14** simply as “**1** + **14**.” This serves to distinguish these preparations – often mixtures – from individual ion pair complexes (isolable in certain cases by fractional recrystallization and identifiable as discrete species in the NMR spectra of certain catalyst-cocatalyst reaction mixtures).^{7, 14} Individual ion pair complexes are referred to in the discussion using unique compound numbers **20 - 24**.

Catalyst systems generated using the present new polynuclear perfluoroaryl cocatalysts generally exhibit greater polymerization stereoregulation *and* higher polymerization rates than systems employing their mononuclear analogs, these differences being quite large in certain cases. As with the mononuclear systems, trends in polymer stereoregularity, the abundances of

specific stereodeflects, polymerization activity, and polymer molar mass are all found to be strongly cocatalyst-dependent. In general, catalyst systems lacking a bridging μ -Me or μ -F cation-anion contact show substantially enhanced rates for both monomer enchainment and stereodeflect-introducing reorganizations and misinsertions. These findings are discussed in detail, with special attention paid to systems in which both high activity and precise stereoregulation are obtained.

EXPERIMENTAL SECTION

Materials and Methods. All manipulations of air-sensitive materials were performed with rigorous exclusion of oxygen and moisture in flamed Schlenk-type glassware on a dual-manifold Schlenk line or interfaced to a high-vacuum line (10^{-6} Torr), or in an N_2 -filled Vacuum Atmospheres or MBraun glove box with a high capacity recirculator (<1 ppm O_2). Argon (Matheson, pre-purified), and propylene (Matheson, polymerization grade) were purified by passage through a supported MnO-packed oxygen removal column and a column packed with activated Davidson 4A molecular sieves. Hydrocarbon solvents (toluene and pentane) were distilled under nitrogen from Na/benzophenone ketyl or passed through columns packed with molecular sieves and supported Cu(0) deoxygenating agent. These solvents were subsequently stored under vacuum over Na/K alloy in Teflon-valved bulbs and distilled on a high-vacuum line immediately prior to use. Deuterated solvents were obtained from Cambridge Isotope Laboratories (all ≥ 99 atom %D), were freeze-pump-thaw degassed, dried over Na/K alloy, and stored in re-sealable flasks. Other nonhalogenated solvents were dried over Na/K alloy, and halogenated solvents were distilled from CaH_2 . $Me_2C(Cp)(Flu)ZrMe_2$ (**1**; Cp = C_5H_4 ,

η^5 -cyclopentadienyl; Flu = C₁₃H₈, η^5 -fluorenyl),²⁰ Me₂Si(OHF)(CpR*)ZrMe₂ (**2**; OHF = C₁₃H₁₆, η^5 -octahydrofluorenyl; CpR* = η^5 -3-(-)-menthylcyclopentadienyl, R* = (1*R*,2*S*,5*R*)-*trans*-5-methyl-*cis*-2-(2-propyl)cyclohexyl ((-)-menthyl)),²¹ B(C₆F₅)₃ (**3**),²² B(*o*-C₆F₅C₆F₄)₃ (**4**),^{9c} Al(C₆F₅)₃·0.5(C₇H₈) (**5**),²³ Ph₃C⁺B(C₆F₅)₄⁻ (**6**),²⁴ and Ph₃C⁺FAl(*o*-C₆F₅C₆F₄)₃⁻ (**7**)^{12a} were prepared according to literature procedures. Ga(C₆F₅)₃ (**8**) was generated *in situ* as described in refs. 13 and 14. Ph₃C⁺FB(C₆F₅)₃⁻ (**9**), Ph₃C⁺FB(*o*-C₆F₅C₆F₄)₃⁻ (**10**), (Ph₃C⁺)_xF_x[Al(C₆F₅)₃]_y^{-x} (x = 1, y = 1, **11**; x = 1, y = 2, **12**; x = 2, y = 3, **13**), Ph₃C⁺(C₆F₅)₃AlFAl(*o*-C₆F₅C₆F₄)₃⁻ (**14**), Ph₃C⁺F[Ga(C₆F₅)₃]₂⁻ (**17**), and Ph₃C⁺XAl(C₆F₅)₃⁻ (X = Cl, **15**; X = Br, **16**) were prepared as described in refs. 13 and 14. Trityl chloride (Ph₃CCl; Aldrich, 98%) was used as received.

Physical and Analytical Measurements. NMR spectra were recorded on Varian UNITY Inova-500 (FT, 500 MHz, ¹H; 125 MHz, ¹³C), UNITY Inova-400 (FT, 400 MHz, ¹H; 100 MHz, ¹³C), Mercury-400 (FT 400 MHz, ¹H; 100 MHz, ¹³C; 377 MHz, ¹⁹F) instruments. Chemical shifts for ¹H and ¹³C spectra were referenced using internal solvent resonances and are reported relative to tetramethylsilane. For ¹³C NMR homopolymer microstructure analyses, 300 -

²⁰ (a) Razavi, A.; Thewalt, U. *J. Organomet. Chem.* **1993**, *445*, 111-114. (b) Razavi, A.; Ferrara, J. *J. Organomet. Chem.* **1992**, *435*, 299-310.

²¹ Obora, Y.; Stern, C. L.; Marks, T. J.; Nickias, P. N. *Organometallics* **1997**, *16*, 2503-2505.

²² Massey, A. G.; Park, A. J. *J. Organomet. Chem.* **1964**, *2*, 245-250.

²³ This compound was prepared as a toluene adduct, see refs 11b and 11c. **CAUTION:** Al(C₆F₅)₃ has been reported to detonate on attempted sublimation at elevated temperatures. Pohlmann, J. L. W.; Brinckmann, F. E. *Z. Naturforsch. B* **1965**, *20b*, 5. Chambers, R. D. *Organomet. Chem. Rev.* **1966**, *1*, 279.

²⁴ (a) Chien, J. C. W.; Tsai, W.-M.; Rausch, M. D. *J. Am. Chem. Soc.* **1991**, *113*, 8570-8571. (b) Yang, X.; Stern, C. L.; Marks, T. J. *Organometallics* **1991**, *10*, 840-842. (c) Ewen, J. A.; Elder, M. J. *Eur. Pat. Appl.* 426637 **1991**; *Chem. Abstr.* **1991**, *115*, 136 987c, 136 988d.

400mg polymer samples were dissolved in 4 mL $C_2D_2Cl_4$ by heating with a heat gun in 10mm NMR tubes, or 50-80mg polymer samples were dissolved in 0.7 mL $C_2D_2Cl_4$ in 5mm NMR tubes. Samples thus prepared were transferred to the NMR spectrometer with the probehead at 125°C, and the probehead and sample were allowed to equilibrate for 10 minutes. A 2.0 s acquisition time was used with a pulse delay of 6.0 s. A total of 4000-6000 transients were accumulated for each spectrum. Pentad signals were assigned according to literature criteria.²⁵ Polymer melting temperatures were measured by differential scanning calorimetry (DSC 2920, TA Instruments, Inc.) from the second scan with a heating rate of 10°C/min. Gel-permeation chromatographic (GPC) analyses of polymer samples were performed at the Dow Chemical Co., Chemical Sciences Catalysis Laboratory, Midland, Michigan, on a Waters Alliance GPCV 2000 high temperature instrument. For each run, a polystyrene/polypropylene universal calibration was carried out using polystyrene standards.

Propylene Polymerization Experiments. Propylene polymerizations were carried out in a 350 mL heavy wall glass pressure reactor (Chemglass Co., maximum pressure, 10 atm), equipped with a septum port, a large stir bar (1000 rpm) to minimize mass transfer effects,²⁶ an

²⁵ (a) Pellecchia, C.; Pappalardo, D.; D'Arco, M.; Zambelli, A. *Macromolecules* **1996**, *29*, 1158. (b) Busico, V.; Cipullo, R.; Corradini, P.; Landriani, L.; Vacatello, M.; Segre, A. L. *Macromolecules* **1995**, *28*, 1887. (c) Miyatake, T.; Miaunuma, K.; Kakugo, M. *Macromol. Symp.* **1993**, *66*, 203. (d) Kakugo, M.; Miyatake, T.; Miaunuma, K. *Stud. Surf. Sci. Catal.* **1990**, *56*, 517. (e) Longo, P.; Grassi, A. *Makromol. Chem.* **1990**, *191*, 2387. (f) Randall, J. C. *J. Polym. Sci., Part B: Polym. Phys.* **1975**, *13*, 889.

²⁶ At 20 °C, rate of C_3H_6 absorption is estimated 0.029 mol/min in toluene at 1.0 atm of C_3H_6 , and propylene mass transfer effects (mass transport coefficient) in the (2-PhInd)₂ZrCl₂/MAO system in toluene (100 mL) are observed to be insensitive to the presence of up to 4 g of isotactic PP with a maximum stirring speed (1460 rpm), See: Lin, S.; Tagge, C. D.; Waymouth, R. M.; Nele, M.; Collins, S.; Pinto, J. C. *J. Am. Chem. Soc.* **2000**, *122*, 11275-11285.

internal thermocouple probe (OMEGA Type K) to monitor possible exotherm effects,^{2d} and connected to a high-pressure manifold equipped with a gas inlet, diaphragm capacitance pressure gauge (0-200 psi), and gas outlet.⁷ **CAUTION: All of these procedures should be performed behind a blast shield.** In a typical procedure, in the glove box, the reactor was charged with dry toluene (50 mL) and the apparatus was assembled, removed, and then connected to the high-pressure manifold. Under rapid stirring, rigorously purified propylene was pressurized into the flask to reach ~ 5 - 6 atm over 5 min, and then slowly released to 1.0 atm over 5 min. This fill and release process was repeated 5 times. The solution was then equilibrated at the desired propylene pressure (1.0-5.0 atm), and the reaction temperature (25°C) was adjusted using an external water bath. The catalytically-active species was freshly generated in 2-4 mL of dry toluene in the glove box. The catalyst solution was then removed from the glove box and quickly injected into the rapidly stirred reaction flask using a gas-tight syringe. The temperature of the reaction mixture during polymerization was monitored in real time using the thermocouple probe. The temperature rise was invariably less than 3°C during these polymerizations, and the temperature was controlled by occasional addition of ice to the external water bath. After a measured time interval, the reaction was quenched by the addition of 10 mL methanol. Another 300-400 mL methanol was then added, and the polymer was collected by filtration, washed with methanol, and dried on the high vacuum line to a constant weight. Polymerization experiments in 1,3-dichlorobenzene were carried out as described above, but with addition of 50 mL dry 1,3-dichlorobenzene by cannula through the septum port. Ion pair complexes were prepared and utilized as described below.

Microstructural Analysis of Polypropylene ^{13}C NMR Spectra. Polymer methyl resonances were assigned according to established criteria,²⁷ and were analyzed at the pentad level. All polymer NMR spectra were collected with identical temperature, solvent, instrument field strength, and acquisition and processing parameters. For systems employing precatalyst **1**, pentad distributions were modeled using the syndiospecific Bernoullian model outlined in Table 16 of Ref. 38a (p. 1316), having probability parameters P_m and P_{mm} of formation for m and mm stereodefects, respectively. Microstructural analyses of polymers prepared using systems with precatalyst **2** are presented in detail in the Discussion.

***In-Situ* Generation of Catalyst Ion Pairs for Polymerization Studies.** $\text{Me}_2\text{C}(\text{Cp})(\text{Flu})\text{ZrMe}_2$ (**1**) or $\text{Me}_2\text{Si}(\text{OHf})(\text{CpR}^*)\text{ZrMe}_2$ (**2**), and the required cocatalyst in a 1:1 ratio were loaded in the glove box into a vial equipped with a septum, and 2.0 – 4.0 mL of toluene was added. The mixture was shaken vigorously at room temperature before use.²⁸ Total amounts used were chosen/refined as required for temperature control and are reported herein (see Tables 1-3).

***In-Situ* Activation of $\text{Me}_2\text{C}(\text{Flu})(\text{Cp})\text{ZrMe}_2$ by 1:1 Ph_3C^+ $\text{FAl}(\text{o-C}_6\text{F}_5\text{C}_6\text{F}_4)_3^-$: $\text{Al}(\text{C}_6\text{F}_5)_3$ for Polymerization.** In the glovebox, Ph_3C^+ $\text{FAl}(\text{o-C}_6\text{F}_5\text{C}_6\text{F}_4)_3^-$ (**7**, 14.0 mg, 0.010 mmol), $\text{Al}(\text{C}_6\text{F}_5)_3$ (**5**, 5.9 mg, 0.010 mmol), and 8.0 mL toluene were loaded into a vial, fitted with a septum. This mixture turned orange immediately. The mixture was next shaken at room temperature for 30 min. $\text{Me}_2\text{C}(\text{Cp})(\text{Flu})\text{ZrMe}_2$ (**1**, 4.0 mg, 0.010 mmol) was then

²⁷ Busico, V.; Cipullo, R.; G. Monaco, R.; Vacatello, M.; Segre, A. L. *Macromolecules* **1997**, *30*, 6251-6263.

²⁸ For cocatalysts **16**, **17**, and **18**, the resulting reaction mixture was injected into the polymerization reactor immediately. No activity was observed when the activation time of **1** + **16** was longer than 20 min.

added to this orange solution. The mixture was shaken vigorously at room temperature for 20 min before use.

***In-Situ* Activation of $\text{Me}_2\text{C}(\text{Flu})(\text{Cp})\text{ZrMe}_2$ by 1:2 $\text{Ph}_3\text{CCl} : \text{Al}(\text{C}_6\text{F}_5)_3$ for Polymerization.** In the glovebox, $(\text{C}_6\text{H}_5)_3\text{CCl}$ (2.8 mg, 0.010 mmol), $\text{Al}(\text{C}_6\text{F}_5)_3$ (**6**, 11.7 mg, 0.020 mmol), and 4.0 mL toluene were loaded into a vial, fitted with a septum. This reaction mixture turned orange immediately, and was monitored by ^{19}F NMR (C_7H_8 , 23°C): δ -123.015 (m, 6 F, *o*-F), -154.960 (m, 3 F, *p*-F), -163.705 (m, 6 F, *m*-F). $\text{Me}_2\text{C}(\text{Cp})(\text{Flu})\text{ZrMe}_2$ (**1**, 3.9 mg, 0.010 mmol) was then added to this orange solution. The mixture was shaken vigorously at room temperature and injected into the polymerization reactor immediately.

***In-Situ* Activation of $\text{Me}_2\text{C}(\text{Flu})(\text{Cp})\text{ZrMe}_2$ by 1:2 $\text{Ph}_3\text{CCl} : \text{Ga}(\text{C}_6\text{F}_5)_3$ for Polymerization.** In the glovebox, $(\text{C}_6\text{H}_5)_3\text{CCl}$ (2.8 mg, 0.010 mmol), $\text{Ga}(\text{C}_6\text{F}_5)_3$ (**8**, 12.0 mg, 0.020 mmol), and 4.0 mL toluene were loaded into a vial, fitted with a septum. This mixture turned orange immediately. $\text{Me}_2\text{C}(\text{Cp})(\text{Flu})\text{ZrMe}_2$ (**1**, 3.9 mg, 0.010 mmol) was then added to this orange solution. The mixture was shaken vigorously at room temperature and immediately injected into the polymerization reactor.

RESULTS

The present series of halo(perfluoroaryl)metallate cocatalysts all activate C_S -symmetric complex **1** and C_1 -symmetric complex **2** to produce ion-pair complexes that are all active for propylene polymerization. These systems exhibit a broad range of activities and stereoselectivities, with selected cases surpassing previously studied catalyst systems in overall performance, giving strong stereoregulation at high polymerization activities. Results are presented in two parts, the first containing results from experiments using precatalyst **1** and the

second giving results from experiments with precatalyst **2**. This is followed by a Discussion in which anion-dependent polymerization features across the present collected results are surveyed and discussed in light of what is known from *ex-situ* study of these systems,¹⁴ and the remarkable combined high activity and stereoregulation performance of cocatalysts **12** and **14** considered in detail.

I. Propylene Polymerization Mediated by $\text{Me}_2\text{C}(\text{Cp})(\text{Flu})\text{ZrMe}_2$ (**1**) Activated with Cocatalysts **5**, **8** - **17**, “ $\text{Ph}_3\text{C}^+ \text{Cl}[\text{Al}(\text{C}_6\text{F}_5)_3]_2^-$,” and “ $\text{Ph}_3\text{C}^+ \text{Br}[\text{Al}(\text{C}_6\text{F}_5)_3]_2^-$.”

Active catalyst systems comprised of the archetypal C_5 -symmetric precatalyst $\text{Me}_2\text{C}(\text{Cp})(\text{Flu})\text{ZrMe}_2$ (**1**; Cp = C_5H_4 , η^5 -cyclopentadienyl; Flu = C_{13}H_8 , η^5 -fluorenyl) activated with cocatalysts **5** and **8** - **17** were investigated in propylene polymerization reactions in toluene solution at 25°C and at 1.0 atm propylene, as were systems **1** + “ $\text{Ph}_3\text{C}^+ \text{Cl}[\text{Al}(\text{C}_6\text{F}_5)_3]_2^-$ ” and **1** + “ $\text{Ph}_3\text{C}^+ \text{Br}[\text{Al}(\text{C}_6\text{F}_5)_3]_2^-$.” The results of these experiments are presented in Table 1 along with results previously obtained from parallel experiments using precatalyst **1** activated with **3**, **4**, **6**, and **7**.⁷ Additionally, system **1** + $(\text{C}_6\text{F}_5)_3\text{AlFAl}(o\text{-C}_6\text{F}_5\text{C}_6\text{F}_4)_3^-$ (**14**) was investigated in polymerizations carried out in toluene solution under 1.0 atm propylene, at reaction temperatures spanning the range -10°C to 60°C, and under 5.0 atm propylene at 60°C. These results appear in Table 2.

Across these collected results, polyolefin product polydispersities are consistent with well-defined single-site processes and are rather anion-insensitive; in contrast, polymer production rates and product molecular weights are highly anion-sensitive. Furthermore, a marked counteranion dependence of product polymer syndiotacticity and relative *m* and *mm* stereodeflect abundance is observed, these new polynuclear perfluoroaryl cocatalysts uniformly

giving enhanced product polymer stereoregularity and exhibiting higher polymerization rates than the corresponding neutrally charged cocatalysts. These anion effects are afforded a detailed treatment in the Discussion section.

As reported previously, the reaction of **1** with cocatalysts **11** - **13** yields mixtures of species $\text{Me}_2\text{C}(\text{Cp})(\text{Flu})\text{ZrMe}^+ \text{FAl}(\text{C}_6\text{F}_5)_3^-$ (**23**) and $\{[\text{Me}_2\text{C}(\text{Cp})(\text{Flu})\text{ZrMe}]_2(\mu\text{-Me})\}^+ [(\text{C}_6\text{F}_5)_3\text{AlFAl}(\text{C}_6\text{F}_5)_3]^-$ (**24**) in different proportions.⁷ These three systems each exhibit similar strong stereoregulation performance ($\sim 86\%$ *rrrr*; Table 1, entries 7-9), with activities being high in general but spanning approximately one order of magnitude. Catalyst system **1** + **12** exhibits the highest polymerization activity among the systems discussed here, outperforming even the highly active benchmark system **1** + $\text{Ph}_3\text{C}^+ \text{B}(\text{C}_6\text{F}_5)_4^-$ (**6**). Fluoro-bridged $\text{Ph}_3\text{C}^+ (\text{C}_6\text{F}_5)_3\text{AlFAl}(o\text{-C}_6\text{F}_5\text{C}_6\text{F}_4)_3^-$ (**14**) also affords high syndiospecificity (85.1% *rrrr*, Table 1, entry 11) and heightened polymerization activity.

The fluoro-bridged gallate cocatalyst **17** also produces highly syndiotactic product polymer (84.3% *rrrr*, Table 1, entry 13), comparable to results achieved with fluoroaluminates **11** - **13**, and exhibits both considerably higher polymerization activity and greater stereoregulation than neutral $\text{Ga}(\text{C}_6\text{F}_5)_3$ (**8**; Table 1, entries 12, 13).²⁹ Importantly, all of these new fluorometallate cocatalysts (**10** - **17**) yield higher product syndiotacticities than do the corresponding neutral cocatalysts **4**, **5**, and **8**, respectively.

The reaction of **1** with the new chloro- and bromoaluminate reagents **15** and **16** produces complex organozirconium mixtures from which only decomposition products can be isolated.¹⁴ However, propylene polymerization experiments again give product polymers with higher

²⁹ Thermal decomposition of the active species may occur at room temperature as the polymerization activity decreases dramatically when prolonged activation times are used in the reaction of **1** with **17**.

syndiotacticity (Table 1, entries 14 and 16) than those produced using the neutral cocatalyst analog **5** (Table 1, entry 6). Note that lower polymerization activities and lower product stereoregularities are observed with haloaluminate cocatalysts **15** and **16** compared to the fluoroaluminate analog. Also note that metallocene **1** can be similarly activated by the reaction product of TrCl or TrBr with Al(C₆F₅)₃ in a 1:2 ratio (**18** and **19**, respectively), and that comparable product syndiotacticities with far greater polymerization activities are achieved (Table 1, entries 15 and 17) in comparison to **1**-based systems activated with isolable cocatalysts **15** and **16**.

The remarkable observed stereocontrol of highly active catalyst system **1** + **14** motivated a survey of the propylene concentration dependence of stereocontrol, activity, and product polymer M_w in these systems. Table 2 presents temperature- and [propylene]-dependence data for **1** + **14**-mediated polymerizations, along with temperature- and [propylene]-dependence data for **1** + **7** that we reported previously.⁷ As in the earlier studies, **1** + **14** exhibits an expected drop in product molar mass and syndiotacticity with rising polymerization temperature. An increase in the rates of both *m* and to a lesser extent *mm* stereodeflect production relative to insertion is also observed (*vide infra* for a detailed analysis of polymer stereodeflect formation and counteranion effects).

II. Propylene Polymerization Mediated by C₁-Symmetric Me₂Si(CpR*)(Octahydrofluorenyl)ZrMe₂ (**2**, R* = (1*R*,2*S*,5*R*)-*trans*-5-methyl-*cis*-2-(2-propyl)cyclohexyl; (-)-menthyl) Activated with Cocatalysts **3**, **6**, **7**, **12** and **14**.

We extend our investigation of cocatalysts **3**, **6**, **7**, **12** and **14** here to include their performance as cocatalysts with C₁-symmetric *ansa*-metallocene precatalyst

Me₂Si(CpR*)(octahydrofluorenyl)ZrMe₂ (**2**, R* = (1*R*,2*S*,5*R*)-*trans*-5-methyl-*cis*-2-(2-propyl)cyclohexyl; (-)-menthyl), known to produce highly isotactic propylene,²¹ and with which preliminary cocatalyst/counteranion effects were also observed.³⁰ Catalyst systems comprised of **2** activated with cocatalysts **3**, **7**, **8**, **12**, and **14** were used in propylene polymerization reactions in toluene solution under 1.0 atm propylene, at 25°C and 60°C, and also in 1,3-dichlorobenzene solution under 1.0 atm propylene at 25°C. Systems **2** + **3**, **2** + **7**, and **2** + **14** were additionally studied in propylene polymerization reactions in toluene solution under 5.0 atm propylene at 60°C. These results are presented in Tables 3 and 4 (see Experimental Section for details and Figure 3 for a graphical representation of polymerization results).

With the exception of **2** + **7** at 25°C, product polydispersities are consistent with well-defined single-site processes. Polymerization activities, product M_w values, product isotacticities, and *rr* stereodeflect abundances are again highly anion-sensitive. The activities of the **12**- and **14**-based catalysts are comparable to that of the B(C₆F₅)₃ (**3**)-derived catalyst. Cocatalyst Ph₃C⁺ B(C₆F₅)₄⁻ (**6**) affords significantly higher activity, in contrast to experiments with metallocene **1** as the precatalyst. Again, the Ph₃C⁺ FAl(*o*-C₆F₅C₆F₄)₃⁻ (**7**)-activated catalyst system exhibits significantly lower activity. Temperature effects are also observed to be significantly cocatalyst-dependent for the C₁-symmetric **2**-based catalyst systems. As with C_S-symmetric precatalyst **1** with the present cocatalysts, product stereoregularity and product molecular weight decrease with increasing temperature.³¹ This effect is most pronounced using

³⁰ Giardello, M. A.; Eisen, M. S.; Stern, C. L.; Marks, T. J. *J. Am. Chem. Soc.* **1995**, *117*, 12114-12129.

³¹ On raising the polymerization temperature, product isotacticity increases for Me₂C(CpR)(Flu)ZrCl₂/MAO while it decreases for Me₂Si(C₅Me₄)(C₅H₃R*)ZrCl₂/MAO. This effect depends on the substituent (R = Me, CMe₂, *t*-Butyl),

cocatalysts **12** and **14**. Surprisingly, activity is also seen to decrease with increasing temperature. This may be due to deactivation via thermal decomposition.

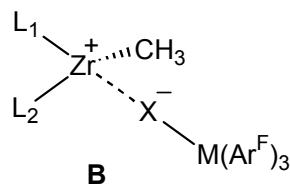
With more polar 1,3-dichlorobenzene as the polymerization solvent, product syndiotacticity, as well as *m* and *mm* stereodefects were indistinguishable for C_S -symmetric **1** + various cocatalyst systems, as reported previously.⁷ In the present study, solvent dependence was also examined for polymerizations mediated by C_1 -symmetric **2** + cocatalysts **3**, **6**, **7**, **12** and **14** under 1.0 atm of propylene pressure at 25°C (Table 4, entries 1-5). As in the case of **1**, compression in the distribution of polymerization activities, product molecular weights, isotacticities, and *rr* stereodefect abundances is observed for the **2**-based catalysts, indicating that polar solvents significantly weaken ion pairing effects on stereocontrol in this system. System **2** + **7** exhibits the most dramatic increase in activity and isoselectivity, again pointing to an exceptionally strong ion-pairing in this system when dissolved in nonpolar media.

DISCUSSION

The activation of group 4 metallocene dimethyls such as **1** or **2** with cocatalysts/activators **3** – **17** yields highly reactive, moisture- and oxygen-sensitive metallocenium perfluoroarylmethylate complexes (eq. 1) that typically exist as 1:1 contact ion-pairs in low- ϵ media, even at catalytically relevant ($<10^{-4}$ M) concentrations.^{10, 11} The anionic portions of these active catalyst systems are in general both sterically encumbered and highly charge-delocalized, exhibiting a rich variety of differing coordinative tendencies, reactivities, and modes of interaction with the cation, and playing a central role in determining the relative

see (a) Kleinschmidt, R.; Reffke, M.; Fink, G. *Macromol. Rapid Commun.* **1999**, *20*, 284-288. (b) Grisi, F.; Longo, P.; Zambelli, A.; Ewen, J. A. *J. Mol. Catal. A: Chem.* **1999**, *140*, 225-233.

rates and stereoselectivities of monomer enchainment, stereodeflect-producing catalyst reorganizations, and polymer chain release processes.^{2, 7} New cocatalysts **9** – **17** (Scheme 1), accessed by combining trityl halides with exceptionally strong perfluoroarylmetalloid Lewis acids, each feature one or more halogen atoms in M–X or M–X–M bonding arrangements, with these metalloid-bound halogen atoms playing a key role in the activation of dimethylzirconocene precatalyst **1** and the cation-anion interactions of the resulting polymerization-active ion-pair complexes (e.g., **B** below). Details of the syntheses, structural, and



solution characteristics of this new series of cocatalysts/activators, as well as their stoichiometric reaction chemistry with $\text{Me}_2\text{C}(\text{Cp})(\text{Flu})\text{ZrMe}_2$ (**1**) and the products of these activation reactions are detailed in a companion contribution.¹⁴

The following Discussion details the performance characteristics of active catalyst systems derived from reaction of C_S -symmetric metallocene **1** with cocatalysts **3** – **17** as mediators for syndiospecific propylene polymerization, and systems derived from reaction of C_1 -symmetric metallocene **2** with cocatalysts **3**, **6**, **7**, **12**, and **14** as mediators for isospecific propylene polymerization. Catalyst system performance is characterized and differentiated herein via the following metrics: a) polymerization activity – here referring to the rate constant for monomer uptake according to the rate law $v_p = k_p[\text{catalyst}][\text{propylene}]$; b) product polymer molar mass distributions – determined by GPC (gel permeation chromatography, also referred to as size exclusion chromatography; see Experimental Section for details); c) polymer melting temperatures – determined via differential scanning calorimetry (see Experimental Section), and

d) the abundances of specific defects in the otherwise stereoregular polymer backbone, as determined by polymer ^{13}C NMR analysis.

This last polymer microstructural metric, described in detail in several reviews and contributions,^{1, 32} is extremely powerful for kinetic analysis of substantially stereoregular polyolefins. The methine carbon atoms in polypropylene will have either *re* (*R*) or *si* (*S*) chirality, and the steric environment experienced by a given methine-bound methyl carbon atom (and thus its ^{13}C NMR chemical shift) will depend on the chirality of the methine carbon to which it is bonded *relative to* the chiralities of its neighbors, and to a lesser degree its neighbors' neighbors, etc. The polymer backbone can be described as consisting of *racemo* (*r*) and *meso* (*m*) steric dyads (adjacent methine stereocenters having different or equal chirality, respectively), with adjacent steric dyads comprising steric triads *mm*, *mr*, and *rr* (see Schemes 2 and 3 for examples), producing characteristic signals in the methyl resonance region of the polymer ^{13}C NMR spectrum (Figure 1). These triad regions contain fine structure associated with longer stereosequences (*n*-ads) that contain the respective triads, and modern high-field NMR techniques allow resolution of a substantial number of these steric *n*-ad resonances.²⁷ The observed distribution across the *n*-ad resonance integrals is a function of the probabilities of the various possible insertion and epimerization events, the outcomes of which determine the chiralities of the methine carbons, and modeling of the steric *n*-ad distribution provides a basis for the estimation of the relative probabilities of these events. Several methods³² have been

³² For recent reviews of propylene insertion, stereoerror production, termination mechanisms, and polypropylene microstructural analysis, see: a) Resconi, L.; Cavallo, L.; Fait, A.; Piemontesi, F. in ref. 1d, 1253 -1346, b) Busico, V.; Cipullo, R. *Prog. Polym. Sci.* **2001**, *26*, 443-533. c) Razavi, A.; Thewalt, U. *Coord. Chem. Rev.* **2006**, *250*, 155-169.

presented for the modeling of experimental steric n -ad distributions via refinement of parameters associated with specific processes thought to occur during propylene polymerization. The most straightforward of these rely on the “stochastic matrix” methodology which can be applied to any catalyst system and generates the probability expressions for all possible steric n -ads as a function of parameters of ones’ choosing.³³

Polypropylenes such as those produced using C_S -symmetric precatalyst **1** + cocatalysts **3** – **17** feature stereosequences consisting substantially of alternating *re* and *si* stereocenters (*r* steric dyads thus predominate), and are termed syndiotactic. This characteristic alternating pattern is generated via consecutive monomer insertions occurring at alternating faces of the catalyst active site, with stereoselectivities that are equal in magnitude but opposite in sense (Scheme 2A). Occasional errors in this regularly alternating succession (“stereodefects”) are generally accepted to arise from a combination of bimolecular monomer misinsertions and unimolecular catalyst-polymeryl stereoinversions (“epimerizations”). The proposed misinsertions include: a) enantiofacial misinsertion – insertion occurring across the “wrong” monomer enantioface (Scheme 2B) and b) back-side misinsertion – insertion at the “wrong” catalyst enantioface (Scheme 2C). The unimolecular catalyst-polymeryl epimerizations include: c) site epimerization – stereoinversion of the catalyst metal center without concomitant insertion (Scheme 2D), and d) chain epimerization – stereoinversion of the polymeryl β carbon atom (Scheme 2E).³² Histories of these events appear in the form of *m* or *mm* stereodefects in the

³³ This is an application of the Markov Chain method, and the stochastic matrix is sometimes referred to as the “transition matrix,” see: A.A. Markov "Extension of the limit theorems of probability theory to a sum of variables connected in a chain," reprinted in Appendix B of: R. Howard. *Dynamic Probabilistic Systems, volume 1: Markov Chains*. John Wiley and Sons, New York, 1971.

polymer backbone, thus contributing to the intensity of *m*- or *mm*-containing steric *n*-ads. For a particular syndiotactic polypropylene polymer sample, the distribution across all observed steric *n*-ads can then be modeled via adjustment of parameters representing the likelihood of events that produce *m* or *mm* stereodeflects (P_m and P_{mm} , respectively) relative to syndiospecific insertion (which produces *r* steric dyads; see Experimental section for details of the parameterization process). The parameter estimates P_m and P_{mm} then constitute key metrics describing the syndioselectivity of the catalyst system. Relative contributions to P_m and P_{mm} from misinsertions vs reorganization processes can be assayed by running series of experiments across which propylene concentration is varied (with all other variables held constant), capitalizing on the differing reaction orders in [propylene] for these processes.^{7, 26, 34}

With metallocene-based catalyst systems employing a C_1 -symmetric precatalyst such as $\text{Me}_2\text{Si}(\text{OHf})(\text{CpR}^*)\text{ZrMe}_2$ (**2**; Scheme 1), the structures and thus the enchainment enantioselectivities of the opposing catalyst sides (directions of monomer approach) are unequal. Moreover, the preferred propylene enantioface may be the same at both sides, or it may not, depending on the details of the active catalyst structure and dynamics, as well as the shape of the potential surface associated with the olefin enchainment process.³⁵ The stereosequences of

³⁴ See, for example: a) Resconi, L.; Fait, A.; Piemontesi, F.; Colonna, M.; Rychlicki, H.; Ziegler, R. *Macromolecules* **1995**, *28*, 6667-76, b) Busico, V.; Cipullo, R.; Cuttillo, F.; Vacatello, M. *Macromolecules* **2002**, *35*, 349-354. c) Nele, M.; Pinto, J. C.; Mohammed, M.; Collins, S. *J. Polym. Sci., A: Polym. Chem.* **2005**, *43*, 1797-1810, Lahelin, M.; Kokko, E.; Lehmus, P.; Pitkaenen, P.; Lofgren, B.; Seppaelae, J. *Macromol. Chem. Phys.* **2003**, *204*, 1323-1337.

³⁵ For relevant computational studies see: a) Tobisch, S.; Ziegler, T. *Organometallics* **2005**, *24*, 256-265, b) Tobisch, S.; Ziegler, T. *Organometallics* **2004**, *23*, 4077-4088, c) Cavallo, L. in *Catalysis by Metal Complexes*; Maseras, F.; Lledós, A.; Eds.; *Computational Modeling of Homogeneous Catalysis*, Kluwer Academic Publishers: Dordrecht, the

polypropylenes prepared using metallocene **2** activated with cocatalysts **3** – **17** consist predominantly of *m* dyads (such polypropylenes are termed isotactic). In principle, the same processes that are described above for the C_5 -symmetric catalyst case are also possible for C_1 -symmetric systems, but with different consequences for the stereosequencing of the polymer backbone (Scheme 3). In the C_1 -symmetric case, site epimerization, occurring with different probabilities at the different enantiofaces of the catalyst active site, may be a key factor in determining stereoregularity, since the catalyst faces are *a priori* expected to exhibit different enantioselectivities. However, the kinetic and microstructural signatures of chain epimerization (Scheme 3E) and site epimerization are indistinguishable from one another, as both processes give rise to changes in *rr* stereodeflect abundance, and both have the same reaction order (zero, in this case) in propylene. For the same reason, back-side misinsertion cannot readily be distinguished from enantiofacial misinsertion here (both processes also produce isolated *rr* stereodeflects and are putatively first-order in [propylene]; see Schemes 3B and 3D). Differences in enantioselectivity should in principle allow for differentiation of site epimerization rates: if, for example, site epimerization (rather than insertion) at the less selective catalyst side can be induced to increase – by an increase in reaction temperature or reduction in monomer concentration – then overall polymer stereoregularity can be expected to increase. However, changes in overall polymer stereoregularity are not as descriptive of mechanistic details as are the abundances of specific stereosequences, the principal difference being in the level of detail.

Netherlands, 2002; Vol. 25, pp 23-56, d) Jensen, V. R.; Borve, K. J. *J. Comp. Chem.* **1998**, *19*, 947-960, e) Lanza, G.; Fragala, I. L.; Marks, T. J. *Organometallics* **2002**, *21*, 5594-5612, f) Lanza, G.; Fragala, I. L.; Marks, T. J. *Organometallics* **2001**, *20*, 4006-4017, g) Lanza, G.; Fragala, I. L.; Marks, T. J. *J. Am. Chem. Soc.* **2000**, *122*, 12 764-12 777.

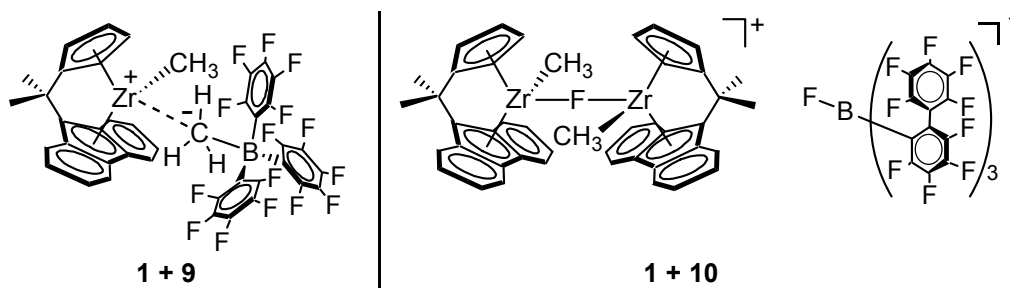
The modeling of steric n -ad distributions in isotactic polypropylenes produced using C_1 -symmetric precatalysts such as **2** is complicated by the fact that the probabilities for different insertion and epimerization events depend on which side of the catalyst is employed; this effectively doubles the number of parameters required for accurate description of polymerization stereoselectivity. Moreover, we have found (*vide infra*) that parameterizations in which this property of C_1 -symmetric systems is accounted for contain inherent parameteric intercorrelations that seriously compromise the extension of this analytical method to the C_1 -symmetric case.

This Discussion is presented in five parts: the first three address catalyst systems derived from C_S -symmetric **1** activated with the present B-, Al- and Ga-containing species, respectively, each section beginning with a brief overview what is known of the structural and solution characteristics and reactivities of each catalyst system, thus setting the stage for a discussion of the nature of the active catalysts under polymerization conditions as manifested in polymerization activities, product polymer molar masses, and product stereoregularities. Al-based system **1** + **14**, yielding a single isolable product ion-pair complex, is unique for its unusual pairing of high activity and excellent stereoregulation performance, and is thus afforded a detailed examination, with studies of both reaction temperature and monomer concentration effects. The fourth part of the Discussion extends and generalizes findings on counteranion effects seen in systems employing C_S -symmetric precatalyst **1**, describing polymerization results from C_1 -symmetric metallocene **2** activated with cocatalysts **3**, **6**, **7**, **12**, and **14**, and describing the effects of varying monomer concentration and solvent polarity for systems **2** + **3**, **2** + **7**, and **2** + **14**. The fifth section is devoted to the challenge of microstructural analysis for polymers produced using C_1 -symmetric metallocene-based catalyst systems. Herein, a series of parameterizations based on different sets of mechanistic possibilities is presented, along with the

results of application of these models to the present data, and a novel numerical method for identifying parametric intercorrelations in these models.

I. Catalyst Systems Derived From $\text{Me}_2\text{C}(\text{Cp})(\text{Flu})\text{ZrMe}_2$ (**1**) Activated with Trityl Perfluoroaryl Fluoroborates $\text{Ph}_3\text{C}^+ \text{FB}(\text{C}_6\text{F}_5)_3^-$ (**9**) and $\text{Ph}_3\text{C}^+ \text{FB}(o\text{-C}_6\text{F}_5\text{C}_6\text{F}_4)_3^-$ (**10**).

As judged by *in-situ* NMR analysis, metallocene $\text{Me}_2\text{C}(\text{Cp})(\text{Flu})\text{ZrMe}_2$ (**1**) reacts readily with cocatalysts **9** and **10**, with methide transfer from the metallocene to the Ph_3C^+ cation and subsequent B–F bond cleavage in both cases. While these chemistries are similar, the soluble reaction products are rather different: **1** + **9** gives $\text{Me}_2\text{C}(\text{Cp})(\text{Flu})\text{ZrMe}^+ \text{MeB}(\text{C}_6\text{F}_5)_3^-$ in 30% yield, and features an intimate cation-anion contact mediated by the $\text{MeB}(\text{C}_6\text{F}_5)_3^-$ methyl substituent (depicted below; this species is also produced via reaction of **1** with $\text{B}(\text{C}_6\text{F}_5)_3$ in quantitative yield).⁷ Yields and reaction stoichiometries for reaction of **1** with **9** suggest formation of an insoluble zirconocene fluoride side-product. ^{19}F NMR spectra of the crude reaction mixture in toluene- d_8 give no evidence of persisting B–F or Zr–F linkages. In contrast, system **1** + **10** affords diastereomeric $[\text{Me}_2\text{C}(\text{Cp})(\text{Flu})\text{ZrMe}]_2(\mu\text{-F})^+ \text{FB}(o\text{-C}_6\text{F}_5\text{C}_6\text{F}_4)_3^-$,



exhibiting no preferred cation-anion contact, together with one equivalent free $\text{B}(o\text{-C}_6\text{F}_5\text{C}_6\text{F}_4)_3$ present in the crude reaction mixture.

Not surprisingly, polymerization results from system **1** + **9** are quite similar to results with catalyst system **1** + $\text{B}(\text{C}_6\text{F}_5)_3$ (**3**), affording similar polymer melting temperatures, molar

mass distributions, and parameter estimates P_m and P_{mm} (see Table 1, entries 1 and 2). Based on these results, it appears highly likely that the active catalysts in systems **1** + **9** and **1** + **3** are identical. The difference in activities can be accounted for in light of the comparatively low yield of $\text{Me}_2\text{C}(\text{Cp})(\text{Flu})\text{ZrMe}^+ \text{MeB}(\text{C}_6\text{F}_5)_3^-$ in reaction of precatalyst **1** with cocatalyst **9**.

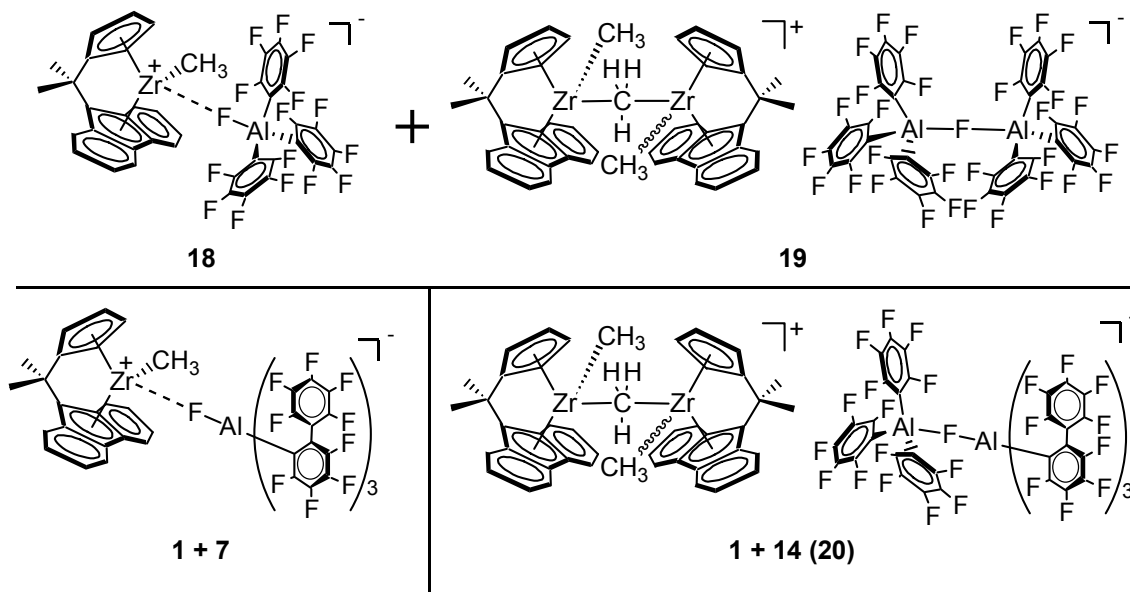
Interestingly, the polymer produced using catalytic system **1** + **10** is also quite similar to that produced using **1** activated with the neutral analog of cocatalyst **10**, $\text{B}(\text{o-C}_6\text{F}_5\text{C}_6\text{F}_4)_3$ (**4**), again with diminished activity (Table 1, entries 3 and 4). While *in-situ* NMR monitoring of the reaction of **1** + **10** indicates ultimate formation of $[\text{Me}_2\text{C}(\text{Cp})(\text{Flu})\text{ZrMe}]_2(\mu\text{-F})^+ \text{FB}(\text{o-C}_6\text{F}_5\text{C}_6\text{F}_4)_3^-$ ¹⁴ together with one equivalent of **4**, transient μ -methyl bridged dinuclear diastereomers $[\text{Me}_2\text{C}(\text{Cp})(\text{Flu})\text{ZrMe}]_2(\mu\text{-Me})^+ \text{MeB}(\text{o-C}_6\text{F}_5\text{C}_6\text{F}_4)_3^-$ are also observed, being the product of reaction **1** + **4**,⁷ and probably arise when free $\text{B}(\text{o-C}_6\text{F}_5\text{C}_6\text{F}_4)_3$ is released upon F atom transfer from **10** to form **21**. The marked similarity in polymerization results between **1** + **10** and **1** + **4** suggests that the active species in these reactions are again the same, and that the observed μ -fluoride bridged dinuclear species (depicted above) has no or extremely low polymerization activity. Another possibility is that, assuming that in this case polymerization proceeds by insertion of propylene into a Zr-C bond and that at least one Zr-F bond remains intact during polymerization, a neutral $\text{Me}_2\text{C}(\text{Cp})(\text{Flu})\text{ZrMeF}$ is close at hand and interacting with the polymerization-active, cationic Zr center as a Lewis base, and that the stereoselectivity of this system is similar to that of **1** + **4** by sheer coincidence.

II. Catalyst Systems Derived From C_s -Symmetric $\text{Me}_2\text{C}(\text{Cp})(\text{Flu})\text{ZrMe}_2$ (1**) Activated with Trityl Perfluoroaryl Fluoroaluminates $(\text{Ph}_3\text{C}^+)_x \text{F}_x[\text{Al}(\text{C}_6\text{F}_5)_3]_y^{x-}$ ($x = 1, y = 1$, **11**; $x = 1, y = 2$, **12**; $x = 2, y = 3$, **13**), $\text{Ph}_3\text{C}^+ (\text{C}_6\text{F}_5)_3\text{AlFAl}(o\text{-C}_6\text{F}_5\text{C}_6\text{F}_4)_3^-$ (**14**), $\text{Ph}_3\text{C}^+ \text{XAl}(\text{C}_6\text{F}_5)_3^-$ ($\text{X} = \text{Cl}$, **15**; $\text{X} = \text{Br}$, **16**), and “ $\text{Ph}_3\text{C}^+ \text{X}[\text{Al}(\text{C}_6\text{F}_5)_3]_2^-$ ” ($\text{X} = \text{Cl}$; $\text{X} = \text{Br}$)**

As judged by NMR spectroscopy, metallocene $\text{Me}_2\text{C}(\text{Cp})(\text{Flu})\text{ZrMe}_2$ (**1**) reacts readily with cocatalysts **11** – **13**, accompanied by methide transfer from the metallocene to the Ph_3C^+ cation but without the formal F atom transfer to Zr observed in the B-based systems. Also, whereas the active catalysts generated using fluoroborates **9** and **10** appear to be the same as those formed with their neutral borane analogs **3** and **4**, this is not the case with the present fluoroaluminate systems.

Activation of **1** with each member of the series $(\text{Ph}_3\text{C}^+)_x \text{F}_x[\text{Al}(\text{C}_6\text{F}_5)_3]_y^{x-}$ (Scheme 1; $x = 1, y = 1$, **11**; $x = 1, y = 2$, **12**; $x = 2, y = 3$, **13**) produces the same two metallocenium ion-pair complexes, mononuclear $\text{Me}_2\text{C}(\text{Cp})(\text{Flu})\text{ZrMe}^+ \text{FAl}(\text{C}_6\text{F}_5)_3^-$ (**18**) and dinuclear diastereomeric $[\text{Me}_2\text{C}(\text{Cp})(\text{Flu})\text{ZrMe}]_2(\mu\text{-Me})^+ \text{F}[\text{Al}(\text{C}_6\text{F}_5)_3]_2^-$ (**19**), with each system gradually decomposing to pure $\text{Me}_2\text{C}(\text{Cp})(\text{Flu})\text{ZrMe}^+ \text{FAl}(\text{C}_6\text{F}_5)_3^-$ (**18**). Their observed ordering in increasing initial **19**:**18** ratio, **1** + **11** (~1:1) < **1** + **13** (~2:3) < **1** + **12** (~1:2)¹⁴ tracks their orders in increasing activity and diminishing stereoregulation, with product syndiotacticities ranging from 85.5% *rrrr* to 86.5% *rrrr* (Table 1, entries 7 – 9), arguing: a) that dinuclear species **19** persists during polymerization without decomposing to form species **18**, b) trinuclear species **13**, whose activation chemistry resembles that of a 1:1 mixture of **11** and **12**, shows analogous polymerization behavior, and c) that, while both ion pairs **18** and **19** are polymerization-active, **19** is more active but less stereoregulating than monomeric **18**. This is in accord with previously observed results:⁷ system **1** + mononuclear fluoroaluminate $\text{Ph}_3\text{C}^+ \text{FAl}(o\text{-C}_6\text{F}_5\text{C}_6\text{F}_4)_3^-$ (**7**), exhibiting a kinetically inert Zr–

1 + 11, 1 + 12, 1 + 13:

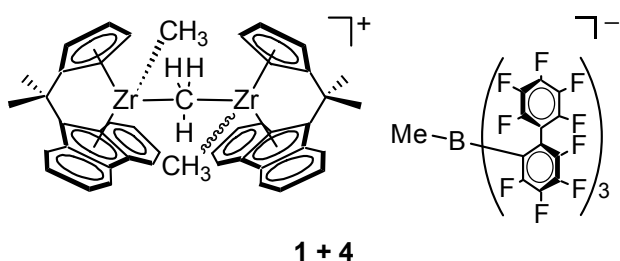


F–Al linkage, shows exceptional polymerization stereoregulation, but with substantially diminished polymerization activity (Table 1, entry 10), consistent with the hypothesis that, in these systems, direct cation-anion interaction via a μ -fluoro bridge (present in **18** but absent in **19**) significantly attenuates propylene insertion but enhances stereoregulation, suppressing the relative rates vs. propagation of both misinsertion and catalyst-polymeryl epimerization pathways.

Asymmetric dinuclear cocatalyst $\text{Ph}_3\text{C}^+ (\text{C}_6\text{F}_5)_3\text{AlFAl}(o\text{-C}_6\text{F}_5\text{C}_6\text{F}_4)_3^-$ (**14**; Scheme 1) activates precatalyst **1** to form stable, diastereomeric $[\text{Me}_2\text{C}(\text{Cp})(\text{Flu})\text{ZrMe}]_2(\mu\text{-Me})^+ (\text{C}_6\text{F}_5)_3\text{AlFAl}(o\text{-C}_6\text{F}_5\text{C}_6\text{F}_4)_3^-$ (**20**), with no formation of a mononuclear analog observed in an *in-situ* NMR study of the activation reaction. Comparison of crystallographic data^{13, 14} indicates that the anion in active catalyst system **1 + 14** is structurally similar to the anion in the trityl salt cocatalyst **14**, with neither ion-pair exhibiting any specific cation-anion interaction in the solid state. ¹⁹F NMR spectroscopic features of these two species are essentially identical, of particular note since in system **1 + 14**, any direct interaction between the Zr ion and the bridging μ -F

moiety is expected to have a profound effect on the ^{19}F NMR chemical shift of the latter.¹⁴

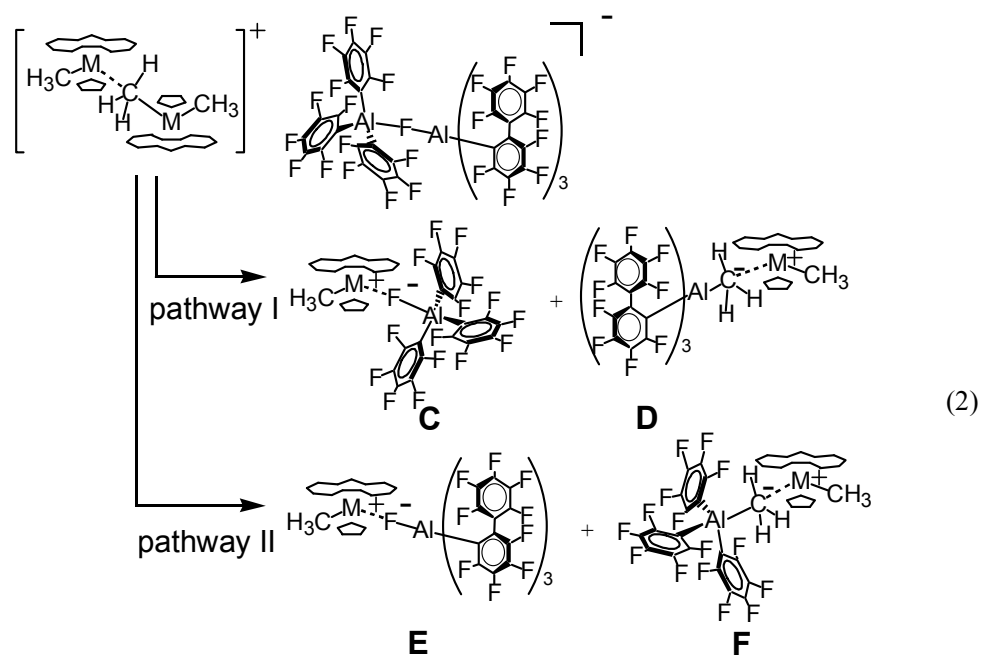
Bridged dinuclear diastereomeric catalyst **1** + **14** (**20**) is highly active for propylene polymerization, and exhibits high overall syndiospecificity (85.1% *rrrr*) with low calculated *m* and *mm* stereodeflect production parameters (Table 1, entry 11). Based on NMR and structural data, this system and species **19** above might be expected to exhibit polymerization activity and stereoregulation characteristics similar to **1** + $\text{B}(o\text{-C}_6\text{F}_5\text{C}_6\text{F}_4)_3$ (**4**), as both systems feature



dinuclear, μ -methyl bridged cationic fragments together with bulky, apparently noninteracting anions. Comparison of polymerization results from systems **1** + **4** and **1** + **14** (Table 1, entries 3 and 11) reveals that, while activities are indeed similar, *rrrr* pentad fractions are dramatically different (82.3% for **1** + **4** vs 85.1% for **1** + **14**), with calculated stereodeflect probabilities P_m and P_{mm} both elevated in system **1** + **4** ($P_m = 2.41\%$ and $P_{mm} = 1.96\%$) compared to system **1** + **14** ($P_m = 2.10\%$ and $P_{mm} = 1.45\%$), suggesting a profound differential counteranion effect.

To understand the above results, there are several possibilities to consider: first, one or the other of these systems may actually contain multiple active species, with distributions across species possibly evolving over the course of polymerization. Reactions with such systems often yield polymeric materials having broad or even polymodal molar mass distributions (seen numerically in large polydispersity indices M_w/M_n) or multiple melt endotherms. Importantly, neither catalyst system **1** + **14** nor **1** + **4** exhibits these features, which while not rigorously proving the presence of uniform catalytically-active species, is consistent with and is the

generally accepted criterion for a single-catalyst scenario.^{1,2} Another possibility is that either **1** + **4** or **1** + **14** undergoes a rapid and complete transformation yielding a fundamentally different catalyst structure from that observed in *ex-situ* studies. In either case, this might involve release of free $\text{Me}_2\text{C}(\text{Cp})(\text{Flu})\text{ZrMe}_2$ upon initiation of polymerization. With **1** + **4**, the presence of excess free $\text{B}(\text{o-C}_6\text{F}_5\text{C}_6\text{F}_4)_3$ would then lead to an improvement in activity, as the newly liberated $\text{Me}_2\text{C}(\text{Cp})(\text{Flu})\text{ZrMe}_2$ becomes activated. This, however, is not observed. For **1** + **14**, there are multiple reaction pathways that might be considered: during polymerization, system **1** + **14** could remain (more or less) intact as species **20**, or separate into two distinct mononuclear ion-pair complexes, according to eq. 2:

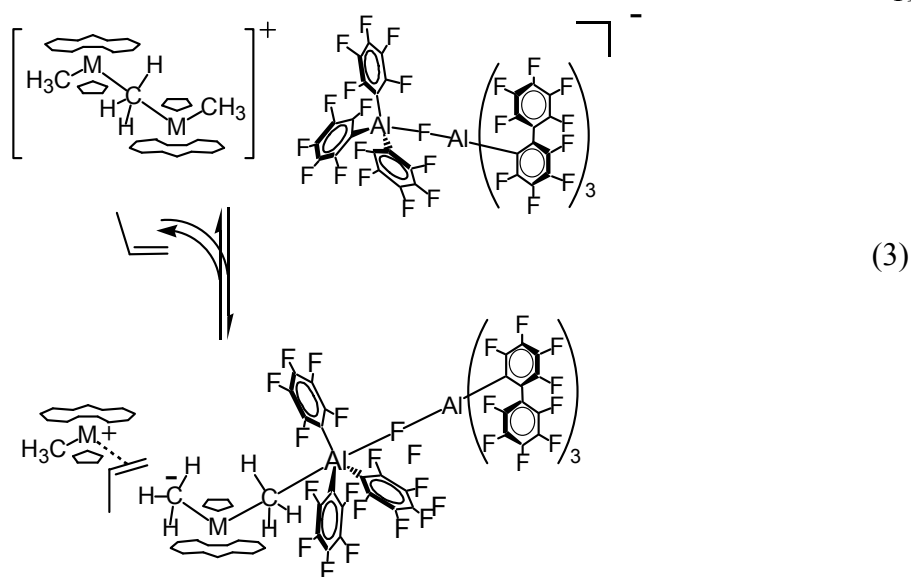


Let us consider the first pathway. In isolation, **1** + **14** does not spontaneously undergo this transformation, possibly reflecting the instability of a neutral $\text{Al}(\text{o-C}_6\text{F}_5\text{C}_6\text{F}_4)_3$ fragment (which, in fact, is found to be insoluble);^{12b} formation of the C–Al bond of $\text{H}_3\text{CAl}(\text{o-C}_6\text{F}_5\text{C}_6\text{F}_4)_3^-$ directly via methide transfer from a neutral metallocene dimethyl to the $[(\text{C}_6\text{F}_5)_3\text{AlFAl}(\text{o-C}_6\text{F}_5\text{C}_6\text{F}_4)_3]^-$ anion via an associative process is unlikely as well, considering the significant steric shielding of

the Al center outer face by the *o*-C₆F₅C₆F₄ ligands.¹⁴ Thus, species **D** of pathway I is unlikely. The second pathway is more reasonable in light of the known behaviors of participating systems; species **E** of pathway II is identical to the active species generated in system **1** + **7**, and species **F**, although inisolable, is expected to resemble the reaction product from **1** + Al(C₆F₅)₃ (**5**), which produces polypropylene but with marginal activity (Table 1, entry 6). However, the polymerization results are inconsistent with this sequence of events as well: firstly, catalysts **1** + **7** and **1** + **14** show widely disparate propensities for stereoerror production (**1** + **7** gives P_m = 0.86% and P_{mm} = 1.52% whereas **1** + **14** gives P_m = 2.10% and P_{mm} = 1.45%); secondly, system **1** + **14** shows a 20-fold higher activity than system **1** + **7**. These results suggest that the anionic portion of species **20** does not fragment irreversibly during polymerization. It is also conceivable that the FAl(*o*-C₆F₅C₆F₄)₃⁻ moiety remains in intimate contact with Al(C₆F₅)₃ and impinges upon the active catalyst metal center, in a reversible version of pathway II above, with Me₂C(Cp)(Flu)ZrMe₂•Al(C₆F₅)₃ acting in an intermediary capacity, or in both modes (eq. 3).

No spectroscopic evidence for a rearrangement analogous to pathway II in eq. 2, nor for the formation of the π -olefin complex³⁶ depicted in eq. 3, obtains from *ex-situ* studies of isolated **1** + **14**. In any event, it is evident that the (C₆F₅)₃AlFAl(*o*-C₆F₅C₆F₄)₃⁻ anion persists during and is intimately involved in polymerization processes. Moreover, the dependence of propylene insertion rates on reaction temperature indicates that the catalyst system may have access to multiple active modes (*vide infra*).

³⁶ a) Stoebenau, E. J., III; Jordan, R. F. *J. Amer. Chem. Soc.*, **2003**, *125*, 3222-3223, b) Casey, C. P.; Carpenetti, D. W., II. *Organometallics* **2000**, *19*, 3970-3977, c) Casey, C. P.; Fisher, J. J. *Inorg. Chim. Acta*, **1998**, *270*, 5-7. d) Casey, C. P.; Hallenbeck, S. L.; Pollock, D. W.; Landis, C. R. *J. Amer. Chem. Soc.*, **1995**, *117*, 9770-9771.



The remarkable product syndiotacticity and very high polymerization activity observed with C_5 -symmetric metallocene precatalyst **1** using fluoro-bridged dinuclear cocatalyst **14** as the activator at 25°C motivated temperature- and [propylene]-dependence studies of this system, for comparison with previously characterized catalyst-cocatalyst systems.⁷ Table 2 presents temperature- and [propylene]-dependence data from **1** + **14** polymerizations, along with previously reported temperature- and [propylene]-dependence data for **1** + **7**, as a basis for comparison.⁷ As in the previously studied cases, **1** + **14** exhibits an expected drop in product molar mass and syndiotacticity with rising polymerization temperature. An increase in the probabilities of both *m* and to a lesser extent *mm* stereodeflect production relative to insertion is also observed. Inspection of Arrhenius plots ($-\ln(k_p)$ vs T^{-1}) for systems **1** + **7** and **1** + **14** (Figure 2) provides added insight into the differences between these two catalytic systems. With **1** + **7**, this plot is linear as expected for a system in which the rate law is invariant with temperature. This indicates that: a) the catalyst system does not show appreciable temperature-dependent decomposition/deactivation behavior over the temperature range, -10 to 25°C, and b) there is only one accessible activation barrier (likely indicating the presence of only one form of active

species). However, with catalyst system **1 + 14**, this plot appears to deviate significantly from linearity, indicating that at least one of the above conditions is violated. Our observations with system **1 + 14** indicate that, with the exception of reactions carried out at 60°C, propylene consumption rates remain constant over the course of polymerization, suggesting that the first condition stated above is not violated. The latter condition could be violated if the catalyst system produces multiple noninteracting active species, however at all reaction temperatures we observe monomodal polymer molar mass distributions having polydispersities ($M_w/M_n \approx 2.0$) consistent with a single, nonliving catalyst (Table 2). Another possibility is that multiple insertion pathways are available, the relative contributions of which are temperature-dependent. This scenario is consistent with a complex catalytic system exhibiting multiple possible modes of cation-anion interaction. Although the data do not favor any specific interpretation of how this might be manifested, one possibility is that an equilibrium following pathway II (eq. 2 above) is operative, with a temperature dependence in equilibrium position.

Increasing the propylene concentration is known to increase the rates of [propylene]-dependent processes vs. those of competing unimolecular processes,³⁷ the effect being greater in systems where unimolecular processes are more facile. Thus, for example, [propylene]-dependent monomer insertion is enhanced vs. unimolecular site epimerization,³⁸ reducing *m*

³⁷ (a) Resconi, L.; Cavallo, L.; Fait, A.; Piemontesi, F. *Chem. Rev.*, **2000**, *100*, 1253-1345. (b) Coates, G. W. *Chem. Rev.*, **2000**, *100*, 1223-1252. (c) Veghini, D.; Henling, L. M.; Burkhardt, T. J.; Bercaw, J. E. *J. Am. Chem. Soc.* **1999**, *121*, 564-573. (d) Ewen, J. A.; Jones, R. L.; Razavi, A.; Ferrara, J. D. *J. Am. Chem. Soc.* **1988**, *110*, 6255-6256.

³⁸ Site epimerization, a stereoinversion at Zr without concomitant propylene insertion, introduces isolated *m* stereodefects in the polymer backbone and is zero-order in [propylene]; see refs. 7 and 37.

stereodeflect abundance and increasing the *rrrr* pentad fraction, while chain release via polymeryl transfer to propylene is enhanced vs. chain release via unimolecular β -hydrogen elimination, lowering M_w inasmuch as β -hydrogen elimination is significant. In the present work, the rates of each of these individual processes are significantly and systematically dependent on cation-anion pairing in the catalyst ion-pair complex, making [propylene]-dependence experiments an important tool in understanding ion pairing effects in single-site olefin polymerization systems. The present studies of the [propylene]-dependence of stereodeflect production using precatalyst **1** and various cocatalysts reveal that: a) increased propylene concentrations are generally accompanied by increases in syndiotacticity, and b) decreases in *m* stereodeflect abundance with corresponding increasing propylene concentration are greater with anions believed to be more weakly coordinating, such as $B(C_6F_5)_4^-$ and $MeB(o-C_6F_5C_6F_4)_3^-$, suggesting that site epimerization in these systems is in general faster.⁷ With increased monomer concentrations (0.36M \rightarrow 2.05M, see Table 2),³⁹ catalyst system **1** + **14** evidences a substantial decrease in the probability of *m* stereodeflect production vs insertion (P_m) and a slight increase in the probability of *mm* stereodeflect production (P_{mm}), with a net increase in total *rrrr* pentad content (63.4 \rightarrow 78.4% *rrrr*, entries 6 and 7). These increases in *rrrr* pentad content are larger than observed for catalyst system **1** + $Ph_3C^+ FAI(o-C_6F_5C_6F_4)_3^-$ (**7**; 70.3 \rightarrow 80.6%), but less than the dramatic increase observed for catalyst system **1** + $Ph_3C^+ B(C_6F_5)_4^-$ (**6**; 50.5 \rightarrow 70.2%).⁴⁰ These results indicate that for **1** + **14**, as with **1** + **7**, *m* stereodeflect production is largely due to unimolecular

³⁹ An empirical model for calculation of solution-phase composition of propylene solutions in toluene and isododecane under relevant conditions is presented in (a) Dariva, C.; Lovisi, H.; Santa Mariac, L. C.; Coutinho, F. M. B.; Oliveira, J. V.; Pinto, J. C. *Can. J. Chem. Eng.* **2003**, *81*, 147-152.

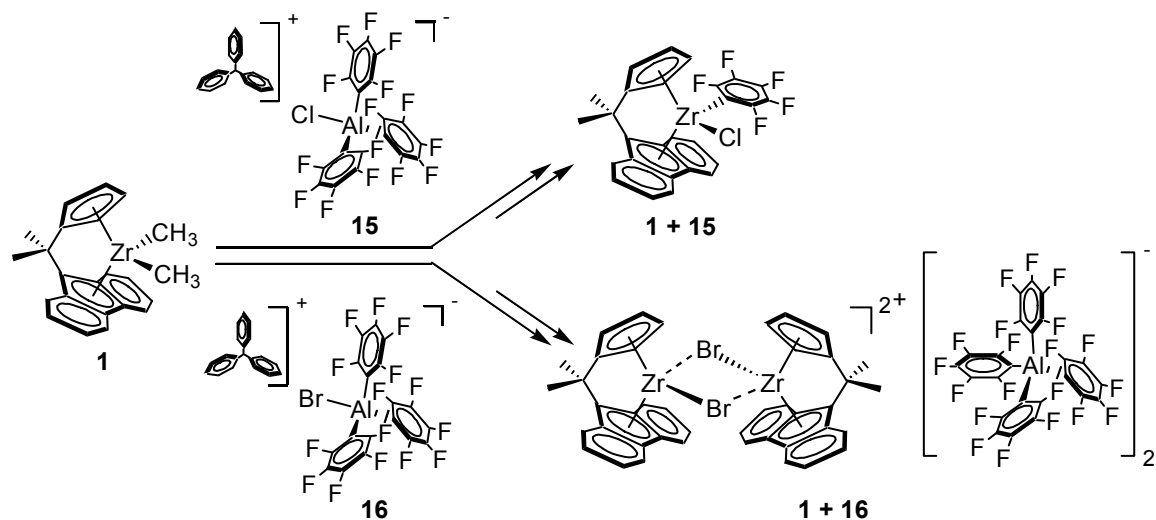
⁴⁰ See entries 16 and 20 of Table 8 in Ref. 7.

site epimerization (Scheme 2D), but that the *mm* stereodeflects arise principally from bimolecular enantiofacial misinsertion (Scheme 2B). Since from these results it appears likely that multiple catalytic modes are operative with the **1** + **14** catalyst system, accurate estimates of kinetic parameters for these processes are inaccessible for individual catalytically active species. In contrast to previously studied systems, increases in product molecular weight are not significant with **1** + **14**, arguing that [propylene]-dependent termination (β -hydrogen transfer to propylene) is significant in comparison with unimolecular termination.⁴¹

In chemistry analogous to the synthesis of species $\text{Ph}_3\text{C}^+ \text{FAl}(\text{C}_6\text{F}_5)_3^-$ (**11**), isolable trityl tris(perfluorophenyl) chloro- or bromoaluminates $\text{Ph}_3\text{C}^+ \text{XAl}(\text{C}_6\text{F}_5)_3^-$ (Scheme 1, X = Cl, **15**; X = Br, **16**) are accessible via reaction of trityl chloride or trityl bromide with $\text{Al}(\text{C}_6\text{F}_5)_3$ (**5**) in 1:1 ratio. Haloaluminates **15** and **16** react rapidly with metallocene $\text{Me}_2\text{C}(\text{Cp})(\text{Flu})\text{ZrMe}_2$ (**1**) forming complex mixtures, that upon attempted purification yielded only decomposition products $\text{Me}_2\text{C}(\text{Cp})(\text{Flu})\text{ZrCl}(\text{C}_6\text{F}_5)$ (from **1** + **15**) and $[\text{Me}_2\text{C}(\text{Cp})(\text{Flu})\text{Zr}(\mu_2\text{-Br})_2]^{2+} [\text{Al}(\text{C}_6\text{F}_5)_4]_2^-$ (from **1** + **16**).¹⁴ The crude mixtures from these reactions are, however moderately active for propylene polymerization (Table 1, entries 14 and 16). Whereas dinuclear fluoroaluminate cocatalyst $\text{Ph}_3\text{C}^+ \text{F}[\text{Al}(\text{C}_6\text{F}_5)_3]_2^-$ (**12**) is also isolable, the chloro- and bromo-analogs are not; however, preparations containing either trityl chloride or trityl bromide and **5** in 1:2 ratio do activate metallocene precatalyst **1** to afford polymerization-active catalyst systems (Table 1, entries 15 and 17). Interestingly, catalyst systems using the putative dinuclear haloaluminates are significantly more active than those of their mononuclear analogs. Comparison of product polymers across this series reveals that, while the active catalyst operating in **1** + $\text{Ph}_3\text{C}^+ \text{ClAl}(\text{C}_6\text{F}_5)_3^-$ (**15**) may be substantially similar to its dinuclear analog, this

⁴¹ Liu, Z.; Somsook, E.; White, C. B.; Rosaaen, K. A.; Landis, C. R. *J. Am. Chem. Soc.* **2001**, *123*, 11193-11207.

does not appear to be the case with **1** + $\text{Ph}_3\text{C}^+ \text{ClAl}(\text{C}_6\text{F}_5)_3^-$ (**16**), the dinuclear analog here



affording reduced stereoselectivity. These polymerization results, together with previously reported NMR, structural, and reactivity studies,^{13, 14} indicate that the chloro- and bromoaluminates are significantly less stable with respect to halogen atom transfer to Zr than are the fluoroaluminates.

III. Catalyst System Derived From C_s -Symmetric $\text{Me}_2\text{C}(\text{Cp})(\text{Flu})\text{ZrMe}_2$ (**1**) Activated with Trityl Perfluoroaryl Fluorogallate $\text{Ph}_3\text{C}^+ \text{F}[\text{Ga}(\text{C}_6\text{F}_5)_3]_2^-$ (**17**).

Isolable trityl fluorobis[tris(perfluorophenyl)gallate] ($\text{Ph}_3\text{C}^+ \text{F}[\text{Ga}(\text{C}_6\text{F}_5)_3]_2^-$; **17**) is accessible via reaction of trityl fluoride with *in situ*-generated $\text{Ga}(\text{C}_6\text{F}_5)_3$ (**8**). Activation of metallocene $\text{Me}_2\text{C}(\text{Cp})(\text{Flu})\text{ZrMe}_2$ (**1**) with both dinuclear **17** and neutral analog **8** yield multiple unidentifiable, insoluble species, as reported previously.¹⁴ Nonetheless, these mixtures are active for propylene polymerization (Table 1, entries 12 and 13). Catalyst system **1** + **17** gives a highly syndiotactic product, comparable with results achieved with fluoroaluminates **11** - **13**, and exhibits both polymerization activity and syndioselectivity that are superior to system **1** + $\text{Ga}(\text{C}_6\text{F}_5)_3$ (**8**; Table 1, entries 12, 13).²⁹

IV. Propylene Polymerization Mediated by C_1 -Symmetric $\text{Me}_2\text{Si}(\text{CpR}^*)(\text{Octahydrofluorenyl})\text{ZrMe}_2$ (2**, $\text{R}^* = (1R,2S,5R)\text{-trans-5-methyl-cis-2-(2-propyl)cyclohexyl; (-)-menthyl}$) Activated with Cocatalysts **3**, **6**, **7**, **12** and **14**.**

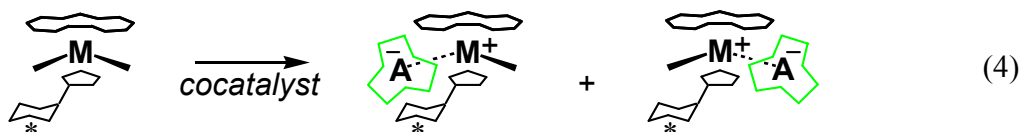
Systematic counteranion effects are readily apparent in catalyst systems using C_S -symmetric metallocene precatalyst $\text{Me}_2\text{C}(\text{Cp})(\text{Flu})\text{ZrMe}_2$ (**1**) and the present family of cocatalyst/activators. We sought to assess the scope and generality of these cocatalyst/activator effects by examining catalyst systems derived from C_1 -symmetric precatalyst $\text{Me}_2\text{Si}(\text{OHf})(\text{CpR}^*)\text{ZrMe}_2$, known to mediate isospecific propylene polymerization,²¹ activated using cocatalysts $\text{B}(\text{C}_6\text{F}_5)_3$ (**3**), $\text{Ph}_3\text{C}^+\text{B}(\text{C}_6\text{F}_5)_4^-$ (**6**), $\text{Ph}_3\text{C}^+\text{FAl}(o\text{-C}_6\text{F}_5\text{C}_6\text{F}_4)_3^-$ (**7**), $\text{Ph}_3\text{C}^+\text{F}[\text{Al}(\text{C}_6\text{F}_5)_3]_2^-$ (**12**) and $\text{Ph}_3\text{C}^+(\text{C}_6\text{F}_5)_3\text{AlFAl}(o\text{-C}_6\text{F}_5\text{C}_6\text{F}_4)_3^-$ (**14**; see Scheme 1 for chemical structures). To parallel prior studies using precatalyst **1**,⁷ we have surveyed the effects of reaction temperature, monomer concentration, and solvent polarity. The collected results are presented in Tables 3 and 4, and graphically in Figure 3. Again, the metrics employed for evaluation of polymerization results include activity, polymer molar mass distributions and melting temperatures, and polymer microstructural analysis. A brief synopsis of the latter technique appears in the introductory paragraphs to this Discussion; here we mention that systems using a C_1 -symmetric metallocene precatalyst present special complexities in this endeavor. These considerations are discussed in detail following examination of reaction temperature, monomer concentration, and solvent effects on the polymerization process.

Reaction temperature effects were surveyed for systems **2** + **3**, **2** + **6**, **2** + **7**, **2** + **12**, and **2** + **14**, with experiments at 25 and 60°C (Table 3). For each system, decreases in polymer molar mass and stereoregularity are observed with increasing temperature, with increases in the

abundances of *rr* and isolated *r* stereodeflects observed in all systems except catalyst **2** + **7**. Systems derived from (perfluoroaryl)fluoroaluminate cocatalysts **7**, **12** and **14** (Scheme 1) exhibit decreases in polymerization activity, whereas (perfluoroaryl)borate systems **2** + **3** and **2** + **6** do not. We ascribe this difference to decreased thermal stability in the fluoroarylaluminate compared to the borate systems. Even in these systems, however, increases in activity with increasing temperature are moderate at best, substantially below the increases predicted from standard Arrhenius behavior, indicating that thermal decomposition is significant for these systems as well.

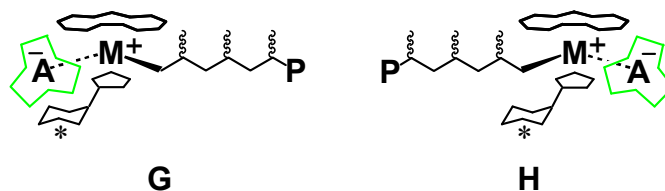
Mechanistic details of the **2**-based catalyst systems have been probed here by studying the effect of changing propylene concentration on the product polymer characteristics. Initial survey of [propylene]-dependence trends for systems **2** + **3**, **2** + **7**, and **2** + **14** reveals strong anion-dependence both in overall stereoselectivities and in the observed changes in overall stereoselectivity with changing [propylene]. In particular, as [propylene] is increased from 0.36M to 2.05M, the reduction in *mmrr* pentad fraction is greatest in system **2** + **14** (~44%; Table 3, entries 6 and 11) less in system **2** + **7** (~35%; Table 3, entries 6 and 11) and, interestingly, least in system **2** + **3** (~10%; Table 3, entries 9 and 12). Interpretation of these trends requires a thorough examination of possible insertion and stereodeflect production pathways.

Activation of a C_1 -symmetric precatalyst with a non-prochiral cocatalyst will in principle generate diastereomeric ion pair complexes, present in different amounts and possibly having quite different polymerization stereoselectivities and activities (eq. 4). Some Lewis-basic



substituent(s) can be expected to preferentially occupy the coordination vacancy adjacent to the

electrophilic cation's polymeryl substituent. This could be the counteranion itself, a neutral metallocene (possibly having a methyl, hydrido, or in select cases a halide substituent carrying substantial electron density), a solvent molecule, or a propylene molecule.^{36, 42} This moiety will provide steric bulk that differs from the polymeryl substituent, thus rendering one epimer thermodynamically distinct from the other (**G** vs **H**). Also, the identity of this substituent may



change during polymerization. For example, an anionic fragment might be partially or fully displaced by incoming monomer;³⁵ subsequent chain-migratory insertion may then occur, with the anion taking up the coordination site recently vacated by the polymeryl (following the “alternating” mechanism, Scheme 3A). Conversely, a chain-migratory insertion might be followed by noninsertive site epimerization to regenerate the original, more stable epimer (“backskip” mechanism, Scheme 3B). Both of the above pathways are in principle available, their relative likelihoods depending on the differences in steric bulk of the polymeryl vs the Lewis base substituent and possibly also the lability of the Lewis base. If insertion is chain-migratory (i.e., if back-side attack leading to nonmigratory insertion is disallowed, see Scheme 3D) the backskip mechanism requires that the anion or Lewis base substituent be sufficiently labile to allow noninsertive site epimerization. Thus, the degree of preference for the backskip over the alternating pathway might be strongly anion-dependent. Significant observed counteranion effects,² particularly arising from large differences in the strength of the cation-

⁴² The “anion” in this case may be a stereochemically dynamic species, possibly even incorporating a coordinated dimethylmetallocene moiety, see eq. 3 above.

anion interaction and based on *ex-situ* NMR, structural, and polymerization evidence,⁷ suggest that the broad diversity of anions generated using cocatalyst species **3**, **6**, **7**, **12**, and **14** (Scheme 1) should provide a sufficient range of cases to test this hypothesis. Cocatalysts **6**, **12**, and **14** are expected to generate anions that interact weakly with the cationic moiety, whereas **3** is expected to yield a more strongly interacting anion, and **7** is expected to produce a system having an extremely strong cation-anion interaction.

A key question arising from the above considerations is whether the polymeryl substituent or the Lewis base/anion preferentially takes up the less sterically hindered side of the catalyst, i.e. the side opposite the pendant R moiety of the Cp ring. This question bears upon the expected effect of monomer concentration changes upon catalyst system stereoregulation. If the backskip pathway is preferred at low propylene concentrations but the alternating pathway is possible, increasing [propylene] should lead to an increase in the relative contribution of the alternating pathway. An increase in polymer stereoregularity is expected if the backskip pathway presents the less stereoselective side for monomer approach, whereas a decrease suggests the opposite situation.⁴³ Importantly, we observe in all cases that overall stereoregularity increases

⁴³ Indeed, an increase in stereoselectivity with increased [propylene] is consistent with a scenario wherein any [propylene]-independent stereodeflect processes are significant, including chain epimerization (Scheme 3E). Studies of chain epimerization in C_2 - and C_1 -symmetric systems generally require forcing conditions (low monomer concentration, high temperature, or both), see: Yoder, J. C.; Bercaw, J. E. *J. Amer. Chem. Soc.* **2002**, *124*, 2548-2555. Also, with C_5 -symmetric zirconocene systems (wherein chain epimerization can be kinetically distinguished from other mechanisms), chain epimerization makes a relatively minor contribution to total stereoerror content, see: c) Veghini, D.; Henling, L. M.; Burkhardt, T. J.; Bercaw, J. E. *J. Amer. Chem. Soc.* **1999**, *121*, 564-573, and ref. 7. The contribution of chain epimerization to stereodeflect abundance cannot be readily distinguished from that of competition between the backskip and alternating mechanisms based solely on polypropylene microstructural

significantly with increasing monomer concentration (Table 3), this effect being most pronounced in system **2** + $\text{Ph}_3\text{C}^+ \text{FAl}(o\text{-C}_6\text{F}_5\text{C}_6\text{F}_4)_3^-$ (**7**), somewhat less so in system **2** + $\text{Ph}_3\text{C}^+ (\text{C}_6\text{F}_5)_3\text{AlFAl}(o\text{-C}_6\text{F}_5\text{C}_6\text{F}_4)_3^-$ (**14**), and least pronounced in system **2** + $\text{B}(\text{C}_6\text{F}_5)_3$ (**3**). Assuming negligible “back-side” misinsertion and chain epimerization (Schemes 3D and 3E), these observations are consistent with a stereoregulation model in which: a) the polymeryl substituent preferentially occupies the more sterically hindered catalyst side (configuration **H** above) with insertion occurring at the less-hindered side (configuration **G** above) and b) the backskip mechanism is favored at lower propylene concentrations, giving way to the alternating mechanism as propylene concentration is increased. The degree of increase in stereoregulation can depend on the degree to which the backskip mechanism is favored at low [propylene] but *also* on the inherent difference in stereoselectivities between the two catalyst sides, *both* of which can be expected to be anion-dependent. A large increase in stereoselectivity with increasing [propylene] may then be attributable either to a substantial shift from a backskip to an alternating mechanism with some moderate difference in stereoselectivities between the catalyst sides, or to a moderate shift towards alternating insertion coupled with a substantial difference in stereoselectivity between the catalyst sides. These possibilities cannot be differentiated, however it is reasonable to conclude that a [propylene]-dependence in stereoregulation *does* indicate a shift from the backskip to the alternating mechanism with increasing [propylene].

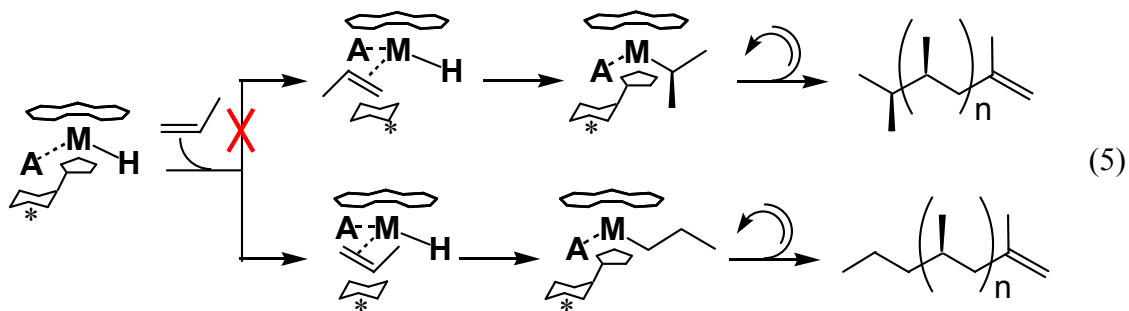
The backskip mechanism involves a step in which the anionic fragment migrates from one catalyst side to the other. If indeed the anion in system **2** + **7** is strongly bound to the cation

analysis; however this is in principle possible using D-labeled propylene, see: Yoder, J. C.; Bercaw, J. E. *J. Amer. Chem. Soc.* **2002**, *124*, 2548-2555, wherein the chain epimerization mechanism is studied for C_2 -symmetric metallocene catalyst systems.

as expected, one predicts based on evidence from system **1** + **7** that this epimerization will be significantly suppressed.⁷ However, the present evidence of [propylene]-dependence in stereoregulation with this system leads also to the following conclusion: with the catalyst system in configuration **G** above, overwhelming steric congestion might both significantly inhibit monomer insertion *and* attenuate the cation-anion interaction at the more congested side, permitting (or forcing) a backskip pathway wherein insertion occurs preferentially at the less-hindered and thus less stereoselective catalyst side (Scheme 3B), with increasing [propylene] leading to an increase in alternating insertion and an increase in overall stereoregulation performance. In contrast, the more loosely-bound ion-pair complex **2** + **14** lacking the cation-anion bridging μ -F moiety should allow insertion at the more hindered side (configuration **G**) but *also* facilitate backskip, again leading to a backskip mechanism that gives way to alternating insertion at elevated [propylene]. These arguments are consistent also with the dramatic observed difference in activity between systems **2** + **7** and **2** + **14**. The observed change in stereoregulation with increasing [propylene] in **2** + **14** may also be attributable in part to an increased propensity for chain epimerization in this system vs **2** + **7**. Chain epimerization likely involves a β -hydrogen elimination step,⁴³ and β -hydrogen elimination leading to chain termination occurs considerably more rapidly in **2** + **14** than in **2** + **7** (*vide infra* for a discussion of polymer molar mass [propylene] dependence and chain termination mechanisms). The above line of reasoning demonstrates that the results themselves are consistent with a scenario in which ion pairing strength is different in these two systems, with the *origin* of the observed stereoselectivity [propylene] dependence then being different as well.

The observation of significant [propylene]-dependence in product polymer M_w 's in **2**-based catalytic systems stands in marked contrast to results using C_S -symmetric precatalyst **1** and

other reported C_1 -symmetric systems.^{2b, 7} Further evidence that termination via β -hydrogen elimination is favored in the present cases comes from the ^1H NMR end group analysis of the product polymers. The presence of the two major endgroups (n -Pr and vinylic, Figure 1) is consistent with chain transfer occurring predominantly if not exclusively via β -hydrogen elimination.³² The absence of detectable isopropyl end groups argues that 2,1 monomer insertion followed by immediate elimination (shown to be first-order in [propylene])⁴¹ does not occur to a significant extent (eq. 5). Also, whereas polymerization activities are significantly anion-



dependent, polymer molar mass values are not. These latter observations indicate a pronounced anion-dependence in polymer chain release rates, with both insertion *and* chain release occurring significantly more slowly in system **2** + **7**. This is fully consistent with observations in analogous C_S -symmetric cases (Table 2) and supports the hypothesis that observed differences in polymerization results arise from differences in the binding strength of the $\text{FAI}(o\text{-C}_6\text{F}_5\text{C}_6\text{F}_4)_3^-$ anion to the cation in **2** + **7** by comparison to the anionic moiety in system **2** + **14**.

Replacement of nonpolar toluene ($\epsilon = 2.38$)⁴⁴ as reaction medium with a more polar solvent provides an elegant test of the hypothesis that cation-anion interactions are of importance in determining polymerization activity and stereoselectivity, since a more polar solvent such as

⁴⁴ Wohlfarth, C. in *Landolt-Börnstein, Numerical Data and Functional Relationships in Science and Technology, New Series*, O. Madelung, ed., Group IV, Macroscopic and Technical Properties of Matter, Volume 6, Springer-Verlag, Berlin, 1991.

1,3-dichlorobenzene ($\epsilon = 5.02$)⁴⁴ can be expected to effect separation of the cation and anion during polymerization, attenuating observed counteranion effects. As seen with catalyst systems employing C_5 -symmetric $\text{Me}_2\text{C}(\text{Cp})(\text{Flu})\text{ZrMe}_2$ (**1**) with cocatalysts $\text{B}(\text{C}_6\text{F}_5)_3$ (**3**), $\text{B}(o\text{-C}_6\text{F}_5\text{C}_6\text{F}_4)_3$ (**4**), $\text{Ph}_3\text{C}^+\text{B}(\text{C}_6\text{F}_5)_4^-$ (**6**), and $\text{Ph}_3\text{C}^+\text{FAl}(o\text{-C}_6\text{F}_5\text{C}_6\text{F}_4)_3^-$ (**7**),⁷ counteranion effects are almost completely suppressed for the present systems in which C_1 -symmetric precatalyst $\text{Me}_2\text{Si}(\text{OHf})(\text{CpR}^*)\text{ZrMe}_2$ is used. We observe a compression in the dispersion of both activities and stereoselectivities across systems **2 + 3**, **2 + 6**, **2 + 7**, **2 + 12**, and **2 + 14** (Table 4, Figure 3).

V. Polymer ¹³C NMR Microstructural/Mechanistic Analysis of Polypropylenes Produced Using C_1 -Symmetric $\text{Me}_2\text{Si}(\text{CpR}^*)(\text{Octahydrofluorenyl})\text{ZrMe}_2$ (2**, $\text{R}^* = (1R,2S,5R)\text{-trans-5-methyl-cis-2-(2-propyl)cyclohexyl}$; $(-)\text{-menthyl}$) Activated with Cocatalysts **3**, **6**, **7**, **12** and **14**.**

The above arguments are based on comparison of overall polymer stereoregularities. Differentiation among stereodeflect processes according to their proposed rate laws is more challenging with C_1 -symmetric catalyst systems than with C_5 -symmetric systems. With C_5 -symmetric systems, *mm*- and *m*-producing processes can be distinguished quantitatively, whereas with C_1 systems, the analogous processes are each expected to afford either *rr* stereodeflects or none at all, thus they cannot be readily differentiated. Another difficulty is manifested in attempts to model steric pentad distributions using the standard parametric approaches. The primary challenge is that of interparametric correlations, i.e. the tendency for a given parametrization to match the experimental data equally well with different sets of parameter estimates.

In the ensuing paragraphs, we present a generalized stochastic model containing parameters that describe the relative contributions of enantiofacial misinsertion and backskip processes. Using this model as a starting point, we examine a collection of submodels based on reasonable simplifying assumptions. We then present a general method for calculating correlation coefficients among the parameters of any stochastic model, taking into account the fact that these regression models are nonlinear in their parameters. Using these tools, we analyze the ^{13}C NMR spectra of the polypropylene samples presented in Tables 3 and 4, generating parameter estimates and correlation matrices for each data set using each model. We analyze the collected results, identifying systematic correlations between the parameters and evaluating each model in terms of its reliability. We then take up a mechanistic question of importance in polymerization stereochemistry: do the present systems operate under a substantially alternating mechanism or with insertion followed by backskip, or are both pathways operative? The findings that emerge from our correlation analyses shed light on whether or not this question can be meaningfully answered for C_1 -symmetric systems based solely on polymer microstructural analysis.

The “stochastic matrix” methodology we employ here can be applied to any catalyst system, and conveniently generates the probability expressions for all possible steric n -ads as a function of parameters of one’s choosing. The basic methodology is described in detail elsewhere,^{33, 45} so one needs only to present the stochastic matrix itself (often referred to as the

⁴⁵ For recent reviews of polypropylene polymerization, stereoerror production, and termination mechanisms and polypropylene microstructural analysis, see: a) Resconi, L.; Cavallo, L.; Fait, A.; Piemontesi, F. in ref. 1d, 1253 - 1346, b) Busico, V.; Cipullo, R. *Prog. Polym. Sci.* **2001**, *26*, 443-533. c) Razavi, A.; Thewalt, U. *Coord. Chem. Rev.* **2006**, *250*, 155-169.

transition matrix) to completely describe the chosen statistical model. The columns of this matrix (\mathbf{A} in conventional notation) are indexed to the possible “states” or outcomes of the present enchainment event, and the rows are indexed (in the same order) to the states of the previous insertion. Reasonably assuming exclusive 1,2 propylene insertion (which places the methyl group of the newly inserted monomer vicinal to the catalyst metal center), these possibilities include $R(A)$ and $S(A)$, the respective probabilities of *re* and *si* insertions at site A of the catalyst-polymeryl complex, along with $R(B)$ and $S(B)$ for insertions at site B. The entries a_{ij} of \mathbf{A} are then probability expressions for an event j following event i . These probability expressions will be simple functions of the parameters arising from the kinetic model chosen. Matrix \mathbf{A} can then be used to construct probability expressions for any steric n -ad, in the present case, each of the ten possible pentads. The included probability parameters are then simultaneously refined until the predicted pentad distribution most closely matches the experimentally determined distribution, using a nonlinear least-squares minimization algorithm.

The basic assumptions implicit in this approach are: i) the polymer can be thought of *both kinetically and structurally* as having infinite length, i.e. that the ratio of terminal and near-terminal methyl resonances to internal methyl resonances in the ^{13}C NMR spectrum is on the order of the spectral S/N ratio or lower (confirmable by determining the olefinic/aliphatic resonance ratios in the ^1H NMR, which typically has a much greater S/N ratio), ii) the probabilities of enantiofacial misinsertion and backskip are not affected by the stereochemistry of the polymeryl stereocenter nearest in the chain to the active site,⁴⁶ iii) the polymer sample is

⁴⁶ For propylene polymerization kinetics, one of the key questions addressable by the stochastic matrix approach is whether stereocontrol is exerted via “site control,” i.e. entirely by the catalyst, or via “chain-end control,” i.e. by the stereochemistry of the last inserted monomer, see: a) Hagihara, H.; Shiono, T.; Ikeda, T. *Macromolecules* **1997**, *30*,

not a mixture of distinct fractions with differing stereoregularities, and iv) polymerization temperature and monomer concentration are uniform and static during polymerization. To these we add a further assumption, that the rates of 2,1- or 3,1-misinsertions are essentially negligible across the present series of experiments.^{43,47} Also, as mentioned above, chain epimerization cannot readily be distinguished from site epimerization based solely on microstructural analysis. As we shall see, however, this is a moot point. The present parameterization is as follows:

4783-4785, b) Venditto, V.; Guerra, G.; Corradini, P.; Fusco, R. *Polymer* **1990**, *31*, 530-537, c) Ewen, J. A., *J. Amer. Chem. Soc.* **1984**, *106*, 6355-6364, d) Shelden, R. A.; Fueno, T.; Tsunetsugu, T.; Furukawa, J. *J. Polym. Sci., Part B* **1965**, *3*, 23-26. e) Shelden, R.; Fueno, T.; Furukawa, J. *J. Polym. Sci., Polym. Phys. Ed.* **1969**, *7*, 763-773, f) Busico, V.; Cipullo, R.; Talarico, G.; Segre, A. L.; Chadwick, J. C. *Macromolecules*, **1997**, *30*, 4786-4790. Indeed, insertion stereoselection can be mediated by a combination of site and chain-end control, and parameters representing the propensity for one over the other can be included in the stochastic matrix. Here we forego this interesting but complicating issue.

⁴⁷ The following references find regioerrors to constitute < 0.5 mol% of insertions : a) Camurati, I.; Nifant'ev, I. E.; Laishevtsev, I. P. *J. Amer. Chem. Soc.* **2004**, *126*, 17040-17049, b) Song, F.; Cannon, R. D.; Bochmann, M. *J. Amer. Chem. Soc.* **2003**, *125*, 7641-7653, see also: refs 34b, 34c.

Parameter	Definition
bB	Backskip at site B
bA	Backskip at site A
rA	Re insertion at site A
rB	Re insertion at site B

The stochastic matrix **A** arising from this set of parameters is as follows:

	R(A)	S(A)	R(B)	S(B)
R(A)	bB × rA	bB × (1 - rA)	(1 - bB) × rB	(1 - bB) × (1 - rB)
S(A)	bB × rA	bB × (1 - rA)	(1 - bB) × rB	(1 - bB) × (1 - rB)
R(B)	(1 - bA) × rA	(1 - bA) × (1 - rA)	bA × rB	bA × (1 - rB)
S(B)	(1 - bA) × rA	(1 - bA) × (1 - rA)	bA × rB	bA × (1 - rB)

The complete set of submodels under consideration are presented in Table 5. Model 1 represents the parameterization arising from matrix **A** with no further assumptions. Model 2, derived from steric arguments and computational studies,^{35, 48} assumes that the preference of the polymeryl substituent for occupation of one catalyst side over the other (*vide supra* and Scheme 2A) combined with the ease of reorganization – interchanging the more- and less-favored configurations – will lead to a negligible probability of backskip at one side. Models 3 (the alternating mechanism) and 4 (the backskip mechanism) are as described above. These models, by no means novel, have been presented previously in various forms to explore pentad or higher

⁴⁸ a) Razavi, A.; Atwood, J. L. *J. Organomet. Chem.* **1996**, *520*, 115-120. b) Baar, C. R.; Levy, C. J.; Min, E. Y. J.; Henling, L. M.; Day, M. W.; Bercaw, J. E. *J. Am. Chem. Soc.* **2004**, *126*, 8216-8231. 2c d 3c 4a b 11 c) Guerra, G.; Cavallo, L.; Moscardi, G.; Vacatello, M. Corradini, P. *Macromolecules* **1996**, *29*, 4834-4845, d) Strauch, J. W.; Faure, J.-L.; Bredeau, S.; Wang, C.; Kehr, G.; Froehlich, R.; Luftmann, H.; Erker, G. *J. Am. Chem. Soc.*, **2004**, *126*, 2089-2104, e) Silanes, I.; Ugalde, J. M. *Organometallics* **2005**, *24*, 3233-3246. Also, see: ref. 45c.

n-ad distributions via the stochastic matrix formulation or via other methods.^{45, 49} Herein we present a systematic evaluation and comparison of all of these models, tested using the present data.

Each of the four models was refined against all 18 sets of experimental pentad distributions appearing in Tables 3 and 4, using a standard nonlinear, quasi-Newton minimization of the mean square about regression, $X^2 = \sum_{i=1 \text{ to } p} (\hat{I}_i - I_i)^2$ of estimated (\hat{I}_i) vs experimental (I_i) pentad integrals.⁵⁰ The reduced mean square $s^2 = X^2/(n - p)$ gives some indication of the strength of the model in light of its number of degrees of freedom ($n - p$; n is the number of observations, in this case the nine pentad integral regions, and p is the number of parameters). The overall suitability of each model is gauged by: a) systematic comparison of $\overline{s^2}$ (averaged over all data sets, see Table 5) and b) determination of a correlation matrix via linearization of the model in the vicinity of the parameter estimates, described below.

For any multiparametric least-squares estimation, it is necessary to assess the risk that the parameters may not be truly independent of one another, i.e., that the solution is unique and that the parameter estimates reflect real physical quantities. The present models are *not* linear in the parameters, the transition matrix **A** and thus the *n*-ad expressions themselves consisting of

⁴⁹ Mohammed, M.; Nele, M.; Al-Humydi, A.; Xin, S.; Stapleton, R. A.; Collins, S. *J. Am. Chem. Soc.* **2003**, *125*, 7930-7941.

⁵⁰ The regression analysis implementation used here is the Solver package available with the standard release of Microsoft® Office Excel 2003 (11.6560.6568) SP2.

polynomials in the parameters $\mathbf{H} = (H_1, \dots, H_i, \dots, H_p)^T$,⁵¹ and thus it is not possible to evaluate them using traditional means available for multiple linear regression, such as Pearson's r test for collinearity, the derivative Variance Inflation Factor, standard variance-covariance matrices, or the F statistic.⁵² However, one can still seek correlations: in any model, if two parameters are correlated, changing either of them by the same amount (in the same direction if they are positively correlated, and in opposite directions if they are negatively correlated) will have the same effect on the calculated n -ad integral values $\hat{\mathbf{I}}$. The partial derivatives of the model function with respect to each parameter H_i in the vicinity of the final parameter estimate \hat{H}_i can be estimated numerically; pairwise comparison of these estimated partial derivatives then gives us an indication of possible correlations.

Construction of correlation matrix $\hat{\mathbf{C}}$ is accomplished in the following way:⁵² letting the model equation for the integral assigned to n -ad ξ_u be $I_u = f(\xi_u, \mathbf{H})$, we may estimate a correlation matrix for the parameters \mathbf{H} by linearizing the model $\mathbf{I} = (I_1, \dots, I_u, \dots, I_p)^T$ over all ξ_u in the vicinity of our calculated $\hat{\mathbf{H}}$, the set of least-squares estimates \hat{H}_i for the parameters H_i . For this purpose, a matrix $\hat{\mathbf{G}}$ can be constructed with elements defined as $\hat{g}_{iu} = \partial \hat{I}_u / \partial \hat{H}_i = \partial f(\xi_u, \hat{\mathbf{H}}) / \partial \hat{H}_i$. The rows of matrix $\hat{\mathbf{G}}$ are indexed to the n -ads, and the columns are indexed to the refinement parameters. Matrix $\hat{\mathbf{G}}^T \hat{\mathbf{G}}$ is a symmetric $p \times p$ matrix having elements i, j that are large in magnitude when both $\hat{g}_{iu} = \partial f(\xi_u, \hat{\mathbf{H}}) / \partial \hat{H}_i$ and $\hat{g}_{ju} = \partial f(\xi_u, \hat{\mathbf{H}}) / \partial \hat{H}_j$ are large for the same u (or u 's). The normalized form

⁵¹ The following conventions of notation are used: a vector or matrix \mathbf{Y} of "true" values or random variables has elements Y_i if it is a vector or y_{ij} if it is a matrix. An estimate of \mathbf{Y} is denoted $\hat{\mathbf{Y}}$ and has elements \hat{Y}_i if it is a vector or \hat{y}_{ij} if it is a matrix. \mathbf{Y}^T is the transpose of \mathbf{Y} , and \mathbf{Y}^{-1} is the inverse of \mathbf{Y} .

⁵² Draper, N. R.; Smith, H. *Applied Regression Analysis*; Wiley Series in Probability and Mathematical Statistics; John Wiley and Sons, Inc.: New York, NY, 1981; pp 458-529.

$\hat{\mathbf{C}}$ of $(\hat{\mathbf{G}}^T \hat{\mathbf{G}})^{-1}$, with elements $\hat{c}_{ij} = \hat{w}_{ij}/(\hat{w}_{ii}\hat{w}_{jj})^{1/2}$, is the correlation matrix of the parameters \mathbf{H} estimated at $\hat{\mathbf{H}}$, based on the assumption that $\partial f(\xi_u, \hat{\mathbf{H}})/\partial \hat{H}_i$ is a good estimate for $\partial f(\xi_u, \mathbf{H})/\partial H_i$. The off-diagonal elements of $\hat{\mathbf{C}}$ range between -1 and 1 , and reflect the degree to which a given change in $\hat{\mathbf{H}}$ can be brought about by changing either \hat{H}_i or \hat{H}_j by the same amount (in the same direction, if \hat{c}_{ij} is positive, or in opposite directions, if \hat{c}_{ij} is negative). For example, if \hat{c}_{ij} is close to 1 , then H_i and H_j are for all intents and purposes, interchangeable.

We do not attempt to explicitly differentiate $f(\xi_u, \mathbf{H})$; in the present case, each $\partial f(\xi_u, \hat{\mathbf{H}})/\partial \hat{H}_i$ is estimated numerically using the central limit method (eq. 6),⁵³

$$\partial f(\xi_u, \hat{\mathbf{H}}) = \lim_{x \rightarrow 0} \frac{f(\xi_u, (\hat{H}_1, \dots, \hat{H}_u + x, \dots, \hat{H}_p)^T) - f(\xi_u, (\hat{H}_1, \dots, \hat{H}_u - x, \dots, \hat{H}_p)^T)}{2x} \quad (6)$$

with $x_{\text{new}} = 0.1 * x_{\text{old}}$ between consecutive iterations on x and the arbitrary convergence criterion $|\Delta \partial f(\xi_u, \hat{\mathbf{H}})/\partial \hat{H}_j| = 1 * 10^{-5}$ for consecutive iterations. A correlation matrix can be calculated using the above approach for each set of experimental data, for each model under consideration. Correlation matrices calculated for each data set under each model are included in the Supporting Information. If \hat{c}_{ij} is small in magnitude, then pairwise correlation between H_i and H_j can be ruled out. On the other hand, a large value for \hat{c}_{ij} appearing in a given correlation matrix does not constitute proof that H_i and H_j are *systematically* correlated (i.e. correlated for every data set), just that the available data do not permit their discrimination. Systematic correlations can be evaluated by examining the results obtained using several data sets. If, for example, the correlation matrices for a sufficiently large collection of data sets show strong possible correlations distributed within the correlation matrices with no apparent pattern, then

⁵³ A description of the central limit theorem and its applications can be found in: Tijms, H. *Understanding Probability: Chance Rules in Everyday Life*, Cambridge: Cambridge University Press, 2004.

any observed large \hat{c}_{ij} values may be coincidental. For each model we can examine the matrices consisting of the average values for \hat{c}_{ij} across all data sets, and their standard deviations. The presence of a substantial average \hat{c}_{ij} value *and* a small standard deviation constitute strong evidence for a systematic correlation. The apparent correlations discussed below arise from fits to *our* data, which has its own idiosyncracies, e.g., large xmr_x integral values. These parameters might *not* appear correlated when other data collections are used. In many cases, a model will converge such that the calculated pentad integrals do not change with respect to one or more parameters, generating nonsingular and thus noninvertible $\hat{\mathbf{G}}^T \hat{\mathbf{G}}$ matrices for some or all data sets. These models can safely be regarded as unsuitable and are labeled “ill-conditioned” in the H_j for which $\partial f(\xi_u, \hat{\mathbf{H}})/\partial \hat{H}_j = 0$ for all u , over the data sets in question. We omit these instances in our comparisons of $\overline{s^2}$ values (*vide infra*). Table 5 gives s^2 values for each of the present data sets under each regression model, and Table 6 provides matrices for each model containing the correlation matrix elements \hat{c}_{ij} averaged over all data sets, together with their standard deviations. Experimental and calculated pentad distributions, along with each correlation matrix, are presented in the Supporting Information.

Model 1 allows backskip at both sides, having $p = 4$. This model is well-conditioned over all data sets. Large \hat{c}_{ij} values are found with many data sets, however the standard deviations across all data sets for these \hat{c}_{ij} values are also large, suggesting that there is no systematic correlation. This model gives values for s^2 ranging from 0.31 to 7.55 with $\overline{s^2} = 1.85$, the lowest among the four models. In general, this model provides the best fits to experimental data. Interestingly, refined values for bB are largely near 1.0, suggesting that submodel 4 would be suitable as well. Also of note, and harder to reconcile with chemical intuition, is that this model also generally gives large values for bA. This suggests a “nonalternating” polymerization

mechanism that occasionally switches between catalyst sides A and B, however this hypothesis does not mesh well with abundant evidence in support of the generally accepted chain-migratory insertion mechanism.^{1a, 31b} Also troubling is that under this model, most data sets give $r_B < 0.5$, suggesting catalyst performance that tends toward C_S symmetry, rather than C_2 symmetry.

Model 2 represents possible backskip at side B but not at A, having $p = 3$. This model tends to give $r_A = r_B$, and is thus ill-conditioned in b_B . In two illustrative cases, $\partial f(\xi_u, \hat{\mathbf{H}})/\partial b_B$ was nonzero for some pentads (probably due to rounding effects), revealing the expected perfect negative correlation between r_A and r_B . A constraint was then added that $r_A > r_B + 0.01$ to break the symmetry of the model. However, under this added constraint, the refined b_B value was invariably 1.0, and the model became equivalent to model 4 (and was thus ill-conditioned in r_B).

Model 3 represents the alternating mechanism, having $p = 2$. This model is well-conditioned for all data sets and gives correlation values \hat{c}_{ij} that are generally near to -0.5, with a quite small standard deviation (0.045) indicating a possible systematic partial correlation. Also of note, the difference in enantioselectivity ($r_A - r_B$) is small (1–6%) for all data sets. Values for s^2 range from 1.68 to 29.7, with $\overline{s^2} = 8.64$ ranking 3rd best.

Model 4 represents the backskip mechanism, with $p = 1$. This model has only one parameter, r_A , and thus has no potential correlations to evaluate. Values for s^2 range from 1.66 to 31.8, with $\overline{s^2} = 9.13$, ranking last among the present models. It is noteworthy that neither this model or model 3 can be said to be more appropriate for the given data (i.e. both appear to perform marginally). However, that model 1 is fairly well-behaved and uniformly gives large values for b_B lends credence to this model.

Analysis of the above models constitutes an investigation of whether a distinction between alternating and backskip mechanisms can be made based on ^{13}C NMR polymer microstructural analysis for this particular family of C_1 -symmetric catalyst systems. Model 1, allowing backskip at both sides, is well-conditioned and apparently free of systematic correlations. However, it is troubling that this model consistently yields large values for both bB and bA. Comparison of models 3 (the alternating mechanism) and 4 (the backskip mechanism) again is uninformative: model 3 appears to suffer from a fatal systematic correlation, and model 4 has no basis for evaluation other than the s^2 values it produces. Based on the above results, it becomes clear that: a) even models that produce reasonable fits to experimental data cannot be rigorously relied upon, and b) that one model might appear to perform better than another by no means indicates that the kinetic assumptions underlying it are more valid. Conversely, the presence of apparent correlations in a given parameterization does not demonstrate that the underlying kinetic model is without merit, just that microstructural analysis alone cannot be used to support it.

Systematic counteranion effects on the absolute rates of specific polyinsertion and reorganization processes, demonstrated rigorously for systems based on C_S -symmetric precatalyst **1**, are not clearly in evidence for the analogous C_1 -symmetric cases. However, it is evident from the above analysis that this is not necessarily due to the absence of such counteranion effects but rather to what can be described as a problem of resolution in the interpretation of polymer microstructural data, i.e. the absence of evidence for counteranion effects does not, in this case, indicate that these effects do not exist. The above analysis can be implemented as described above in any standard spreadsheet application; in the interest of knowing what can and cannot be concluded based on experimental results, the authors invite the

polymer chemistry community to take advantage of this nonlinear correlation technique where appropriate for kinetic modeling of polymer microstructural data.

CONCLUSIONS

In this contribution we have detailed the propylene polymerization performance of a series of metallocene-based catalyst systems derived from a new family of well-defined, sterically encumbered and charge-delocalized single-molecule cocatalysts combined with archetypal C_S -symmetric precatalyst $\text{Me}_2\text{C}(\text{Cp})(\text{Flu})\text{ZrMe}_2$ (**1**; $\text{Cp} = \text{C}_5\text{H}_4$, η^5 -cyclopentadienyl; $\text{Flu} = \text{C}_{13}\text{H}_8$, η^5 -fluorenyl) and C_1 -symmetric precatalyst $\text{Me}_2\text{Si}(\text{OHF})(\text{CpR}^*)\text{ZrMe}_2$, (**2**; $\text{OHF} = \text{C}_{13}\text{H}_{16}$, η^5 -octahydrofluorenyl; $\text{CpR}^* = \eta^5$ -3-(-)-menthylcyclopentadienyl). These catalyst systems are in general thermally robust and in some cases produce highly stereoregular polypropylenes with unprecedented high polymerization activities. The cocatalysts are mononuclear and polynuclear fluoro- perfluoroarylborate, -aluminate, and -gallate species and represent a broad class of trityl halide adducts of neutral, highly Lewis acidic perfluoroarylmetalloid species. Details of the synthesis, characterization, and activation chemistry of these new cocatalysts have been described in a separate contribution.¹⁴

As observed in previous cocatalyst studies, observables such as polymer stereoregularity, stereodeflect abundances, molar mass, and polymerization activity are all found to be strongly dependent on catalyst-cocatalyst ion pairing strength, with catalyst systems derived from these new polynuclear perfluoroaryl cocatalysts in general exhibiting greater stereoregulation and polymerization activities than earlier systems employing their neutral analogs. Similar to previous findings, using more polar 1,3-dichlorobenzene as reaction medium, product polymer molar mass, stereoregularity, and activity are found to converge, indicating that ion pairing plays

an important role in determining the relative rates of termination and stereodeflect production processes vs termination.

Catalyst species observed by *ex-situ* spectroscopy to lack a μ -Me or μ -F linkage between the cation and anion exhibit the greatest polymerization activities and also a heightened proclivity for stereodeflect-introducing reorganizations, with the former effect being dramatically stronger in specific cases. In these cases, unprecedented stereocontrol is observed together with very high polymerization activities, constituting a significant advance in catalyst system development for stereoselective olefin polymerization. In the most dramatic examples, we observe syndioselectivities (and catalyst thermal stabilities) on par with highly stereoregulating but much less active catalyst systems, and polymerization activities similar to very active (and thermally unstable) but poorly stereoregulating catalyst systems.

Findings using C_1 -symmetric precatalyst **2** with the present series of cocatalysts support the hypothesis that the presence or absence of a cation-anion bridging moiety (μ -F or μ -Me) significantly affects the relative rates of insertion and competing stereodeflect production and termination processes. From [propylene]-dependence experiments, enhanced termination via β -hydrogen elimination is observed in systems in which no cation-anion bridging moiety is detected, and attenuated β -hydrogen elimination in systems in which a kinetically inert cation-anion contact does exist. Based on these observations we can differentiate between the contrasting origins for observed similarities in [propylene]-independent stereodeflect production rates in these systems: in the bridged $Zr^+\cdots X^-$ systems, suppression of insertion at the more hindered catalyst side leads to formation of *rr* stereodeflects via a backskip mechanism that gives way to alternating insertion at elevated [propylene], whereas in the unbridged systems, both backskip (facilitated here by more facile anion migration rather than inhibited insertion) *and*

chain epimerization (involving a β -hydrogen elimination step) are likely operative as [propylene]-independent *rr* stereodeflect production processes.

The important topic of polypropylene ^{13}C NMR microstructural analysis is examined in the case of polymers produced using a C_1 -symmetric metallocene precatalyst, with a standard parametric model based on a combination of enantiofacial misinsertion and backskip mechanisms, and a collection of its submodels, assessed using a precise method for quantifying interparametric correlations. The result is a significantly clearer picture of the advantages and inherent dangers of using the stochastic approach to interpret polymerization results obtained using a C_1 -symmetric precatalyst. While this analysis underscores the care that must be taken in interpreting such results, observations on overall stereoregulation and chain release behavior in the present series of polymerization results obtained using C_1 -symmetric precatalyst **2** plus the present cocatalysts are consistent with the general hypothesis, previously detailed using C_5 -symmetric precatalyst **1**, that ion pairing strength is of central importance in determining the relative rates of individual insertion, reorganization, stereodeflect production, and chain release processes available during metallocene-mediated propylene polymerization.

The unusual combination of high activity and high stereoselectivity observed in catalyst systems formed by combining precatalysts **1** or **2** with new bulky fluoroaryl cocatalysts **12** or **14** may stem in part from the presence of an additional, neutral Lewis-basic dimethylmetallocene fragment that outcompetes the bulky, charge-delocalized anion for occupancy of the catalyst's open coordination site. This hypothesis suggests directions for continued improvements in stereospecific olefin polymerization catalyst systems based on further exploration and elucidation of cocatalyst chemistry and kinetics.

Acknowledgements. Financial support by DOE (DE-FG02-86ER1351) is gratefully acknowledged. M.-C. C. thanks Dow Chemical for a postdoctoral fellowship, Dr. M. Oishi for helpful discussions, and Dr. P. Nickias of Dow for GPC measurements. C. Z. thanks the Italian CNR for a postdoctoral fellowship, and A. M. S. thanks the University of Jordan for a sabbatical leave. J. A. S. R. thanks Dr. Marta Sales of Northwestern University for helpful discussions.

Supporting Information. Experimental and calculated pentad distributions, along with correlation matrices for each stochastic model employed are presented in Appendix II.

Figure 1. ^{13}C NMR of the isotactic polypropylene generated from $\text{Me}_2\text{Si}(\text{OHf})(\text{CpR}^*)\text{ZrMe}_2$ (**2**) + $\text{Ph}_3\text{C}^+\text{B}(\text{C}_6\text{F}_5)_4^-$ (**6**) under 1.0 atm of propylene at 60°C in toluene (Table 3, entry 8).

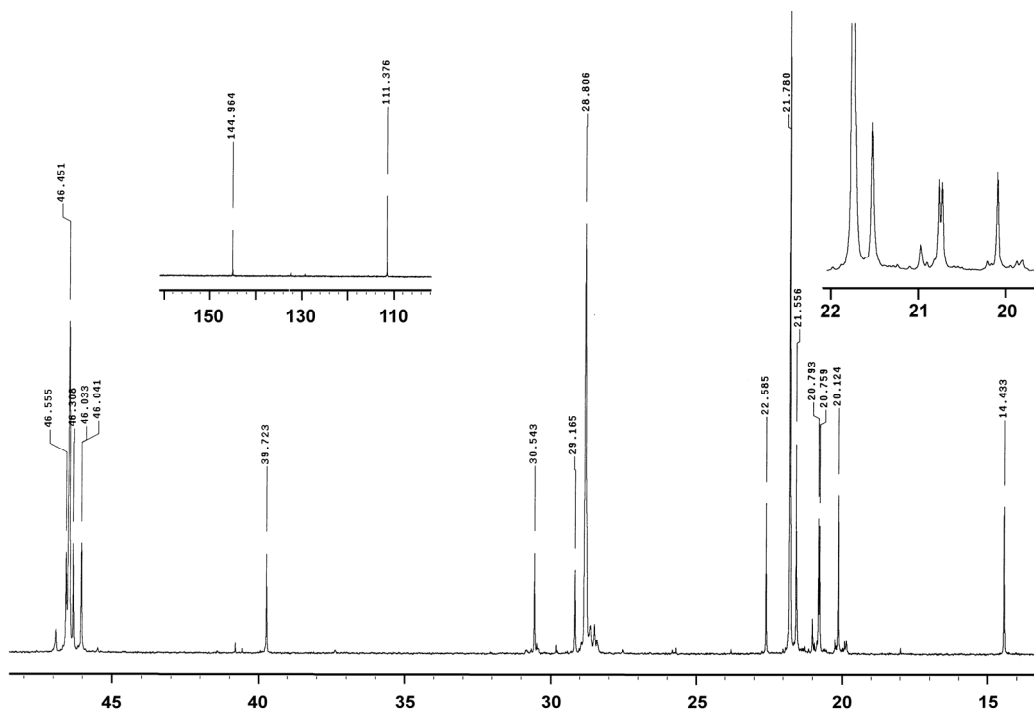


Figure 2. Plots of $-\ln(k_p)$ vs. $1/(\text{polymerization temperature})$ for $\text{Me}_2\text{C}(\text{Cp})(\text{Flu})\text{ZrMe}_2$ (**1**) + cocatalysts $\text{Ph}_3\text{C}^+ \text{FAl}(\text{o-C}_6\text{F}_5\text{C}_6\text{F}_4)_3^-$ (**7**) and $\text{Ph}_3\text{C}^+ (\text{C}_6\text{F}_5)_3\text{AlFAl}(\text{o-C}_6\text{F}_5\text{C}_6\text{F}_4)_3^-$ (**14**) under 1.0 atm propylene over the temperature range of -10° to 25°C in toluene (Table 2; k_p values corrected for [propylene] temperature dependence).⁴⁰ Lines accompanying the data points are presented as a guide to the eye.

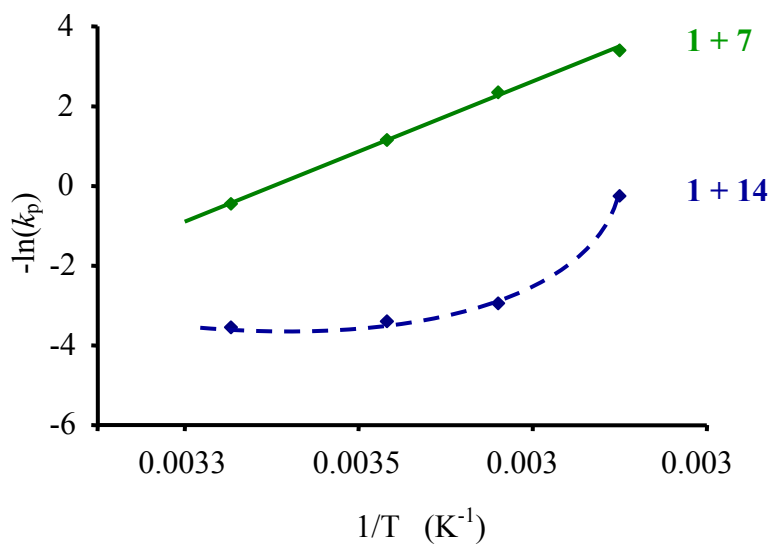


Figure 3. **A.** Polymerization activity as a function of solvent, temperature, and propylene pressure, **B.** *mmmm* (%) data for polypropylenes produced by C_1 -symmetric metallocene $\text{Me}_2\text{Si}(\text{OHf})(\text{CpR}^*)\text{ZrMe}_2$ (**2**) + the indicated cocatalysts (labeling defined in Scheme 1) under the specified polymerization conditions.

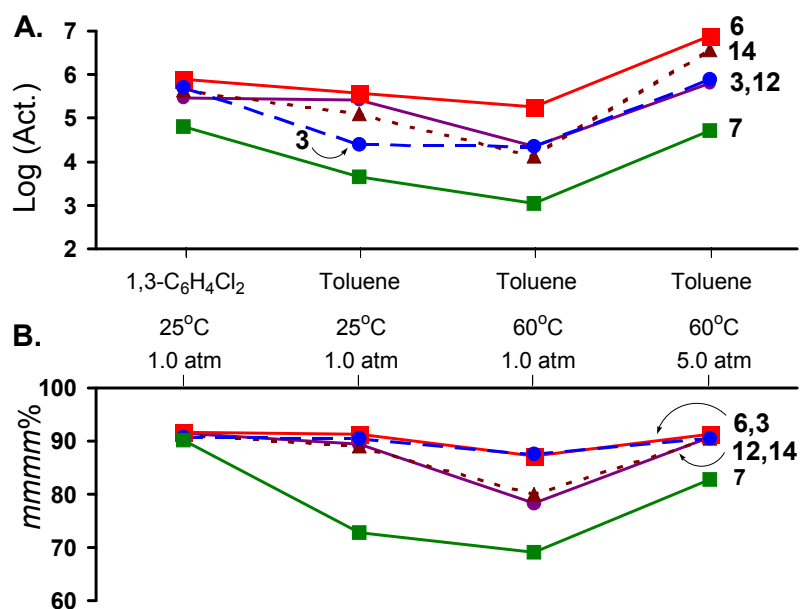


Table 1. Comparison of propylene polymerization results with Me₂C(Cp)(Flu)ZrMe₂(1)+ the indicated cocatalysts at 25°C under 1.0 atm of propylene.^a

Exp. No.	Cocatalysts (R = C ₆ F ₅ ; R' = C ₁₂ F ₉)	<i>umol</i>	Time (min)	PP (g)	ΔT ^c (°C)	T _m ^d (°C)	k _{p,apparent} ^e (M ⁻¹ s ⁻¹)	<i>rrrr</i> ^f (%)	P _m (%)	P _{mm} (%)	M _w ^g (x10 ³)	M _w /M _n
1 ^b	BR ₃ (3)	20	40	5.9	1	101.4	3.5	68.5	6.85	1.92	79	1.81
2	Ph ₃ C ⁺ FBR ₃ ⁻ (9)	10	60	0.87	1	104.5	0.69	69.4	6.72	1.80	81	1.99
3 ^b	BR' ₃ (4)	10	5	2.92	3	130.3	28	82.3	2.41	1.96	101	1.85
4	Ph ₃ C ⁺ FBR' ₃ ⁻ (10)	20	12	1.39	1	137.6	2.8	82.2	2.40	1.87	94	2.11
5 ^b	Ph ₃ C ⁺ BR' ₄ ⁻ (6)	4.8	1.25	0.89	3	130.7	71	82.6	2.39	1.87	112	1.95
6	AlR ₃ (5)	20	45	0.84	1	139.5	0.45	83.1	2.00	2.14	74	2.2
7	Ph ₃ C ⁺ FAIR ₃ ⁻ (11)	10	4	1.32	2	142.1	16	86.5	1.70	1.42	138	1.95
8	Ph ₃ C ⁺ F(AIR ₃) ₂ ⁻ (12)	1.6	2	0.79	2	143.7	120	85.5	1.90	1.49	147	2.08
9	(Ph ₃ C ⁺) ₂ F ₂ (AIR ₃) ₃ ²⁻ (13)	2.5	3	0.99	1	143.5	63	86.3	1.80	1.39	144	1.98
10 ^b	Ph ₃ C ⁺ FAIR' ₃ ⁻ (7)	20	75	5	0.5	145.7	1.6	89.4	0.86	1.52	147	1.85
11	Ph ₃ C ⁺ (AIR ₃ FAIR' ₃) ⁻ (14)	2.6	5	0.94	1	145.8	35	85.1	2.10	1.45	121	1.91
12	GaR ₃ (8)	20	40	1.3	0.5	138.0	0.78	82.5	2.10	2.13	77	2.85
13	Ph ₃ C ⁺ F(GaR ₃) ₂ ⁻ (17)	10	3	1.17	3	140.5	19	84.3	2.00	1.70	129	1.93
14	Ph ₃ C ⁺ ClAIR ₃ ⁻ (15)	15	12	0.94	10	139.5	2.5	85.9	1.60	1.76	107	1.86
15	“Ph ₃ C ⁺ Cl(AIR ₃) ₂ ” ^h	10	5	1.56	1	139.9	15	85.6	1.70	1.76	127	1.89
16	Ph ₃ C ⁺ BrAIR ₃ ⁻ (16)	15	60	3.1	0.5	137.9	1.6	85.1	1.60	2.03	126	1.81
17	“Ph ₃ C ⁺ Br(AIR ₃) ₂ ” ^h	10	15	1.24	0.5	138.4	3.9	81.4	2.40	2.06	108	1.77

^a In 54 mL of toluene with precise polymerization temperature control (exotherm < 3°C); estimated [propylene] = 0.83M for the present conditions, see ref. 39. ^b See Ref. 7. ^c Internal temperature variation (±). ^d Second scan by DSC. ^e Taken as a measure of activity. Determined from polymerization yield, assuming the rate law: $v_p = k_p[\text{catalyst}][\text{propylene}]$; assumes 100% of catalyst metal sites are active. ^f Calculated values from ¹³C NMR pentad analysis. Complete pentad distributions appear in the Supporting Information. ^g GPC relative to polystyrene standards. ^h Cocatalyst prepared in situ with a 1:2 ratio of Ph₃CCl or Ph₃CBr and Al(C₆F₅)₃.

Table 2. Propylene polymerization results with $\text{Me}_2\text{C}(\text{Cp})(\text{Flu})\text{ZrMe}_2$ (**1**) + the indicated cocatalysts.^a

Exp. No.	Cocatalysts (R = C_6F_5 ; R' = C_{12}F_9)	μmol	Temp ($^\circ\text{C}$)	$[\text{C}_3\text{H}_6]^b$	Time (min)	PP (g)	ΔT^c ($^\circ\text{C}$)	T_m^d ($^\circ\text{C}$)	k_p^{apparent} ($\text{M}^{-1}\text{s}^{-1}$)	PI^f (%)	P_m (%)	P_{mm} (%)	M_w^g ($\times 10^{-3}$)	M_w/M_n
1	$\text{Ph}_3\text{C}^+[\text{R}_3\text{AlFAIR}']_3^-$ (14)	4.1	-10	2.83	16	0.6	1	158.1	1.3	91.4	0.628	1.29	254	2
2		2.6	0	1.87	4	0.92	0.5	156.5	19	92.3	0.657	1.06	233	1.95
3		2.6	10	1.31	3	0.76	1.5	149.3	29	88.7	1.00	1.60	174	1.99
4		2.6	25	0.83	5	0.94	1	145.8	35	85.0	1.43	2.09	129	1.91
5		3	40	0.56	6	1.33	1	131.5	52	80.0	2.84	2.17	96	1.96
6		2.6	60	0.36	12	0.78	1	97.8	28	63.4	8.00	2.52	69	1.87
7		1.8	60	2.05 ^h	2	1.7	2.5	131.8	91	78.4	2.39	2.91	62	2.43
8	$\text{Ph}_3\text{C}^+\text{FAIR}'_3^-$ (7) ⁱ	20	-10	2.83	180	0.85	n.o. ^j	156.5	0.033	94.2	0.284	0.96	290	1.86
9		20	0	1.87	60	0.54	n.o.	154.5	0.095	93.8	0.273	1.06	242	2.04
10		20	10	1.31	75	1.58	n.o.	151.2	0.32	92.5	0.446	1.19	204	1.96
11		20	25	0.83	75	5.00	n.o.	145.7	1.6	89.4	0.857	1.54	147	1.85
12		20	40	0.56	60	0.51	n.o.	136.0	0.30	83.9	1.77	2.07	104	2.09
13		20	60	0.36	30	0.25	n.o.	N.O.	0.46	70.3	5.43	2.62	66.5	1.95
14		20	60	2.05 ^h	30	2.92	2	127.2	0.94	80.6	2.21	2.52	71	1.86

^a In 54 mL of toluene with precise polymerization temperature control (exotherm $< 3^\circ\text{C}$). ^b Propylene pressure = 1.0 atm unless otherwise indicated, see Ref. 39. ^c Internal temperature variation (\pm). ^d Second scan by DSC. ^e Taken as a measure of activity. Determined from polymerization yield, assuming the rate law: $v_p = k_p[\text{catalyst}][\text{propylene}]$; assumes 100% of catalyst metal sites are active. ^f Pentad analysis by ^{13}C NMR. Complete pentad distributions appear in the Supporting Information. ^g GPC relative to polystyrene standards. ^h Propylene pressure = 5.0 atm, see ref. 7. ⁱ See Ref. 39. ^j Not observed ($\Delta T = 0^\circ\text{C}$).

Table 3. Propylene polymerization results with $\text{Me}_2\text{Si}(\text{OHF})(\text{CpR}^*)\text{ZrMe}_2$ (**2**) + the indicated cocatalysts.^a

Exp. No.	Cocatalysts (R = C_6F_5 ; R' = C_{12}F_9)	μmol	Temp ($^\circ\text{C}$)	$[\text{C}_3\text{H}_6]^b$	Time (min)	PP (g)	ΔT^c ($^\circ\text{C}$)	T_m^d ($^\circ\text{C}$)	k_p^{apparent} ($\text{M}^{-1}\text{s}^{-1}$) ^e	M_w^f ($\times 10^3$)	M_w/M_n	Pentad Fraction (%) ^g		
												<i>mmmm</i>	<i>mmrr</i>	<i>xmrx</i>
1	$\text{Ph}_3\text{C}^+ [\text{R}_3\text{Al FAIR}'_3]^-$ (14)	20	25	0.83	30	2.583	1	147.9	2.1	14.2	2.65	81.9	4.11	2.34
2	$\text{Ph}_3\text{C}^+ [\text{R}_3\text{Al FAIR}'_3]^-$ (12)	15.4	25	0.83	20	0.632	1	145.8	0.98	10.1	2.81	80.2	4.18	2.86
3	$\text{Ph}_3\text{C}^+ \text{BR}_4^-$ (6)	20	25	0.83	20	2.51	1	144.8	3.0	6.4	2.11	83.1	2.96	3.65
4	BR_3 (3)	12.5	25	0.83	240	1.25	1	141.0	0.20	4.0	2.20	79.4	2.56	5.38
5	$\text{Ph}_3\text{C}^+ \text{FAIR}'_3^-$ (7)	30	25	0.83	240	0.55	0.5	134.0	0.036	16.4	7.82	61.9	8.65	5.82
6	$\text{Ph}_3\text{C}^+ [\text{R}_3\text{Al FAIR}'_3]^-$ (14)	10	60	0.36	60	0.221	1	n.d. ^h	0.40	1.01	1.28	54.9	6.27	9.65
7	$\text{Ph}_3\text{C}^+ [\text{R}_3\text{Al FAIR}'_3]^-$ (12)	20	60	0.36	90	0.393	1	n.d.	0.24	0.87	1.25	56.2	5.59	10.6
8	$\text{Ph}_3\text{C}^+ \text{BR}_4^-$ (6)	20	60	0.36	10	0.617	2	n.d.	3.4	0.87	1.27	61.1	3.77	10.1
9	BR_3 (3)	30	60	0.36	45	0.496	1	n.d.	0.40	0.65	1.21	55.6	3.28	13.2
10	$\text{Ph}_3\text{C}^+ \text{FAIR}'_3^-$ (7)	40	60	0.36	420	0.315	1	n.d.	0.021	1.22	1.41	46.6	8.09	10.4
11	$\text{Ph}_3\text{C}^+ [\text{R}_3\text{Al FAIR}'_3]^-$ (14)	8	60	2.05 ⁱ	30	2.588	1	138.0	2.1	3.41	2.06	77.7	3.52	4.88
12	BR_3 (3)	10	60	2.05 ⁱ	30	3.837	1	129.6	2.5	1.44	1.60	69.2	2.95	8.19
13	$\text{Ph}_3\text{C}^+ \text{FAIR}'_3^-$ (7)	20	60	2.05 ⁱ	180	3.142	1	137.7	0.17	4.59	2.29	69.0	5.22	5.44

^a In 54 mL of toluene with precise polymerization temperature control (exotherm < 3 $^\circ\text{C}$). ^b Propylene pressure = 1.0 atm unless otherwise indicated, see Ref. 39. ^c Internal temperature variation (\pm). ^d Second scan by DSC. ^e Taken as a measure of activity. Determined from polymerization yield, assuming the rate law: $v_p = k_p[\text{catalyst}][\text{propylene}]$; assumes 100% of catalyst metal sites are active. ^f GPC relative to polystyrene standards. ^g Pentad analysis by ^{13}C NMR. Complete pentad distributions appear in the Supporting Information. ^h Not determined. ⁱ Propylene pressure = 5.0 atm, See Ref. 39.

Table 4. Propylene polymerization results with $\text{Me}_2\text{Si}(\text{OHf})(\text{CpR}^*)\text{ZrMe}_2$ (**2**) + the indicated cocatalysts at 25°C under 1.0 atm of propylene, with 1,3-dichlorobenzene as solvent.^a

Exp. No.	Cocatalysts (R = C ₆ F ₅ ; R' = C ₁₂ F ₉)	μmol	Time (min)	PP (g)	ΔT^b (°C)	T_m^c (°C)	$k_p[\text{C}_3\text{H}_6]^d$ (s ⁻¹)	M_w^e (x10 ³)	M_w/M_n	Pentad Fraction (%) ^f		
										<i>mmmm</i>	<i>mmrr</i>	<i>xmrxx</i>
1	$\text{Ph}_3\text{C}^+ [\text{R}_3\text{Al FAIR}'_3]^-$ (14)	10	25	1.186	1	147.5	1.9	14.2	2.65	83.7	3.11	2.86
2	$\text{Ph}_3\text{C}^+ [\text{R}_3\text{Al FAIR}_3]^-$ (12)	5	20	0.748 8	1	147.5	3.0	10.1	2.81	85.3	2.67	2.60
3	$\text{Ph}_3\text{C}^+ \text{BR}_4^-$ (6)	10	10	1.282	2	146.4	5.1	6.4	2.11	83.3	3.01	2.98
4	BR_3 (3)	30	6	1.512	2.5	139.3	3.3	4.0	2.20	74.6	3.62	5.33
5	$\text{Ph}_3\text{C}^+ \text{FAIR}'_3^-$ (7)	20	90	1.899	0.3	145.8	0.42	16.4	7.82	78.5	3.75	3.94

^a In 50 mL of 1,3-dichlorobenzene + 4mL toluene (solvent for injected catalyst solution) with precise polymerization temperature control (exotherm < 3°C). ^b Internal temperature variation (\pm). ^c Second scan by DSC. ^d Taken as a measure of activity. Determined from polymerization yield, assuming the rate law: $v_p = k_p[\text{catalyst}][\text{propylene}]$; assumes 100% of catalyst metal sites are active. Propylene solubility unknown for present solvent system. ^e GPC relative to polystyrene standards. ^f Pentad analysis by ¹³C NMR. Complete pentad distributions appear in the Supporting Information.

Table 5. Submodel Descriptions, Assumptions, and Parameterizations for C_1 -Symmetric Metallocene-Mediated Propylene Polymerization.

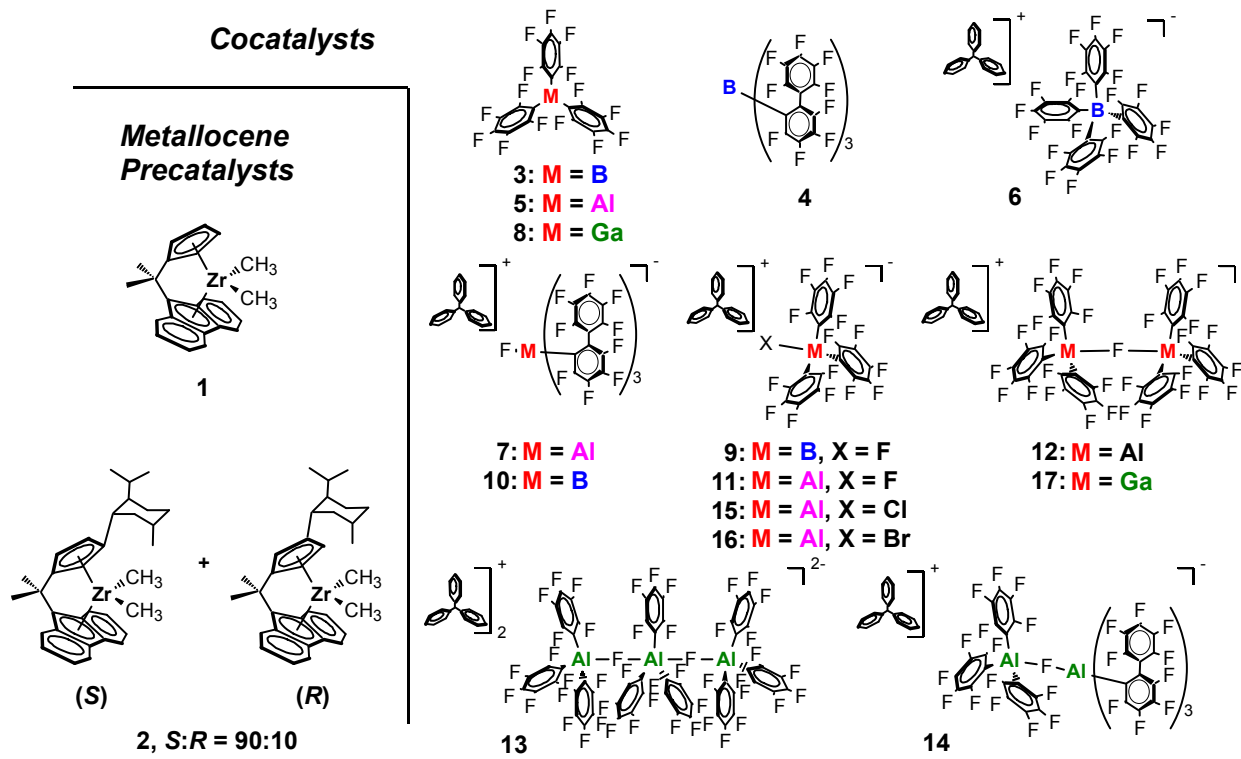
Model	Parameters	Description	$\overline{s^2}$
1	bB bA rA rB	Possible backskip at both catalyst sides.	1.86
2	bB rA rB	Possible backskip at B but not A	5.34
3	rA rB	No backskip at either side (alternating mechanism).	8.64
4	rA	Inevitable backskip at B (backskip mechanism).	9.13

Table 6. Correlation Matrices for Models 1 - 3: Means and Standard Deviations Across All Data Sets for C_1 -Symmetric Metallocene-Mediated Propylene Polymerization.^a

1	bB	bA	rA	rB
bB	1	<i>0.498</i>	<i>0.742</i>	<i>0.650</i>
bA	0.617	1	<i>0.492</i>	<i>0.535</i>
rA	0.185	0.680	1	<i>0.741</i>
rB	-0.368	-0.595	-0.460	1
2	bB	rA	rB	
bB	1	<i>0.122</i>	<i>0.122</i>	
rA	0.215	1	<i>0.000</i>	
rB	-0.215	-1.00	1	
3	rA	rB		
rA	1	<i>0.0451</i>		
rB	-0.480	1		

^a. The model number appears in the upper left-hand corner of each array. Model 4, having one parameter, is not shown. Elements below the diagonal are mean \hat{c}_{ij} values across all data sets for which the model is well-conditioned. Elements above the diagonal (shown in italics) are the corresponding standard deviations.

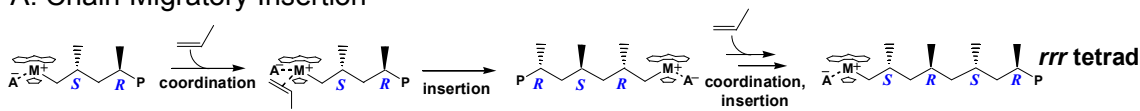
Scheme 1. Chemical Structures, Compounds 1 - 17.



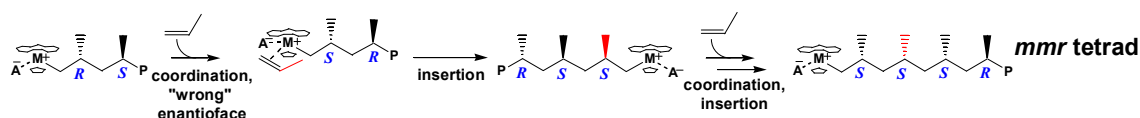
Scheme 2. Syndiospecific Propylene Polymerization and Stereodeflect Mechanisms – C_S -

Symmetric Precatalyst

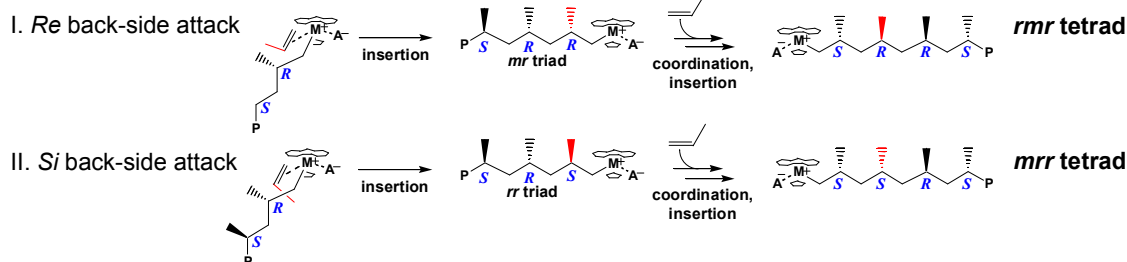
A. Chain-Migratory Insertion



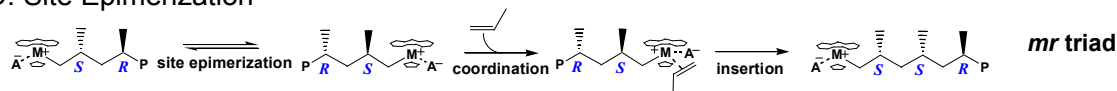
B. Enantiofacial Misinsertion



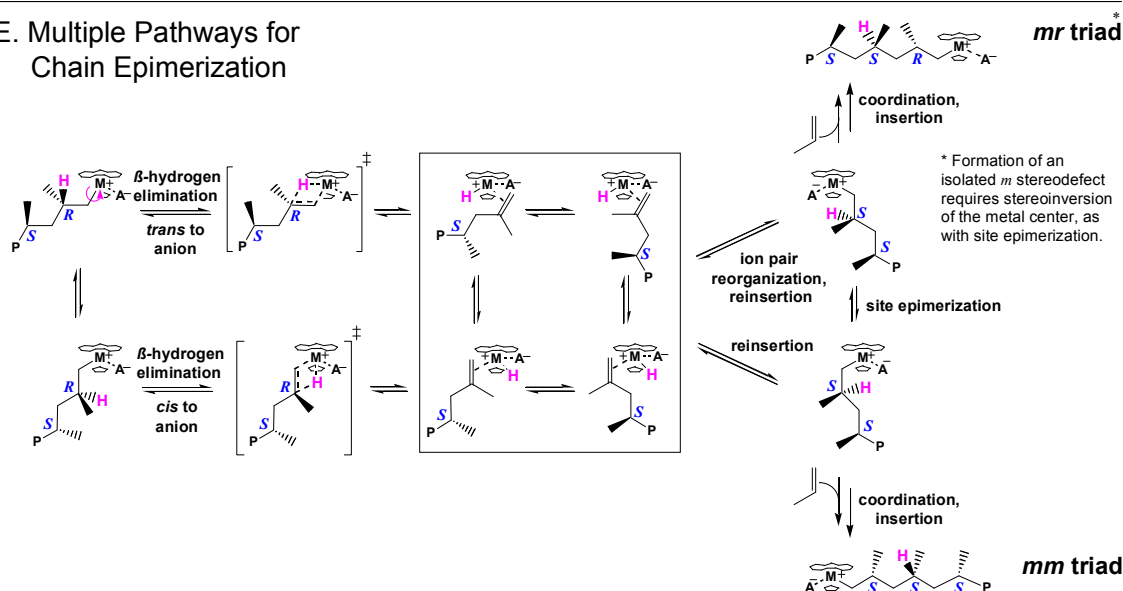
C. "Back-Side" Misinsertion



D. Site Epimerization



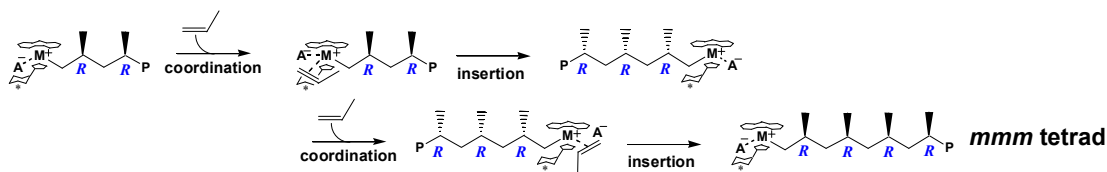
E. Multiple Pathways for Chain Epimerization



Scheme 3. Isospecific Propylene Polymerization and Stereodeflect Mechanisms – C_1 -

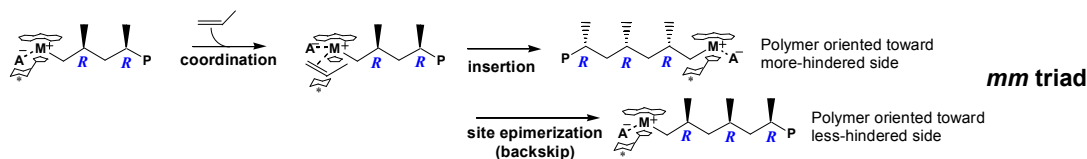
Symmetric Precatalyst.

A. Isospecific Polymerization -- Alternating Mechanism

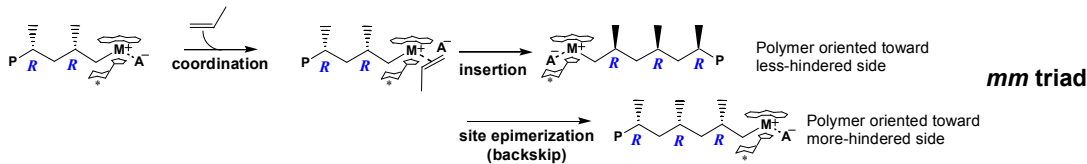


B. Isospecific Polymerization -- Backskip Mechanism

I. Preferred orientation: Polymer toward less-hindered side (higher isoselectivity)

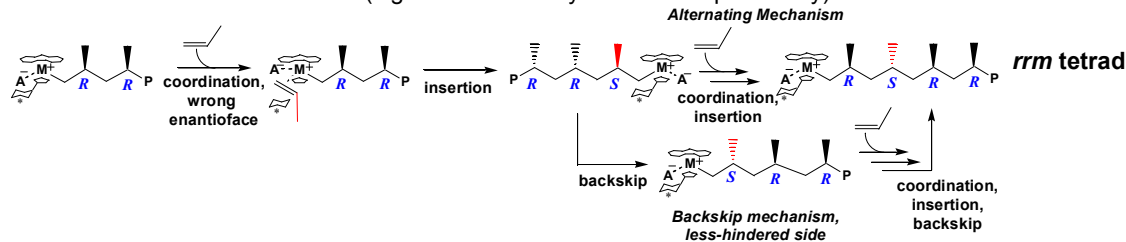


II. Preferred orientation: Polymer toward more-hindered side (lower isoselectivity)

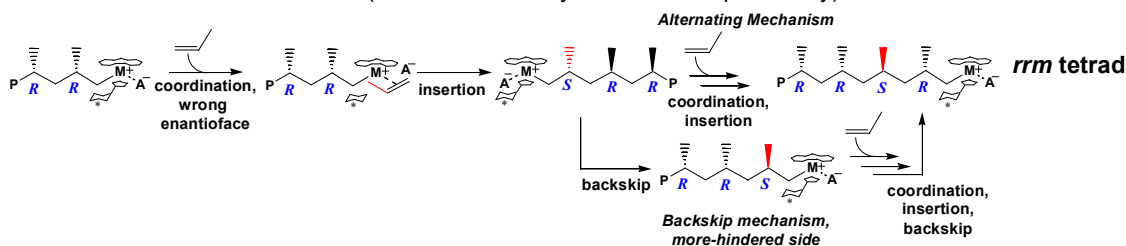


C. Enantiofacial Misinsertion -- Alternating and Backskip Mechanisms

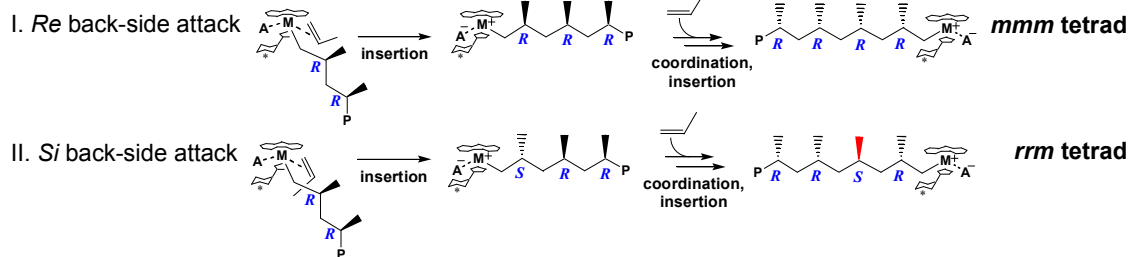
I. At more-hindered site (higher isoselectivity => reduced probability)



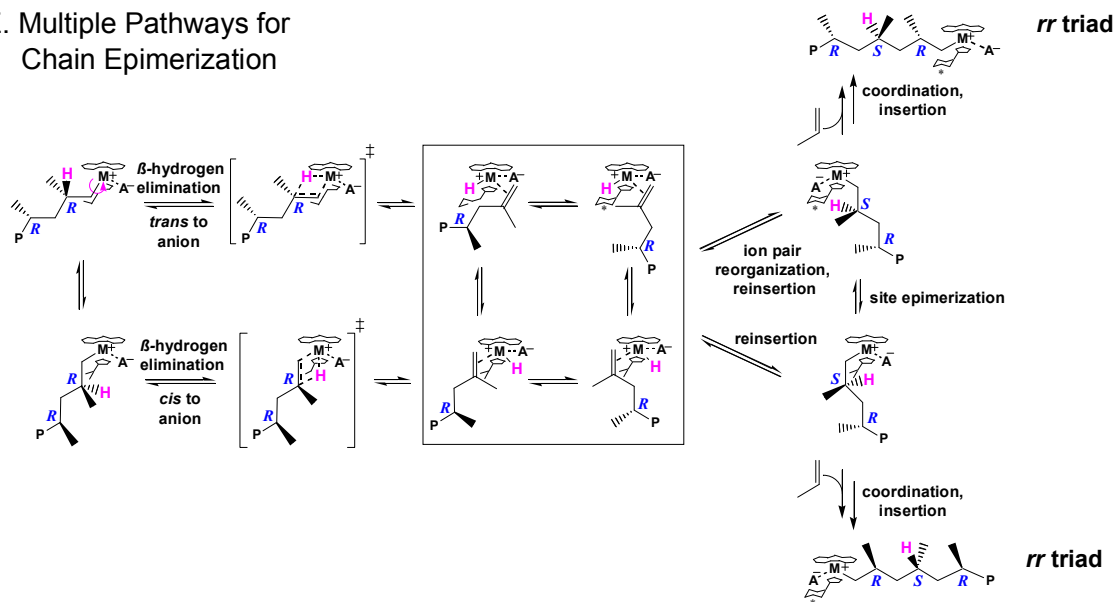
II. At less-hindered site (lower isoselectivity => increased probability)



D. "Back-Side" Misinsertion



E. Multiple Pathways for Chain Epimerization



Supporting Information

Marked Counteranion Effects on Single-Site Olefin Polymerization Processes.

Correlations of Ion Pair Structure and Dynamics with Polymerization

Activity, Chain Transfer, and Syndioselectivity.

Ming-Chou Chen, John A. Roberts, and Tobin J. Marks*

Department of Chemistry, Northwestern University

Evanston, Illinois 60208-3113

Figure 1. Full-page, low peak-threshold EXSY spectrum for **10** at 127°C, $\tau_m = 800$ ms.

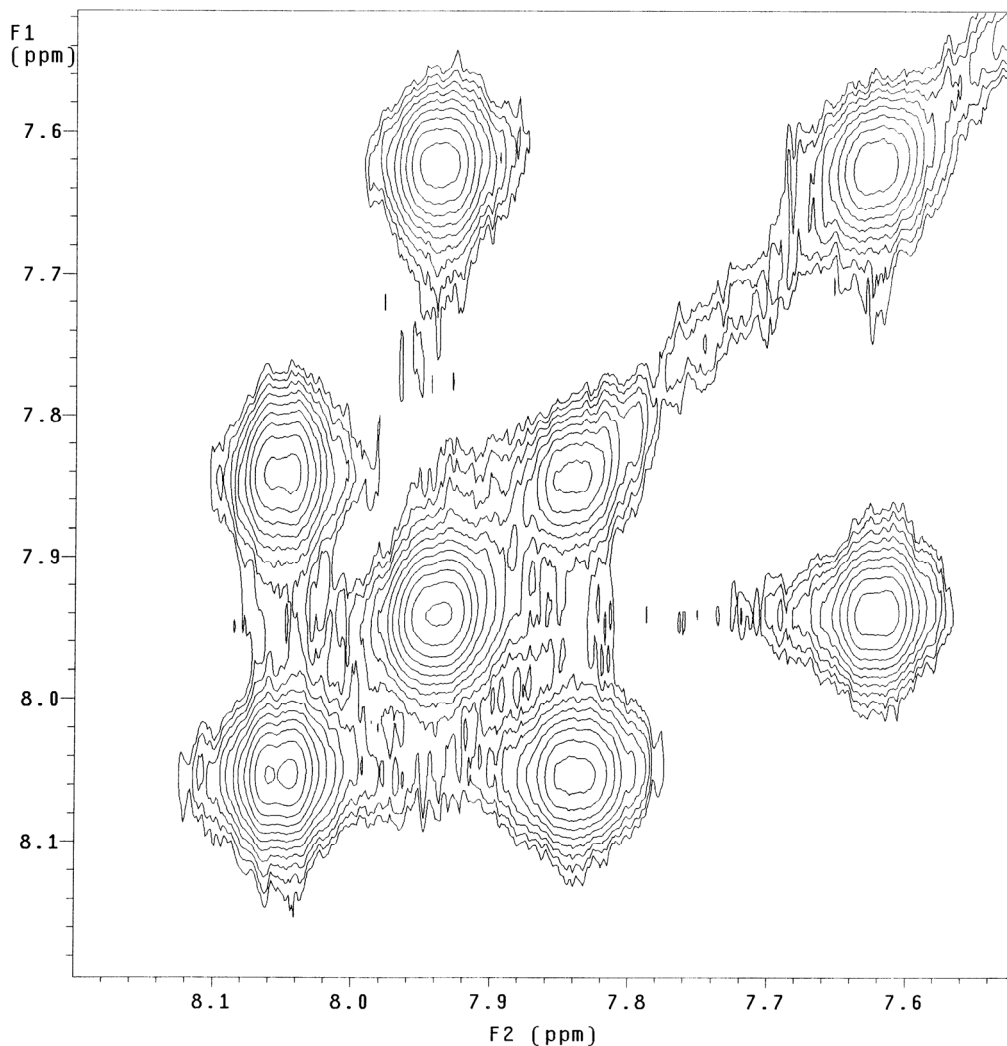


Table 1. Propylene Polymerization Results for the Reactions Mediated by **1** + IndicatedCocatalysts under 1.0 atm of Propylene from -10° to $40^{\circ}\text{C}^{\text{a}}$

Exp No	Cocat. (Cat)	T_p ($^{\circ}\text{C}$)	Cat. (μmol)	Time (h)	Polymer yeild (g)	Activity ($\times 10^6$) ^b	$rrmr^{\text{c}}$ (%)
1	3(7)	-10	20	0.5	0.50	0.050	2.2
2	3(7)	-5	20	0.5	0.72	0.072	2.8
3	3(7)	0	20	0.5	1.14	0.114	3.4
4	3(7)	3.5	20	0.67	2.03	0.152	4.0
5	3(7)	7.5	20	0.67	2.77	0.207	4.9
6	3(7)	10	20	1	4.68	0.234	5.5
7	3(7)	13.5	20	0.417	2.29	0.275	7.0
8	3(7)	17.5	20	0.5	3.34	0.334	8.3
9	3(7)	21	20	0.67	5.06	0.378	9.6
10	3(7)	25	20	0.5	4.36	0.436	10.7
11	5(9)	-10	1.5	0.083	1.18	9.44	0.6
12	5(9)	-5	1.275	0.050	0.571	8.96	0.8 ^d
13	5(9)	0	1.275	0.050	0.735	11.53	1.0
14	5(9)	5	1.992	0.050	1.047	10.51	1.5 ^d
15	5(9)	10	1.275	0.033	0.42	9.8	2.0
16	5(9)	15	1.275	0.039	0.639	12.89	2.8
17	5(9)	19	2.754	0.033	1.075	11.71	3.4 ^d
18	5(9)	21	1.275	0.050	0.575	9.02	3.7
19	5(9)	25	1.275	0.050	0.724	11.35	4.4
20	5(9)	29	2.100	0.050	1.460	13.90	5.5
21	5(9)	33	2.100	0.050	1.338	12.74	6.5
22	5(9)	37	1.366	0.050	0.921	13.49	7.9

^a In 50 mL of toluene with precise polymerization temperature control (exotherm $< 3^{\circ}\text{C}$). ^b Units: g polymer/(mol cat.*atm*h). ^c Pentad analysis by ^{13}C NMR. ^d Low-temperature values for % $rrmr$ determined from back- extrapolation using high-temperature line fits.

Table 2. Results from polymerizations in which the amount of added MAO is varied.

Polymerization conditions: 1.0 atm propylene, 50mL toluene.

MAO ^a (eq.)	Temp (°C)	<i>rmmr</i> (%)	<i>rrmm</i> (%)	<i>rrmr</i> (%)	<i>rrrr</i> (%)	<i>Activity</i> ^b
60	25	1.2	2.4	2.4	89.3	3.96
1500	25	1.1	2.3	2.4	89.6	2.4
1500 ^c	25	1.0	2.3	2.6	89.3	0.57
60	60	2.0	4.2	12.1	63	1.49
1500 ^c	60	1.9	3.7	11.7	63.6	0.10

^a eq = Equivalents added MAO vs metallocene. Solvent from as-shipped MAO is removed under vacuum prior to use. ^b Activity units: 10⁶ g polymer/(mol cat.*atm*h).

^c MAO is used as a solution purchased from Aldrich Chemical Co.

Refinement details, Polypropylene ¹³C NMR pentad analysis (1 of 10)

COCATALYST: B(C₆F₅)₃
 [C₃H₆] = 0.363 M
 T = -10°C

pentad	experimental	calculated	weighting multiplier
mmmm	0.0008	0.0002	1.0
mmmr	0.0017	0.0010	1.0
rmmr	0.0130	0.0128	1.4
mmrr	0.0243	0.0260	1.8
mrrm+rmrr	0.0231	0.0242	1.8
rrmm	0.0041	0.0010	1.1
rrrr+rrrm+mrrm	0.9330	0.9347	1.0

$P_m = 0.0125$
 $P_{mm} = 0.0141$
 weighted resid: 0.000024
 standard resid: 0.000020

COCATALYST: B(C₆F₅)₃
 [C₃H₆] = 0.363 M
 T = 25°C

pentad	experimental	calculated	weighting multiplier
mmmm	0.0026	0.0006	1.1
mmmr	0.0043	0.0052	1.1
rmmr	0.0164	0.0175	1.5
mmrr	0.0337	0.0368	2.3
mrrm+rmrr	0.1058	0.1064	12.4
rrmm	0.0175	0.0101	1.5
rrrr+rrrm+mrrm	0.8197	0.8234	1.0

$P_m = 0.0666$
 $P_{mm} = 0.0196$
 weighted resid: 0.000193
 standard resid: 0.000125

COCATALYST: B(C₆F₅)₃
 [C₃H₆] = 0.363 M
 T = 0°C

pentad	experimental	calculated	weighting multiplier
mmmm	0.0010	0.0003	1.0
mmmr	0.0020	0.0016	1.1
rmmr	0.0133	0.0144	1.4
mmrr	0.0261	0.0293	1.9
mrrm+rmrr	0.0349	0.0369	2.4
rrmm	0.0108	0.0018	1.3
rrrr+rrrm+mrrm	0.9119	0.9157	1.0

$P_m = 0.0197$
 $P_{mm} = 0.0162$
 weighted resid: 0.000181
 standard resid: 0.000133

COCATALYST: B(C₆F₅)₃
 [C₃H₆] = 0.363 M
 T = 40°C

pentad	experimental	calculated	weighting multiplier
mmmm	0.0016	0.0016	1.0
mmmr	0.0092	0.0117	1.3
rmmr	0.0218	0.0241	1.7
mmrr	0.0476	0.0513	3.2
mrrm+rmrr	0.1624	0.1628	43.0
rrmm	0.0389	0.0262	2.6
rrrr+rrrm+mrrm	0.7184	0.7223	1.0

$P_m = 0.1208$
 $P_{mm} = 0.0248$
 weighted resid: 0.000916
 standard resid: 0.000369

COCATALYST: B(C₆F₅)₃
 [C₃H₆] = 0.363 M
 T = 10°C

pentad	experimental	calculated	weighting multiplier
mmmm	0.0002	0.0003	1.0
mmmr	0.0026	0.0021	1.1
rmmr	0.0132	0.0136	1.4
mmrr	0.0262	0.0279	1.9
mrrm+rmrr	0.0547	0.0553	3.8
rrmm	0.0070	0.0030	1.2
rrrr+rrrm+mrrm	0.8960	0.8979	1.0

$P_m = 0.0308$
 $P_{mm} = 0.0153$
 weighted resid: 0.000037
 standard resid: 0.000029

COCATALYST: B(C₆F₅)₃
 [C₃H₆] = 0.363 M
 T = 60°C

pentad	experimental	calculated	weighting multiplier
mmmm	0.0055	0.0058	1.1
mmmr	0.0234	0.0290	1.8
rmmr	0.0367	0.0379	2.5
mmrr	0.0716	0.0806	5.6
mrrm+rmrr	0.2086	0.2094	114.0
rrmm	0.0765	0.0559	6.3
rrrr+rrrm+mrrm	0.5776	0.5815	1.0

$P_m = 0.1971$
 $P_{mm} = 0.0418$
 weighted resid: 0.008432
 standard resid: 0.001424

Refinement details, Polypropylene ^{13}C NMR pentad analysis (2 of 10)

COCATALYST: $\text{Ph}_3\text{C}^+\text{B}(\text{C}_6\text{F}_5)_4^-$
 $[\text{C}_3\text{H}_6] = 0.363 \text{ M}$
 $T = -10^\circ\text{C}$

pentad	experimental	calculated	weighting multiplier
mmmm	0.0000	0.0001	1.0
mmmr	0.0000	0.0004	1.0
rmmr	0.0108	0.0105	1.3
mmrr	0.0200	0.0211	1.6
mrrm+rmrr	0.0080	0.0089	1.2
rrmm	0.0036	0.0004	1.1
rrrr+rrrm+mrrm	0.9576	0.9586	1.0

$P_m = 0.0043$
 $P_{mm} = 0.0112$
weighted resid: 0.000017
standard resid: 0.000015

COCATALYST: $\text{Ph}_3\text{C}^+\text{B}(\text{C}_6\text{F}_5)_4^-$
 $[\text{C}_3\text{H}_6] = 0.363 \text{ M}$
 $T = 25^\circ\text{C}$

pentad	experimental	calculated	weighting multiplier
mmmm	0.0001	0.0004	1.0
mmmr	0.0016	0.0022	1.0
rmmr	0.0150	0.0163	1.5
mmrr	0.0325	0.0333	2.2
mrrm+rmrr	0.0434	0.0441	2.9
rrmm	0.0075	0.0025	1.2
rrrr+rrrm+mrrm	0.8998	0.9012	1.0

$P_m = 0.0239$
 $P_{mm} = 0.0187$
weighted resid: 0.000047
standard resid: 0.000038

COCATALYST: $\text{Ph}_3\text{C}^+\text{B}(\text{C}_6\text{F}_5)_4^-$
 $[\text{C}_3\text{H}_6] = 0.363 \text{ M}$
 $T = 0^\circ\text{C}$

pentad	experimental	calculated	weighting multiplier
mmmm	0.0000	0.0002	1.0
mmmr	0.0007	0.0007	1.0
rmmr	0.0114	0.0120	1.3
mmrr	0.0231	0.0243	1.8
mrrm+rmrr	0.0144	0.0156	1.4
rrmm	0.0053	0.0006	1.1
rrrr+rrrm+mrrm	0.9452	0.9466	1.0

$P_m = 0.0078$
 $P_{mm} = 0.0130$
weighted resid: 0.000035
standard resid: 0.000030

COCATALYST: $\text{Ph}_3\text{C}^+\text{B}(\text{C}_6\text{F}_5)_4^-$
 $[\text{C}_3\text{H}_6] = 0.363 \text{ M}$
 $T = 40^\circ\text{C}$

pentad	experimental	calculated	weighting multiplier
mmmm	0.0014	0.0006	1.0
mmmr	0.0046	0.0049	1.1
rmmr	0.0177	0.0191	1.5
mmrr	0.0376	0.0398	2.5
mrrm+rmrr	0.0855	0.0861	7.8
rrmm	0.0142	0.0073	1.4
rrrr+rrrm+mrrm	0.8391	0.8422	1.0

$P_m = 0.0514$
 $P_{mm} = 0.0227$
weighted resid: 0.000135
standard resid: 0.000091

COCATALYST: $\text{Ph}_3\text{C}^+\text{B}(\text{C}_6\text{F}_5)_4^-$
 $[\text{C}_3\text{H}_6] = 0.363 \text{ M}$
 $T = 10^\circ\text{C}$

pentad	experimental	calculated	weighting multiplier
mmmm	0.0000	0.0002	1.0
mmmr	0.0014	0.0011	1.0
rmmr	0.0126	0.0135	1.4
mmrr	0.0253	0.0273	1.9
mrrm+rmrr	0.0214	0.0232	1.7
rrmm	0.0082	0.0010	1.2
rrrr+rrrm+mrrm	0.9311	0.9337	1.0

$P_m = 0.0119$
 $P_{mm} = 0.0149$
weighted resid: 0.000098
standard resid: 0.000077

COCATALYST: $\text{Ph}_3\text{C}^+\text{B}(\text{C}_6\text{F}_5)_4^-$
 $[\text{C}_3\text{H}_6] = 0.363 \text{ M}$
 $T = 60^\circ\text{C}$

pentad	experimental	calculated	weighting multiplier
mmmm	0.0023	0.0022	1.1
mmmr	0.0131	0.0149	1.4
rmmr	0.0258	0.0276	1.9
mmrr	0.0546	0.0590	3.8
mrrm+rmrr	0.1698	0.1703	50.5
rrmm	0.0436	0.0305	2.9
rrrr+rrrm+mrrm	0.6908	0.6956	1.0

$P_m = 0.1308$
 $P_{mm} = 0.0306$
weighted resid: 0.001198
standard resid: 0.000430

Refinement details, Polypropylene ¹³C NMR pentad analysis (3 of 10)

COCATALYST: MAO
[C₃H₆] = 0.363 M
T = -10°C

pentad	experimental	calculated	weighting multiplier
mmmm	0.0000	0.0001	1.0
mmmr	0.0000	0.0002	1.0
rmmr	0.0076	0.0069	1.2
mmrr	0.0134	0.0139	1.4
mrrm+rmrr	0.0059	0.0061	1.2
rmm	0.0005	0.0002	1.0
rrrr+rrrm+mrrm	0.9725	0.9727	1.0

$P_m = 0.0030$
 $P_{mm} = 0.0072$
weighted resid: 0.000001
standard resid: 0.000001

COCATALYST: MAO
[C₃H₆] = 0.363 M
T = 25°C

pentad	experimental	calculated	weighting multiplier
mmmm	0.0000	0.0002	1.0
mmmr	0.0000	0.0010	1.0
rmmr	0.0126	0.0123	1.4
mmrr	0.0238	0.0250	1.8
mrrm+rmrr	0.0240	0.0248	1.8
rmm	0.0048	0.0010	1.1
rrrr+rrrm+mrrm	0.9347	0.9358	1.0

$P_m = 0.0128$
 $P_{mm} = 0.0135$
weighted resid: 0.000026
standard resid: 0.000022

COCATALYST: MAO
[C₃H₆] = 0.363 M
T = 0°C

pentad	experimental	calculated	weighting multiplier
mmmm	0.0000	0.0001	1.0
mmmr	0.0000	0.0003	1.0
rmmr	0.0100	0.0083	1.3
mmrr	0.0156	0.0166	1.5
mrrm+rmrr	0.0085	0.0087	1.2
rmm	0.0004	0.0003	1.0
rrrr+rrrm+mrrm	0.9656	0.9658	1.0

$P_m = 0.0043$
 $P_{mm} = 0.0087$
weighted resid: 0.000006
standard resid: 0.000005

COCATALYST: MAO
[C₃H₆] = 0.363 M
T = 40°C

pentad	experimental	calculated	weighting multiplier
mmmm	0.0000	0.0003	1.0
mmmr	0.0004	0.0019	1.0
rmmr	0.0151	0.0136	1.5
mmrr	0.0263	0.0279	1.9
mrrm+rmrr	0.0485	0.0489	3.3
rmm	0.0058	0.0025	1.2
rrrr+rrrm+mrrm	0.9039	0.9050	1.0

$P_m = 0.0268$
 $P_{mm} = 0.0153$
weighted resid: 0.000030
standard resid: 0.000024

COCATALYST: MAO
[C₃H₆] = 0.363 M
T = 10°C

pentad	experimental	calculated	weighting multiplier
mmmm	0.0000	0.0001	1.0
mmmr	0.0000	0.0003	1.0
rmmr	0.0093	0.0084	1.3
mmrr	0.0156	0.0169	1.5
mrrm+rmrr	0.0101	0.0108	1.3
rmm	0.0026	0.0003	1.1
rrrr+rrrm+mrrm	0.9625	0.9633	1.0

$P_m = 0.0054$
 $P_{mm} = 0.0088$
weighted resid: 0.000011
standard resid: 0.000009

COCATALYST: MAO
[C₃H₆] = 0.363 M
T = 60°C

pentad	experimental	calculated	weighting multiplier
mmmm	0.0020	0.0010	1.1
mmmr	0.0060	0.0076	1.2
rmmr	0.0196	0.0212	1.6
mmrr	0.0413	0.0449	2.7
mrrm+rmrr	0.1205	0.1211	17.2
rmm	0.0251	0.0139	1.9
rrrr+rrrm+mrrm	0.7855	0.7902	1.0

$P_m = 0.0791$
 $P_{mm} = 0.0248$
weighted resid: 0.000483
standard resid: 0.000264

Refinement details, Polypropylene ¹³C NMR pentad analysis (4 of 10)COCATALYST: Ph₃C⁺FAI(2-C₆F₅C₆F₄)₃⁻[C₃H₆] = 0.363 M

T = -10°C

pentad	experimental	calculated	weighting multiplier
mmmm	0.0001	0.0001	1.0
mmmr	0.0001	0.0003	1.0
rmmr	0.0094	0.0090	1.3
mmrr	0.0167	0.0181	1.5
mrrm+rmrr	0.0048	0.0060	1.1
rmm	0.0039	0.0002	1.1
rrrr+rrrm+mrrm	0.9651	0.9663	1.0

P_m = 0.0029P_{mm} = 0.0095

weighted resid: 0.000023

standard resid: 0.000020

COCATALYST: Ph₃C⁺FAI(2-C₆F₅C₆F₄)₃⁻[C₃H₆] = 0.363 M

T = 25°C

pentad	experimental	calculated	weighting multiplier
mmmm	0.0000	0.0002	1.0
mmmr	0.0010	0.0009	1.0
rmmr	0.0143	0.0139	1.4
mmrr	0.0265	0.0280	1.9
mrrm+rmrr	0.0160	0.0171	1.5
rmm	0.0047	0.0008	1.1
rrrr+rrrm+mrrm	0.9376	0.9391	1.0

P_m = 0.0086P_{mm} = 0.0152

weighted resid: 0.000029

standard resid: 0.000024

COCATALYST: Ph₃C⁺FAI(2-C₆F₅C₆F₄)₃⁻[C₃H₆] = 0.363 M

T = 0°C

pentad	experimental	calculated	weighting multiplier
mmmm	0.0003	0.0001	1.0
mmmr	0.0004	0.0003	1.0
rmmr	0.0088	0.0099	1.2
mmrr	0.0186	0.0198	1.6
mrrm+rmrr	0.0043	0.0059	1.1
rmm	0.0055	0.0003	1.1
rrrr+rrrm+mrrm	0.9622	0.9637	1.0

P_m = 0.0028P_{mm} = 0.0104

weighted resid: 0.000043

standard resid: 0.000037

COCATALYST: Ph₃C⁺FAI(2-C₆F₅C₆F₄)₃⁻[C₃H₆] = 0.363 M

T = 40°C

pentad	experimental	calculated	weighting multiplier
mmmm	0.0012	0.0004	1.0
mmmr	0.0028	0.0020	1.1
rmmr	0.0165	0.0177	1.5
mmrr	0.0332	0.0360	2.3
mrrm+rmrr	0.0308	0.0331	2.1
rmm	0.0107	0.0019	1.3
rrrr+rrrm+mrrm	0.9048	0.9088	1.0

P_m = 0.0174P_{mm} = 0.0203

weighted resid: 0.000183

standard resid: 0.000133

COCATALYST: Ph₃C⁺FAI(2-C₆F₅C₆F₄)₃⁻[C₃H₆] = 0.363 M

T = 10°C

pentad	experimental	calculated	weighting multiplier
mmmm	0.0000	0.0001	1.0
mmmr	0.0008	0.0005	1.0
rmmr	0.0109	0.0110	1.3
mmrr	0.0210	0.0222	1.7
mrrm+rmrr	0.0081	0.0092	1.2
rmm	0.0040	0.0004	1.1
rrrr+rrrm+mrrm	0.9552	0.9565	1.0

P_m = 0.0045P_{mm} = 0.0118

weighted resid: 0.000022

standard resid: 0.000019

COCATALYST: Ph₃C⁺FAI(2-C₆F₅C₆F₄)₃⁻[C₃H₆] = 0.363 M

T = 60°C

pentad	experimental	calculated	weighting multiplier
mmmm	0.0017	0.0008	1.0
mmmr	0.0062	0.0058	1.2
rmmr	0.0198	0.0214	1.6
mmrr	0.0419	0.0447	2.8
mrrm+rmrr	0.0870	0.0879	8.1
rmm	0.0162	0.0081	1.5
rrrr+rrrm+mrrm	0.8273	0.8315	1.0

P_m = 0.0527P_{mm} = 0.0261

weighted resid: 0.000213

standard resid: 0.000137

Refinement details, Polypropylene ^{13}C NMR pentad analysis (5 of 10)

COCATALYST: $\text{B}(2\text{-C}_6\text{F}_5\text{C}_6\text{F}_4)_3$
 $[\text{C}_3\text{H}_6] = 0.363 \text{ M}$
 $T = -10^\circ\text{C}$

pentad	experimental	calculated	weighting multiplier
mmmm	0.0000	0.0002	1.0
mmmr	0.0000	0.0005	1.0
rmmr	0.0117	0.0119	1.3
mmrr	0.0233	0.0240	1.8
mrrm+rmrr	0.0086	0.0093	1.2
rmm	0.0036	0.0005	1.1
rrrr+rrrm+mrrm	0.9528	0.9536	1.0

$P_m = 0.0045$
 $P_{mm} = 0.0128$
 weighted resid: 0.000015
 standard resid: 0.000013

COCATALYST: $\text{B}(2\text{-C}_6\text{F}_5\text{C}_6\text{F}_4)_3$
 $[\text{C}_3\text{H}_6] = 0.363 \text{ M}$
 $T = 25^\circ\text{C}$

pentad	experimental	calculated	weighting multiplier
mmmm	0.0000	0.0004	1.0
mmmr	0.0018	0.0023	1.0
rmmr	0.0172	0.0168	1.5
mmrr	0.0324	0.0345	2.2
mrrm+rmrr	0.0428	0.0439	2.9
rmm	0.0085	0.0025	1.2
rrrr+rrrm+mrrm	0.8973	0.8996	1.0

$P_m = 0.0237$
 $P_{mm} = 0.0194$
 weighted resid: 0.000077
 standard resid: 0.000058

COCATALYST: $\text{B}(2\text{-C}_6\text{F}_5\text{C}_6\text{F}_4)_3$
 $[\text{C}_3\text{H}_6] = 0.363 \text{ M}$
 $T = 0^\circ\text{C}$

pentad	experimental	calculated	weighting multiplier
mmmm	0.0000	0.0002	1.0
mmmr	0.0010	0.0007	1.0
rmmr	0.0129	0.0130	1.4
mmrr	0.0249	0.0261	1.8
mrrm+rmrr	0.0122	0.0134	1.4
rmm	0.0044	0.0006	1.1
rrrr+rrrm+mrrm	0.9446	0.9460	1.0

$P_m = 0.0066$
 $P_{mm} = 0.0141$
 weighted resid: 0.000026
 standard resid: 0.000022

COCATALYST: $\text{B}(2\text{-C}_6\text{F}_5\text{C}_6\text{F}_4)_3$
 $[\text{C}_3\text{H}_6] = 0.363 \text{ M}$
 $T = 40^\circ\text{C}$

pentad	experimental	calculated	weighting multiplier
mmmm	0.0015	0.0008	1.0
mmmr	0.0046	0.0057	1.1
rmmr	0.0193	0.0212	1.6
mmrr	0.0408	0.0444	2.7
mrrm+rmrr	0.0870	0.0881	8.0
rmm	0.0202	0.0081	1.7
rrrr+rrrm+mrrm	0.8266	0.8317	1.0

$P_m = 0.0529$
 $P_{mm} = 0.0259$
 weighted resid: 0.000468
 standard resid: 0.000280

COCATALYST: $\text{B}(2\text{-C}_6\text{F}_5\text{C}_6\text{F}_4)_3$
 $[\text{C}_3\text{H}_6] = 0.363 \text{ M}$
 $T = 10^\circ\text{C}$

pentad	experimental	calculated	weighting multiplier
mmmm	0.0008	0.0003	1.0
mmmr	0.0011	0.0012	1.0
rmmr	0.0149	0.0152	1.4
mmrr	0.0290	0.0307	2.0
mrrm+rmrr	0.0184	0.0200	1.6
rmm	0.0060	0.0010	1.2
rrrr+rrrm+mrrm	0.9297	0.9317	1.0

$P_m = 0.0101$
 $P_{mm} = 0.0168$
 weighted resid: 0.000049
 standard resid: 0.000040

COCATALYST: $\text{B}(2\text{-C}_6\text{F}_5\text{C}_6\text{F}_4)_3$
 $[\text{C}_3\text{H}_6] = 0.363 \text{ M}$
 $T = 60^\circ\text{C}$

pentad	experimental	calculated	weighting multiplier
mmmm	0.0030	0.0022	1.1
mmmr	0.0123	0.0144	1.4
rmmr	0.0263	0.0275	1.9
mmrr	0.0545	0.0587	3.8
mrrm+rmrr	0.1640	0.1644	44.5
rmm	0.0405	0.0283	2.7
rrrr+rrrm+mrrm	0.6995	0.7046	1.0

$P_m = 0.1237$
 $P_{mm} = 0.0316$
 weighted resid: 0.000984
 standard resid: 0.000383

Refinement details, Polypropylene ¹³C NMR pentad analysis (6 of 10)

COCATALYST: B(C₆F₅)₃
 [C₃H₆] = 0.363 M
 T = 60°C

pentad	experimental	calculated	weighting multiplier
mmmm	0.0041	0.0062	1.1
mmmr	0.0225	0.0305	1.7
rmmr	0.0360	0.0388	2.4
mmrr	0.0713	0.0825	5.6
xmrx	0.2105	0.2115	118.6
rmm	0.0837	0.0580	7.5
rrrr+rrrm+mrrm	0.5718	0.5725	1.0

$P_m = 0.2023$
 $P_{mm} = 0.0432$
 weighted resid: 0.015313
 standard resid: 0.002239

COCATALYST: B(C₆F₅)₃
 [C₃H₆] = 1.60 M
 T = 60°C

pentad	experimental	calculated	weighting multiplier
mmmm	0.0030	0.0018	1.1
mmmr	0.0104	0.0122	1.3
rmmr	0.0243	0.0257	1.8
mmrr	0.0502	0.0549	3.4
xmrx	0.1517	0.1522	34.2
rmm	0.0365	0.0235	2.5
rrrr+rrrm+mrrm	0.7239	0.7296	1.0

$P_m = 0.1096$
 $P_{mm} = 0.0300$
 weighted resid: 0.000975
 standard resid: 0.000416

COCATALYST: B(C₆F₅)₃
 [C₃H₆] = 0.760 M
 T = 60°C

pentad	experimental	calculated	weighting multiplier
mmmm	0.0014	0.0028	1.0
mmmr	0.0147	0.0178	1.4
rmmr	0.0282	0.0297	2.0
mmrr	0.0575	0.0630	4.0
mrrm+rmrr	0.1897	0.1902	76.9
rmm	0.0557	0.0398	3.9
rrrr+rrrm+mrrm	0.6527	0.6566	1.0

$P_m = 0.1586$
 $P_{mm} = 0.0288$
 weighted resid: 0.002463
 standard resid: 0.000667

COCATALYST: B(C₆F₅)₃
 [C₃H₆] = 2.05 M
 T = 60°C

pentad	experimental	calculated	weighting multiplier
mmmm	0.0024	0.0016	1.1
mmmr	0.0100	0.0111	1.3
rmmr	0.0231	0.0250	1.8
mmrr	0.0497	0.0533	3.4
mrrm+rmrr	0.1417	0.1421	27.4
rmm	0.0312	0.0203	2.2
rrrr+rrrm+mrrm	0.7419	0.7467	1.0

$P_m = 0.1283$
 $P_{mm} = 0.0328$
 weighted resid: 0.001266
 standard resid: 0.000472

COCATALYST: B(C₆F₅)₃
 [C₃H₆] = 1.18 M
 T = 60°C

pentad	experimental	calculated	weighting multiplier
mmmm	0.0037	0.0024	1.1
mmmr	0.0153	0.0154	1.5
rmmr	0.0258	0.0284	1.9
mmrr	0.0556	0.0607	3.9
mrrm+rmrr	0.1675	0.1680	48.1
rmm	0.0430	0.0300	2.9
rrrr+rrrm+mrrm	0.6890	0.6951	1.0

$P_m = 0.1283$
 $P_{mm} = 0.0328$
 weighted resid: 0.001266
 standard resid: 0.000472

Refinement details, Polypropylene ^{13}C NMR pentad analysis (7 of 10)COCATALYST: $\text{Ph}_3\text{C}^+\text{B}(\text{C}_6\text{F}_5)_4^-$ $[\text{C}_3\text{H}_6] = 0.363 \text{ M}$ $T = 60^\circ\text{C}$

	experimental	calculated	weighting multiplier
pentad			
mmmm	0.0024	0.0024	1.1
mmmr	0.0133	0.0156	1.4
rmmr	0.0260	0.0284	1.9
mmrr	0.0549	0.0607	3.8
xmrx	0.1703	0.1708	50.9
rmrm	0.0481	0.0311	3.2
rrrr+rrrm+mrrm	0.6850	0.6909	1.0

 $P_m = 0.1318$ $P_{mm} = 0.0323$

weighted resid: 0.002245

standard resid: 0.000730

COCATALYST: $\text{Ph}_3\text{C}^+\text{B}(\text{C}_6\text{F}_5)_4^-$ $[\text{C}_3\text{H}_6] = 1.60 \text{ M}$ $T = 60^\circ\text{C}$

	experimental	calculated	weighting multiplier
pentad			
mmmm	0.0006	0.0008	1.0
mmmr	0.0040	0.0057	1.1
rmmr	0.0212	0.0210	1.7
mmrr	0.0417	0.0439	2.8
xmrx	0.0893	0.0899	8.5
rmrm	0.0156	0.0083	1.5
rrrr+rrrm+mrrm	0.8276	0.8304	1.0

 $P_m = 0.0542$ $P_{mm} = 0.0255$

weighted resid: 0.000153

standard resid: 0.000100

COCATALYST: $\text{Ph}_3\text{C}^+\text{B}(\text{C}_6\text{F}_5)_4^-$ $[\text{C}_3\text{H}_6] = 0.760 \text{ M}$ $T = 60^\circ\text{C}$

	experimental	calculated	weighting multiplier
pentad			
mmmm	0.0015	0.0013	1.0
mmmr	0.0077	0.0096	1.2
rmmr	0.0231	0.0237	1.8
mmrr	0.0471	0.0504	3.2
mmrm+rmrr	0.1305	0.1309	21.4
rmrm	0.0273	0.0170	2.0
rrrr+rrrm+mrrm	0.7628	0.7671	1.0

 $P_m = 0.0881$ $P_{mm} = 0.0285$

weighted resid: 0.000446

standard resid: 0.000230

COCATALYST: $\text{Ph}_3\text{C}^+\text{B}(\text{C}_6\text{F}_5)_4^-$ $[\text{C}_3\text{H}_6] = 2.05 \text{ M}$ $T = 60^\circ\text{C}$

	experimental	calculated	weighting multiplier
pentad			
mmmm	0.0009	0.0008	1.0
mmmr	0.0044	0.0050	1.1
rmmr	0.0207	0.0216	1.7
mmrr	0.0428	0.0448	2.9
mmrm+rmrr	0.0736	0.0744	5.9
rmrm	0.0136	0.0063	1.4
rrrr+rrrm+mrrm	0.8440	0.8471	1.0

 $P_m = 0.0679$ $P_{mm} = 0.0317$

weighted resid: 0.000850

standard resid: 0.000440

COCATALYST: $\text{Ph}_3\text{C}^+\text{B}(\text{C}_6\text{F}_5)_4^-$ $[\text{C}_3\text{H}_6] = 1.18 \text{ M}$ $T = 60^\circ\text{C}$

	experimental	calculated	weighting multiplier
pentad			
mmmm	0.0013	0.0013	1.0
mmmr	0.0078	0.0085	1.2
rmmr	0.0223	0.0249	1.7
mmrr	0.0484	0.0525	3.3
mmrm+rmrr	0.1066	0.1076	12.6
rmrm	0.0270	0.0123	1.9
rrrr+rrrm+mrrm	0.7867	0.7929	1.0

 $P_m = 0.0679$ $P_{mm} = 0.0317$

weighted resid: 0.000850

standard resid: 0.000440

Refinement details, Polypropylene ¹³C NMR pentad analysis (8 of 10)

COCATALYST: MAO
[C₃H₆] = 0.363 M
T = 60°C

	experimental	calculated	weighting multiplier
pentad			
mmmm	0.0030	0.0012	1.1
mmmr	0.0068	0.0085	1.2
rmmr	0.0205	0.0228	1.7
mmrr	0.0422	0.0483	2.8
xmrx	0.1209	0.1219	17.3
rmm	0.0313	0.0146	2.2
rrrr+rrrm+mrrm	0.7753	0.7827	1.0

$P_m = 0.0799$
 $P_{mm} = 0.0275$
weighted resid: 0.001286
standard resid: 0.000620

COCATALYST: MAO
[C₃H₆] = 1.60 M
T = 60°C

	experimental	calculated	weighting multiplier
pentad			
mmmm	0.0000	0.0004	1.0
mmmr	0.0013	0.0028	1.0
rmmr	0.0176	0.0175	1.5
mmrr	0.0348	0.0359	2.3
xmrx	0.0523	0.0529	3.6
rmm	0.0084	0.0033	1.2
rrrr+rrrm+mrrm	0.8856	0.8871	1.0

$P_m = 0.0292$
 $P_{mm} = 0.0204$
weighted resid: 0.000053
standard resid: 0.000041

COCATALYST: MAO
[C₃H₆] = 0.760 M
T = 60°C

	experimental	calculated	weighting multiplier
pentad			
mmmm	0.0000	0.0006	1.0
mmmr	0.0042	0.0047	1.1
rmmr	0.0184	0.0191	1.6
mmrr	0.0369	0.0397	2.5
mrrm+rmrr	0.0828	0.0836	7.3
rmm	0.0160	0.0069	1.5
rrrr+rrrm+mrrm	0.8417	0.8452	1.0

$P_m = 0.0496$
 $P_{mm} = 0.0227$
weighted resid: 0.000224
standard resid: 0.000146

COCATALYST: MAO
[C₃H₆] = 2.05 M
T = 60°C

	experimental	calculated	weighting multiplier
pentad			
mmmm	0.0000	0.0005	1.0
mmmr	0.0019	0.0025	1.0
rmmr	0.0183	0.0181	1.6
mmrr	0.0352	0.0370	2.4
mrrm+rmrr	0.0411	0.0421	2.7
rmm	0.0083	0.0026	1.2
rrrr+rrrm+mrrm	0.8952	0.8973	1.0

$P_m = 0.0380$
 $P_{mm} = 0.0261$
weighted resid: 0.000564
standard resid: 0.000342

COCATALYST: MAO
[C₃H₆] = 1.18 M
T = 60°C

	experimental	calculated	weighting multiplier
pentad			
mmmm	0.0000	0.0007	1.0
mmmr	0.0047	0.0045	1.1
rmmr	0.0202	0.0214	1.6
mmrr	0.0401	0.0443	2.7
mrrm+rmrr	0.0648	0.0668	4.8
rmm	0.0192	0.0054	1.6
rrrr+rrrm+mrrm	0.8510	0.8568	1.0

$P_m = 0.0380$
 $P_{mm} = 0.0261$
weighted resid: 0.000564
standard resid: 0.000342

Refinement details, Polypropylene ^{13}C NMR pentad analysis (9 of 10)COCATALYST: $\text{Ph}_3\text{C}^+\text{FAI}(2\text{-C}_6\text{F}_5\text{C}_6\text{F}_4)_3^-$ $[\text{C}_3\text{H}_6] = 0.363 \text{ M}$ $T = 60^\circ\text{C}$

	experimental	calculated	weighting multiplier
pentad			
mmmm	0.0016	0.0009	1.0
mmmr	0.0062	0.0059	1.2
rmmr	0.0198	0.0218	1.6
mmrr	0.0419	0.0455	2.8
xmrx	0.0873	0.0884	8.1
rmm	0.0190	0.0082	1.6
rrrr+rrrm+mrrm	0.8241	0.8293	1.0

 $P_m = 0.0531$ $P_{mm} = 0.0268$

weighted resid: 0.000386

standard resid: 0.000235

COCATALYST: $\text{Ph}_3\text{C}^+\text{FAI}(2\text{-C}_6\text{F}_5\text{C}_6\text{F}_4)_3^-$ $[\text{C}_3\text{H}_6] = 1.60 \text{ M}$ $T = 60^\circ\text{C}$

	experimental	calculated	weighting multiplier
pentad			
mmmm	0.0000	0.0005	1.0
mmmr	0.0005	0.0026	1.0
rmmr	0.0204	0.0195	1.7
mmrr	0.0381	0.0397	2.5
xmrx	0.0379	0.0388	2.5
rmm	0.0083	0.0025	1.2
rrrr+rrrm+mrrm	0.8947	0.8964	1.0

 $P_m = 0.0205$ $P_{mm} = 0.0227$

weighted resid: 0.000073

standard resid: 0.000056

COCATALYST: $\text{Ph}_3\text{C}^+\text{FAI}(2\text{-C}_6\text{F}_5\text{C}_6\text{F}_4)_3^-$ $[\text{C}_3\text{H}_6] = 0.760 \text{ M}$ $T = 60^\circ\text{C}$

	experimental	calculated	weighting multiplier
pentad			
mmmm	0.0000	0.0006	1.0
mmmr	0.0020	0.0035	1.1
rmmr	0.0198	0.0195	1.6
mmrr	0.0386	0.0401	2.6
mrrm+rmrr	0.0575	0.0582	4.0
rmm	0.0099	0.0041	1.3
rrrr+rrrm+mrrm	0.8722	0.8740	1.0

 $P_m = 0.0325$ $P_{mm} = 0.0232$

weighted resid: 0.000075

standard resid: 0.000056

COCATALYST: $\text{Ph}_3\text{C}^+\text{FAI}(2\text{-C}_6\text{F}_5\text{C}_6\text{F}_4)_3^-$ $[\text{C}_3\text{H}_6] = 2.05 \text{ M}$ $T = 60^\circ\text{C}$

	experimental	calculated	weighting multiplier
pentad			
mmmm	0.0000	0.0006	1.0
mmmr	0.0016	0.0030	1.0
rmmr	0.0219	0.0211	1.7
mmrr	0.0414	0.0431	2.8
mrrm+rmrr	0.0402	0.0413	2.7
rmm	0.0090	0.0030	1.3
rrrr+rrrm+mrrm	0.8858	0.8880	1.0

 $P_m = 0.0289$ $P_{mm} = 0.0275$

weighted resid: 0.000262

standard resid: 0.000174

COCATALYST: $\text{Ph}_3\text{C}^+\text{FAI}(2\text{-C}_6\text{F}_5\text{C}_6\text{F}_4)_3^-$ $[\text{C}_3\text{H}_6] = 1.18 \text{ M}$ $T = 60^\circ\text{C}$

	experimental	calculated	weighting multiplier
pentad			
mmmm	0.0016	0.0008	1.0
mmmr	0.0050	0.0040	1.1
rmmr	0.0221	0.0227	1.7
mmrr	0.0432	0.0466	2.9
mrrm+rmrr	0.0507	0.0528	3.4
rmm	0.0135	0.0042	1.4
rrrr+rrrm+mrrm	0.8637	0.8689	1.0

 $P_m = 0.0289$ $P_{mm} = 0.0275$

weighted resid: 0.000262

standard resid: 0.000174

Refinement details, Polypropylene ^{13}C NMRCOCATALYST: $\text{B}(2\text{-C}_6\text{F}_5\text{C}_6\text{F}_4)_3$ $[\text{C}_3\text{H}_6] = 0.363 \text{ M}$ $T = 60^\circ\text{C}$

	experimental	calculated	weighting multiplier
pentad			
mmmm	0.0020	0.0022	1.1
mmmr	0.0116	0.0146	1.3
rmmr	0.0257	0.0276	1.9
mmrr	0.0542	0.0590	3.7
mrrm+rmrr	0.1650	0.1655	45.5
rmm	0.0445	0.0288	3.0
rrrr+rrrm+mrrm	0.6970	0.7022	1.0

 $P_m = 0.1251$ $P_{mm} = 0.0317$

weighted resid: 0.001696

standard resid: 0.000598

COCATALYST: $\text{B}(2\text{-C}_6\text{F}_5\text{C}_6\text{F}_4)_3$ $[\text{C}_3\text{H}_6] = 1.60 \text{ M}$ $T = 60^\circ\text{C}$

	experimental	calculated	weighting multiplier
pentad			
mmmm	0.0000	0.0009	1.0
mmmr	0.0037	0.0058	1.1
rmmr	0.0214	0.0219	1.7
mmrr	0.0445	0.0457	3.0
mrrm+rmrr	0.0858	0.0863	7.8
rmm	0.0150	0.0079	1.5
rrrr+rrrm+mrrm	0.8296	0.8314	1.0

 $P_m = 0.0515$ $P_{mm} = 0.0269$

weighted resid: 0.000126

standard resid: 0.000087

COCATALYST: $\text{B}(2\text{-C}_6\text{F}_5\text{C}_6\text{F}_4)_3$ $[\text{C}_3\text{H}_6] = 0.760 \text{ M}$ $T = 60^\circ\text{C}$

	experimental	calculated	weighting multiplier
pentad			
mmmm	0.0009	0.0014	1.0
mmmr	0.0085	0.0099	1.2
rmmr	0.0237	0.0246	1.8
mmrr	0.0491	0.0522	3.3
mrrm+rmrr	0.1278	0.1283	20.2
rmm	0.0272	0.0166	2.0
rrrr+rrrm+mrrm	0.7628	0.7670	1.0

 $P_m = 0.0858$ $P_{mm} = 0.0303$

weighted resid: 0.000464

standard resid: 0.000238

COCATALYST: $\text{B}(2\text{-C}_6\text{F}_5\text{C}_6\text{F}_4)_3$ $[\text{C}_3\text{H}_6] = 2.05 \text{ M}$ $T = 60^\circ\text{C}$

	experimental	calculated	weighting multiplier
pentad			
mmmm	0.0011	0.0011	1.0
mmmr	0.0062	0.0066	1.2
rmmr	0.0234	0.0248	1.8
mmrr	0.0488	0.0518	3.3
mrrm+rmrr	0.0807	0.0819	7.0
rmm	0.0191	0.0080	1.6
rrrr+rrrm+mrrm	0.8207	0.8257	1.0

 $P_m = 0.0645$ $P_{mm} = 0.0306$

weighted resid: 0.000465

standard resid: 0.000266

COCATALYST: $\text{B}(2\text{-C}_6\text{F}_5\text{C}_6\text{F}_4)_3$ $[\text{C}_3\text{H}_6] = 1.18 \text{ M}$ $T = 60^\circ\text{C}$

	experimental	calculated	weighting multiplier
pentad			
mmmm	0.0025	0.0012	1.1
mmmr	0.0079	0.0079	1.2
rmmr	0.0220	0.0242	1.7
mmrr	0.0475	0.0511	3.2
mrrm+rmrr	0.1025	0.1034	11.5
rmm	0.0223	0.0113	1.7
rrrr+rrrm+mrrm	0.7953	0.8008	1.0

 $P_m = 0.0645$ $P_{mm} = 0.0306$

weighted resid: 0.000465

standard resid: 0.000266

Supporting Information

Diverse Stereocontrol Effects Induced by Weakly Coordinating Anions.

Stereospecific Olefin Polymerization Pathways at Archetypal C_S - and C_1 -

Symmetric Metallocenium Catalysts Using Mono- and Polynuclear

Halo-Perfluoroarylmatalates as Cocatalysts.

John A. S. Roberts, Ming-Chou Chen, Afif M. Seyam, Liting Li, Cristiano Zuccaccia, Nicholas

G. Stahl, and Tobin J. Marks*

Department of Chemistry, Northwestern University

Evanston, Illinois 60208-3113

Experimental and Calculated Pentad Distributions with Correlation Matrices for Entries in Tables 1 and 2.

Table 1 Experiment 2
pentad distributions

	experimental	calculated
m m m m	0	0.053
m m m r	0.301	0.482
r m m r	1.749	1.636
m m r r	3.052	3.435
x m r x	10.452	10.723
r m r m	2.138	0.995
r r r r	69.196	69.416
r r r m	12.144	12.681
m r r m	1.123	0.58

correlation matrix

	Pm	1-Pmm
Pm	1	0.861278
1-Pmm	0.861278	1

refinement results

X2	2.207
Xr2	0.315286
Pm	0.06716
Pmm	0.017823

Table 1 Experiment 4
pentad distributions

	experimental	calculated
m m m m	0	0.058
m m m r	0.161	0.251
r m m r	2.154	2.082
m m r r	3.313	4.23
x m r x	2.56	3.269
r m r m	1.424	0.233
r r r r	82.401	82.713
r r r m	6.979	7.015
m r r m	1.136	0.15

correlation matrix

	Pm	1-Pmm
Pm	1	0.848159
1-Pmm	0.848159	1

refinement results

X2	3.851
Xr2	0.550143
Pm	0.016865
Pmm	0.024233

Table 1 Experiment 6
pentad distributions

	experimental	calculated
m m m m	0	0.04
m m m r	0.011	0.221
r m m r	1.577	1.713
m m r r	2.571	3.496
x m r x	3.093	4.008
r m r m	0.919	0.231
r r r r	82.881	83.09
r r r m	7.487	7.052
m r r m	1.64	0.15

correlation matrix

	Pm	1-Pmm
Pm	1	0.845457
1-Pmm	0.845457	1

refinement results

X2	4.682
Xr2	0.668857
Pm	0.021437
Pmm	0.019701

Table 1 Experiment 7
pentad distributions

	experimental	calculated
m m m m	0.013	0.038
m m m r	0.014	0.177
r m m r	1.771	1.729
m m r r	2.67	3.508
x m r x	2.316	2.906
r m r m	2.07	0.167
r r r r	84.898	85.298
r r r m	5.709	6.069
m r r m	0.54	0.109

correlation matrix

	Pm	1-Pmm
Pm	1	0.8463
1-Pmm	0.8463	1

refinement results

X2	5.175
Xr2	0.739286
Pm	0.015032
Pmm	0.01962

Table 1 Experiment 8
pentad distributions

	experimental	calculated
m m m m	0	0.037
m m m r	0.104	0.173
r m m r	1.713	1.701
m m r r	2.61	3.451
x m r x	2.213	2.886
r m r m	1.504	0.163
r r r r	85.182	85.482
r r r m	5.974	6.002
m r r m	0.823	0.106

correlation matrix

	Pm	1-Pmm
Pm	1	0.844554
1-Pmm	0.844554	1

refinement results

X2	3.57
Xr2	0.51
Pm	0.014938
Pmm	0.019269

Table 1 Experiment 9
pentad distributions

	experimental	calculated
m m m m	0	0.033
m m m r	0	0.153
r m m r	1.492	1.616
m m r r	2.528	3.276
x m r x	1.976	2.701
r m r m	0.99	0.144
r r r r	86.118	86.303
r r r m	5.989	5.679
m r r m	1.079	0.094

correlation matrix

	Pm	1-Pmm
Pm	1	0.840519
1-Pmm	0.840519	1

refinement results

X2	2.941
Xr2	0.420143
Pm	0.01394
Pmm	0.018173

Table 1 Experiment 11
pentad distributions

	experimental	calculated
m m m m	0.018	0.039
m m m r	0	0.156
r m m r	1.869	1.767
m m r r	2.503	3.573
x m r x	1.467	2.278
r m r m	1.531	0.141
r r r r	86.03	86.404
r r r m	5.52	5.554
m r r m	1.063	0.09

correlation matrix

	Pm	1-Pmm
Pm	1	0.839859
1-Pmm	0.839859	1

refinement results

X2	4.858
Xr2	0.694
Pm	0.011475
Pmm	0.019892

Table 1 Experiment 12
pentad distributions

	experimental	calculated
m m m m	0.154	0.045
m m m r	0.296	0.24
r m m r	1.961	1.821
m m r r	2.847	3.716
x m r x	3.505	4.002
r m r m	2.215	0.244
r r r r	82.038	82.54
r r r m	6.478	7.233
m r r m	0.505	0.159

correlation matrix

	Pm	1-Pmm
Pm	1	0.846103
1-Pmm	0.846103	1

refinement results

X2	5.86
Xr2	0.837143
Pm	0.021348
Pmm	0.021087

Table 1 Experiment 13
pentad distributions

	experimental	calculated
m m m m	0.132	0.042
m m m r	0.009	0.202
r m m r	1.696	1.791
m m r r	2.623	3.64
x m r x	2.46	3.255
r m r m	2.035	0.194
r r r r	83.768	84.251
r r r m	6.145	6.5
m r r m	1.132	0.126

correlation matrix

	Pm	1-Pmm
Pm	1	0.839257
1-Pmm	0.839257	1

refinement results

X2	6.482
Xr2	0.926
Pm	0.016996
Pmm	0.0205

Table 1 Experiment 14
pentad distributions

	experimental	calculated
m m m m	0	0.027
m m m r	0	0.153
r m m r	1.358	1.446
m m r r	2.453	2.94
x m r x	2.748	3.33
r m r m	0.631	0.159
r r r r	85.923	85.884
r r r m	6.637	5.959
m r r m	0.705	0.104

correlation matrix

	Pm	1-Pmm
Pm	1	0.844417
1-Pmm	0.844417	1

refinement results

X2	1.654
Xr2	0.236286
Pm	0.017595
Pmm	0.016223

Table 1 Experiment 15
pentad distributions

	experimental	calculated
m m m m	0	0.029
m m m r	0	0.161
r m m r	1.493	1.502
m m r r	2.491	3.054
x m r x	2.785	3.342
r m r m	0.902	0.165
r r r r	85.506	85.569
r r r m	6.485	6.07
m r r m	0.594	0.108

correlation matrix

	Pm	1-Pmm
Pm	1	0.844718
1-Pmm	0.844718	1

refinement results

X2	1.61
Xr2	0.23
Pm	0.017644
Pmm	0.016913

Table 1 Experiment 16
pentad distributions

	experimental	calculated
m m m m	0	0.026
m m m r	0	0.162
r m m r	1.278	1.404
m m r r	2.404	2.862
x m r x	3.106	3.792
r m r m	0.597	0.18
r r r r	85.361	85.145
r r r m	7.497	6.311
m r r m	0.825	0.117

correlation matrix

	Pm	1-Pmm
Pm	1	0.843845
1-Pmm	0.843845	1

refinement results

X2	2.849
Xr2	0.407
Pm	0.020285
Pmm	0.01578

Table 1 Experiment 17
pentad distributions

	experimental	calculated
m m m m	0.405	0.06
m m m r	1.299	0.285
r m m r	1.904	2.083
m m r r	3.065	4.248
x m r x	3.191	3.908
r m r m	2.304	0.275
r r r r	80.56	81.368
r r r m	6.277	7.595
m r r m	0.995	0.179

correlation matrix

	Pm	1-Pmm
Pm	1	0.845877
1-Pmm	0.845877	1

refinement results

X2	10.266
Xr2	1.466571
Pm	0.020616
Pmm	0.024491

Table 2 Experiment 1
pentad distributions

	experimental	calculated
m m m m	0	0.016
m m m r	0.789	0.062
r m m r	1.227	1.199
m m r r	1.67	2.412
x m r x	0.778	1.264
r m r m	1.325	0.055
r r r r	90.982	91.397
r r r m	3.133	3.559
m r r m	0.206	0.035

correlation matrix

	Pm	1-Pmm
Pm	1	0.839584
1-Pmm	0.839584	1

refinement results

X2	3.313
Xr2	0.473286
Pm	0.006277
Pmm	0.012904

Table 2 Experiment 2
pentad distributions

	experimental	calculated
m m m m	0	0.011
m m m r	0	0.048
r m m r	0.644	0.998
m m r r	1.518	2.008
x m r x	0.724	1.305
r m r m	2.239	0.044
r r r r	92.179	92.337
r r r m	3.439	3.221
m r r m	0.101	0.028

correlation matrix

	Pm	1-Pmm
Pm	1	0.838282
1-Pmm	0.838282	1

refinement results

X2	5.603
Xr2	0.800429
Pm	0.006571
Pmm	0.010643

Table 2 Experiment 3
pentad distributions

	experimental	calculated
m m m m	0.003	0.025
m m m r	0.372	0.107
r m m r	1.433	1.448
m m r r	2.207	2.924
x m r x	1.499	1.978
r m r m	1.439	0.097
r r r r	88.24	88.66
r r r m	4.223	4.698
m r r m	0.585	0.063

correlation matrix

	Pm	1-Pmm
Pm	1	0.839968
1-Pmm	0.839968	1

refinement results

X2	3.291
Xr2	0.470143
Pm	0.01001
Pmm	0.015962

Table 2 Experiment 4
pentad distributions

	experimental	calculated
m m m m	0	0.043
m m m r	0.893	0.189
r m m r	1.637	1.838
m m r r	2.843	3.726
x m r x	2.134	2.794
r m r m	1.692	0.174
r r r r	84.454	84.967
r r r m	5.583	6.157
m r r m	0.929	0.112

correlation matrix

	Pm	1-Pmm
Pm	1	0.840326
1-Pmm	0.840326	1

refinement results

X2	5.318
Xr2	0.759714
Pm	0.014326
Pmm	0.020944

Table 2 Experiment 5
pentad distributions

	experimental	calculated
m m m m	0.074	0.05
m m m r	0.187	0.3
r m m r	1.706	1.85
m m r r	3.176	3.797
x m r x	4.646	5.168
r m r m	1.48	0.337
r r r r	79.628	79.952
r r r m	8.013	8.328
m r r m	1.089	0.218

correlation matrix

	Pm	1-Pmm
Pm	1	0.845462
1-Pmm	0.845462	1

refinement results

X2	2.962
Xr2	0.423143
Pm	0.028413
Pmm	0.021727

Table 2 Experiment 6
pentad distributions

	experimental	calculated
m m m m	0	0.102
m m m r	0.653	0.782
r m m r	1.917	2.15
m m r r	4.24	4.551
x m r x	11.821	12.214
r m r m	2.472	1.424
r r r r	63.204	63.381
r r r m	14.18	14.559
m r r m	1.54	0.837

correlation matrix

	Pm	1-Pmm
Pm	1	0.856209
1-Pmm	0.856209	1

refinement results

X2	2.1
Xr2	0.3
Pm	0.080004
Pmm	0.025211

Table 2 Experiment 7
pentad distributions

experimental		calculated
m m m m	0.33	0.084
m m m r	0.69	0.389
r m m r	2.145	2.407
m m r r	4.74	4.923
x m r x	4.677	4.506
r m r m	2.795	0.374
r r r r	77.784	78.407
r r r m	6.735	8.667
m r r m	0.104	0.242

correlation matrix

	Pm	1-Pmm
Pm	1	0.841648
1-Pmm	0.841648	1

refinement results

X2	10.282
Xr2	1.468857
Pm	0.023945
Pmm	0.029143

matrix of correlation average s

	Pm	1-Pmm
Pm	1	0.850409
1-Pmm	0.850409	1

matrix of correlation standard deviation

	Pm	1-Pmm
Pm	0	0.012155
1-Pmm	0.012155	0

Experimental and Calculated Pentad Distributions for Each Entry in Tables 3 and 4.

Table 3 Experiment 1

experimental		pentad distributions			
		calculated			
m m m m	81.9	81.916	82.833	82.788	82.833
m m m r	5.818	4.959	6.36	7.038	6.36
r m m r	1.447	0.572	0.127	0.153	0.127
m m r r	4.114	4.92	6.36	5.385	6.36
x m r x	2.341	2.322	0.507	0.477	0.507
r m r m	0.571	1.163	0.254	0.239	0.253
r r r r	0.412	0.578	0.127	0.094	0.127
r r r m	1.19	1.156	0.254	0.307	0.253
m r r m	2.208	2.45	3.18	3.519	3.18
refinement results		model 1, p = 4	model 2, p = 3	model 3, p = 2	model 4, p = 1
X2		2.59	13.32	11.75	13.32
Xr2		0.52	0	1.68	1.66
bB		1	0.64	0	1
bA		0.99	0	0	0
rA		1	0.96	0.96	0.96
rB		0.83	0.96	0.97	0

Table 3 Experiment 2

experimental		pentad distributions			
		calculated			
m m m m	80.214	80.32	81.208	81.149	81.208
m m m r	6.488	6.215	6.905	7.804	6.905
r m m r	1.398	0.523	0.153	0.192	0.153
m m r r	4.185	4.766	6.905	5.614	6.905
x m r x	2.864	3.383	0.612	0.566	0.612
r m r m	0.587	1.035	0.306	0.283	0.306
r r r r	0.326	0.393	0.153	0.106	0.153
r r r m	1.587	1.076	0.306	0.385	0.306
m r r m	2.351	2.289	3.452	3.902	3.452
refinement results		model 1, p = 4	model 2, p = 3	model 3, p = 2	model 4, p = 1
X2		1.93	18.14	15.38	18.14
Xr2		0.39	3.02	2.2	2.27
bB		0.99	0.63	0	1
bA		0.94	0	0	0
rA		0.98	0.96	0.95	0.96
rB		0.23	0.96	0.97	0

Table 3 Experiment 3

experimental		pentad distributions			
		calculated			
mmmm	83.109	83.125	84.114	84.043	84.114
mmmr	5.932	5.672	5.923	7.007	5.923
rmmr	0.344	0.439	0.108	0.148	0.108
mmrr	2.955	3.305	5.923	4.37	5.923
xmrx	3.649	3.931	0.432	0.379	0.432
rmrm	0.219	0.819	0.216	0.19	0.216
rrrr	0.141	0.283	0.108	0.063	0.108
rrrm	1.992	0.863	0.216	0.297	0.216
mrrm	1.661	1.564	2.961	3.503	2.961
refinement results		model 1, p = 4	model 2, p = 3	model 3, p = 2	model 4, p = 1
		1.94	25.07	21.03	25.07
		0.39	0	3	3.13
		0.99	0.63	0	1
		0.95	0	0	0
		1	0.97	0.96	0.97
		0.14	0.97	0.97	0

Table 3 Experiment 4

experimental		pentad distributions			
		calculated			
mmmm	79.411	79.429	80.763	80.661	80.764
mmmr	7.138	6.718	7.052	8.677	7.052
rmmr	0.457	0.644	0.161	0.237	0.161
mmrr	2.561	3.172	7.052	4.727	7.052
xmrx	5.384	5.75	0.643	0.536	0.643
rmrm	0.412	1.262	0.321	0.268	0.321
rrrr	0.207	0.366	0.161	0.082	0.161
rrrm	2.88	1.232	0.321	0.474	0.321
mrrm	1.549	1.427	3.526	4.338	3.526
refinement results		model 1, p = 4	model 2, p = 3	model 3, p = 2	model 4, p = 1
	X2	4.2	55.04	45.78	55.04
	Xr2	0.84	0	6.54	6.88
	bB	0.98	0.63	0	1
	bA	0.92	0	0	0
	rA	1	0.96	0.95	0.96
	rB	0.17	0.96	0.97	0

Table 3 Experiment 5

		pentad distributions			
experimental		calculated			
mmmm	61.912	62.001	62.463	62.393	62.463
mmmr	11.452	11.237	12.341	13.514	12.341
rmmr	1.354	1.148	0.668	0.78	0.668
mmrr	8.646	9.365	12.341	10.642	12.341
xmrx	5.82	6.237	2.674	2.549	2.674
rmmr	1.219	2.19	1.337	1.275	1.337
rrrr	0.884	0.946	0.668	0.532	0.668
rrrm	3.602	2.315	1.337	1.559	1.337
mrrm	5.112	4.56	6.171	6.757	6.171
refinement results		model 1, p = 4	model 2, p = 3	model 3, p = 2	model 4, p = 1
	X2	3.7	31.43	26.5	31.43
	Xr2	0.74	0	3.79	3.93
	bB	0.99	0.57	0	1
	bA	0.97	0	0	0
	rA	0.96	0.91	0.9	0.91
	rB	0.22	0.91	0.92	0

Table 3 Experiment 6

		pentad distributions			
experimental		calculated			
mmmm	54.902	55.116	55.297	55.158	55.298
mmmr	12.884	12.079	13.94	16.397	13.94
rmmr	2.545	1.798	0.985	1.288	0.985
mmrr	6.269	7.944	13.94	10.409	13.94
xmrx	9.649	10.805	3.941	3.537	3.941
rmmr	1.924	3.555	1.97	1.769	1.97
rrrr	1.41	1.384	0.985	0.668	0.985
rrrm	6.087	3.62	1.97	2.576	1.97
mrrm	4.33	3.699	6.97	8.198	6.97
refinement results		model 1, p = 4	model 2, p = 3	model 3, p = 2	model 4, p = 1
	X2	14.54	119.24	96.34	119.24
	Xr2	2.91	0	13.76	14.9
	bB	0.96	0.58	0	1
	bA	0.94	0	0	0
	rA	0.99	0.89	0.87	0.89
	rB	0.24	0.89	0.91	0

Table 3 Experiment 7

		pentad distributions			
experimental		calculated			
mmmm	56.207	56.343	56.616	56.476	56.616
mmmr	12.921	12.187	13.669	16.273	13.669
rmmr	1.812	1.726	0.921	1.232	0.921
mmrr	5.591	7.095	13.669	9.927	13.669
xmrx	10.564	11.34	3.685	3.259	3.685
rmmr	1.39	3.431	1.842	1.629	1.842
rrrr	1.255	1.228	0.921	0.602	0.921
rrrm	6.348	3.409	1.842	2.464	1.842
mrrm	3.911	3.24	6.834	8.137	6.834
refinement results		model 1, p = 4	model 2, p = 3	model 3, p = 2	model 4, p = 1
X2		16.68	143.25	117.24	143.25
Xr2		3.34	0	16.75	17.91
bB		0.95	0.58	0	1
bA		0.93	0	0	0
rA		1	0.89	0.87	0.89
rB		0.23	0.89	0.92	0

Table 3 Experiment 8

		pentad distributions			
experimental		calculated			
mmmm	61.103	61.216	62.11	61.942	62.11
mmmr	12.048	11.11	12.427	15.327	12.427
rmmr	1.845	1.536	0.682	0.981	0.682
mmrr	3.769	5.691	12.427	8.284	12.427
xmrx	10.109	10.791	2.729	2.298	2.729
rmmr	0.995	3.183	1.365	1.149	1.365
rrrr	0.964	0.984	0.682	0.393	0.682
rrrm	6.434	2.989	1.365	1.962	1.365
mrrm	2.734	2.5	6.213	7.663	6.213
refinement results		model 1, p = 4	model 2, p = 3	model 3, p = 2	model 4, p = 1
X2		21.86	169.94	138.25	169.94
Xr2		4.37	0	19.75	21.24
bB		0.95	0.57	0	1
bA		0.9	0	0	0
rA		1	0.91	0.89	0.91
rB		0.24	0.91	0.94	0

Table 3 Experiment 9

experimental		pentad distributions			
		calculated			
m m m m	55.628	55.638	55.905	55.74	55.905
m m m r	13.758	13.045	13.816	17.227	13.816
r m m r	1.641	1.773	0.955	1.383	0.955
m m r r	3.284	6.264	13.816	8.943	13.816
x m r x	13.194	12.712	3.821	3.176	3.821
r m r m	1.055	3.67	1.911	1.588	1.911
r r r r	1.141	0.974	0.955	0.561	0.955
r r r m	7.802	3.198	1.911	2.767	1.911
m r r m	2.498	2.726	6.908	8.614	6.908
refinement results		model 1, p = 4	model 2, p = 3	model 3, p = 2	model 4, p = 1
X2		37.75	254.25	207.88	254.25
Xr2		7.55	0	29.7	31.78
bB		0.93	0.6	0	1
bA		0.87	0	0	0
rA		1	0.89	0.87	0.89
rB		0.23	0.89	0.93	0

Table 3 Experiment 10

experimental		pentad distributions			
		calculated			
m m m m	46.606	46.857	46.217	46.089	46.217
m m m r	13.153	12.376	15.501	17.651	15.501
r m m r	3.055	2.407	1.503	1.836	1.503
m m r r	8.091	9.993	15.501	12.394	15.501
x m r x	10.389	11.693	6.012	5.595	6.012
r m r m	3.249	4.823	3.006	2.798	3.006
r r r r	2.271	2.138	1.503	1.142	1.503
r r r m	7.447	4.937	3.006	3.671	3.006
m r r m	5.74	4.776	7.751	8.825	7.751
refinement results		model 1, p = 4	model 2, p = 3	model 3, p = 2	model 4, p = 1
X2		16.13	106.56	88.74	106.56
Xr2		3.23	0	12.68	13.32
bB		0.97	0.54	0	1
bA		0.96	0	0	0
rA		0.96	0.86	0.84	0.86
rB		0.33	0.86	0.88	0

Table 3 Experiment 11

		pentad distributions			
experimental		calculated			
m m m m	77.673	77.526	79.032	78.946	79.032
m m m r	7.072	5.036	7.618	8.947	7.618
r m m r	1.156	1.006	0.192	0.259	0.192
m m r r	3.515	4.981	7.618	5.713	7.618
x m r x	4.875	4.053	0.769	0.684	0.769
r m r m	0.414	2.017	0.385	0.342	0.385
r r r r	0.486	1.009	0.192	0.118	0.192
r r r m	2.803	2.012	0.385	0.519	0.385
m r r m	2.005	2.47	3.809	4.473	3.809
refinement results		model 1, p = 4	model 2, p = 3	model 3, p = 2	model 4, p = 1
X2		10.7	45.95	39.79	45.95
Xr2		2.14	7.66	5.68	5.74
bB		1	0.62	0	1
bA		1	0	0	0
rA		1	0.95	0.95	0.95
rB		0.76	0.95	0.97	0

Table 3 Experiment 12

		pentad distributions			
experimental		calculated			
m m m m	69.231	69.315	70.695	70.544	70.695
m m m r	10.222	9.476	10.159	12.698	10.159
r m m r	1.446	1.102	0.391	0.585	0.391
m m r r	2.946	4.421	10.159	6.531	10.159
x m r x	8.187	8.787	1.563	1.28	1.563
r m r m	0.717	2.262	0.782	0.64	0.782
r r r r	0.46	0.623	0.391	0.202	0.391
r r r m	4.75	2.079	0.782	1.17	0.782
m r r m	2.042	1.935	5.079	6.349	5.079
refinement results		model 1, p = 4	model 2, p = 3	model 3, p = 2	model 4, p = 1
X2		12.78	124.14	100.6	124.14
Xr2		2.56	0	14.37	15.52
bB		0.96	0.59	0	1
bA		0.89	0	0	0
rA		1	0.93	0.92	0.93
rB		0.21	0.93	0.96	0

Table 3 Experiment 13

experimental		pentad distributions			
		calculated			
mmmm	69.01	69.19	70.495	70.411	70.495
mmmr	8.282	7.832	10.216	11.535	10.216
rmmr	2.083	1.225	0.397	0.492	0.397
mmrr	5.225	6.293	10.216	8.317	10.216
xmrx	5.442	6.281	1.586	1.473	1.586
rmmr	1.692	2.51	0.793	0.736	0.793
rrrr	1.239	1.091	0.397	0.284	0.397
rrrm	3.659	2.566	0.793	0.985	0.793
mrrm	3.368	3.009	5.108	5.768	5.108
refinement results		model 1, p = 4	model 2, p = 3	model 3, p = 2	model 4, p = 1
X2		4.83	61.32	55.12	61.32
Xr2		0.97	0	7.87	7.66
bB		0.99	0.59	0	1
bA		0.95	0	0	0
rA		0.98	0.93	0.92	0.93
rB		0.33	0.93	0.94	0

Table 4 Experiment 1

experimental		pentad distributions			
		calculated			
mmmm	83.736	83.812	84.708	84.646	84.708
mmmr	5.593	5.334	5.718	6.639	5.718
rmmr	1.12	0.418	0.1	0.132	0.1
mmrr	3.106	3.545	5.718	4.399	5.718
xmrx	2.858	3.291	0.399	0.358	0.399
rmmr	0.244	0.797	0.199	0.179	0.199
rrrr	0.169	0.28	0.1	0.062	0.1
rrrm	1.525	0.837	0.199	0.265	0.199
mrrm	1.649	1.687	2.859	3.319	2.859
refinement results		model 1, p = 4	model 2, p = 3	model 3, p = 2	model 4, p = 1
X2		1.74	18.1	15.21	18.1
Xr2		0.35	0	2.17	2.26
bB		0.99	0.65	0	1
bA		0.94	0	0	0
rA		0.99	0.97	0.96	0.97
rB		0.18	0.97	0.97	0

Table 4 Experiment 2

experimental		pentad distributions			
		calculated			
mmmm	85.336	85.411	86.339	86.281	86.339
mmmr	4.842	4.617	5.148	5.99	5.148
rmmr	1.058	0.413	0.079	0.106	0.079
mmrr	2.67	3.126	5.148	3.943	5.148
xmrx	2.604	3.001	0.316	0.283	0.316
rmmr	0.292	0.807	0.158	0.142	0.158
rrrr	0.144	0.297	0.079	0.049	0.079
rrrm	1.493	0.844	0.158	0.211	0.158
mrrm	1.562	1.483	2.574	2.995	2.574
refinement results		model 1, p = 4	model 2, p = 3	model 3, p = 2	model 4, p = 1
X2		1.56	16.26	13.86	16.26
Xr2		0.31	0	1.98	2.03
bB		0.99	0.66	0	1
bA		0.94	0	0	0
rA		0.99	0.97	0.97	0.97
rB		0.2	0.97	0.98	0

Table 4 Experiment 3

experimental		pentad distributions			
		calculated			
mmmm	83.301	83.373	84.344	84.278	84.344
mmmr	5.68	5.355	5.843	6.84	5.843
rmmr	1.023	0.461	0.105	0.141	0.105
mmrr	3.009	3.526	5.843	4.417	5.843
xmrx	2.985	3.471	0.419	0.373	0.419
rmmr	0.544	0.922	0.209	0.186	0.209
rrrr	0.129	0.304	0.105	0.063	0.105
rrrm	1.654	0.932	0.209	0.282	0.209
mrrm	1.675	1.656	2.922	3.42	2.922
refinement results		model 1, p = 4	model 2, p = 3	model 3, p = 2	model 4, p = 1
X2		1.63	20.33	16.94	20.33
Xr2		0.33	0	2.42	2.54
bB		0.99	0.65	0	1
bA		0.92	0	0	0
rA		0.99	0.97	0.96	0.97
rB		0.21	0.97	0.97	0

Table 4 Experiment 4

		pentad distributions			
experimental		calculated			
mmmm	74.616	74.723	76.036	75.925	76.036
mmmr	8.131	7.554	8.567	10.26	8.567
rmmr	1.383	0.862	0.255	0.355	0.255
mmrr	3.619	4.562	8.567	6.143	8.567
xmrx	5.332	6.125	1.019	0.886	1.019
rmmr	0.74	1.704	0.51	0.443	0.51
rrrr	0.412	0.612	0.255	0.148	0.255
rrrm	3.485	1.746	0.51	0.71	0.51
mrrm	2.282	2.113	4.283	5.13	4.283
refinement results		model 1, p = 4	model 2, p = 3	model 3, p = 2	model 4, p = 1
X2		6.16	59.49	49.42	59.49
Xr2		1.23	0	7.06	7.44
bB		0.98	0.61	0	1
bA		0.94	0	0	0
rA		1	0.95	0.94	0.95
rB		0.21	0.95	0.96	0

Table 4 Experiment 5

		pentad distributions			
experimental		calculated			
mmmm	78.455	78.414	79.739	79.663	79.739
mmmr	6.714	5.144	7.388	8.55	7.388
rmmr	1.407	0.886	0.179	0.235	0.179
mmrr	3.751	5.093	7.388	5.722	7.388
xmrx	3.94	3.574	0.716	0.647	0.716
rmmr	0.773	1.782	0.358	0.323	0.358
rrrr	0.425	0.889	0.179	0.115	0.179
rrrm	2.246	1.776	0.358	0.47	0.358
mrrm	2.29	2.529	3.694	4.275	3.694
refinement results		model 1, p = 4	model 2, p = 3	model 3, p = 2	model 4, p = 1
X2		6.18	33	28.33	33
Xr2		1.24	0	4.05	4.13
bB		1	0.62	0	1
bA		1	0	0	0
rA		1	0.96	0.95	0.96
rB		0.78	0.96	0.97	0

Correlation Matrices for Each Entry in Tables 3 and 4 Under Each Refinement Model.

Table 3	Experiment	1			
	model	1			
			bB	bA	rA
			rB		
	bB		1	0.605919	-0.952626
	bA		0.605919	1	-0.335266
	rA		-0.952626	-0.335266	1
	rB		-0.949395	-0.325406	0.999932
					1

Table 3	Experiment	2			
	model	1			
			bB	bA	rA
			rB		
	bB		1	0.947391	0.626145
	bA		0.947391	1	0.837381
	rA		0.626145	0.837381	1
	rB		-0.535424	-0.69818	-0.796226
					1

Table 3	Experiment	3			
	model	1			
			bB	bA	rA
			rB		
	bB		1	-0.161904	-0.647539
	bA		-0.161904	1	0.617015
	rA		-0.647539	0.617015	1
	rB		0.608183	0.349261	0.168976
					1

Table 3	Experiment	4			
	model	1			
			bB	bA	rA
			rB		
	bB		1	0.941969	0.755463
	bA		0.941969	1	0.927144
	rA		0.755463	0.927144	1
	rB		-0.669004	-0.690151	-0.609889
					1

Table 3	Experiment	5			
	model	1			
			bB	bA	rA
			rB		
	bB		1	-0.206416	-0.364162
	bA		-0.206416	1	0.983895
	rA		-0.364162	0.983895	1
	rB		0.439893	-0.963376	-0.982251
					1

Table 3	Experiment	6			
	model	1			
			bB	bA	rA
			rB		
	bB		1	0.652256	0.590157
	bA		0.652256	1	0.996337
	rA		0.590157	0.996337	1
	rB		-0.572466	-0.992572	-0.995039
					1

model 2

	bB	rA	rB
bB			
rA			
rB			

model 3

	rA	rB
rA	1	-0.516301
rB	-0.516301	1

model 2

	bB	rA	rB
bB	1	0.12953	-0.129526
rA	0.12953	1	-1
rB	-0.129526	-1	1

model 3

	rA	rB
rA	1	-0.511581
rB	-0.511581	1

model 2

	bB	rA	rB
bB			
rA			
rB			

model 3

	rA	rB
rA	1	-0.522191
rB	-0.522191	1

model 2

	bB	rA	rB
bB			
rA			
rB			

model 3

	rA	rB
rA	1	-0.512814
rB	-0.512814	1

model 2

	bB	rA	rB
bB			
rA			
rB			

model 3

	rA	rB
rA	1	-0.441941
rB	-0.441941	1

model 2

	bB	rA	rB
bB			
rA			
rB			

model 3

	rA	rB
rA	1	-0.41914
rB	-0.41914	1

Table 3		Experiment 7				
		model 1	bB	bA	rA	rB
bB			1	0.332109	0.237206	-0.201995
bA			0.332109	1	0.994093	-0.984651
rA			0.237206	0.994093	1	-0.988192
rB			-0.201995	-0.984651	-0.988192	1

Table 3		Experiment 8				
		model 1	bB	bA	rA	rB
bB			1	0.970068	0.8378	-0.857758
bA			0.970068	1	0.940357	-0.926929
rA			0.8378	0.940357	1	-0.894811
rB			-0.857758	-0.926929	-0.894811	1

Table 3		Experiment 9				
		model 1	bB	bA	rA	rB
bB			1	0.959745	0.755111	-0.762336
bA			0.959745	1	0.901533	-0.850767
rA			0.755111	0.901533	1	-0.794378
rB			-0.762336	-0.850767	-0.794378	1

Table 3		Experiment 10				
		model 1	bB	bA	rA	rB
bB			1	0.976725	0.944722	-0.947807
bA			0.976725	1	0.992719	-0.993282
rA			0.944722	0.992719	1	-0.997193
rB			-0.947807	-0.993282	-0.997193	1

Table 3		Experiment 11				
		model 1	bB	bA	rA	rB
bB			1	0.888456	-0.965711	-0.964388
bA			0.888456	1	-0.73884	-0.735435
rA			-0.965711	-0.73884	1	0.999975
rB			-0.964388	-0.735435	0.999975	1

Table 3		Experiment 12				
		model 1	bB	bA	rA	rB
bB			1	0.982165	0.898264	-0.893008
bA			0.982165	1	0.96056	-0.933591
rA			0.898264	0.96056	1	-0.894532
rB			-0.893008	-0.933591	-0.894532	1

model 2

	bB	rA	rB
bB			
rA			
rB			

model 3

	rA	rB
rA	1	-0.425008
rB	-0.425008	1

model 2

	bB	rA	rB
bB			
rA			
rB			

model 3

	rA	rB
rA	1	-0.447867
rB	-0.447867	1

model 2

	bB	rA	rB
bB			
rA			
rB			

model 3

	rA	rB
rA	1	-0.425143
rB	-0.425143	1

model 2

	bB	rA	rB
bB			
rA			
rB			

model 3

	rA	rB
rA	1	-0.382893
rB	-0.382893	1

model 2

	bB	rA	rB
bB	1	0.301448	-0.301468
rA	0.301448	1	-1
rB	-0.301468	-1	1

model 3

	rA	rB
rA	1	-0.505644
rB	-0.505644	1

model 2

	bB	rA	rB
bB			
rA			
rB			

model 3

	rA	rB
rA	1	-0.479768
rB	-0.479768	1

Table 3	Experiment 13 model 1				
		bB	bA	rA	rB
	bB	1	0.869929	0.124218	-0.197397
	bA	0.869929	1	0.576481	-0.628985
	rA	0.124218	0.576481	1	-0.840135
	rB	-0.197397	-0.628985	-0.840135	1

Table 4	Experiment 13 model 1				
		bB	bA	rA	rB
	bB	1	0.151804	-0.718464	0.74872
	bA	0.151804	1	0.237062	0.330899
	rA	-0.718464	0.237062	1	-0.141805
	rB	0.74872	0.330899	-0.141805	1

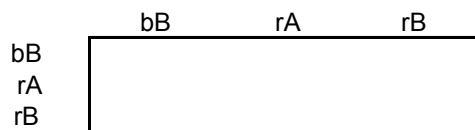
Table 4	Experiment 1 model 1				
		bB	bA	rA	rB
	bB	1	-0.594897	-0.91492	0.81158
	bA	-0.594897	1	0.630967	-0.452618
	rA	-0.91492	0.630967	1	-0.558909
	rB	0.81158	-0.452618	-0.558909	1

Table 4	Experiment 2 model 1				
		bB	bA	rA	rB
	bB	1	0.993013	0.96043	-0.956079
	bA	0.993013	1	0.984879	-0.977318
	rA	0.96043	0.984879	1	-0.969544
	rB	-0.956079	-0.977318	-0.969544	1

Table 4	Experiment 3 model 1				
		bB	bA	rA	rB
	bB	1	0.980857	0.959318	-0.94936
	bA	0.980857	1	0.995147	-0.989227
	rA	0.959318	0.995147	1	-0.990077
	rB	-0.94936	-0.989227	-0.990077	1

Table 4	Experiment 4 model 1				
		bB	bA	rA	rB
	bB	1	0.815646	0.203551	0.221243
	bA	0.815646	1	0.732452	0.744641
	rA	0.203551	0.732452	1	0.999719
	rB	0.221243	0.744641	0.999719	1

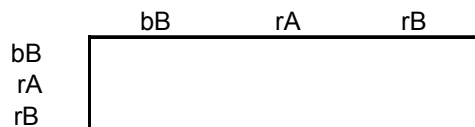
model 2



model 3

	rA	rB
rA	1	-0.474174
rB	-0.474174	1

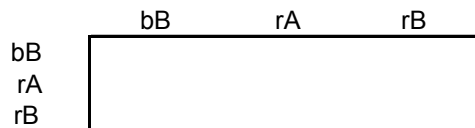
model 2



model 3

	rA	rB
rA	1	-0.523556
rB	-0.523556	1

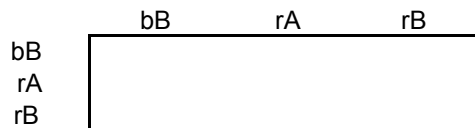
model 2



model 3

	rA	rB
rA	1	-0.528641
rB	-0.528641	1

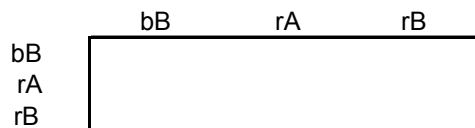
model 2



model 3

	rA	rB
rA	1	-0.522627
rB	-0.522627	1

model 2



model 3

	rA	rB
rA	1	-0.496325
rB	-0.496325	1

model 2



model 3

	rA	rB
rA	1	-0.507481
rB	-0.507481	1

average	model	1				
			bB	bA	rA	rB
	bB		1	0.616935	0.184942	-0.368155
	bA		0.616935	1	0.679662	-0.595427
	rA		0.184942	0.679662	1	-0.460243
rB		-0.368155	-0.595427	-0.460243	1	

stdev	model	1				
			bB	bA	rA	rB
	bB		0	0.498402	0.742334	0.650479
	bA		0.498402	0	0.492441	0.535401
	rA		0.742334	0.492441	0	0.741114
rB		0.650479	0.535401	0.741114	0	

avedev/average	model	1				
			bB	bA	rA	rB
	bB		0	0.643863	3.444797	1.511232
	bA		0.643863	0	0.505243	0.676249
	rA		3.444797	0.505243	0	1.286279
rB		1.511232	0.676249	1.286279	0	

kurtosis	model	1				
			bB	bA	rA	rB
	bB			0.698079	-1.431856	-0.941155
	bA		0.698079		3.831935	1.416484
	rA		-1.431856	3.831935		0.384085
rB		-0.941155	1.416484	0.384085		

model 2
average

	bB	rA	rB
bB	1	0.215489	-0.215497
rA	0.215489	1	-1
rB	-0.215497	-1	1

model 3
average

	rA	rB
rA	1	-0.480172
rB	-0.480172	1

model 2
stdev

	bB	rA	rB
bB	0	0.121565	0.121581
rA	0.121565	0	3.4E-12
rB	0.121581	3.41E-12	0

model 3
stdev

	rA	rB
rA	0	0.045123
rB	0.045123	0

model 2
stdev/average

	bB	rA	rB
bB	0	0.398904	0.398942
rA	0.398904	0	2.41E-12
rB	0.398942	2.41E-12	0

model 3
stdev/average

	rA	rB
rA	0	0.079935
rB	0.079935	0

model 2
kurtosis

	bB	rA	rB
bB	#DIV/0!	#DIV/0!	#DIV/0!
rA	#DIV/0!	#DIV/0!	#DIV/0!
rB	#DIV/0!	#DIV/0!	

model 3
kurtosis

	rA	rB
rA		-0.673098
rB	-0.673098	

John A. S. Roberts

(773)531-0338 • jrobert1@northwestern.edu

Profile

A creative, practical experimentalist with a strong chemical intuition and natural scientific mindset. Able to visualize/describe chemical architectures and complex, time-dependent processes, and apply mathematical/statistical approaches to data analysis. Able to strategize, evaluate evidence and arguments, and communicate succinctly. Comfortable working alone or as part of a team, equating team and individual success. Can produce research ideas and contribute constructively to ongoing research dialogue. Appreciates rapid advances but insists on quality, craftsmanship, and completeness in the products of chemical research. Able to absorb knowledge in new areas and new techniques, integrate knowledge across disparate disciplines.

Research Interests

- Low-impact, renewable chemical methods for energy conversion and storage
- Catalytic hydrogen production
- Photoinduced modulation of bond enthalpies and reactivities
- Molecular switching and logic componentry
- Development of solid- and solution-state light-harvesting methods
- New solid-state architectures, synthetic methodologies, analytical techniques
- Interfacing of solid-state, nanoscale, and molecular scale architectures
- Electronics applications for materials
- Integration of solid-state and solution catalysis
- Research data management and knowledge base building

Expertise

- Homogeneous olefin polymerization catalysis
- Polyolefin chemistry
- Synthetic organometallic chemistry
- Stereoselective olefin polymerization kinetics

John A. S. Roberts

(773)531-0338 • jrobert1@northwestern.edu

- Polymer microstructural analysis
- Development and application of mathematical models and statistical analyses for kinetic data and polymer stereosequence distributions
- Single crystal X-ray crystallographic analysis (small molecules and clusters)
- Multidimensional NMR spectroscopy (NOE, EXSY, COSY, HSQC)
- Dynamic NMR acquisition and data analysis for fluxional systems
- Varian VNMR script programming
- Mass spectrometry (MALDI, GCMS)
- Gas, liquid and solid IR, UV/VIS spectroscopy
- Gel permeation chromatography
- Inert-atmosphere manipulations (glovebox, Schlenk, glass high vacuum techniques)
- Scientific glassblowing

Education

- Ph.D., Inorganic Chemistry, Northwestern University, Evanston, IL. December 2006
Thesis Topic: *Counteranion effects in stereoselective propylene polymerization mediated by homogeneous metallocene ion-pair complexes*
Thesis Committee: Tobin Marks (Advisor), Kenneth Poepelmeier, James Ibers
- B.S., Mathematics, University of Wisconsin, Madison. Awarded 2001. Emphasis on linear and abstract algebra (group/field theory), development of mathematical proofs.

Graduate Publications

Roberts, John A. S.; Chen, Ming-Chou; Marks, Tobin J. **Diverse Stereocontrol Effects Induced by Weakly Coordinating Anions. Stereospecific Olefin Polymerization Pathways at**

John A. S. Roberts

(773)531-0338 • jrobert1@northwestern.edu

Archetypal C_5 - and C_1 -Symmetric Metallocenium Catalysts Using Mono and Polynuclear Halo Perfluoroarylmethylates as Cocatalysts. Manuscript submitted for publication.

Chen, M.-C.; Roberts, J. A. S.; Seyam, A. M.; Li, L.; Zuccaccia, C.; Stahl, N. G.; Marks, T. J. **Diversity in weakly coordinating anions. Mono- and polynuclear halo-perfluoroarylmethylates as cocatalysts for stereospecific olefin polymerization: synthesis, structure, and reactivity.** *Organometallics* **2006**, *25*, 2833-2850s.

Schneider, Sven; Roberts, John A. S.; Salata, Michael R.; Marks, Tobin J. **Mixed diketonate thiolate copper(I) precursors for materials synthesis: control of Cu₂S-forming thermolysis pathways by manipulating Lewis acid and base cluster building blocks.** *Angew. Chem., Int. Ed.*, **2006**, *45*(11), 1733-1736.

Chen, Ming-Chou; Roberts, John A. S.; Marks, Tobin J. **New mononuclear and polynuclear perfluoroarylmethylate cocatalysts for stereospecific olefin polymerization.** *Organometallics*, **2004**, *23*(5), 932-935.

Chen, Ming-Chou; Roberts, John A. S.; Marks, Tobin J. **Marked counteranion effects on single-site olefin polymerization processes: Correlations of ion-pair structure and dynamics with polymerization activity, chain transfer, and syndiospecificity.** *J. Am. Chem. Soc.*, **2004**, *126*(14), 4605-4625.

Zuccaccia, Cristiano; Stahl, Nicholas G.; Macchioni, Alceo; Chen, Ming-Chou; Roberts, John A. S.; Marks, Tobin J. **NOE and PGSE NMR spectroscopic studies of solution structure and aggregation in metallocenium ion-pairs.** *J. Am. Chem. Soc.*, **2004**, *126*(5), 1448-1464.

John A. S. Roberts

(773)531-0338 • jrobert1@northwestern.edu

Graduate Presentations and Awards

Roberts, John A. S.; Chen, Ming-Chou; Marks, Tobin J. **Marked Counteranion Effects on Single-Site Olefin Polymerization Processes. Correlations of Ion Pair Structure and Dynamics with Polymerization Activity, Chain Transfer, and Syndioselectivity** (Poster), presented at:

- International Symposium on Relations between Homogeneous and Heterogeneous Catalysis (ISHHC-XI), Northwestern University, July 2003
- The Annual Scientific Meeting of the Institute for Environmental Catalysis (IEC), Northwestern University, March 2002

Roberts, John A. S. **Catalyst Ion-Pairing Effects on the Stereochemistry of Propylene Polymerization** (Seminar), presented at:

- Northwestern University Inorganic Chemistry Seminar Series

Northwestern University Academy Fellowship. Awarded January 2002. Extended to two years' duration.

Undergraduate Publications

Saulys, Dovas A.; Kuech, Thomas F.; Roberts, John A. **A safe alternative to the use of silane, WARF (Wisconsin Alumni Research Foundation) Disclosure P03104US.** Materials Research Science and Engineering Center, University of Wisconsin, Madison.

Guzei, Ilia A.; Roberts, John; Saulys, Dovas A. **Pseudosymmetry in pyridinium tetrachloro(oxo)pyridineniobate(V) pyridine solvate.** *Acta Crystallogr., Sect. C: Cryst. Struct. Commun.* **2002**, C58(3), m141-m143.

John A. S. Roberts

(773)531-0338 • jrobert1@northwestern.edu

Research and Teaching Experience

Teaching Assistant, General and Analytical Chemistry, University of Wisconsin, Madison, Spring 2000.

Teaching Assistant, General and Analytical Chemistry, Northwestern University, Evanston, IL, academic year 2001.

Research Assistant, Materials Research Science and Engineering Center, University of Wisconsin, Madison, 1998-2000. Advisors: Prof. Donald Gaines (Dept. of Chemistry), Dr. Dovas Saulys.